Development of a prefactored high-order compact scheme for low-speed aeroacoustics

Ivan Spisso

Department of Engineering

University of Leicester

A thesis submitted for the degree of

Doctor of Philosophy

2013

Development of a prefactored high-order compact scheme for low-speed aeroacoustics

Ivan Spisso

A new class of cost-optimized prefactored high-order compact schemes is developed for shock-free error-bounded aeroacoustic applications. The cost-optimization theory of Pirozzoli (2007), based on the minimization of the computational cost for a given level of error, is applied to a class of prefactored compact sixth-order schemes. They are extended to obtain a new class of time-explicit cost-optimized schemes.

Appropriate high-order prefactored boundary closures are coupled with the new interior schemes. Their effect on the stability and accuracy of the interior schemes and their wave propagation characteristics in Fourier space are investigated. More conventional non-reflecting boundary conditions are shown to display an impedance mis-match, reducing the order of accuracy of the overall scheme. An 11-point stencil with double precision accuracy is used as the prefactored interior boundary stencil. It shows a better performance in spectral sense compared to the equivalent ones available in literature. An eigenvalue analysis is performed, to verify the stability of the prefactored cost-optimized schemes coupled with the boundary closures. Characteristics based boundary conditions and absorbing layers are evaluated.

A parallelization strategy, based on a finite-sized overlapping interface, is presented and weak scalability tests results are shown.

The theoretical roll-off error of the new schemes agree well with the computed norm error roll-off between the analytical prediction and the numerical experiments, for a monochromatic sinusoidal test-case. There is a good agreement between the predicted percentage cost-saving of the one-dimensional cost function and the savings in computational time from the numerical tests. A 22% computational cost-saving at the design level of error is achieved.

Sample applications to broadband and two-dimensional space benchmark problems demonstrate the low error-bounded and high-order accuracy characteristics of the baseline scheme for aeroacoustic applications.

Acknowledgement

Well, it is not easy to say thanks to all the people that help and support me during these years. First of all, I want to thank Dr. Rona, who has been supervisor and mentor of my PhD studies. Thanks to Dr. Emmanuel Georgoulis, for his attentive mathematical insight. Thanks has to be given to all the fellows, friends and colleguas at the University of Leicester, starting from Mohammed Fekry Farah El-Dosoky, up to Massimiliano Canali. Thanks to Marco Grottadaurea, Manuele Monti and Davide DiPasquale and to all the fellows of the AeroTranet Consortium, travel mates during the AeroTraNet Consortium's adventure.
Thanks to Dr. P. Ghillani, former student and a colleague which gave me the opportunity to learn with his long and useful discussions.
A special thanks has to be given to Prof. Pirozzoli and Dr. M. Bernardini, who acts as hosting members during my PhD studies, for their hospitality and advises.
Thanks to all the CINECA's staff to provide me the computational time, precious help and support.
Of course, thanks to Valeria for her invaluable patience and care along these years. Thanks to my parents, who fostered me to chase up my way.

The rigorous theoretical approach is most useful in providing understanding of the basic phenomena... In most cases, the rigorous model is a simplification or idealization of the actual conditions ... the shortcomings of the model can be overshadowed by the gain in knowledge and understanding achieved (Kraft & Motsinger, 1991).

This thesis has been typeset using LaTeX.

Contents

List of figures **xi**

List of tables **xiii**

1 Introduction **1**

1.1 Context 1

1.2 Aims and objectives 3

1.3 Thesis outline 5

2 Numerical background **7**

2.1 Spatial discretization 7

2.2 Time-marching schemes for CAA 12

2.3 Performance analysis of finite-difference schemes 14

2.4 Cost-performance trade-off for CAA algorithms 16

2.5 Spatial and temporal error analysis 20

2.5.1 Spatial and temporal resolving efficiency 24

3 Numerical Method **26**

3.1 Governing Equations 28

3.1.1 Derivation of the quasi-linear Euler Equations 28

3.1.2 Linearized Euler Equations 29

3.1.2.1 Non-dimensional form 31

3.1.2.2 Characteristic form 32

3.2 Spatial Discretization 36

3.2.1 Interior scheme 36

3.2.2 Computational efficiency 41

3.2.3 Optimization of the finite-difference scheme . . . 47
3.2.4 Prefactorization . . . 52
3.3 Temporal Integration . . . 57
3.3.1 Effect of time integration . . . 57
3.3.2 Baseline temporal solver . . . 58
3.3.3 Cost-optimized temporal solver . . . 58
3.4 Predicted performance of the cost-optimized schemes . . . 66
3.5 Perimetrical scheme . . . 74
3.5.1 Spatial Differentiation . . . 74
3.5.2 Eigenvalue analysis . . . 88
3.6 Artificial Boundary Conditions . . . 97
3.6.1 Characteristic based boundary conditions . . . 97
3.6.1.1 Subsonic inflow . . . 98
3.6.1.2 Subsonic outflow . . . 99
3.6.1.3 Inviscid wall . . . 100
3.6.2 Absorbing layers . . . 102
3.6.2.1 *Type* I Absorbing layer . . . 103
3.6.2.2 *Type* II Absorbing layer . . . 103
3.7 Chapter summary and achievements . . . 106

4 MPI single domain decomposition 108
4.1 Parallelization strategy . . . 108
4.2 Weak scalability tests . . . 109
4.3 Further work . . . 110
4.4 Chapter summary and achievements . . . 112

5 Verification and Validation 113
5.1 One-Dimensional Test-Cases . . . 113
5.1.1 Monochromatic sinusoidal wave . . . 113
5.1.2 Gaussian pulse . . . 132
5.2 Two-Dimensional Test-Cases . . . 136
5.2.1 Propagation of an acoustic wave in unbounded domain . . . 136
5.3 Chapter summary and achievements . . . 139

6 Conclusion **142**

A Appendix **144**

A.1 Derivation of the amplification factor for the time integration 144

A.2 LODI system along y axis 144

A.3 Coefficients for FD schemes 151

A.4 Eigenvalue spectrum 161

A.5 Efficiency comparison 168

A.6 Time Integration 185

A.7 Boundaries error 186

A.8 Wavenumber performance of the FD schemes with closures 188

A.8.1 Derivation of the coefficients for the prefactored operators for higher-order accuracy 188

A.8.2 Boundary stencils 194

A.8.3 Prefactored one-sided boundary stencil 194

A.8.3.1 Derivation of the coefficients 194

A.8.3.2 Wave propagation characteristics 207

A.9 Validation results 217

A.9.1 Monochromatic sinusoidal wave 217

References **227**

List of Figures

2.1 Variation of discrete function $f_i = f(x_i)$ along uniformly discretised streamwise length L. 8

2.2 Iso-contours of normalized 'local' error function and normalized one-dimensional cost function for $C1122/RK4$ scheme. 17

2.3 Iso-contours of normalized 'local' and 'global' error functions for $C1122/RK4$ scheme. 19

2.4 Iso-contour level $\tilde{\epsilon} = 10^{-4}$ of normalized 'local' error function versus normalized cost function in one and two dimensions for $C1122/RK4$ scheme. 21

2.5 Iso-contour of normalized 'local' error function and normalized one-dimensional cost function for $C1122/RK4$ scheme. 23

2.6 Iso-contours of the normalized approximate 'local' and 'global' error functions for $C1122/RK4$ scheme. 25

3.1 Pseudo-wavenumber diagram for the centred finite-difference schemes reported in Tabs. 3.1 and 3.2. 37

3.2 Dispersive error for the centred finite-difference schemes reported in Tabs. 3.1 and 3.2. 37

3.3 Group velocity for the centred finite-difference schemes reported in Tabs. 3.1 and 3.2. 38

3.4 Optimal 'local' error, reduced wavenumber and Courant number as a function of cost for the centred spatial discretizations listed in Fig. 3.1 coupled with RK4 time integration in one space dimension. 42

3.5 Optimal 'global' error, reduced wavenumber and Courant number as a function of cost for the centred spatial discretizations listed in Fig. 3.1 coupled with RK4 time integration in one space dimension. 43

3.6 Contours of normalized 'local' error function and corresponding normalized one-dimensional cost function for the $C1122$ and the TamDRP scheme. 46
3.7 Optimal 'local' error, reduced wavenumber and Courant number as a function of cost for the centred spatial discretizations selected in Fig. 3.1 coupled with the RK4 time integration in two space dimensions. 48
3.8 Optimal 'global' error, reduced wavenumber and Courant number as a function of cost for the centred spatial discretizations selected in Fig. 3.1 coupled with the RK4 time integration in two space dimensions. 49
3.9 Contours of normalized 'local' error function for C1122 scheme, normalized one-dimensional cost function, and normalized two-dimensional cost function. 50
3.10 Optimal values of coefficients α_1, non-optimal and optimal 'spatial resolving efficiency' $\breve{\kappa}^*$ for the tridiagonal compact scheme $C1122$ of eq. (3.29). 51
3.11 Dispersive and dissipative errors for the $C1122$ and cost-optimized $C12\mathsf{epsm}5$, $C12\mathsf{epsm}4$, $C12\mathsf{epsm}3$ schemes. 52
3.12 Dispersive characteristics of the prefactored classical $C1122$ and cost-optimized $C12\mathsf{epsm}5$, $C12\mathsf{epsm}4$, $C12\mathsf{epsm}3$ schemes. 56
3.13 Optimal 'local' error, reduced wavenumber and Courant number as a function of cost for the centred spatial discretizations selected in Fig. 3.1 coupled with the RK3 time integration in two space dimensions. 59
3.14 Contours of normalized 'local' error function for $C1122$ scheme coupled with RK3 and RK4 time integration scheme. 60
3.15 Optimal 'global' error, reduced wavenumber and Courant number as a function of cost for the centred spatial discretizations selected in Fig. 3.1 coupled with the RK3 time integration in two space dimensions. 61
3.16 Optimal values of temporal resolving efficiencies $\breve{z}^*(\tilde{\epsilon})$, γ_3 and γ_4 for second order, four stage optimized RK time integration scheme. 64
3.17 Stability foot-prints for the classical and cost-optimized RK4 time integration schemes. 64
3.18 Amplification rate $|r|$ and difference in phase δ for the classical and cost-optimized RK4 time integration schemes. 65
3.19 Temporal dissipation E_d and phase error E_δ in logarithmic scale for the classical and cost-optimized RK4 time integration schemes. 65

3.20 Contours of normalized 'local' error function for the cost-optimized scheme and the non-optimized baseline solver $C1122/RK4$. 69
3.21 Contours of normalized 'local' error function for the cost-optimized epsm4 scheme and for the corresponding non-optimal baseline $C1122/RK4$ scheme. . 70
3.22 Contours of normalized 'local' error function for the cost-optimized epsm5 scheme and for the corresponding non-optimal baseline $C1122/RK4$ scheme. . 71
3.23 Optimal 'local' error, reduced wavenumber and Courant number as a function of the two-dimensional cost for the baseline $C1122/RK4$ scheme and the cost-optimized epsm5, epsm4, epsm3 schemes. 72
3.24 Iso-level of the normalized 'local' error function $e(\kappa, \sigma)$ for the cost-optimized epsm4 scheme and of the cost function in two dimensional space. 73
3.25 Boundary closure error propagation inside the computational domain. 76
3.26 Sketch of the backward and forward sweeps at the interior boundary $i = 1 \equiv N$. 79
3.27 Dispersive characteristics of the prefactored one-sided boundary stencils for $i = 1$. 82
3.28 Dispersive characteristics of the forward prefactored interior 11-point stencils for i-th node. 86
3.29 Effect of boundary closures of eq. (A.88) on the eigenvalue spectrum s^* for the classical Padè $C1111$ scheme. 91
3.30 Eigenvalue spectrum for the classical $C1122$ scheme and the cost-optimized $C12$epsm$n$ schemes, with $n = 5, 4, 3$. 92
3.31 Eigenvalue spectrum for the fourth-order prefactored compact $C1122$ scheme of Ashcroft & Zhang (2003) coupled with third-order boundary closure. 94
3.32 Eigenvalue spectrum for the prefactored classical $C1122$ scheme coupled with the one-sided boundary stencils of Ashcroft & Zhang (2003). 94
3.33 Eigenvalue spectrum for the prefactored classical $C1122$ scheme and the cost-optimized $C12$epsm$n$. 95
3.34 Characteristic velocities λ_i for subsonic inflow at $x = a$ and $x = b$. 99
3.35 Characteristic velocities λ_i for subsonic outflow at $x = a$ and $x = b$. 100
3.36 Characteristic velocities λ_i for a subsonic inflow at $x = a$ and an inviscid wall at $x = b$. 101
3.37 Sketch of the outflow absorbing layer at the computational domain boundary $x = b$. 105

4.1 Domain decomposition and communication scheme with 4 blocks ($m = n = 2$). 109
4.2 Solution to test-case of Sec. 5.2.1 with the MPI domain decomposition. 111
4.3 Domain decomposition and communication scheme with slab decomposition: (a) decomposition in Y direction; (b) decomposition in X direction. 112

5.1 Solution to *LAE* equation with monochromatic sinusoidal wave of eq. (5.2). . . 116
5.2 Solution to *LAE* equation with monochromatic sinusoidal wave of eq. (5.2), over the domain $-2 \leq x \leq 3$. 118
5.3 Comparison of the theoretical dissipative error e_0 from Fig. 3.11(b) with the computed normalized $\overline{L}_2$ norm error for the monochromatic sinusoidal wave. . 119
5.4 Numerical grid used for the computed iso-maps reported in Fig 5.5. 121
5.5 Comparison between the theoretical and the computed iso-contours of normalized 'local' error function for the monochromatic sinusoidal wave. 123
5.6 Theoretical and numerical contours of optimal 'local' error error function as a function of the one-dimensional cost for the monochromatic sinusoidal wave. . 124
5.7 Comparison of the theoretical and numerical optimal 'local' error versus cost, reduced wavenumber and Courant number as a function of the one-dimensional cost for the monochromatic sinusoidal wave. 127
5.8 Theoretical and numerical optimal 'local' error versus cost as a function of the one-dimensional cost function, and measured elapsed time versus the normalized computed $\overline{L}_2$ norm error for the monochromatic sinusoidal wave. 128
5.9 Numerical and physical reflected waves at outlet boundary: Fig. 5.9(a) LAE; Fig. 5.9(b) LEE. 134
5.10 Solution to *LAE* equation with initial Gaussian profile. 135
5.11 Propagation of a two-dimensional acoustic pulse on an unbounded domain at non-dimensional $t = 30$ with fixed $\sigma = 0.05$. 138

A.1 Scaled pseudo-wavenumber diagram for a selection of explicit centered finite-difference schemes. 155
A.2 Dispersive error for a selection of explicit centered finite-difference schemes. . 156
A.3 Absolute maximum real parts of the eigenvalues of eq. (3.67) varying the number of nodes. 164
A.4 Iso-contours of normalized 'local' and 'global' error function $C0011/RK4$, and normalized one-dimensional cost function. 168

A.5 Iso-contours of normalized 'local' and 'global' error function $C0033/RK4$, and normalized one-dimensional cost function. 169
A.6 Iso-contours of normalized 'local' and 'global' error function $TamDRP/RK4$, and normalized one-dimensional cost function. 170
A.7 Iso-contours of normalized 'local' and 'global' error function $C1122/RK4$, and normalized one-dimensional cost function. 171
A.8 Iso-contours of normalized 'local' and 'global' error function $C2233/RK4$, and normalized one-dimensional cost function. 172
A.9 Iso-contours of normalized 'local' and 'global' error function $Lui\&Lele/RK4$, and normalized one-dimensional cost function. 173
A.10 Iso-contours of normalized 'local' and 'global' error function $Kim/RK4$, and normalized one-dimensional cost function. 174
A.11 Iso-contours of normalized 'local' and 'global' error function $C0011/RK4$, and normalized two-dimensional cost function. 175
A.12 Iso-contours of normalized 'local' and 'global' error function $C0033/RK4$, and normalized two-dimensional cost function. 176
A.13 Iso-contours of normalized 'local' and 'global' error function $Tam/RK4$, and normalized two-dimensional cost function. 177
A.14 Iso-contours of normalized 'local' and 'global' error function $C1122/RK4$, and normalized two-dimensional cost function. 178
A.15 Iso-contours of normalized 'local' and 'global' error function $C2233/RK4$, and normalized two-dimensional cost function. 179
A.16 Iso-contours of normalized 'local' and 'global' error function $Lui\&Lele$, and normalized two-dimensional cost function. 180
A.17 Iso-contours of normalized 'local' and 'global' error function $Kim/RK4$, and normalized one-dimensional cost function. 181
A.18 Iso-contours of normalized 'local' and 'global' error function $C0011/RK3$, and normalized two-dimensional cost function. 182
A.19 Iso-contours of normalized 'local' and 'global' error function $C0033/RK3$, and normalized two-dimensional cost function. 183
A.20 Iso-contours of normalized 'local' and 'global' error function $Tam/RK3$, and normalized two-dimensional cost function 184

A.21 Stability foot-prints, dissipation rate and phase error for the third-order *RK*3 and fourth-order *RK*4 time integration schemes. 185
A.22 Solution to *LAE* equation with monochromatic sinusoidal wave of eq. (5.2), over the central domain $0 \leq x \leq 1$. 219
A.23 Enlarged view of the comparison between the theoretical and the computed 'local' error function $e(\kappa, \sigma)$ for the monochromatic sinusoidal wave. 220
A.24 Theoretical and numerical contours of optimal 'local' error error function as a function of the one-dimensional cost for the monochromatic sinusoidal wave. . 221

List of Tables

3.1 Coefficients for explicit centred finite-difference schemes $CPQRS$ in Fig. 3.1. $P = Q = 0$, $R = S$, $\alpha_0 = 1$, $a_0 = 0$, $a_{-j} = a_j$ in eq. (2.1). The number of algebraic operation per node N_{op} has been taken from Colonius & Lele (2004). 39

3.2 Coefficients for implicit centred finite-difference schemes $CPQRS$ in Fig. 3.1. $P = Q \neq 0$, $R = S$, $\alpha_0 = 1$, $a_0 = 0$, $a_{-j} = a_j$ in eq. (2.1). The number of algebraic operation per node N_{op} has been taken from Colonius & Lele (2004). 39

3.3 Spatial discretization coefficients of classical and optimized schemes. 51

3.4 Prefactored spatial discretization coefficients of the classical and optimized schemes. 55

3.5 Runge-Kutta coefficients and performance for the classical and optimized time integration schemes; $\check{z}^*(\tilde{\epsilon})_{nonopt}$ is relative to the classical RK4 time integration scheme. For all schemes $\gamma_1 = 1$, $\gamma_2 = 1/2$. 63

3.6 Performance of cost-optimized schemes for different target errors in two dimensional space. 68

3.7 Approximate optimal operating points of cost-optimized schemes for different target errors in two dimensional space. 68

3.8 Real part of the first two positive eigenvalue pairs $s^*_{1,2}$ and $s^*_{3,4}$ from eq. (3.67) for different number of nodes N. Classical prefactored $C1122$, cost-optimized $C1122$epsm5, $C1122$epsm4 and $C1122$epsm3 interior schemes. 96

5.1 Stability and accuracy limits for the classical $C1122$ and the cost-optimized $C1122$epsm$n$ (with $n = 5, 4, 3$) schemes. Standard $RK4$ is used for the time integration ($z_s = 2.83$, $z_d = 0.7323$). 114

5.2 Stability limits for the classical $C1122$ and the cost-optimized epsm$n$ (with $n = 5, 4, 3$) schemes. 119

5.3 Absolute percentage difference Δc_1^* between theoretical and numerical cost-optimal operating points as function of the one-dimensional cost for the monochromatic sinusoidal wave. The brackets report, respectively, theoretical and numerical cost-optimal values. The bold values are used in following Tab. 5.5. . . 125

5.4 Measured computational elapsed *time* in secs. and computed normalized $\overline{L}_2$ norm error for the classical $C1122$ and the cost-optimized schemes epsm$n$ at the computed optimal cost-error operational points. Final non-dimensional time $T = 1$. 129

5.5 Measured computational elapsed *time* in secs. and computed normalized $\overline{L}_2$ norm error for the classical $C1122$ and the cost-optimized schemes epsm$n$ at the computed optimal cost-error operational points. Final non-dimensional time $T = 1, 10, 100, 500$. 130

5.6 Comparison of the percentage cost-saving $\Delta\tilde{c}_1^*$ and measured elapsed time-saving $\Delta t\%$ of the cost optimized schemes with respect to the classical baseline scheme, at the nominal optimal design levels of error $\tilde{\epsilon}$. $\Delta\tilde{c}_1^*$ from Tab. 5.3, and $\Delta t\%$ from Tab. 5.5. 131

5.7 Numerical set-up for Fig. 5.11(c) with aggressive optimization. 137

A.1 Coefficients of the classical centred explicit $CPQRS$ schemes, $P = Q = 0$, $R = S$, $\alpha_0 = 1$, $a_0 = 0$, $a_{-j} = a_j$. 153

A.2 Coefficients of the optimized centered explicit schemes, $Q = R = 0$, $\alpha_0 = 1$, $q = r$, $a_0 = 0$, $a_{-j} = a_j$. 154

A.3 Coefficients for the boundary formulas at i-th point from eq. (A.88). 160

A.4 Maximum real parts of the eigenvalues from eq. (3.67) varying the number of nodes N for the classical $C1122$ and the cost-optimized $C12$epsm5, $C12$epsm4 and $C12$epsm3 interior schemes. 163

A.5 Spatial and temporal resolution for the numerical tests reported in Fig. 5.1(b). . 217

A.6 Spatial resolution for the numerical tests reported in iso-maps of Fig. 5.5, $k = 2\pi$. N_p is the number of point per period. Final time $t = 1$. $\sigma_{min} = 0.01$. $\sigma_{max} = 1.422$, see eq. (5.2). 218

Nomenclature

Roman characters

$\mathbf{d}, \mathbf{C}$	vectors
$\mathbf{I}$	Unitary matrix
$\mathbf{S}$	Right eigenvectors matrix
$\mathbf{S}^{-1}$	Left eigenvectors matrix
L_i	amplitude of i-th characteristic wave
l_i^T	i-th left eigenvector
M	Mach number
r_j^T	j-th right eigenvector
$\bar{k}$	pseudo-wavenumber
$\mathbf{A}, \mathbf{B}$	Jacobian matrices
$\mathbf{E}, \mathbf{F}$	inviscid fluxes vectors
$\mathbf{Q}$	vector of conservative variables
$\mathbf{U}$	vector of primitive variables
$\tilde{c}_{n_D}$	optimal normalized computational cost in n_D dimensions.
C	computational cost
c	speed of sound
c_g	group velocity
c_{n_D}	normalized computational cost in n_D dimensions.
c_p	phase speed
e_0	spatial numerical error
e_t	total energy per unit mass
J_0	zeroth-order Bessel function
N_λ	number of points per wavelength
p	static pressure
r	amplification factor
r_e	exact amplification factor
a	finite-difference coefficients
$\mathbb{C}$	Complex numbers
E	L_2 relative error
e	normalized error
E_δ	temporal dispersion, or phase error
E_d	temporal dissipation error
f	function
h	grid spacing
i	imaginary unit
i	index
k	wavenumber
L	streamwise length
N	number of nodes
n	number of time steps, Sec. 2.3
n	order of accuracy, Sec. 2.1
N_{op}	number of operations per node
p	number of RK stages, Sec. 2.2
p	number of processors, Sec. 4.2
P, Q, R, S	indexes of stencil point
$\mathbb{R}$	Real numbers

NOMENCLATURE

s	Laplace complex variable
t, T	time
$\mathbf{U}$	vector quantity
u, v	Cartesian velocity components in the x and y directions
x	streamwise flow-normal coordinate
y	spanwise coordinate
z	complex plane
z_s	stability limit

Greek characters

λ_i	i-th eigenvalue
$\mathbf{\Lambda}$	Diagonal matrix
α	finite-difference coefficients
α_1	coefficient
α_l	Runge-Kutta coefficients
$\overline{\kappa}$	scaled pseudo-wavenumber
$\breve{\kappa}^*$	spatial resolving efficiency
$\breve{z}^*$	temporal resolving efficiency
δ_{ij}	Kronecker delta function
ϵ	target relative error
η	coefficient
γ	specific heats ratio
γ_m	Runge-Kutta coefficients
κ	scaled wavenumber
λ	wavelength
ω	angular frequency
ρ	density
σ	Courant number
$\tilde{\epsilon}$	target normalized error
ε_I	spatial dissipative error
ε_R	spatial dispersive error
δ	difference in phase
g	damping coefficient

Superscripts

$\prime$	finite difference approximation
$\prime$	small perturbation state, Sec. 3.1.2
*	non-dimensional form
$0, n, l, p$	time level
$\tilde{}$	Fourier Transform

Subscripts

0	initial or reference value
i	independent node index

Other Symbols

Δt	time step size
$\Delta x, \Delta y$	spatial steps size
$\mathfrak{I}$	Imaginary part
$\mathfrak{R}$	Real part

Acronyms

CAA	Computational AeroAcoustic
HPC	High Performance Computing
LAE	Linear Advection Equation
LEE	Linearized Euler Equations
ODE	Ordinary Differential Equation
PDE	Partial Differential Equation
RK	Runge-Kutta

Chapter 1

Introduction

1.1 Context

The field of Computational AeroAcoustics (CAA) has grown rapidly during the last decade due to a renaissance of interest in aeroacoustic phenomena driven by a more stringent aircraft noise legislation (ACARE, 2009; UK, 2003) and the related growing demand by aerospace, automotive and other industries for accurate and reliable noise prediction models.
CAA concerns with the accurate numerical prediction of aerodynamically generated noise as well as its propagation and far-field characteristics. The numerical algorithms used in CAA are used not only as noise prediction tools, but also to evaluate new approaches for noise reduction and control. Different aeroacoustic problems often exhibit different flow physics. As a result, there is no single algorithm that can be used to simulate all problems with adequate resolution and accuracy.
The major computational challenges facing CAA are (Colonius & Lele, 2004; Tam, 2004):

- Aeroacoustics problems are inherently unsteady by definition.
- Aeroacoustics problems typically involve frequencies range that spreads over a wide bandwidth. Numerical methods able to resolve the high frequency waves with extremely short wavelength are needed.
- Acoustic waves usually have small amplitudes. They are very small compared to the mean flow. Often times, the sound intensity is five to six orders smaller. To compute sound waves accurately, a numerical scheme has to reproduce the wave propagation phenomena ensuring a tolerable level of numerical error.

- In most aeroacoustics problems, interest is in the sound waves radiated to the far field. This requires a solution that is uniformly valid from the source region all the way to the measurement point at many acoustic wavelengths away. Because of the long propagation distance, computational aeroacoustics schemes must have minimal numerical dispersion and dissipation. Also, they should propagate the waves at the correct wave speeds and isotropic irrespective of the orientation of the computational mesh.

- Acoustic waves decay very slowly when they reach the computational domain boundaries. Appropriate non-reflecting boundary conditions have to be imposed, to avoid the reflection of the outgoing acoustic waves back into the computational domain boundary. The imposition of stable and accurate boundary conditions is of utmost importance in CAA.

An elucidate example of the challenges of modelling problems of sound radiation and propagation is given by the trailing edge noise at low speed (Colonius & Lele, 2004; Wang & Moin, 2000). In such a case, there is an extreme spatial contrast between the hydrodynamic and acoustic length scales. It is extremely hard to directly capture both scales in a low Mach number unsteady flow. To be able to tackle with Direct Noise Computation such class of problems very demanding computational resources are needed. The dramatic growth in computational resources in the last two decades has enabled the CFD practitioners to model such problems.
Any investigator developing a new CAA algorithm or applying an existing method must ensure that the method adequately addresses the aforementioned challenges. Several CAA methods have emerged in last two decades (Colonius & Lele, 2004; Kurbatskii & Mankbadi, 2004; Rock *et al.*, 2004) and the progress on the state of art is documented in the four proceedings of the CAA workshops on benchmark problems (Hardin & Tam, 1996; Hardin *et al.*, 1995, 2000). In practice, these stringent requirements have dictated the use of high-order accurate numerical methods, and in particular compact and optimized finite-difference scheme for the spatial discretization (Lele, 1992) and Runge-Kutta (RK) time marching schemes (Hirsch, 2007). These schemes have, in same manner, been optimized for wave propagation to reduce the required number of grid points per wavelength while still ensuring tolerable levels of numerical errors. Hixon (2000) has introduced a prefactorization method to reduce the non-dissipative central-difference stencil of the compact schemes to two lower-order biased stencils which have easily solved reduced matrices. The advantages of these schemes over traditional compact schemes

arise from their reduced stencil size and the independent nature of the resultant factored matrices. By reducing the stencil size of the compact schemes, the prefactorization method reduces the required number of boundary stencils, thereby simplifying boundary specification (Hixon, 1996).

Ashcroft & Zhang (2003) has extended the factorization concept to a broader class of compact schemes using a more general derivation strategy, which combines Fourier analysis with the notation of a numerical wavenumber. This class of optimized prefactored schemes enhances the wave propagation characteristics of the schemes. The proposed schemes exhibits better wave propagation characteristics than the standard prefactored compact ones.

The rapid development of many CAA codes has drawn the attention to the need for careful validation of the codes and comparisons of not only the accuracy of different schemes, but also the computational speed comparison for identical problems. The issue of computational efficiency of finite-difference schemes has been investigated in details by Colonius & Lele (2004), and later on by Spisso & Rona (2007). Those authors have considered the behaviour of several types of spatial discretizations, implicitly assuming exact time integration. The error associated with approximate time integration is usually considered separately from the spatial error.

Pirozzoli (2007) has developed a general strategy for the analysis of finite-difference schemes for wave propagation problems, trying to involve time integration in the analysis in a natural way. The analysis of the global discretization error has shown the occurrence of two approximately independent sources of error, associated with the space and time discretizations. The improvement of the performance of the global scheme can be achieved by trying to separately minimize the two contributions. The analysis leads to rational and simple criteria for deriving optimized space- and time-discretization schemes, based on the concepts of spatial and temporal resolving efficiency. A careful design of the space- and time-discretization schemes, as well as an appropriate choice of the grid spacing and of the time step, can yield substantial computer time savings.

1.2 Aims and objectives

The aim of the present work is to develop a novel algorithm based on the prefactoriztion of Hixon (2000) to reduce the computational cost for a given level of error. The ideal field of application of the newly developed code is sought to be low Mach number error-bounded aeroacoustic applications.

The objectives that has been achieved to get this aim are:

- A new prefactored cost-optimized scheme is developed to minimize the computational cost for a given level of error. This work extends the theory of Pirozzoli (2007) to the prefactored compact high-order schemes of Hixon (2000).
- Theoretical prediction for spatial and temporal error bounds are determined and compared against benchmark classical schemes. The performance of popular schemes for *CAA* applications and the cost-optimized schemes are compared in terms of computational efficiency.
- High-order boundary closures, which are accurate and stable within a given Fourier space envelope, are coupled with the interior prefactored schemes. The stability of the prefactored cost-optimized schemes coupled with these boundary closures is verified by an eigenvalue analysis.
- To aid parallelization, an appropriate interior boundary stencil is developed, which is an improvement over the equivalent one of Hixon (2000) and Ashcroft & Zhang (2003).
- The scheme has shown a good scalability, for execution on *HPC* (High Performance Computing) clusters, up to 128 processors.
- A monochromatic sinusoidal test-case has verified the theoretical roll-off error against the computed $\overline{L}_2$ norm error, indicating that the cost-optimized schemes perform according to the design high-order accuracy characteristics for this class of problems.
- Numerical experiments have verified that the design cost-optimization of the schemes is achieved. A 22% computational cost-saving at the design level of error is recorded. The percentage cost-saving is envisaged to be higher for a level of error one decade lower than the design level of error and even more in a multi-dimensional space.
- Sample applications to broad-band and multi-dimensional space benchmark problems (Hardin *et al.*, 1995) have shown the low error-bounded and high-order accuracy characteristics of the baseline scheme.

1.3 Thesis outline

This thesis is divided into six chapters and it is organized as follows.
Chapter 1 introduces the context (Sec. 1.1), aims and objectives of this work, and the expected outcomes (Sec. 1.2).
Chapter 2 reviews the numerical background that will be used onwards. Specifically, the concepts of finite-difference approximation and the related concepts of numerical wavenumber are summarized in Sec. 2.1, and the time marching schemes for CAA are considered in Sec. 2.2. The theory of the cost-optimization of Pirozzoli (2007), based on the optimization of the computational cost for a given error level, is reviewed in Secs. 2.3 and 2.4. The decoupling of the spatial and temporal error is discussed in Sec. 2.5.
Chapter 3 describes the numerical method used in the present work. The governing equations that will be solved in the present study, that are the Linearized Advection Equation (LAE) and the Linearized Euler Equations (LEE), are presented. The derivation of the LEE in non-dimensional and in characteristic form starting for the Euler equations is reported in Sec. 3.1. Section 3.2 presents the interior baseline spatial discretization method used, that is a class of tridiagonal compact schemes. The most common finite-difference schemes used in CAA are reviewed and compared in term of computational efficiency. The spatial cost-optimization technique, based on the maximization of the spatial resolving efficiency is presented, and it is extend to the class of sixth-order prefactored compact scheme of Hixon (2000). Section 3.3 analyses the impact on the computational cost of using different time integration schemes. The temporal cost-optimization technique, based on the maximization of the temporal resolving efficiency, is presented. A temporal stability and accuracy analysis of the cost-optimized is shown. Section 3.4 shows the predicted performance of the combined space and time cost-optimization schemes for the same level of error, predicting a computational advantage at their design level of error. Section 3.5 shows the effect of the perimetrical scheme on the interior scheme. Two methods of treating near-boundary points are presented and compared against the equivalent boundary treatments available in literature. The first approach is a prefactored sixth-order explicit one-sided finite-difference scheme that uses a seven-point stencil, the second is a prefactored explicit central scheme with an 11-point stencil. The wave propagation characteristics of these boundary closures is examined. An eigenvalue analysis is performed to verify the stability of the new developed cost-optimized prefactored schemes coupled with the selected boundary closures. Section 3.6 details the artificial boundary conditions used in

the present study. Three implementation of boundary conditions are shown: the subsonic inflow, the subsonic outflow and the inviscid wall. Two type of absorbing layer technique are discussed.

Chapter 4 presents the parellization strategy adopted for the serial code, based on MPI single domain decomposition and finite-sized overlap region. Weak scalability tests on the state-of-art HPC cluster are presented.

Chapter 5 shows the verification and validation of the numerical method against simple benchmarks problems. Section 5.1 presents the one-dimensional test-cases analysed, that are the the monochromatic sinusoidal wave and the broadband Gaussian pulse. The performance of the new 11-point boundary stencil in double precision accuracy is evaluated. The effect of the boundary closure on the L_2 norm error is studied using the monochromatic sinusoidal wave. The theoretical findings of the theory of the cost-optimization are compared against numerical tests, by measuring the effective computed elapsed time during the numerical tests using the classical and the cost-optimized schemes. Section 5.2 presents the two-dimensional test-case analysed.

Finally, Chapter 6 summarizes the numerical findings, reports the conclusions and the main limitations.

Chapter 2

Numerical background

This chapter reviews the numerical background that will be used onwards. Specifically, the concepts of finite-difference approximation and the related concepts of numerical wavenumber are introduced in Sec. 2.1, the time marching schemes for CAA are reviewed in Sec. 2.2, and the theory of the cost-optimization of Pirozzoli (2007) is summarized. The concepts of optimization of the computational cost for a given error level, of the 'spatial resolving efficiency' and of the 'temporal resolving efficiency' are introduced in Sec. 2.3 and Sec. 2.4.

2.1 Spatial discretization

Splitting the discussion of spatial and temporal discretization into two parts assumes to use the method-of-lines, with a two-stages discretization. Stage one gives a 'semi-discrete' formulation of the governing equations that are discrete in space and continuous in time.
In this section, the basic concepts of finite-difference approximation and the related definitions of numerical wavenumber and group velocity are summarized. Consider the values of a function $f(x)$ on a set of N nodes indexed by i, with an uniformly spaced mesh along the streamwise length L, as shown in Fig. 2.1. The independent variable at the nodes is $x_i = (i-1)h$, where $h = L/(N-1)$ is the uniform grid spacing, for $1 \leq i \leq N$.
The finite difference approximation f'_i to the first derivative $\dfrac{\partial f(x_i)}{\partial x}$ at node i, using a $(R+S+1)$ point stencil, depends on the function values at the nodes near i (Lele, 1992) and is given by:

$$\sum_{j=-P}^{Q} \alpha_j \, f'_{i+j} = \frac{1}{h} \sum_{j=-R}^{S} a_j \, f_{i+j} + O(h^n), \tag{2.1}$$

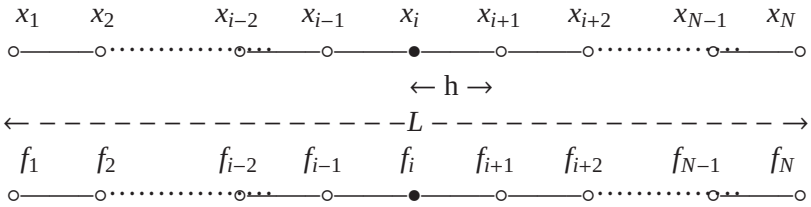

Figure 2.1: Variation of discrete function $f_i = f(x_i)$ along uniformly discretised streamwise length L.

with $(S + R) \geq 1$ to be able to determine the relations among the coefficients a_j, $Q \leq S$ and $P \leq R$. If $P = Q = 0$, then the scheme is explicit. Implicit schemes, also named Padè or compact, have $(P \vee Q) \neq 0$, and the solution of a simultaneous system of equations is required to determine the approximation to the derivative of all nodes $1 \leq i \leq N$. The coefficients α_j, a_j that appear in eq. (2.1) are typically chosen to give the largest possible order of accuracy denoted by the exponent n, for given stencil width, thus minimizing the truncation error. By Taylor series expansion of eq. (2.1), the maximum possible exponent n_{max} is given by

$$n_{max} = P + Q + R + S, \tag{2.2}$$

provided that $|R + S| \geq 1$. Of particular interest in CAA is the measure of error in the wave propagation characteristics of a single Fourier component of $f(x)$ (Colonius & Lele, 2004; Spisso & Rona, 2007).

The finite difference equation (2.1) is a special case of the following equation with respect to the continuous variable x:

$$\sum_{j=-P}^{Q} \alpha_j \, f'(x + j\,h) = \frac{1}{h} \sum_{j=-R}^{S} a_j \, f(x + j\,h) + O(h^n), \tag{2.3}$$

which discretizes into eq. (2.1) by setting $x = x_i$. The Fourier transform of the function $f(x)$ is:

$$\tilde{f}(k) = \int_{-\infty}^{\infty} f(x)\, e^{-\mathrm{i}\,k\,x} dx, \tag{2.4}$$

where $\mathrm{i} = \sqrt{-1}$, k is the wavenumber, and the tilde "˜" represents the transformed function.

Given a monochromatic wave of wavelength λ, resolved with N_λ number of points per wavelength, the equation

$$N_\lambda = \frac{\lambda}{h} = \frac{2\pi}{\kappa}, \tag{2.5}$$

is used to relate the scaled wavenumber

$$\kappa = k\,h \tag{2.6}$$

to the wavelength λ.

According to the Nyquist-Shannon sampling theorem, the spectrum of wavelengths representable on the discretised domain varies from

$$\lambda_{min} = 2h, \tag{2.7}$$

to

$$\lambda_{max} = 2L. \tag{2.8}$$

Equation (2.5) gives the minimum wavenumber $k_{min} = \pi/L$, which is related to the maximum wavelength $2L$, and the maximum wavenumber $k_{max} = \pi/h$, corresponding to the minimum wavelength $2h$ and to $N_\lambda = 2$, the so called odd-even oscillation. In the case of a broadband signal, if the highest significant frequency component of the original signal is resolved according to eq. (2.7), then the lower wavenumber components will be resolved down to k_{min}.

Taking the Fourier transform of both sides of eq. (2.3) gives:

$$\overline{\kappa}(\kappa) = \overline{k}\,(k)\,h = \frac{1}{\mathrm{i}}\frac{\sum_{j=-R}^{S} a_j e^{\mathrm{i}\,j\kappa}}{\sum_{j=-P}^{Q} \alpha_j e^{\mathrm{i}\,j\kappa}}, \tag{2.9}$$

where $\overline{\kappa} = \overline{k}\,h$ is the scaled pseudo-wavenumber. The scaled wavenumber and the scaled pseudo-wavenumber are both non-dimensional values, $\kappa \in \mathbb{R}$, $0 < |\kappa| \leq \pi$, and generally $\overline{\kappa} \in \mathbb{C}$, with real and imaginary part $\Re[\overline{\kappa}]$ and $\Im[\overline{\kappa}]$. It is desirable to make $\overline{\kappa}$ equal to κ. However, it is impossible to build up a perfect match between $\overline{\kappa}$ and κ over the entire wavenumber range due to the limitation of numerical discretization. In practice, the scaled pseudo-wavenumber $\overline{\kappa}$ implies a certain deviation from the true scaled wavenumber κ, which increases as $\kappa \to \pi$ (for $\kappa = \pi$, $\overline{\kappa} = 0$, see Fig. 3.1). This deviation results in spatial numerical error:

$$e_0(\kappa) = \left|\frac{\overline{\kappa}(\kappa) - \kappa}{\kappa}\right|, \tag{2.10}$$

where the real part represents the dispersive error

$$\varepsilon_R(\kappa) = \left|\frac{\Re\,[\overline{\kappa}(\kappa)] - \kappa}{\kappa}\right|, \tag{2.11}$$

and the imaginary part the dissipative error

$$\varepsilon_I(\kappa) = \left| \frac{\Im\left[\bar{\kappa}(\kappa)\right]}{\kappa} \right|. \tag{2.12}$$

It is possible to optimize the coefficients a_j, α_j of eq. (2.1) to reduce such errors, rather than maximizing the formal order of accuracy n (Bogey & Bailly, 2004; Lele, 1992; Tam & Web, 1993). When centered difference schemes ($R = S$) approximate an hyperbolic system of first-order Partial Differential Equation (PDE), it will be shown in Sec.3.2 that they disperse but do not dissipate the Fourier components of the solution. This is an important advantage in turbulence and aeroacoustic computations, wherein the phase and amplitude of the propagating disturbances, spreading over a wide wavenumbers range, are required to propagate over long distances with minimal numerical dispersion and dissipation.
The dispersion and dissipation of the Fourier components depends on the choice of the particular PDE to be modelled. The LAE

$$\frac{\partial u}{\partial t} + c\frac{\partial u}{\partial x} = 0, \qquad u(x,0) = u_0(x), \tag{2.13}$$

which models the advection of the scalar quantity u, at constant speed of sound c, is a simple and explicative example to elucidate the dispersive nature of the numerical approximation. Assuming the sinusoidal monochromatic initial condition

$$u_0(x) = \hat{u}_0 e^{\mathbf{i}kx}, \tag{2.14}$$

the solution is determined by the method of characteristics. In fact, on infinite or periodic domain, eq. (2.13) admits solutions of the form (Vichnevetsky, 1987):

$$u(x,t) = \hat{u}_0 e^{\mathbf{i}(-\omega t + kx)}, \tag{2.15}$$

when the angular frequency ω and the wavenumber k are related by the dispersion relation

$$\omega = c\,k. \tag{2.16}$$

Equation (2.16) states that all Fourier components of the solution of the *LAE* equation travel with the same constant phase speed $\frac{\omega}{k} = c$. Waveforms comprised of a superposition of modes (broadband signals) retain their shape as they propagate, and are therefore called non-

dispersive (Whitham, 1974). When the spatial derivative in eq. (2.13) is approximated using one of the finite difference schemes given in eq. (2.1), the semi-discrete approximation of the LAE becomes

$$\frac{\partial u_i}{\partial t} + \frac{c}{h} \sum_{j=-R}^{S} a_j \, u_{i+j} = 0. \tag{2.17}$$

The Fourier transform of eq. (2.17) is:

$$\frac{\partial \tilde{u}_i}{\partial t} + \mathbf{i}\, c\, \bar{k}(k)\, \tilde{u}_i = 0, \tag{2.18}$$

and the dispersion relation given by eq. (2.16) in semi-discrete form becomes:

$$\frac{\omega\, h}{c} = \bar{\kappa}(\kappa). \tag{2.19}$$

In equation (2.17), the phase speed c_p of the disturbances is now given by:

$$\frac{c_p}{c} = \frac{\omega}{ck} = \frac{\bar{\kappa}(\kappa)}{\kappa}, \tag{2.20}$$

and therefore different Fourier components travel at different phase speeds. Such a system is said to be dispersive, as waveforms comprised of a linear superposition of modes do not retain their identity as they propagate. The discretized equations behave mathematically like a dispersive wave system, even though the waves supported by the original system of *PDE*s are non-dispersive (Tam & Web, 1993; Vichnevetsky & Bowles, 1982). The group velocity c_g is the velocity at which sinusoidal waves propagate energy in a dispersive medium (Lighthill, 1978; Vichnevetsky, 1987). The group velocity in eq. (2.17) is given by:

$$\frac{c_g}{c} = \frac{\partial \bar{\kappa}(\kappa)}{\partial \kappa} = \frac{1}{c}\frac{\partial \omega}{\partial k}. \tag{2.21}$$

Tam (1995) showed that, when the group velocity is equal to 1, the scheme has the same group velocity as the original system of *PDE*s and the modelled waves, the so-called smooth waves, propagate with the correct wave speed. The numerical scheme becomes dispersive in the wavenumber range where the group velocity is not equal to 1. These waves are usually referred in literature as spurious waves (Colonius & Lele, 2004; Tam & Web, 1993; Vichnevetsky, 1987). A detailed analysis of the wave propagation characteristics of the centered finite difference schemes will be presented in Sec. 3.2.

2.2 Time-marching schemes for CAA

Section 2.1 has considered the spatial discretization of the governing equations, by which the *PDE*s are reduced to a semi-discrete system of *ODE*s that are continuous in time. An approximate method for the time integration is now considered. Two types of the most popular time-marching schemes in the CAA community are the single-step Runge-Kutta methods and multi-step Adams-Bashforth schemes. Other time-integration approaches include leap-frog schemes and coupled space-time discretization algorithms. Runge-Kutta schemes are considered as time advancing schemes in the present work.

The time evolution equation of a general non-autonomous system of ODEs is written as:

$$\frac{d\mathbf{U}}{dt} = F(\mathbf{U}(t), t), \tag{2.22a}$$

$$\mathbf{U}(t_o) = \mathbf{U}^{(0)}, \tag{2.22b}$$

where $\mathbf{U}$ represents the vector containing the solution values at spatial mesh nodes and the operator F contains the discretization of the spatial derivatives.

An explicit p-stage, single-step, two-level, low-storage RK scheme advances the solution from the time level $t = t_n$ to $t_n + \Delta t$ as:

$$\begin{aligned} &\mathbf{U}^{(0)} = \mathbf{U}^n, \\ &\mathbf{U}^{(l)} = \mathbf{U}^n + \alpha_l \, \Delta t \, F\left(\mathbf{U}^{(l-1)}\right) \qquad \text{for} \quad l = 1, \ldots, p, \\ &\mathbf{U}^{n+1} = \mathbf{U}^{(p)}, \end{aligned} \tag{2.23}$$

where α_l are the coefficients of the algorithm and Δt is the time step.

If F is linear, so that $F(\mathbf{U}) = \mathbf{A}\mathbf{U}$, eq. (2.23) can be rewritten as:

$$\mathbf{U}^{n+1} = \mathbf{U}^n + \sum_{j=1}^{p} \gamma_j \, \Delta t^j \, \frac{\partial^j \mathbf{U}^n}{\partial t^j}, \tag{2.24}$$

where

$$\gamma_j = \prod_{l=p-j+1}^{p} \alpha_l \qquad \text{for} \quad j = 1, \ldots, p. \tag{2.25}$$

In the case of $p = 4$, eq. (2.24) becomes:

$$\mathbf{U}^{n+1} = \mathbf{U}^n + \underbrace{\alpha_4}_{\gamma_1} \Delta t \frac{\partial \mathbf{U}^n}{\partial t} + \underbrace{\alpha_4\alpha_3}_{\gamma_2} \Delta t^2 \frac{\partial^2 \mathbf{U}^n}{\partial t^2} + \underbrace{\alpha_4\alpha_3\alpha_2}_{\gamma_3} \Delta t^3 \frac{\partial^3 \mathbf{U}^n}{\partial t^3} + \underbrace{\alpha_4\alpha_3\alpha_2\alpha_1}_{\gamma_4} \Delta t^4 \frac{\partial^4 \mathbf{U}^n}{\partial t^4}. \quad (2.26)$$

The classical way to define the coefficients of an explicit p-stage RK scheme of pth-order is by matching the corresponding coefficients of the Taylor Series expansion of $\mathbf{U}(t_n + \Delta t)$. This gives:

$$\gamma_m = \frac{1}{m!}, \quad m = 1, \cdots, p. \quad (2.27)$$

Equation (2.27) gives the maximum order of accuracy, or the minimum truncation error, which can be obtained with a pth-stage RK scheme.

Applying a temporal Fourier transform to eq. (2.24), as in Appendix A.1, the amplification factor of the algorithm is obtained as (Hirsch, 2007):

$$r(\kappa, \sigma) = \frac{\tilde{\mathbf{U}}^{n+1}}{\tilde{\mathbf{U}}^n} = 1 + \sum_{j=1}^{p} \gamma_j \left(-\mathrm{i}\, c\, \bar{k}(k) \Delta t\right)^j = 1 + \sum_{j=1}^{p} \gamma_j \left(-\mathrm{i}\, \sigma\, \bar{\kappa}(\kappa)\right)^j, \quad (2.28)$$

where σ is the Courant number:

$$\sigma = \frac{c\Delta t}{h}. \quad (2.29)$$

The amplification factor in the case of null spatial error, for which $\bar{\kappa} = \kappa$ in eq. (2.9), is:

$$r_t\left(z, \gamma_j\right) = 1 + \sum_{j=1}^{p} \gamma_j \left(-\mathrm{i}\, \sigma\, \kappa\right)^j = 1 + \sum_{j=1}^{p} \gamma_j \left(-\mathrm{i}\, z\right)^j \quad (2.30)$$

with $z = \sigma\kappa$. The stability limit z_s is given by the following condition:

$$z_s = \max\left\{z,\ |r_t(z, \gamma_j)| \leq 1\right\}. \quad (2.31)$$

The stability footprints are the locus of points in the complex z plane where the amplification factor in case of null spatial error of eq. (2.30) is equal to unity, i.e. $|r_t = 1|$. On the other hand, the amplification factor of the exact time integration r_e for the LAE is obtained in a fully discretized domain (see eq. (2.36) in Sec. 2.3) as:

$$r_e = \frac{u_i^{n+1}}{u_i^n} = e^{-\mathbf{i}\, c\, \bar{k}(k) \Delta t} = e^{-\mathbf{i}\, \sigma\, \bar{\kappa}(\kappa)}. \quad (2.32)$$

Equation (2.28) clearly shows that the amplification factor of the finite-difference scheme is a Maclaurin series expansion of exponential function given by eq. (2.32).
To compare the numerical and exact amplification factor, the following ratio is used:

$$\frac{r}{r_e} = |r|\, e^{-\mathbf{i}\delta}, \tag{2.33}$$

where $|r|$ and δ are, respectively, the amplification rate and the difference in phase of the RK scheme. The following quantities

$$E_d = 1 - |r| \tag{2.34}$$

and

$$E_\delta = \frac{\delta}{\pi} \tag{2.35}$$

are, respectively, a measure of the temporal dissipation and dispersion (or phase) error, as reported by Berland *et al.* (2006).
Rather than using eq. (2.27), the coefficients γ_m of eq. (2.25) may be chosen to minimize the dissipation and phase error (Bogey & Bailly, 2004; Hu *et al.*, 1996). A detailed analysis of the stability and accuracy of the explicit RK schemes will be discussed in Sec. 3.3.
Implicit RK methods are an alternative way of integrating the governing equations in CAA; they can use large time steps, resulting in savings of computational resources. These schemes are useful for modelling problems at a low Mach number with acoustic waves of low frequency, such as acoustic combustion instabilities. However, they can exhibit stability problems due to the stiffness associated with high-frequency acoustic waves that require the addition of a small amount of numerical dissipation (Wall *et al.*, 2002). Collis & Colonius (1997) have also noted problems related to the stiffness associated with geometric and/or coordinate system singularities.

2.3 Performance analysis of finite-difference schemes

The linearised advection equation (2.13) offers a good platform for testing the performance of finite-difference schemes. The exact solution to the *LAE* equation given by eq. (2.15), in a fully discretized domain at time $T = n\Delta t$, reads as:

$$u_i^n = u(x, T) = \hat{u}_0\, e^{\mathbf{i}kx} e^{-\mathbf{i}n\sigma\kappa}. \tag{2.36}$$

The linear finite difference approximation of eq. (2.13) has the approximate solution (Vichnevetsky & Bowles, 1982):

$$v(x,T) = \hat{u}_0\, e^{\mathbf{i}kx} r^n. \tag{2.37}$$

Following the work of Pirozzoli (2007), the solution error is defined as the distance in L_2 norm of the approximate solution from the exact solution at time T:

$$|v(\cdot\,,T) - u(\cdot\,,T)|_2 = \left(\frac{1}{\lambda}\int_{x_0}^{x_0+\lambda} |v(x,T) - u(x,T)|^2 dx\right)^{1/2} = |r^n - e^{-\mathbf{i}n\sigma\kappa}|\,|\hat{u}_0|. = |r^n - e^{-\mathbf{i}n\sigma\kappa}|\,|u_0(\cdot\,)|_2. \tag{2.38}$$

Let $\delta r \equiv r - e^{-\mathbf{i}\sigma\kappa}$ be the difference between the approximate and the exact amplification factor; r^n can be expressed as:

$$r^n = \left(e^{-\mathbf{i}\sigma\kappa} + \delta r\right)^n = e^{-\mathbf{i}n\sigma\kappa}\left(1 + \delta r\, e^{\mathbf{i}\sigma\kappa}\right)^n \approx e^{-\mathbf{i}n\sigma\kappa}\left(1 + n\delta r e^{\mathbf{i}\sigma\kappa}\right), \tag{2.39}$$

under the hypothesis that $|\delta r| \ll 1$; which is true for any reasonably accurate scheme and will be checked a posteriori. So it is possible to rewrite:

$$r^n - e^{-\mathbf{i}n\sigma\kappa} \approx n\delta r e^{-\mathbf{i}(n-1)\sigma\kappa} \tag{2.40}$$

and finally, remembering that by definition $|e^{-\mathbf{i}\sigma\kappa}| = 1$,

$$|r^n - e^{-\mathbf{i}n\sigma\kappa}| \approx n \cdot |r\,(\kappa,\sigma) - e^{-\mathbf{i}\sigma\kappa}|. \tag{2.41}$$

Let E be the relative L_2 error norm at time T:

$$E = \frac{|v(\cdot\,,T) - u(\cdot\,,T)|_2}{|u_0(\cdot\,)|_2} = (ckT) \cdot \frac{|r\,(\kappa,\sigma) - e^{-\mathbf{i}\sigma\kappa}|}{\sigma\kappa}, \tag{2.42}$$

where $n = (ckT)\,/\,(\sigma\kappa)$ from eqs. (2.16) and (2.6).

The computational cost C of solving numerically eq. (2.37) is assumed to be proportional to (Colonius & Lele, 2004):

- the total number of points, L/h;
- the number of operations per node N_{op} required by the spatial discretization;
- the number of RK stages, p;
- the number of time steps $n = T/\Delta t$;

this gives:

$$C \propto pN_{op}TL\frac{1}{\Delta t\, h} = pN_{op}\cdot(ckT)\cdot(kL)\cdot\frac{1}{\sigma\kappa^2}. \tag{2.43}$$

In equations (2.42) and (2.43), the non-dimensional groups ckT and kL are, respectively, the number of wavelengths travelled by a wave of phase speed in a time interval T and the number of wavelengths contained in the computational domain. Their values are defined by the initial flow condition of eq. (2.14) and by the extent of the computational domain and are independent from the space and time discretization. The space and time discretization affects E and C through p, N_{op}, and $r(\kappa,\sigma)$. The analysis of the performance of finite-difference schemes for a given physical problem (i.e. for given values of the non-dimensional groups ckT, kL) can be performed in terms of normalized error $e(\kappa,\sigma)$ and one-dimensional cost functions $c_1(\kappa,\sigma)$:

$$e(\kappa,\sigma) \equiv \frac{E}{(ckT)} = \frac{|r(\kappa,\sigma) - e^{-\mathbf{i}\sigma\kappa}|}{\sigma\kappa}, \tag{2.44a}$$

$$c_1(\kappa,\sigma) \equiv \frac{C}{(ckT)\cdot(kL)} = pN_{op}\,\frac{1}{\sigma\kappa^2}. \tag{2.44b}$$

2.4 Cost-performance trade-off for CAA algorithms

Optimizing the performance of a given scheme (i.e. for given values of p, N_{op}), for a given problem (i.e. for a given value of ckT, kL) amounts to requiring that the computational cost is minimum for a given error level. This can be done by specifying a target level for the relative error, say ϵ, which implies

$$e(\kappa,\sigma) = \frac{\epsilon}{ckT} \equiv \tilde{\epsilon}, \tag{2.45}$$

and finding a pair of values $(\kappa^*(\tilde{\epsilon}),\sigma^*(\tilde{\epsilon}))$ that minimize the cost metric and that satisfy both the stability limitation $|r(\kappa,\sigma)|\leq 1,\ \forall\kappa$ and the limitation on the maximum value of Courant number $\sigma \leq \sigma_{max}$:

$$\sigma_{max} = \frac{z_s}{\max\limits_{\kappa\in(0,\pi)} \overline{\kappa}(\kappa)}, \tag{2.46}$$

which depends upon both the spatial and temporal discretizations.

The interpretation of the optimization problem is made particularly simple by inspection of the iso-lines of the normalized error $e(\kappa,\sigma)$ and the normalized cost function $c(\kappa,\sigma)$ in the (κ,σ) plane, as done in Fig. 2.2 for a sixth-order compact spatial discretization scheme coupled

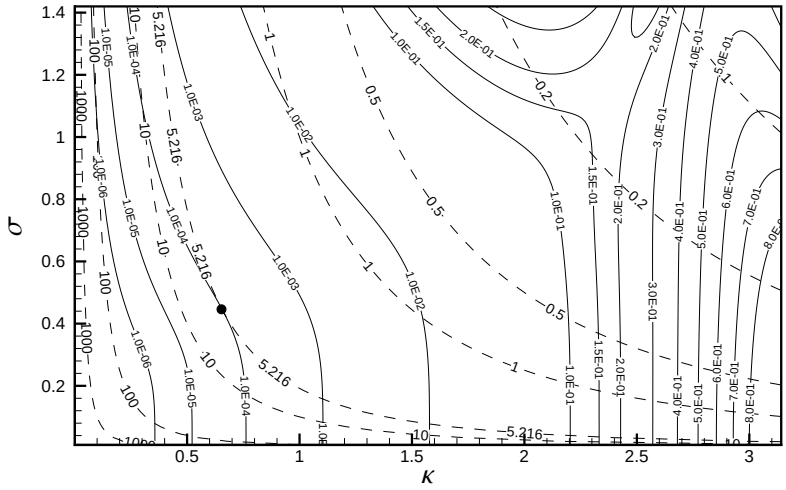

Figure 2.2: Iso-contours of normalized 'local' error function $e(\kappa, \sigma)$ (solid lines) and normalized one-dimensional cost function $1/(\sigma\kappa^2)$ (dashed lines), for $C1122/RK4$ scheme.

with a four-stage, fourth-order time integration, labelled as $C1122/RK4$. In this example, the upper boundary corresponds to $\sigma_{max} = 1.422$. For any specified value of $\tilde{\epsilon}$, a pair of values $(\kappa^*(\tilde{\epsilon}), \sigma^*(\tilde{\epsilon}))$ is sought to minimize $\dfrac{1}{\sigma\kappa^2}$ and which corresponds to the tangency point of the two families of curves (iso-error and iso-cost). The corresponding normalized one-dimensional 'optimal' cost is given by:

$$\tilde{c}_1(\tilde{\epsilon}) = c_1\left(\kappa^*(\tilde{\epsilon}), \sigma^*(\tilde{\epsilon})\right) = pN_{op}\,\frac{1}{\sigma^*\kappa^{*2}}. \tag{2.47}$$

For the $C1122/RK4$ scheme, Fig. 2.2 shows the 'optimal' working condition, with a black dot, relative to $\tilde{\epsilon} = 10^{-4}$, given by the pair of values $(\kappa^*(\tilde{\epsilon}),\ \sigma^*(\tilde{\epsilon})) = (0.653, 0.449)$. The associated 'optimal' normalized cost is $\tilde{c}_1(\tilde{\epsilon}) = 187.77$.

From equations (2.44a) and (2.44b), the normalized cost function is concave and the normalized error function is (almost always) convex in the $[\kappa, \sigma]$ plane. In addition, since the iso-cost lines are steeper than the iso-error lines at large σ, it follows that for any iso-error curve there is a unique point in which a curve of the iso-cost family is tangent to it (Bernardini & Pirozzoli, 2009).

Dealing with nonlinear propagation problems of broadband signals requires to resolving a wavenumber spectrum of finite width, say $|\kappa| \leq \check{\kappa}$ and propagation velocities $|c| \leq \check{c}$, which

implies $\check{\kappa} = \check{k}h$ and $\check{\sigma} = \check{c}\Delta t/h$. The formulas for the error and cost metric in this case read as:

$$E = \left(\check{c}\check{k}T\right) \cdot \frac{|r\left(\kappa,\sigma\right) - e^{-\mathbf{i}\sigma\kappa}|}{\check{\sigma}\check{\kappa}}, \tag{2.48}$$

$$C \sim \left(\check{c}\check{k}T\right) \cdot \left(\check{k}L\right) \cdot \check{c}_1\left(\check{\kappa},\check{\sigma}\right); \tag{2.49}$$

with

$$\check{c}_1(\check{\kappa},\check{\sigma}) = pN_{op}\,\frac{1}{\check{\sigma}\check{\kappa}^2}, \tag{2.50}$$

being $n = (\check{c}\check{k}T)/(\check{k}L)$.

The accuracy requirement enforced in this case dictates that the relative error E is less than the target level $\tilde{\epsilon}$ used as a threshold $\forall\,(\kappa,\sigma)$:

$$E \leq \tilde{\epsilon} = \frac{\epsilon}{\check{c}\check{k}T}, \quad \forall\ (\kappa,\sigma) \in [0,\check{\kappa}] \times [0,\check{\sigma}]\,. \tag{2.51}$$

The normalized error reads as:

$$\check{e}(\check{\kappa},\check{\sigma}) \equiv \frac{1}{\left(\check{c}\check{k}T\right)} \cdot \max_{(\kappa,\sigma)\in[0,\check{\kappa}]\times[0,\check{\sigma}]} E \tag{2.52}$$

and substituting eq. (2.48) in eq. (2.52) follows:

$$\check{e}(\check{\kappa},\check{\sigma}) = \frac{1}{\check{\sigma}\check{\kappa}} \cdot \max_{(\kappa,\sigma)\in[0,\check{\kappa}]\times[0,\check{\sigma}]} |r\left(\kappa,\sigma\right) - e^{-\mathbf{i}\sigma\kappa}| \leq \tilde{\epsilon}. \tag{2.53}$$

The only change with respect to the monochromatic wave propagation problem of Sec. 2.3 is the replacement of the normalized error function $e(\kappa,\sigma)$ of eq. (2.45) with $\check{e}(\check{\kappa},\check{\sigma})$, as defined in eq. (2.53), which represents the maximum of the normalized error e in the entire range of relevant wavenumbers and Courant numbers. The iso-contour lines of the normalized 'local' error function $e(\kappa,\sigma)$ and 'global' error function $\check{e}(\check{\kappa},\check{\sigma})$ for $C1122/RK4$ are reported in Fig. 2.3. The 'global' error (dotted lines) differs from the 'local' one (dashed lines) only near the points of local extrema of $\check{e}(\check{\kappa},\check{\sigma})$. The interpretation of Fig. 2.3 goes along the same lines as for Fig. 2.2. The accuracy requirement of eq. (2.51) implicitly assumes the same importance for all flow scales. In some situations, however, such as for the numerical simulation of tonal noise aeroacoustic problems of turbulent flows, one may wish to accurately compute the energy containing scales responsible for the tonal noise generation and relax the targeted error of smaller, less energetic length scales. Pirozzoli (2007) suggested that this might be achieved by introducing an appropriate weighing function in the wavenumber space in the definition of the error, similarly

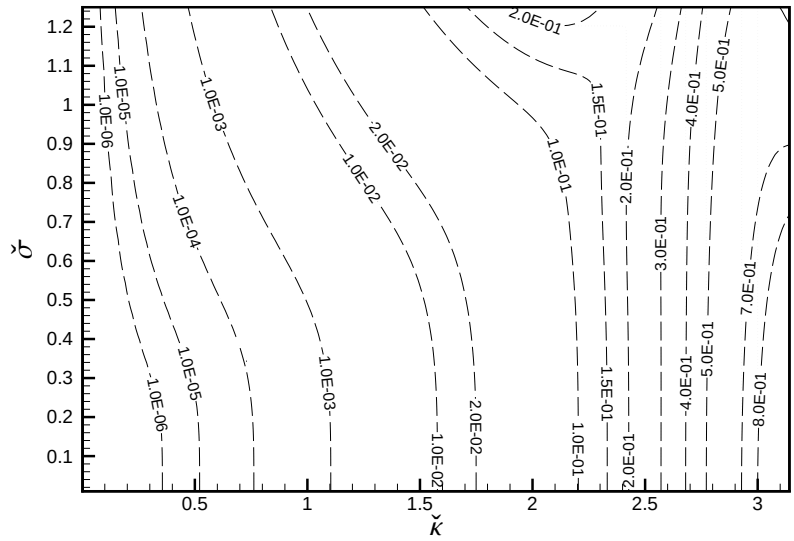

Figure 2.3: Iso-contours of normalized 'local' error function $e(\kappa,\sigma)$ (dashed lines) and 'global' error function $\check{e}(\check{\kappa},\check{\sigma})$ (dotted lines), for $C1122/RK4$ scheme.

to what was done in past by Tam & Web (1993) and Bogey & Bailly (2004) to minimize the dispersion error in wavenumber space.

The effect of the number of spatial dimensions can be partially accounted for in the analysis by assuming again the *LAE* as the working model for a monochromatic plane wave propagating in an n_D space. Lele (1992) has shown that the discrete anisotropic propagation properties depend on the alignment of the wavefront with the numerical grid and on the spatial resolution (or number of points per wavelength N_λ). The well resolved waves are essentially isotropic, whereas short waves are anisotropic with the greatest error along ±45° diagonals to the mesh lines, as reported in the polar plot of anisotropy by Colonius & Lele (2004). By assuming: (i) an uniform regular Cartesian mesh and (ii) wave propagation along the grid lines, it is possible to follow the same one-dimensional analysis from eqs. (2.49) to (2.53) with a new definition of the cost function that takes in account the total number of points, which is now V/h^{n_D}, where V is the volume of the computational domain and n_D is the number of spatial dimensions. This gives:

$$C \sim (\check{c}\check{k}T)\cdot(\check{k}^{n_D}V)\cdot\check{c}_{n_D}(\check{\kappa},\check{\sigma}) \tag{2.54}$$

where the normalized cost function for an n_D dimensional problem is given by:

$$\check{c}_{n_D}(\check{\kappa}, \check{\sigma}) = pN_{op} \frac{1}{\check{\sigma}\check{\kappa}^{n_D+1}}, \tag{2.55}$$

in place of eqs. (2.49) and (2.50). Figure 2.4 shows that the optimal values of κ and σ for a given normalized error level $\tilde{\epsilon}$, $(\kappa^*(\tilde{\epsilon}), \sigma^*(\tilde{\epsilon}))$ do not significantly differs from those found in the one-dimensional analysis. The 'optimal' value relative to the normalized two-dimensional iso-cost function for a target error $\tilde{\epsilon} = 10^{-4}$ is reported with a blue dot located at $(\kappa^*(\tilde{\epsilon}), \sigma^*(\tilde{\epsilon})) = (0.694, 0.388)$. The associated 'optimal' normalized cost is $\tilde{c}_2(\tilde{\epsilon}) = 276.75$. This location, shown in the detailed enlargement of Fig. 2.4(a) in Fig. 2.4(b), is very close to that of the optimal pair $(\kappa^*(\tilde{\epsilon}), \sigma^*(\tilde{\epsilon})) = (0.653, 0.449)$ obtained in one-dimensional case, reported with a black dot, which corresponds to $\tilde{c}_1(\tilde{\epsilon}) = 187.77$. As consequence, schemes capable of operating at higher values of reduced wavenumber κ are more advantageous for multi-dimensional simulations, because of the increased importance of κ in the cost metric of eq. (2.55). Accordingly, high-order and optimized schemes are expected to yield a lower computational cost over low-order ones for a target level of error. The validity of these arguments will be further discussed in Sec. 3.2.2, where the effect of the number of spatial dimensions is analysed.

2.5 Spatial and temporal error analysis

The 'local' normalized error function $e(\kappa, \sigma)$ defined in eq. (2.44a) can be readily related to the error definitions reported by Lele (1992) and Hu *et al.* (1996). Specifically, for $\sigma \to 0$, it is possible to rewrite:

$$r(\kappa, \sigma) = 1 - \mathbf{i}\sigma\overline{\kappa}(\kappa) + O(\sigma^2), \tag{2.56a}$$

$$e^{-\mathbf{i}\sigma\kappa} = 1 - \mathbf{i}\sigma\kappa + O(\sigma^2). \tag{2.56b}$$

Substituting equations (2.56a) and (2.56b) in eq. (2.44a), this becomes eq. (2.10). Therefore,

$$\underset{\sigma\to 0}{e(\kappa, \sigma)} \equiv e_0(\kappa), \tag{2.57}$$

which is the definition of the relative error in wavenumber space used by Lele (1992) assuming zero time integration error. Lele (1992) considered in his analysis only centered schemes, for which $\kappa \in \mathbb{R}$, while the present definition equally applies to upwind/backwind schemes, for

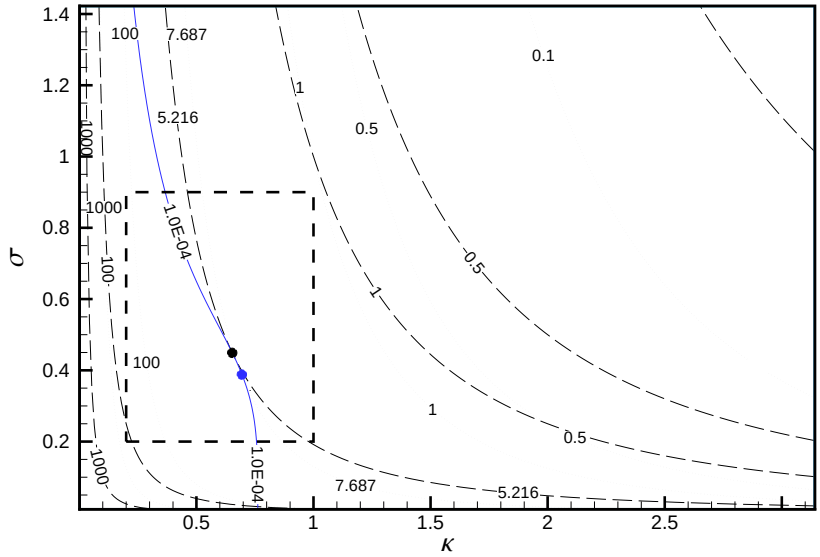

(a)

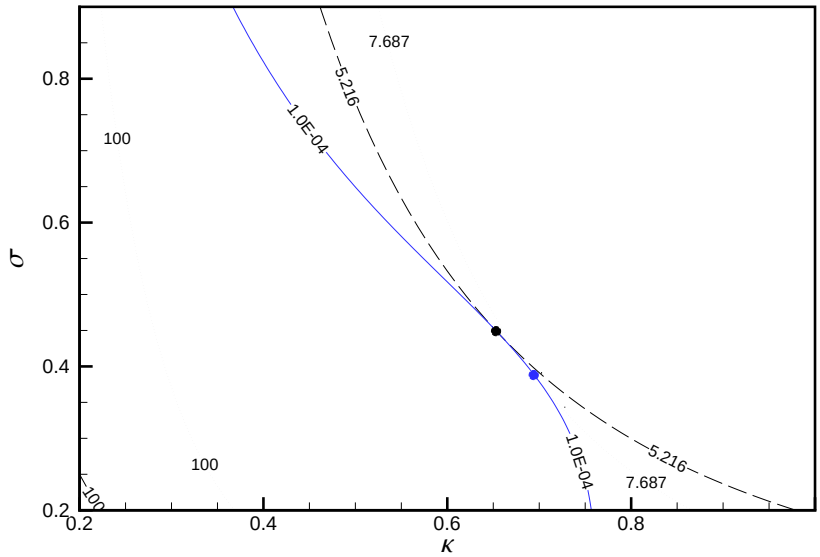

(b)

Figure 2.4: Fig. 2.4(a), Iso-contour level $\tilde{\epsilon} = 10^{-4}$ of normalized 'local' error function (blue continuous line) versus normalized cost function in one (black long dashed lines) and two (black dotted lines) dimensions for the $C1122/RK4$ scheme. Fig. 2.4(b), Zoom of the rectangular area reported in Fig. 2.4(a).

which $\kappa \in \mathbb{C}$.

On the other hand, by setting $\bar{\kappa} = \kappa$, as reported in eq. (2.30) by assuming zero spatial error, the definition of time discretization error used by Hu *et al.* (1996) is obtained:

$$e(\underset{\bar{\kappa}=\kappa}{\kappa}, \sigma) \equiv e_t(z) = \frac{\left|\sum_{j=0}^{p} (-\mathrm{i}\, z)^j - e^{-\mathbf{i}z}\right|}{z} = \frac{\left|r_t\left(z, \gamma_j\right) - e^{-\mathbf{i}z}\right|}{z}, \tag{2.58}$$

Hu *et al.* (1996) then proceed to squaring the numerator of eq. (2.58) and adjusting the last RK coefficient by minimizing it as a function of z.

Figure 2.6(a) shows the error functions from eqs. (2.44a), (2.57), and (2.58) on the $[\kappa, \sigma]$ plane. The error functions are derived from the same C1122/RK4 scheme as in Figs. 2.2 and 2.3. For small Courant numbers, at which $\sigma \to 0$, the error from eq. (2.57) in Fig. 2.6(a) (black dotted lines) overlaps that given by eq. (2.57) (long-dashed dark blue lines). Therefore, at $\sigma \to 0$, the error is uniquely function of the scaled wavenumber κ. As σ increases, the dotted black curves start to bend, eventually becoming equilateral hyperbolas, and the error becomes function of $z = \sigma\kappa$, as given in eq. (2.58) (long-dashed light blue lines). Figure 2.6(a) shows that, to a good approximation

$$e(\kappa, \sigma) \approx \max(e_0(\kappa), e_t(z)). \tag{2.59}$$

In a similar way, the 'global' normalized error function $\check{e}(\check{\kappa}, \check{\sigma})$ defined in eq. (2.53) approximates to

$$\check{e}(\check{\kappa}, \check{\sigma}) \approx \max(\check{e}_0(\check{\kappa}), \check{e}_t(\check{z})), \tag{2.60}$$

where the 'global' spatial error $\check{e}_0(\check{\kappa})$ is given by

$$\check{e}_0(\check{\kappa}) \equiv \underset{\sigma\to 0}{\check{e}}(\check{\kappa}, \check{\sigma}) \equiv \frac{1}{\check{\kappa}} \max_{0\le\kappa\le\check{\kappa}} |\bar{\kappa}(\kappa) - \kappa|\,, \tag{2.61}$$

and the 'global' temporal error $\check{e}_t(\check{z})$ is given by

$$\check{e}_t(\check{z}) \equiv \underset{\bar{\kappa}=\kappa}{\check{e}}(\check{\kappa}, \check{\sigma}) \equiv \frac{1}{\check{z}} \max_{0\le z\le\check{z}} \left|\sum_{j=0}^{p} (-\mathrm{i}\, z)^j - e^{-\mathbf{i}z}\right|, \tag{2.62}$$

where $\check{z} = \check{\sigma}\check{\kappa}$. Figure 2.6(b) shows that eq. (2.60) is a good approximation of the global error from eqs. (2.61) and (2.62), following the same arguments as in Fig. 2.6(a).

The condition of optimal scheme performance for a given error level $\tilde{\epsilon}$ implies the condition of tangency of the associated iso-error curve with the normalized iso-cost curves $\check{c}_{n_D} \sim$

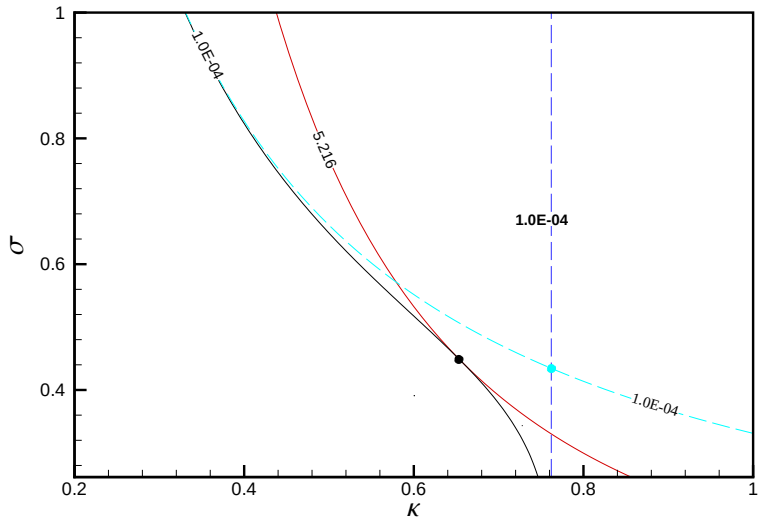

Figure 2.5: Iso-contour of normalized 'local' error function $\tilde{\epsilon} = 10^{-4}$ (solid black lines) and normalized one-dimensional cost function $1/(\sigma\kappa^2)$ (red solid lines), for $C1122/RK4$ scheme. The long-dash dark and light blue lines represent the corresponding approximation given respectively by eq. (2.57) and (2.58).

$1/(\check{\sigma}\check{\kappa}^{n_D+1})$, which occurs near the bend of $\check{e}(\check{\kappa},\check{\sigma}) = \tilde{\epsilon}$ curve, which, according to the approximation (2.60), is realized when

$$\check{e}_0(\check{\kappa}) = \check{e}_t(\check{z}) = \tilde{\epsilon}. \tag{2.63}$$

Figure 2.5 clearly shows the concepts aforementioned. Figure 2.5 highlights the iso-contour of the normalized 'local' error $\tilde{\epsilon} = 10^{-4}$ by black solid line and the corresponding normalized one-dimensional cost function $1/(\sigma\kappa^2)$ with the red solid lines, for the $C1122/RK4$ scheme. The 'exact' cost-optimal condition is obtained as the tangency point between the two curves, and it is reported by the black circle. The long-dashed dark and light blue lines represent the corresponding approximation given respectively by eqs. (2.57) and (2.58). The condition of tangency of the iso-error and iso-cost curves for the normalized error level $\tilde{\epsilon} = 10^{-4}$ under the spatial and temporal approximation is shown by the light blue circle, and it is realized when

$$e_0(\kappa) = e_t(z) = \tilde{\epsilon}. \tag{2.64}$$

Figure 2.5 shows, by visual inspection, that the approximation of eq. (2.59) is valid, due the proximity of the black and blue circle.

2.5.1 Spatial and temporal resolving efficiency

The problem of determining the optimal performance of a given scheme can be approximately decoupled into two sub-problems, by considering the influence of space and time discretization separately, by: (i) computing the optimal reduced wavenumber according to

$$\check{\kappa}^*(\tilde{\epsilon}) \equiv \check{e}_0^{-1}(\tilde{\epsilon}) \tag{2.65}$$

and (ii) computing the optimal Courant number by:

$$\check{\sigma}^*(\tilde{\epsilon}) = \check{z}^*(\tilde{\epsilon})/\check{\kappa}^*(\tilde{\epsilon}); \quad \check{z}^*(\tilde{\epsilon}) \equiv \check{e}_t^{-1}(\tilde{\epsilon}); \tag{2.66}$$

The quantities $\check{\kappa}^*(\tilde{\epsilon})$ and $\check{z}^*(\tilde{\epsilon})$ will be denoted, respectively, as 'spatial resolving efficiency' and 'temporal resolving efficiency' for a given value of normalized error $\tilde{\epsilon}$. The associated 'optimal' normalized cost is

$$\tilde{c}(\tilde{\epsilon}) = c_{n_D}(\check{\kappa}^*(\tilde{\epsilon}), \check{z}^*(\tilde{\epsilon})) = pN_{op}\,\frac{1}{\check{\sigma}^*\check{\kappa}^{*n_D+1}}. \tag{2.67}$$

Equations (2.59) and (2.63) allow to consider the spatial and temporal discretization separately in the present analysis to develop cost-optimized schemes. Specifically, cost-optimized finite-difference schemes for a specific target level $\tilde{\epsilon}$ can be designed by trying to maximize $\check{\kappa}^*(\tilde{\epsilon})$ and $\check{z}^*(\tilde{\epsilon})$ in eq. (2.67), which amounts to optimize separately the spatial and temporal discretization for the same target error level. The 'spatial resolving efficiency' and the 'temporal resolving efficiency' are equivalent in case of single and multi-scale problem, as shown in Fig. 2.6. In fact, the 'local' error function $e(\kappa, \sigma)$ differs from the 'global' one $\check{e}(\check{\kappa}, \check{\sigma})$ only near the points of local extrema of $\check{e}(\check{\kappa}, \check{\sigma})$, which does not affect the approximate decoupling of space and time discretization. These arguments will be used in Secs. 3.2.3 and 3.3.3 to separately optimize respectively spatial and temporal scheme for a specific target error level $\tilde{\epsilon}$.

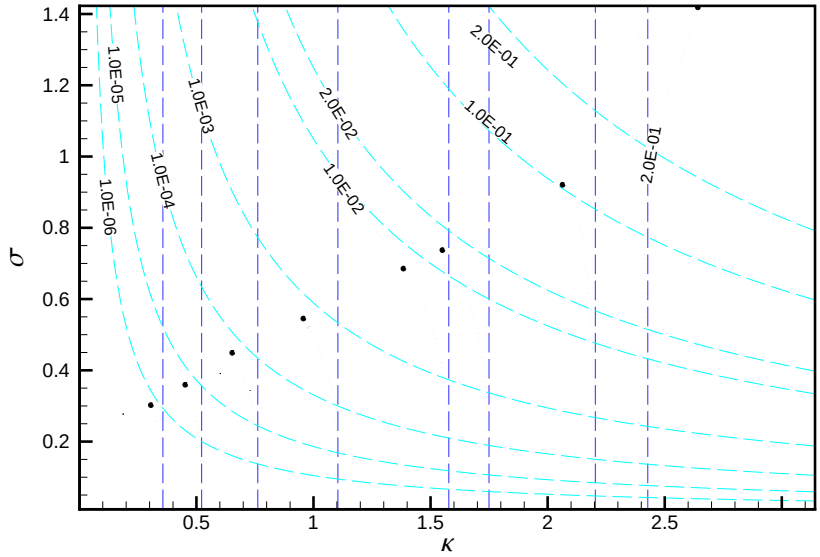

(a)

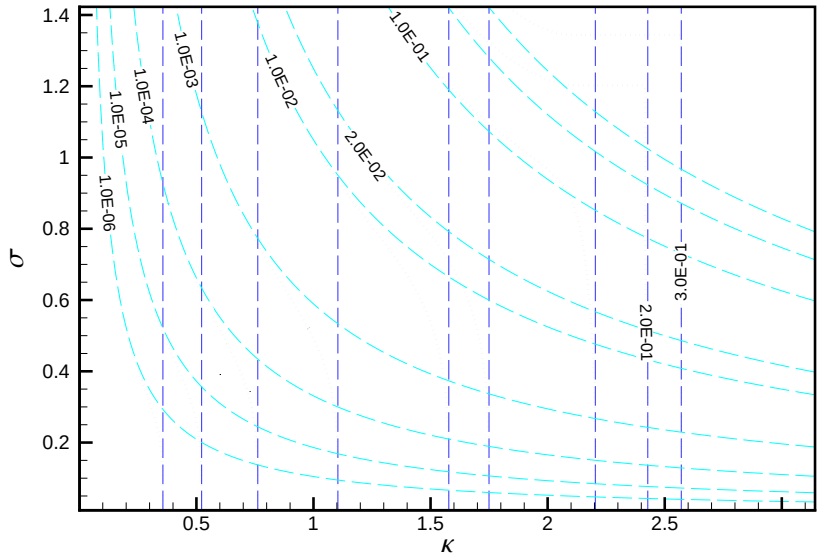

(b)

Figure 2.6: Fig. 2.6(a), Iso-contours of normalized 'local' error function $e(\kappa, \sigma)$ (black dotted lines); long-dashed dark and light blue lines represent the corresponding approximation given respectively by eq. (2.57) and (2.58) for $C1122/RK4$ scheme; filled black dots indicates the 'optimal' working condition. Fig. 2.6(b), Iso-contours of normalized 'global' error function $\check{e}(\check{\kappa}, \check{\sigma})$; long-dashed light and dark blue lines represent the corresponding approximation given respectively by eq. (2.61) and (2.62) for $C1122/RK4$ scheme.

Chapter 3

Numerical Method

This chapter presents the numerical method used in the present work.

Section 3.1 reports the governing equations that will be solved in the present study, that are the LAE and the LEE. The derivation of the LEE in non-dimensional and in characteristic form starting from the 2-D strong conservative form of the Euler equations is reported.

Section 3.2 introduces the spatial discretization method used. The most common finite-difference schemes used in CAA are reviewed and compared in term of computational efficiency. The effect of the spatial discretization and the number of physical dimensions on the computational cost is analysed. The spatial cost-optimization technique, based on the maximization of the spatial resolving efficiency $\check{\kappa}^*$ for a given value of normalized error $\tilde{\epsilon}$, is presented. The cost-optimized schemes are extended to the class of sixth-order prefactored compact schemes of Hixon (2000).

Section 3.3 analyses the impact on the computational cost of using different time integration schemes for a two dimensional problem for various spatial discretization schemes. The temporal cost-optimization technique, based on the maximization of the temporal resolving efficiency $\check{z}^*$ for a given value of normalized error $\tilde{\epsilon}$, is presented.

Section 3.4 shows the predicted performance of the combined space and time cost-optimization for the same level of error. A computational advantage is predicted by using cost-optimized scheme to model wave propagation problems at their design operational point.

Section 3.5 discusses the effect of the perimetrical scheme on the interior scheme. Two methods of treating near-boundary points are presented and compared against the boundary treatments of Hixon (2000) and Ashcroft & Zhang (2003). The first approach is a prefactored sixth-order explicit one-sided finite-difference scheme that uses a seven-point stencil, the second is a pref-

actored explicit central scheme with an 11-point stencil. The wave propagation characteristics of these boundary closures are examined. An new 11-point stencil with double precision accuracy is derived. It shows a better performance in spectral sense compared to the equivalent ones of Hixon (2000) and Ashcroft & Zhang (2003).

An eigenvalue analysis is performed to verify under which conditions the prefactored cost-optimized schemes coupled with the selected boundary closures generate a numerically stable algorithm.

Section 3.6 details the artificial boundary conditions used in the present study. Three implementations are shown: the subsonic inflow, the subsonic outflow and the inviscid wall. Two type of absorbing layer technique are discussed. The first one is the absorbing layer technique by Richards *et al.* (2004), that directly forces the solution to a target flow state within the absorbing layer. The second one is a zonal characteristic based boundary condition proposed by Sandberg & Sandham (2006).

Section 5.3 summarizes the work presented and highlights the main achievements of this chapter.

The code for the computational efficiency comparison used in Secs. 3.2.2 and 3.3.1 has been written by the author using `Matlab®`. The serial finite-difference code has been written, from scratch, by the author in `Fortan` 90. The parallel version of the code, reported in Ch. 4, has been written together with Dr. P. Ghillani (I. Spisso & Rona, 2009).

3.1 Governing Equations

This work concerns with the application of high-order finite-differences to compressible aeroacoustic problems. Specifically, numerical predictions are sought of sound generated aerodynamically by flow interaction with solid boundaries. This class of problems is governed by the Linearised Euler Equations (LEE). The LEE are first-order coupled partial differential equations in space and time. This system of hyperbolic equations, are a multi-variable version of the *LAE*. Therefore, the numerical method is first tested against benchmark solutions of the *LAE* of eq. (2.13) and then further tested against problems governed by the LEE.
The following Secs. 3.1.1 and 3.1.2 report the derivation of the the LEE in non-dimensional and characteristic form starting from the Euler equations.

3.1.1 Derivation of the quasi-linear Euler Equations

The inviscid Euler equations are derived by the application of the principles of conservation of mass, momentum, and energy to an arbitrary volume of inviscid fluid. They derives from the Navier-Stokes equations for a calorically perfect gas with zero viscosity and heat conduction terms (Anderson *et al.*, 1984). The 2-D Euler equations are commonly recast in *strong* or *vector* conservative form suitable for numerical computation as

$$\frac{\partial \mathbf{Q}}{\partial t} + \frac{\partial \mathbf{E}}{\partial x} + \frac{\partial \mathbf{F}}{\partial y} = 0, \tag{3.1}$$

where **Q**, **E** and **F**

$$\mathbf{Q} = \begin{bmatrix} \rho \\ \rho u \\ \rho v \\ \rho e_t \end{bmatrix}, \quad \mathbf{E} = \begin{bmatrix} \rho u \\ \rho u^2 + p \\ \rho v u \\ \rho \left(e_t + p\right) u \end{bmatrix}, \quad \mathbf{F} = \begin{bmatrix} \rho v \\ \rho u v \\ \rho v^2 + p \\ \rho \left(e_t + p\right) v \end{bmatrix} \tag{3.2}$$

are, respectively, the vector of conservative variables and the vectors of the inviscid fluxes, $e_t = p/[(\gamma - 1)\rho] + (u^2 + v^2)/2$ is the total energy per unit mass and γ is the ratio of the specific heats.

The Euler equations have several important mathematical properties that are illustrated in the classical fluid dynamics textbook (Hirsch, 2007). The hyperbolicity allows to re-cast the system of equations (3.1) in characteristic form, meaning that the projection of the equations

in any spatial direction gives rise to a system of coupled wave-like equations. This property will be used to re-write the system of equations (3.1) as a multi-variable version of the *LAE* as reported in following Sec. 3.1.2.2.

The system of equations (3.1) can be written in the so-called *quasi-linear* form, where the spatial derivatives of the flow variables are pre-multiplied by the Jacobian matrices as follow

$$\frac{\partial \mathbf{U}}{\partial t} + \mathbf{A}\frac{\partial \mathbf{U}}{\partial x} + \mathbf{B}\frac{\partial \mathbf{U}}{\partial y} = 0, \tag{3.3}$$

where **U**, **A** and **B**

$$\mathbf{U} = \begin{bmatrix} \rho \\ u \\ v \\ p \end{bmatrix}, \quad \mathbf{A} = \begin{bmatrix} u & \rho & 0 & 0 \\ 0 & u & 0 & 1/\rho \\ 0 & 0 & u & 0 \\ 0 & \rho c^2 & 0 & u \end{bmatrix}, \quad \mathbf{B} = \begin{bmatrix} v & 0 & \rho & 0 \\ 0 & v & 0 & 0 \\ 0 & 0 & v & 1/\rho \\ 0 & 0 & \rho c^2 & v \end{bmatrix} \tag{3.4}$$

are, respectively, the vector of primitive variables and the Jacobian matrices.

The system of equations (3.3) lead to results equivalent to the ones from the system of equations (3.1) when the flow field does not contain strong variations in the flow state (i.e. smooth flows), and has the computational advantage of requiring the differentiation with respect to the various space directions on the same vector of primitive variables **U**, instead of computing the derivatives sequentially on the vectors **E** and **F**. The quasi-linear forms of the Euler equations allow for the definition of the *linearized* formulation that is often used in CAA.

3.1.2 Linearized Euler Equations

The system of equations (3.3) is linearized with respect to a reference state given by the uniform mean density ρ_0, pressure p_0, x-velocity u_0 and y-velocity v_0, so that the flow state is given by the sum of the reference state plus its small perturbation $()'$ about the mean:

$$\begin{cases} \rho = \rho_0 + \rho' \\ u = u_0 + u' \\ v = v_0 + v' \\ p = p_0 + p'. \end{cases} \tag{3.5}$$

The governing equations can be written in dimensional non-conservative form as

$$\frac{\partial \mathbf{U}}{\partial t} + \mathbf{A}_0 \frac{\partial \mathbf{U}}{\partial x} + \mathbf{B}_0 \frac{\partial \mathbf{U}}{\partial y} = 0 \tag{3.6}$$

where the constant-coefficient matrices $\mathbf{A}_0$ and $\mathbf{B}_0$ are

$$\mathbf{A}_0 = \begin{bmatrix} u_0 & \rho_0 & 0 & 0 \\ 0 & u_0 & 0 & 1/\rho_0 \\ 0 & 0 & u_0 & 0 \\ 0 & \rho_0 c_0^2 & 0 & u_0 \end{bmatrix}, \quad \mathbf{B}_0 = \begin{bmatrix} v_0 & 0 & \rho_0 & 0 \\ 0 & v_0 & 0 & 0 \\ 0 & 0 & v_0 & 1/\rho_0 \\ 0 & 0 & \rho_0 c_0^2 & v_0 \end{bmatrix}. \tag{3.7}$$

In this case, the Jacobian matrices $\mathbf{A}_0$, $\mathbf{B}_0$ do not depend on the actual state of the flow but on the reference state that is considered constant throughout the computation at any point of the field. This particular form of the equations has the computational advantage of avoiding to update the Jacobian matrices at each time step. They can be computed and stored in memory once and for all at the beginning of simulation.

This linearised form of the Euler equations suits only certain classes of problems in which the perturbations are of small amplitude so that the non-linear effect can be considered negligible and the mean value of the flow variables does not vary in time. This is the class of problems typically involved in CAA.

3.1.2.1 Non-dimensional form

By using the following length scales:

$$\begin{aligned} &\Delta x = \Delta y = \text{length scale} \\ &c_0 \text{ (ambient sound speed)} = \text{velocity scale} \\ &\rho_0 = \text{density scale} \end{aligned} \tag{3.8}$$

and assuming a calorically perfect gas, for which

$$c_0^2 = \frac{\gamma p_0}{\rho_0}, \tag{3.9}$$

it is possible to define the following non-dimensional variables:

$$\rho^* = \frac{\rho'}{\rho_0} \quad x^* = \frac{x}{\Delta x} \quad y^* = \frac{y}{\Delta x} \quad t^* = t\frac{c_0}{\Delta x} \quad u^* = \frac{u'}{c_0} \quad v^* = \frac{v'}{c_0} \quad M_x = \frac{u_0}{c_0} \quad M_y = \frac{v_0}{c_0} \quad p^* = \frac{p'}{\rho_0 c_0^2}, \tag{3.10}$$

where M_x and M_y are, respectively, the constant mean flow Mach number components in the x and y directions. Consistently with the normalized length scales in (3.8), pressure is normalized by $\rho_0 c_0^2$ and time by $\Delta x/c_0$.

Equation (3.6) can be recast in the non-dimensional form

$$\frac{\partial \mathbf{U}^*}{\partial t^*} + \mathbf{A}_0^* \frac{\partial \mathbf{U}^*}{\partial x^*} + \mathbf{B}_0^* \frac{\partial \mathbf{U}^*}{\partial y^*} = 0, \tag{3.11}$$

where the vector $\mathbf{U}^*$, and the matrices $\mathbf{A}_0^*$ and $\mathbf{B}_0^*$ are given by:

$$\mathbf{U}^* = \begin{bmatrix} \rho^* \\ u^* \\ v^* \\ p^* \end{bmatrix}, \quad \mathbf{A}_0^* = \begin{bmatrix} M_x & 1 & 0 & 0 \\ 0 & M_x & 0 & 1 \\ 0 & 0 & M_x & 0 \\ 0 & 1 & 0 & M_x \end{bmatrix}, \quad \mathbf{B}_0^* = \begin{bmatrix} M_y & 0 & 1 & 0 \\ 0 & M_y & 0 & 0 \\ 0 & 0 & M_y & 1 \\ 0 & 0 & 1 & M_y \end{bmatrix}. \tag{3.12}$$

3.1.2.2 Characteristic form

Consider the boundaries located at x_1 and x_N as shown in Fig. 2.1. The governing equations of eq. (3.11) can be re-cast as

$$\frac{\partial \mathbf{U}^*}{\partial t^*} + \mathbf{A_0}^* \frac{\partial \mathbf{U}^*}{\partial x^*} + \mathbf{C} = 0 \quad \mathbf{C} = \mathbf{B}_0^* \frac{\partial \mathbf{U}^*}{\partial y^*}, \tag{3.13}$$

where the **C** vector contains no partial derivative in either x^* or t^*.

The $\mathbf{A}_0^*$ matrix can be decomposed by Principal Component Analysis solving the characteristic equation $det(\mathbf{A}_0^* - \lambda_i \mathbf{I}) = 0$. This gives $\mathbf{A}_0^* = \mathbf{S}\mathbf{\Lambda}\mathbf{S}^{-1}$, where $\mathbf{\Lambda}$ is a diagonal matrix with elements:

$$\lambda_1 = M_x - 1, \quad \lambda_2 = \lambda_3 = M_x, \quad \lambda_4 = M_x + 1, \tag{3.14}$$

and **S** and its inverse $\mathbf{S}^{-1}$ are, respectively, the right and left eigenvector matrices, as shown later.

The system of equation (3.11) is hyperbolic, since the eigenvalues of $\mathbf{A}_0^*$ and $\mathbf{B}_0^*$ (see Sec. A.2) are real and ordered so that $\lambda_1 \leq \lambda_2 \leq \ldots \lambda_m$ (Thompson, 1990). The eigenvalues λ_1 and λ_4 are the non-dimensional velocities of sound waves moving in the negative and positive x directions; λ_2 is the convection velocity (the speed at which entropy waves travel), while λ_3 is the velocity at which the v-velocity is advected along the y-direction by a vorticity wave. The characteristic velocities are constant because they derive from the linearized matrix $\mathbf{A}_0$, which is a constant-element matrix. The algebraic multiplicity, that is the multiplicity of the eigenvalue as a root of the characteristic equation, of the eigenvalues λ_1 and λ_4 is equal to 1; the algebraic multiplicity of the double eigenvalue $\lambda_2 = \lambda_3$ is equal to 2.

The corresponding left eigenvectors l_i^T are derived by solving the linear system of coupled equations $l_i^T \cdot (\mathbf{A}_0 - \lambda_i \mathbf{I}) = 0$, for $i = 1, \ldots, 4$. This gives

$$l_1^T = (0, -1, 0, 1) \tag{3.15a}$$

$$l_2^T = (1, 0, 0, -1) \tag{3.15b}$$

$$l_3^T = (0, 0, 1, 0) \tag{3.15c}$$

$$l_4^T = (0, 1, 0, 1). \tag{3.15d}$$

The third relation (3.15c) is derived by setting $l_3^T \cdot (\mathbf{A}_0 - \lambda_3 \mathbf{I})^2 = 0$, with the exponent of the term $(\mathbf{A}_0 - \lambda_3 \mathbf{I})$ set to 2, to take into account for the algebraic multiplicity of the double eigenvalue

$\lambda_2 = \lambda_3$.

The amplitude of the characteristic waves L_i's, associated with each characteristic velocity λ_i, are

$$L_i = \lambda_i l_i^T \frac{\partial \mathbf{U}^*}{\partial x^*}. \tag{3.16}$$

Substituting for l_i^T in eq. (3.16) gives

$$L = \begin{pmatrix} L_1 \\ L_2 \\ L_3 \\ L_4 \end{pmatrix} = \begin{bmatrix} \lambda_1 \left(\frac{\partial p^*}{\partial x^*} - \frac{\partial u^*}{\partial x^*} \right) \\ \lambda_2 \left(\frac{\partial \rho^*}{\partial x^*} - \frac{\partial p^*}{\partial x^*} \right) \\ \lambda_3 \frac{\partial v^*}{\partial x^*} \\ \lambda_4 \left(\frac{\partial p^*}{\partial x^*} + \frac{\partial u^*}{\partial x^*} \right) \end{bmatrix}, \tag{3.17}$$

where L_1 and L_4 are, respectively, the left and right going acoustic wave amplitudes, L_2 is the entropy wave amplitude, and L_3 is the shear wave amplitude.

The system of linear equations (3.17) can be solved for $\frac{\partial \mathbf{U}^*}{\partial x^*}$ to give the x-derivatives of the primitive variables:

$$\frac{\partial \rho^*}{\partial x^*} = \frac{L_2}{\lambda_2} + \frac{1}{2}\left(\frac{L_4}{\lambda_4} + \frac{L_1}{\lambda_1} \right) \tag{3.18a}$$

$$\frac{\partial u^*}{\partial x^*} = \frac{1}{2}\left(\frac{L_4}{\lambda_4} - \frac{L_1}{\lambda_1} \right) \tag{3.18b}$$

$$\frac{\partial v^*}{\partial x^*} = \frac{L_3}{\lambda_3} \tag{3.18c}$$

$$\frac{\partial p^*}{\partial x^*} = \frac{1}{2}\left(\frac{L_4}{\lambda_4} + \frac{L_1}{\lambda_1} \right). \tag{3.18d}$$

The **S** matrix and its inverse are given by:

$$S^{-1} = \begin{pmatrix} l_1^T \\ l_2^T \\ l_3^T \\ l_4^T \end{pmatrix} = \begin{bmatrix} 0 & -1 & 0 & 1 \\ 1 & 0 & 0 & -1 \\ 0 & 0 & 1 & 0 \\ 0 & 1 & 0 & 1 \end{bmatrix}, \tag{3.19}$$

$$S = \begin{pmatrix} r_1 & r_2 & r_3 & r_4 \end{pmatrix} = \begin{bmatrix} \frac{1}{2} & 1 & 0 & \frac{1}{2} \\ -\frac{1}{2} & 0 & 0 & \frac{1}{2} \\ 0 & 0 & 1 & 0 \\ \frac{1}{2} & 0 & 0 & \frac{1}{2} \end{bmatrix}, \tag{3.20}$$

with $\mathbf{S}^{-1}\mathbf{S} = \mathbf{I}$, and $l_i^T \cdot r_j = \delta_{ij}$, where r_j is the j-th right eigenvector and δ_{ij} is the Kronecker delta function.

The **d** vector is given by:

$$\mathbf{d} = \begin{pmatrix} d_1 \\ d_2 \\ d_3 \\ d_4 \end{pmatrix} = \mathbf{S} \cdot L = \begin{bmatrix} \frac{1}{2} & 1 & 0 & \frac{1}{2} \\ -\frac{1}{2} & 0 & 0 & \frac{1}{2} \\ 0 & 0 & 1 & 0 \\ \frac{1}{2} & 0 & 0 & \frac{1}{2} \end{bmatrix} \begin{pmatrix} L_1 \\ L_2 \\ L_3 \\ L_4 \end{pmatrix} = \begin{bmatrix} L_2 + \frac{1}{2}(L_1 + L_4) \\ \frac{1}{2}(L_4 - L_1) \\ L_3 \\ \frac{1}{2}(L_4 + L_1) \end{bmatrix}. \tag{3.21}$$

The non-dimensional governing equation (3.11) can be now re-written as

$$\frac{\partial \mathbf{U}^*}{\partial t^*} + \mathbf{d} + B_0^* \frac{\partial \mathbf{U}^*}{\partial y^*} = 0, \tag{3.22}$$

or in extended form:

$$\frac{\partial \rho^*}{\partial t^*} + \left[L_2 + \frac{1}{2}(L_1 + L_4) \right] + M_y \frac{\partial \rho^*}{\partial y^*} + \frac{\partial v^*}{\partial y^*} = 0 \tag{3.23a}$$

$$\frac{\partial u^*}{\partial t^*} + \left[\frac{1}{2}(L_4 - L_1) \right] + M_y \frac{\partial u^*}{\partial y^*} = 0 \tag{3.23b}$$

$$\frac{\partial v^*}{\partial t^*} + L_3 + M_y \frac{\partial v^*}{\partial y^*} + \frac{\partial p^*}{\partial y^*} = 0 \tag{3.23c}$$

$$\frac{\partial p^*}{\partial t^*} + \left[\frac{1}{2}(L_4 + L_1) \right] + M_y \frac{\partial p^*}{\partial y^*} + \frac{\partial v^*}{\partial y^*} = 0 \tag{3.23d}$$

The system of equations (3.23) is an uncoupled system of linearized equations along y-constant lines, which can be solved as *ODE*s at the x boundaries. The resulting equations allow to interpret the changes in flow state as a linear combination of one-dimensional waves normal to the x boundary, by considering the flow locally (i.e. at boundaries nodes) as inviscid and one-dimensional. The relations obtained by this method are not 'physical' conditions but should be viewed as compatibility relations between the choices made for the physical boundary con-

ditions and the amplitudes of waves crossing the boundary. This development has implicitly assumed that the waves that are arriving at the boundary are 1-D waves with no curvature and that these waves are arriving normal to the boundary. In realistic flows, the waves are multi-dimensional, with an unknown curvature. Thus, while this approximation gives a clear guideline as to which physical quantities must be specified by the CFD practitioner along the computational domain boundaries, the actual form of these waves (the eigenvectors) is not generally accurate (Colonius, 2004). The formulation of eq. (3.23) will be used in Sec. 3.6.1 to formulate approximate 1-D boundary closures. Section 3.6 will present the absorbing layer technique that will be used in the present work together with the characteristic formulation of eq. (3.23).

Alternative approaches to infer the flow state at the computational boundaries are the Asymptotic Expansion Method (Tam & Web, 1993) and Perfectly Matched Layer (Hu, 1996). An extensive review of the the artificial boundary condition for the simulation of inflow, outflow and far-field problems for compressible flow is given by Colonius (2004).

3.2 Spatial Discretization

3.2.1 Interior scheme

A class of tridiagonal compact schemes with five point stencils $C1122$ is obtained by setting ($P = Q = 1$, $R = S = 2$) in eq. (2.1). This gives:

$$\alpha_1 f'_{i-1} + f'_i + \alpha_1 f'_{i+1} = \frac{1}{h}\left(a_{-2} f_{i-2} + a_{-1} f_{i-1} + a_1 f_{i+1} + a_2 f_{i+2}\right) + O(h^4), \tag{3.24}$$

where the coefficients are given by:

$$\begin{cases} a_2 = -a_{-2} = \dfrac{1}{12}(4\alpha_1 - 1) \\ a_1 = -a_{-1} = \dfrac{1}{3}(\alpha_1 + 2) \end{cases} \tag{3.25}$$

The leading term of truncation error $O(h^4)$ in eq. (3.24) is given by $\frac{4}{5!}(3\alpha_1 - 1)\, h^4 f^{(5)}$, where $f^{(5)}$ is $\dfrac{d^5 f_i}{dh^5}$.

As $\alpha_1 \to 0$, this family merges into the well-known fourth-order explicit central finite-difference $C0011$ scheme. Similarly, for $\alpha_1 = 1/4$, the classical Padè $C1111$ scheme is recovered. By setting

$$\alpha_1 = 1/3, \quad a_1 = 7/9, \quad a_2 = 1/36, \tag{3.26}$$

the leading term of the truncation error order vanishes and the scheme is formally sixth-order accurate, with a truncation error of $\frac{4}{7!}h^6 f^{(7)}$ (Lele, 1992).

Figure 3.1 shows the dispersive characteristics of a selection of centred classical and optimized finite-difference schemes, the coefficients for which are reported in Tabs. 3.1 and 3.2. Because these schemes are centred, $S = R$ in eq. (2.1). Taking $P = Q$ in eq. (2.1), equation (2.9) becomes

$$\bar{\kappa}(\kappa) = \frac{\sum_{j=1}^{S} 2a_j \sin(j\kappa)}{1 + \sum_{j=1}^{Q} 2\alpha_j \cos(j\kappa)}, \tag{3.27}$$

so that $\bar{\kappa}(\kappa) \in \mathbb{R}$ and the spatial error is purely dispersive, i.e. $e_0(\kappa) \equiv \varepsilon_R(\kappa)$.

The range of wavenumbers over which the scaled pseudo-wavenumber $\bar{\kappa}$ approximates the exact differentiation within a specified error tolerance defines the set of *well-resolved* waves, also named smooth, physical or '*p*' waves; the remaining right-hand side of the spectrum in Fig. 3.1 is populated by *poorly-resolved*, spurious, numerical or '*q*' waves. It is evident from Fig. 3.1 that the high-order schemes (fourth order and higher) have a better spectral resolution com-

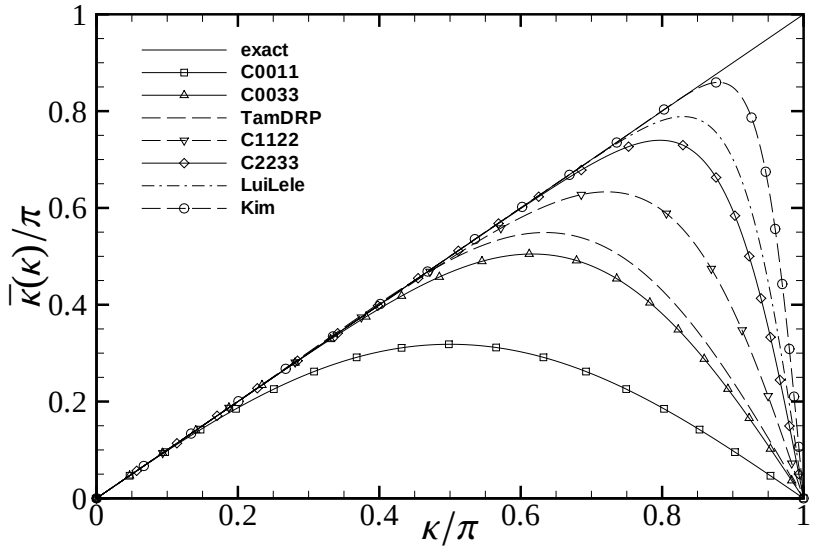

Figure 3.1: Pseudo-wavenumber diagram for the centred finite-difference schemes reported in Tabs. 3.1 and 3.2.

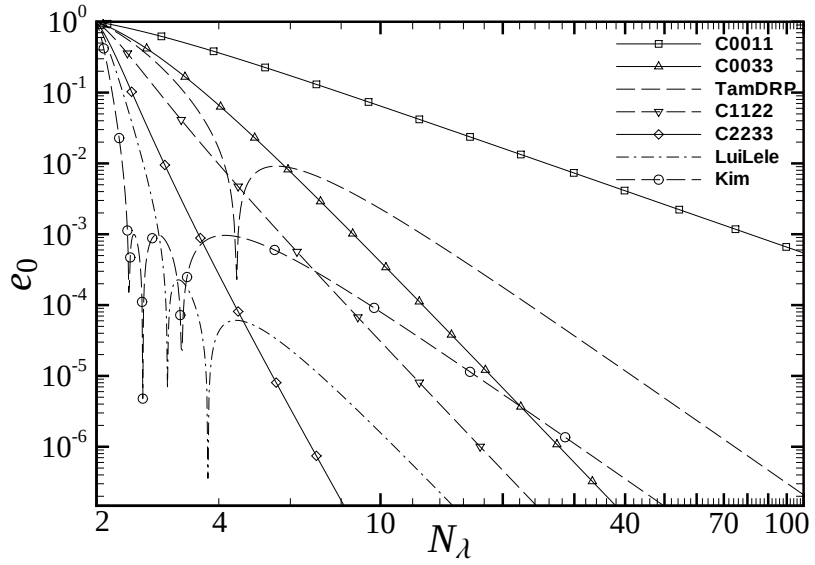

Figure 3.2: Dispersive error for the centred finite-difference schemes reported in Tabs. 3.1 and 3.2. Lines and symbols as in Fig. 3.1.

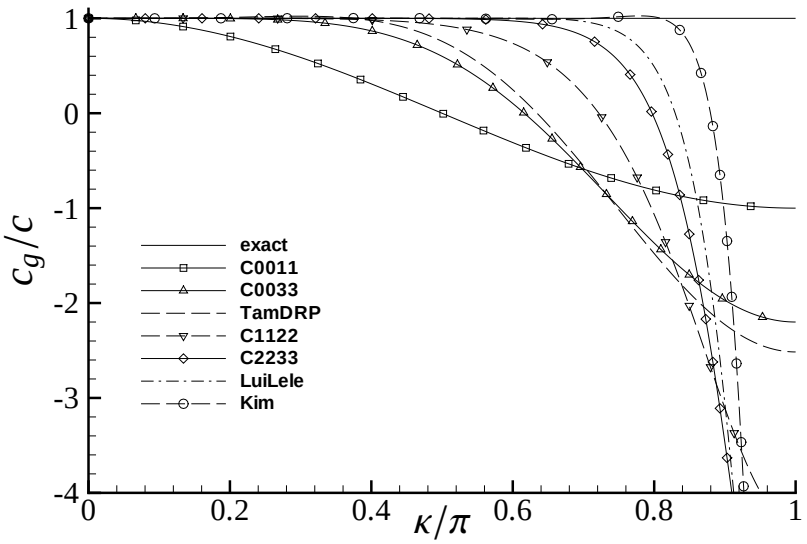

(a)

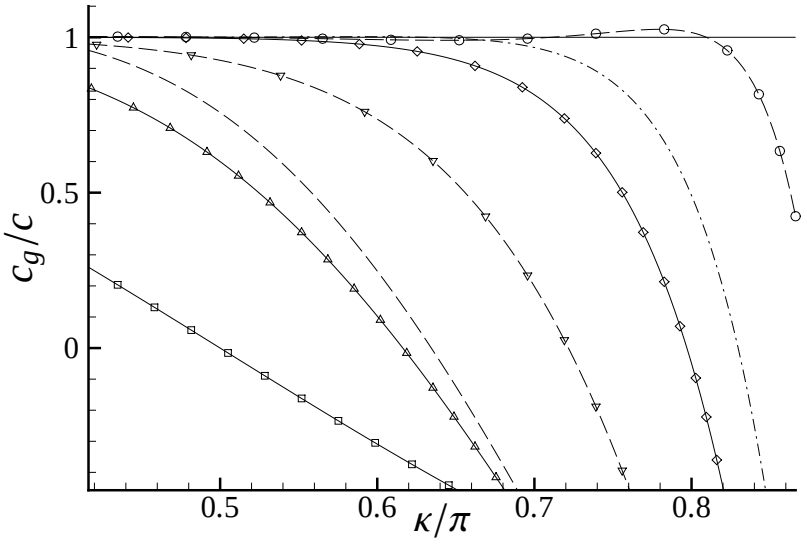

(b)

Figure 3.3: Fig.3.3(a), group velocity for the centred finite-difference schemes reported in Tabs. 3.1 and 3.2. Lines and symbols as in Fig. 3.1. Fig.3.3(b), enlarged view of Fig.3.3(a) ($0.41\pi \leq \kappa \leq 0.86\pi$).

	$C0011$	$C0033$	TamDRP
α_1	0	0	0
α_2	0	0	0
a_1	0.5	3/4	0.799266426974156
a_2	0	-3/20	-0.189413141579325
a_3	0	1/60	0.026519952061497
$\overline{\kappa}_{max}$	0.99	1.58	1.72
stencil size	3	7	7
N_{op}	2	8	8
Order (n)	2	6	4

Table 3.1: Coefficients for explicit centred finite-difference schemes *CPQRS* in Fig. 3.1. $P = Q = 0$, $R = S$, $\alpha_0 = 1$, $a_0 = 0$, $a_{-j} = a_j$ in eq. (2.1). The number of algebraic operation per node N_{op} has been taken from Colonius & Lele (2004).

	$C1122$	$C2233$	LuiLele	Kim
α_1	1/3	1/2	0.5381301488732363	0.5862704032801503
α_2	0	1/20	0.0666331901238811	0.09549533555017055
a_1	7/9	17/24	0.683788862199635	0.6431406736919156
a_2	1/36	101/60	0.20585704252707	0.2586011023495066
a_3	0	1/600	0.00308679724778108	0.007140953479797375
$\overline{\kappa}_{max}$	1.99	2.32	2.47	2.7
stencil size	5	7	7	7
N_{op}	9	17	17	17
Order (n)	6	10	6	4

Table 3.2: Coefficients for implicit centred finite-difference schemes *CPQRS* in Fig. 3.1. $P = Q \neq 0$, $R = S$, $\alpha_0 = 1$, $a_0 = 0$, $a_{-j} = a_j$ in eq. (2.1). The number of algebraic operation per node N_{op} has been taken from Colonius & Lele (2004).

pared with their low-order counterpart, as indicated also by the maximum value of the scaled pseudo-wavenumber $\bar{\kappa}_{max}$ in Tabs. 3.1 and 3.2. The drawback of the use of a high order scheme is given by the longer stencil in this type of schemes.

For a given level of accuracy, explicit schemes employ a large computational stencil, while compact schemes use a smaller stencil. For example, to obtain sixth-order accuracy, the C0033 scheme employs a seven point stencil, while the C1122 needs a smaller five point stencil. On the other hand, the compact schemes have two disadvantages: first, a matrix has to be inverted to obtain the spatial derivative at each grid point, although this multi-diagonal matrix inversion can be done efficiently using the Thomas algorithm (Press & Firm, 1996). Secondly, the boundary stencils have a large effect on the stability and accuracy of the scheme, as reported in Secs. 3.5, by Carpenter *et al.* (1993b) and Tam & Dong (1993). Figures 3.1 and 3.2 indicate that the optimized schemes have a better wave resolution performance compared with the classical equivalent stencil size (see. TamDRP versus C0033), and a one to two order of magnitude lower error in the region of *poorly-resolved* waves, but they degrade their performance in the region of *well-resolved* waves.

A common feature of all centred schemes is that, for a given frequency, there are two solutions to the dispersion relation given in eq. (3.27), one for the *well-resolved* and the other for the *poorly-resolved* waves (Vichnevetsky & Bowles, 1982). For the *well-resolved* waves, the group velocity is positive and these waves approach the solution of the original PDE as the grid is refined. The *poorly-resolved* waves have a negative group velocity and they are not a physical solution of eq. (2.13). For the C0011 classical explicit second order scheme, the speed of propagation of the grid-to-grid oscillation wave ($\kappa/\pi = 1$) is equal and opposite to physical wave speed c of eq. (2.13). As the order of the scheme is increased, the speed of propagation of the *poorly-resolved* waves assumes an higher negative supersonic speed ($c < -1$). Figure 3.3 shows that the compact schemes propagate with the correct phase speed for a wider spectrum of wavenumbers compared to the explicit schemes, but the very *poorly-resolved* waves, near to the grid-to-grid oscillation, travel with an unphysical supersonic speed greater than the one of the explicit schemes. Finally, the compact optimized schemes of Lui&Lele and Kim have a maximum value of group velocity c_g/c slightingly bigger than 1, respectively at $\kappa/pi = 0.5$ and $\kappa/\pi = 0.78$.

3.2.2 Computational efficiency

In order to compare the performance of different schemes, it is sufficient to analyse the normalized error versus cost relation, accounting for the operation count estimate reported by Colonius & Lele (2004). As discussed in Sec. 2.4, the problem is formulated in terms of obtaining a computational result with the same error from different schemes and identifying which scheme produces such result at the lowest computational cost. In general, the cost of the computation is a function of the acceptable level of error $\tilde{\epsilon}$, the spatial discretization scheme CPQRS, the number of spatial dimensions of the problem n_D, and the time integration scheme t. Therefore

$$c^* = f\left(\tilde{\epsilon}, CPQRS, n_D, t\right). \tag{3.28}$$

The efficiency comparison formally consist of finding the minima in the manifold of eq. (3.28) in its four-dimensional space $(\tilde{\epsilon}, CPQRS, n_D, t)$. As the present work aims at identifying an efficient numerical scheme for CAA applications, the parameter space is constrained to the spatial discretization schemes of Tabs. 3.1 and 3.2, two physical spatial dimensions ($n_D = 1, 2$), and two time integration schemes ($t = RK3, RK4$). Furthermore, from eq. (2.55), the effects of the independent variables $(CPQRS, n_D, t)$ are shown to be linear factors of the cost.

Effect of space discretization

The effect of the spatial discretization schemes on the computational cost is considered for one-dimensional time-dependent simulations ($n_D = 1$), time-advanced by a fourth-stage fourth-order RK time integration scheme ($t = RK4$). The results of the analysis are shown in Fig. 3.4 and Fig. 3.5 for the centred spatial discretizations listed in Fig. 3.1. Figures 3.4 and 3.5 show the 'local' and the 'global' error functions, respectively.

Figures 3.4(a) and 3.5(a) show the effects of changing the spatial discretization scheme on the cost-error functions. For a normalized error of $\tilde{\epsilon} \approx 10^{-1}$, all the schemes collapse in same cost region between $6 \leq c_1^* \leq 15$. This is the region encircled in Figure 3.4(a), the so-called knuckle region discussed by Colonius & Lele (2004), in which all the schemes have a comparable computational cost. However, when a normalized error lower that 10^{-1} is required, high-order and optimized schemes reveal their superiority. For example, for a given normalized 'local' error $\tilde{\epsilon} = 1.24 \times 10^{-4}$, the optimized scheme by Lui&Lele offers a cost saving over the corresponding compact tenth-order equivalent stencil-size C2233 scheme of approximately 50%, as detailed in Fig. 3.4(b), which shows an enlargement of the area in the dashed rectangle of Fig. 3.4(a).

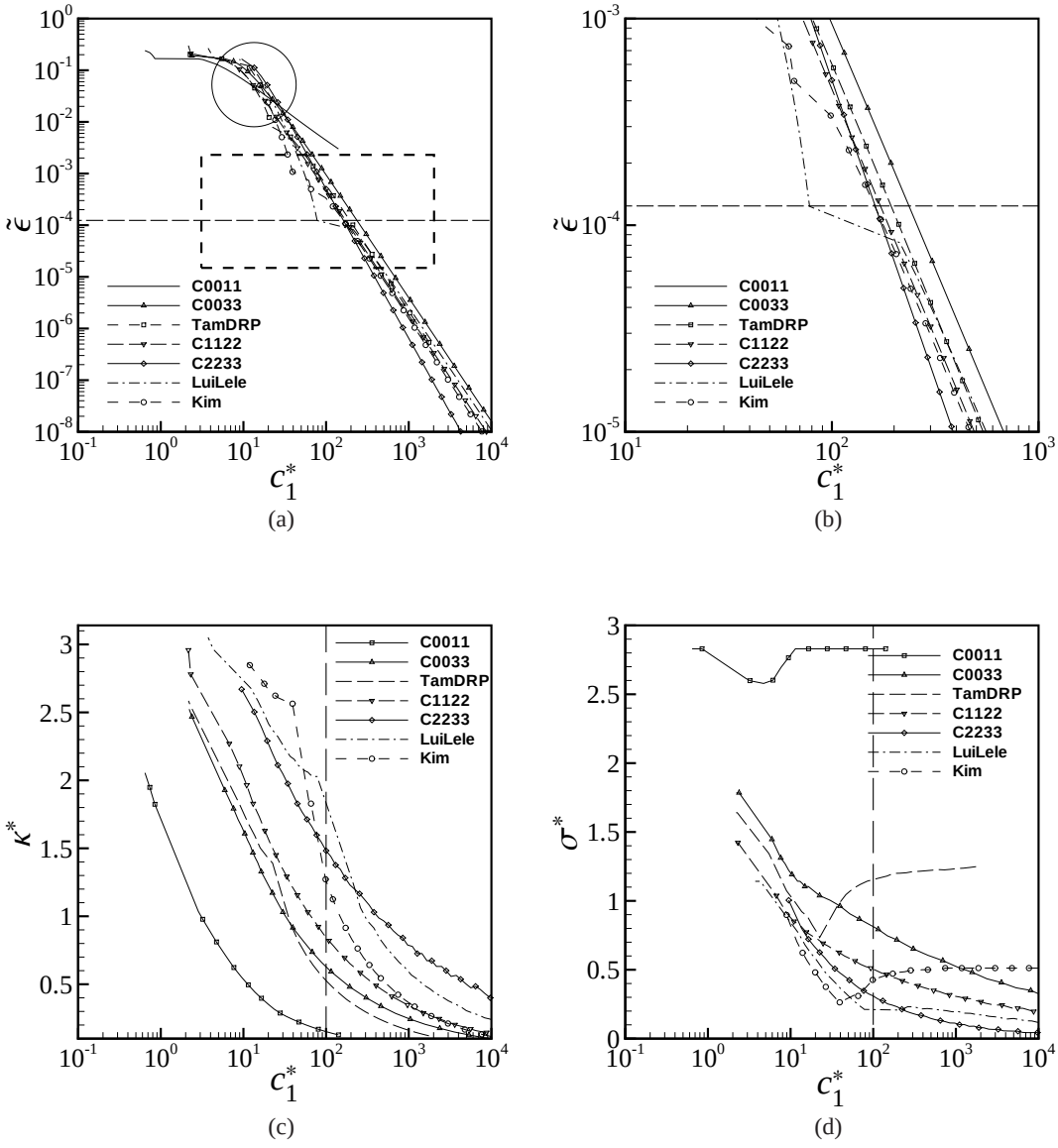

Figure 3.4: Optimal 'local' error (a, b), reduced wavenumber (c) and Courant number (d) as a function of cost for the centred spatial discretizations listed in Fig. 3.1 coupled with RK4 time integration in one space dimension.

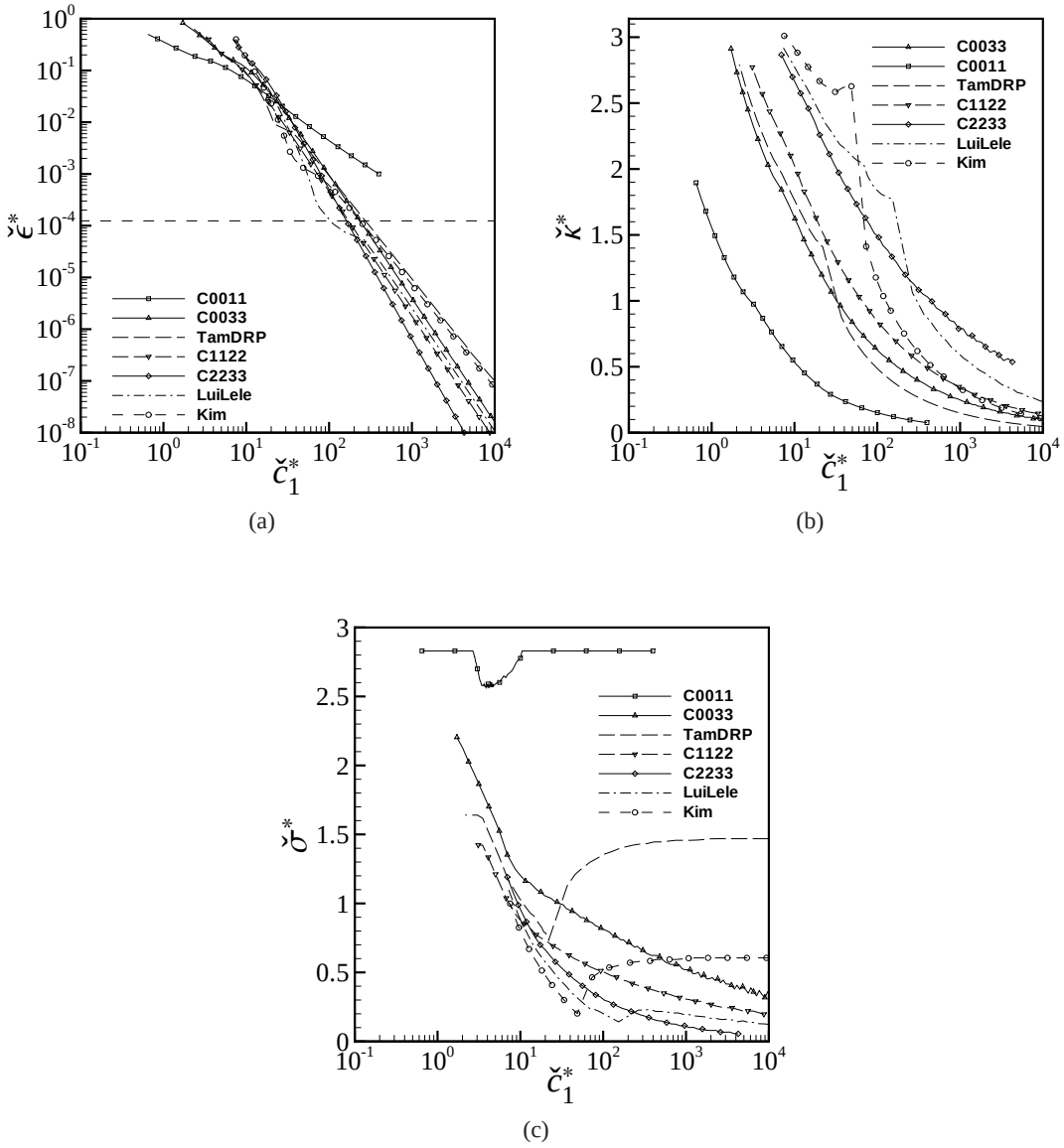

Figure 3.5: Optimal ‘global’ error (a), reduced wavenumber (b) and Courant number (c) as a function of cost for the centred spatial discretizations listed in Fig. 3.1 coupled with RK4 time integration in one space dimension.

In Fig. 3.4(b), the intercept of the $\tilde{\epsilon} = 1.24 \times 10^{-4}$ dashed horizontal line with the C2233 line determines a cost of $c_1^* = 162.46$, as compared with the intercept of the same line with the Lui&Lele line which determines a cost $c_1^* = 78.50$. The same trend is observed for the 'global' error reported in Fig. 3.5(a).

Figure 3.4(c) shows which wavenumber is best modelled by the schemes in Tabs. 3.1 and 3.2 when each scheme is operated at its most effective cost-error condition. The $c_1^* = 10^2$ long dashed vertical line can be taken as representative of a fixed amount of computational resources available to the CFD practitioner. The intercept of this line with the C0011 curve at $\kappa^* = 0.15$ indicates that this low-order scheme is best used for modelling wave propagating problems resolved with more than $N_\lambda = 40$ points per wavelength (see eq. (2.5)). The C0011, as a low-order scheme, is known to be able to resolve waves with 12-15 points per wavelength, but this operational point is not cost-optimal. For the same computational resources $c_1^* = 10^2$, the C1122 scheme resolves best the propagation of waves with $\kappa^* = 0.84$, corresponding to $N_\lambda = 7$, and it is therefore more appropriate for a coarser mesh representation when working at its cost-optimal point. A similar behaviour is displayed in Fig. 3.5(b) where the cost of the schemes is expressed by the 'global' error $\check{\epsilon}$ of eq. (2.53).

Figures 3.6(a) and 3.6(b) show the iso-contours of the normalized 'local' error function of eq. (2.44a) and the normalized one-dimensional cost function of eq. (2.44b) for the C1122 and TamDRP schemes in the non-dimensional wavenumber-frequency plane (κ, σ). The filled black circles mark the tangency condition between the two families of curves. This location represents the Courant number σ^* at which the numerical scheme should be time-marched for representing the propagation of a wavenumber κ at the lowest computational cost. Figure 3.6(a) shows that, over the wavenumber range $0.5 < \kappa < 0.8$ over which the C1122 scheme resolves waves of at least six points per wavelength, the computation can be time-marched at a Courant number approaching 0.5. For $\kappa < 0.5$, where the model resolves physical waves with greater spatial accuracy by increasing the number of points per wavelength, the computation must be time-marched at a lower Courant number. Figure 3.6(b) shows that, for the same wavenumber range $0.5 < \kappa < 0.8$, the optimal Courant number with the TamDRP scheme is close to 1. For $\kappa < 0.5$, the computation can be time-marched at a higher value of the Courant number, which reduces the overall computational time. Appendix A.5 shows that this trend is a common feature among the high-order schemes with optimized stencil coefficients (see Figs. A.6 and A.10).

Figure 3.6(a) shows that the Courant number increases monotonically with wavenumber when

the C1122 scheme is operating at its 'optimal' cost-error working point. With the TamDRP scheme that uses optimized spatial stencil coefficients, Figure 3.6(b) reveals that the 'optimal' Courant number for this scheme is not monotonic and it is decreasing with increasing wavenumber over the well-resolved portion of the wavenumber spectrum. This trend is summarized for the different spatial discretization schemes in Figures 3.4(d) and 3.5(c), respectively, for 'local' and 'global' errors. The optimal working points in the (κ, σ) plane for the schemes listed Tabs. 3.1 and 3.2 are plotted in Figure 3.4(d). The vertical long dashed line at the $c_1^* = 10^2$ defines the same availability of computational resources as in Fig. 3.4(c). To the right of this line, high-order schemes achieve the steep design roll-off error as in Fig. 3.4(b), and is therefore the operational space of interest for CAA applications. Using the C2233 scheme in an application where $c_1^* > 10^2$ requires a reduction in the Courant number with increasing computational cost. The reverse trend is shown by the spatial stencil-optimized schemes TamDRP and Kim. Fig. 3.5(c) displays the same analysis based on the global cost for which the same trends are shown as in Fig. 3.4(d).

Effect of number of space dimensions

Figures 3.7(a) and 3.8(a) show the relations between the computational cost and the operational condition of the schemes when applied to a two-dimensional problem for which $n_D = 2$. The global trend does not differ too much from the one-dimensional curves reported in Figs. 3.4(a) and 3.5(a) as already noted in Sec. 2.4. In fact, eq. (2.55) states that the only change in the contours of one and two-dimensional iso-cost is given by a $1/\kappa$ shift in the (κ, σ) plane. This behaviour can be observed in Fig. 3.9, where the 'optimal' working points for the 'local' error function of the C1122 scheme are compared between a one dimensional and a two dimensional computation. The 'optimal' working conditions for each of the two computations are represented respectively by non-filled and filled circles. Over the well resolved wavenumber range $\kappa < 0.8$ corresponding to wave resolved over more than $N_\lambda = 7$, the optimal Courant number at which a two dimensional computation is time-marched is slightly higher than the optimal Courant for time marching a one dimensional computation. The difference in the optimal Courant number increases monotonically with increasing κ. This indicates that increasing the number of dimensions gives a best operating point for the C1122 scheme involving a time-step that is slightly higher but substantially far from the stability limit which is indicated by the horizontal dashed line in Fig. 3.9. This result is encouraging for the application of cost-optimized schemes to three-dimensional real engineering applications.

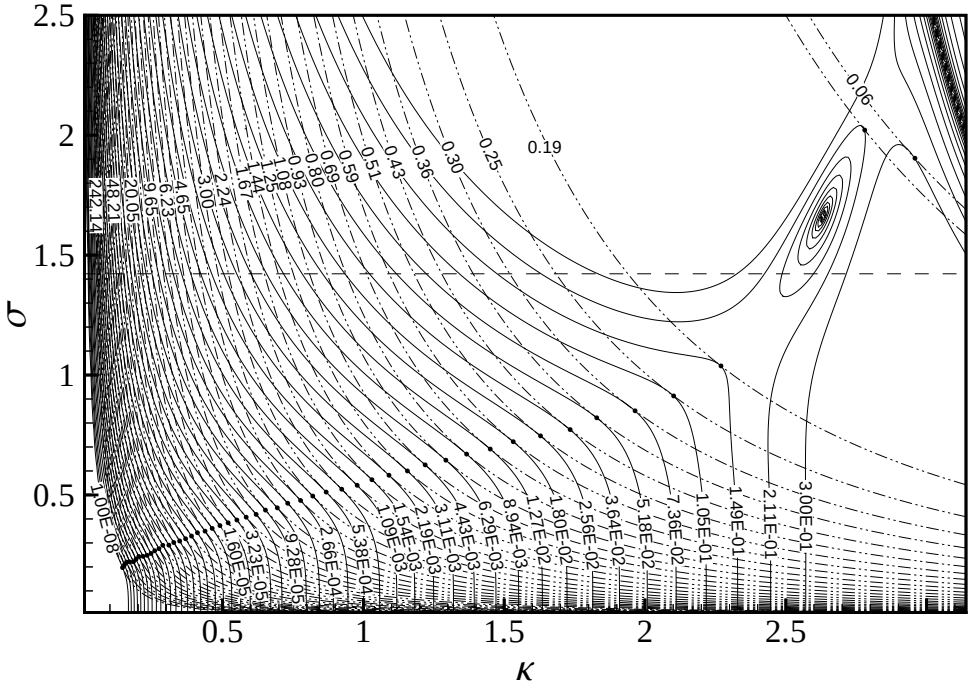

(a) C1122, constant ratio $e(\kappa,\sigma)$ contour spacing of 0.7037 between 10^{-8} and 0.3.

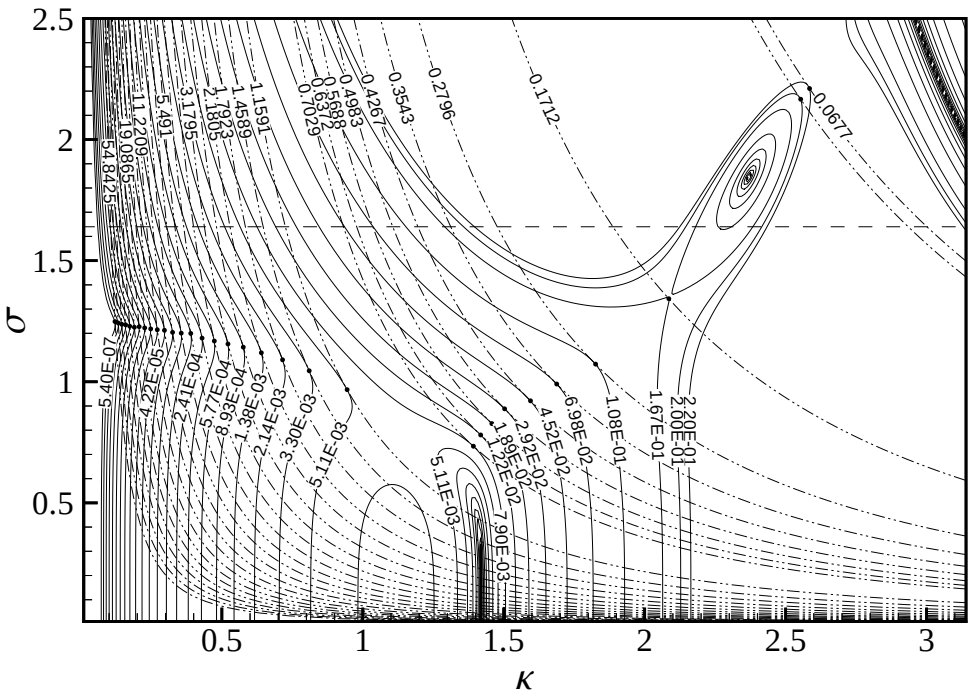

(b) TamDRP, constant ratio $e(\kappa,\sigma)$ contour spacing of 0.6466 between 5.4×10^{-7} and 0.22.

Figure 3.6: Contours of normalized 'local' error function $e(\kappa,\sigma)$ (solid black lines) and corresponding normalized one-dimensional cost function $c_1(\kappa,\sigma)$ (long dashed-dotted black lines) for the C1122 (a) and the TamDRP (b) scheme. The filled black circles represent the 'optimal' working condition; the black dashed line corresponds to the stability limit σ_{max}.

Figures 3.7(b,c) and 3.8(b,c) show the effect of changing the spatial discretization scheme on the reduced wavenumber and Courant number in two space dimensions. The schemes documented in Figures 3.7(b,c) and 3.8 (b,c) are those of Tabs. 3.1 and 3.2, coupled with RK4 time integration. Figures 3.7(b) and 3.8(b) indicate, for $c_2^* \leq 2 \times 10^2$, an higher operational wavenumber for the optimized Lui&Lele scheme with respect to the non-optimized C2233 scheme. Figures 3.7(c) and 3.8(c) show an increment in the optimal operational Courant number over these c_2^* region for the Lui&Lele scheme. As in the one-dimensional analysis of Fig. 3.4 and 3.5 the two-dimensional scheme performance analysis of Figures 3.7 and 3.8 indicates that the space-optimized Lui&Lele and Kim schemes are best run at higher Courant number with respect to their non-optimal counter-parts, in applications where the demands on resolution and therefore computational cost are significant, i.e. $c_2^* \geq 10^2$.

3.2.3 Optimization of the finite-difference scheme

On the basis of the discussion reported at the end of Sec. 2.5, optimized finite-difference schemes can be tailored to a specific target normalized error level $\tilde{\epsilon}$. This dictates the most cost-effective Courant and wavenumber that the model resolves, which corresponds to a specific spatial discretization for these schemes. The author has adopted as baseline spatial scheme the tridiagonal compact schemes with five point stencil $C1122$ of eq. (3.24) with

$$\begin{cases} a_2 = -a_{-2} = \dfrac{1}{12}(4\alpha_1 - 1) \\ a_1 = -a_{-1} = \dfrac{1}{3}(\alpha_1 + 2) \end{cases} \tag{3.29}$$

where α_1 is a free-parameter. The specific choice of $\alpha_1 = 1/3$ yields the C1122 sixth-order scheme. The author has attempted to find the C1122 scheme that maximizes the resolving efficiency $\breve{\kappa}^*$ as a function of the normalized error level $\tilde{\epsilon}$. This new class of schemes will be labelled as $C1122\mathsf{epsm}n$, where n represents the exponent in the target $\tilde{\epsilon} = 10^{-n}$ normalized error level. The optimal value of the coefficient α_1 is reported in tabular form for representative values of $\tilde{\epsilon}$ in Table 3.3 and plotted in Fig. 3.10, that reports also the data on the spatial resolving efficiency of the non-optimized C1122 scheme. Figure 3.10 shows that optimized space discretization schemes use higher values of the spatial coefficients α_1 and $\breve{\kappa}^*$ than the non-optimized ones. The wavenumber $\breve{\kappa}^*$ that is resolved most cost-effectively is also higher than the non-optimized one. Cost-optimized spatial discretizations tailored to a specific error level can outperform a C1122 sixth-order scheme, yielding $40 \div 50\%$ increase in the spatial

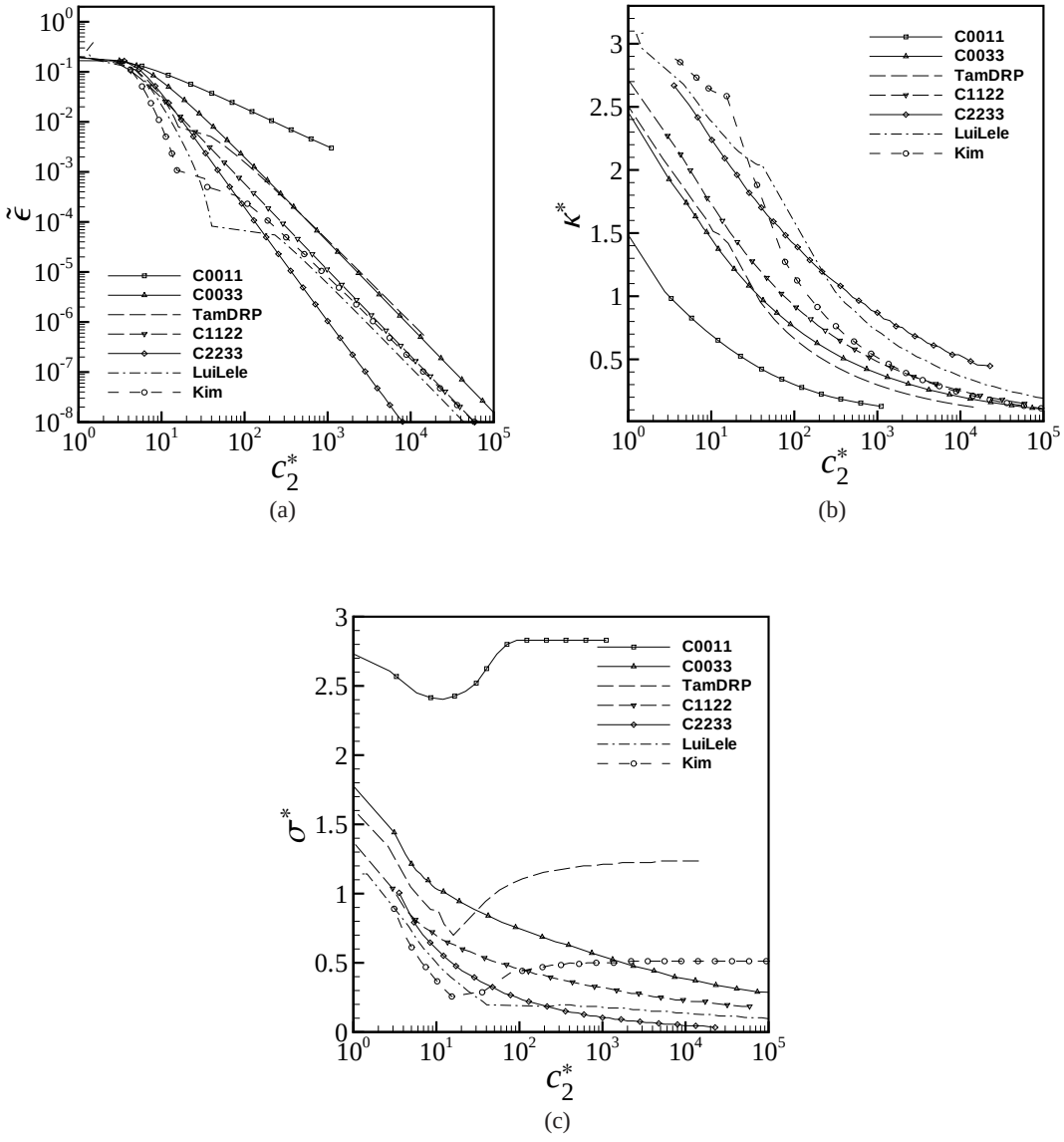

Figure 3.7: Optimal 'local' error (a), reduced wavenumber (b) and Courant number (c) as a function of cost for the centred spatial discretizations selected in Fig. 3.1 coupled with the RK4 time integration in two space dimensions.

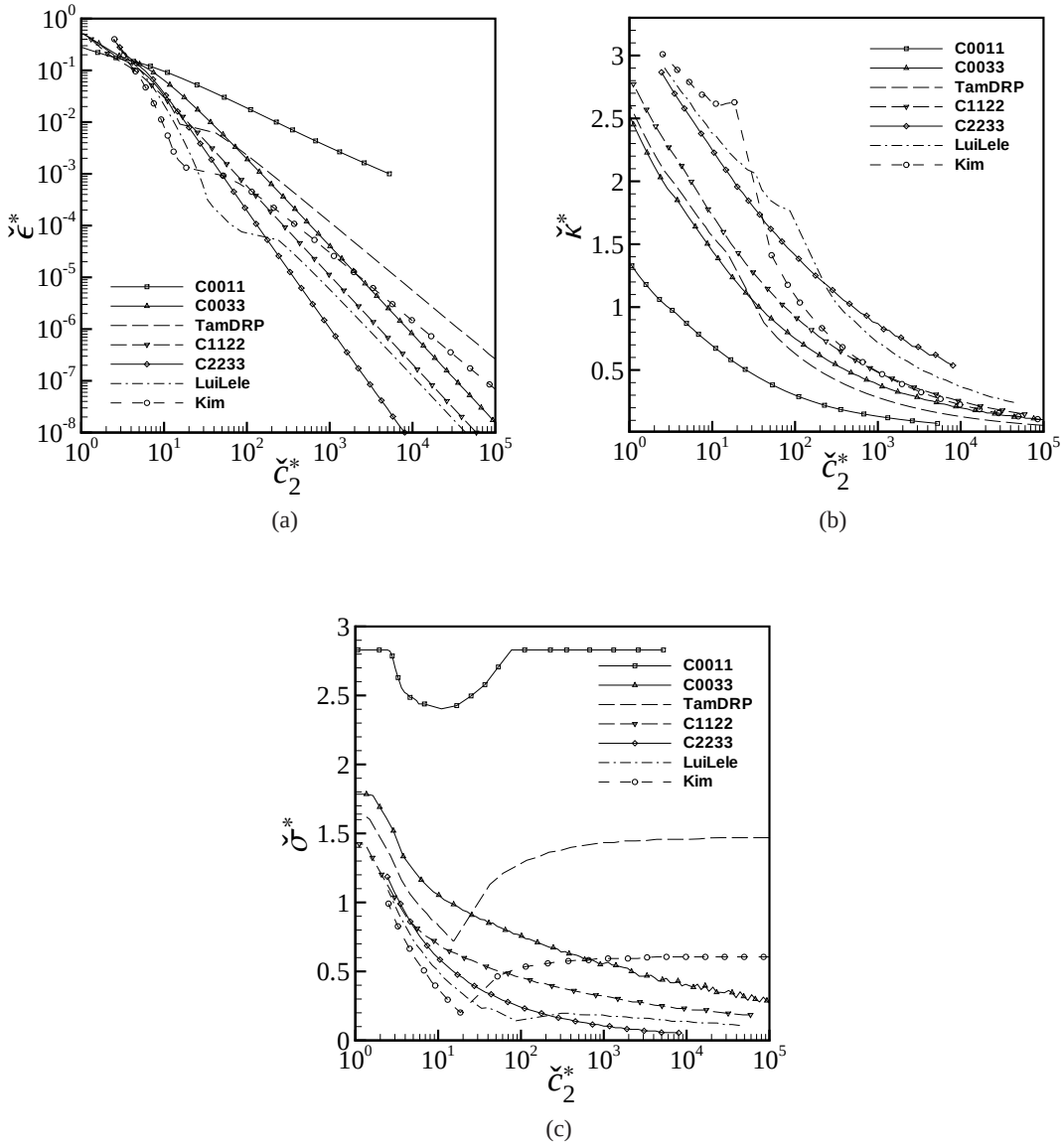

Figure 3.8: Optimal 'global' error (a), reduced wavenumber (b) and Courant number (c) as a function of cost for the centred spatial discretizations selected in Fig. 3.1 coupled with the RK4 time integration in two space dimensions.

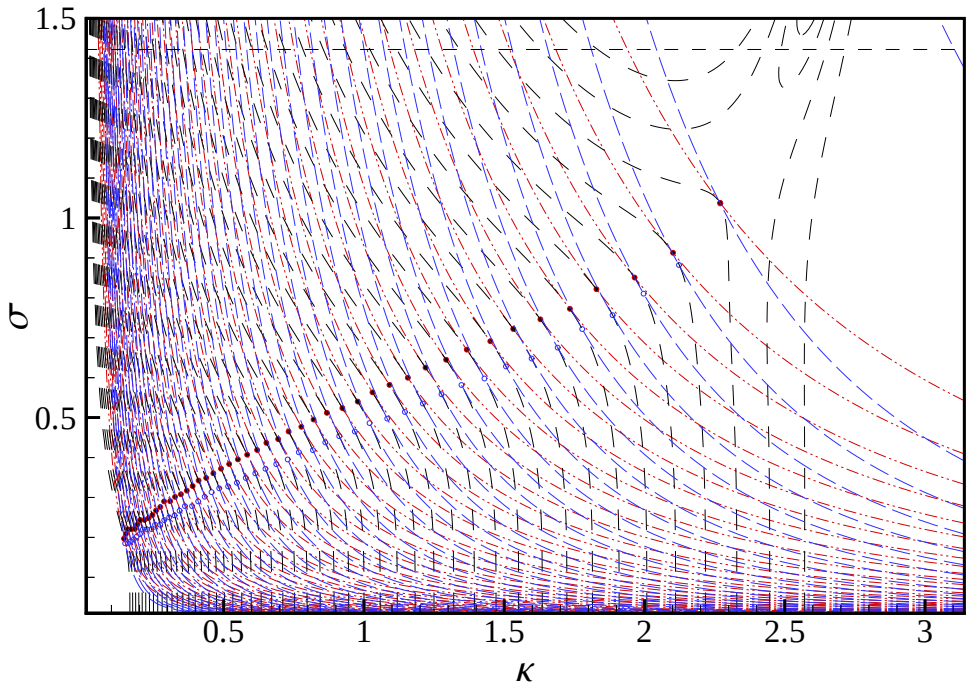

Figure 3.9: Contours of normalized 'local' error function $e(\kappa, \sigma)$ (dashed black lines) for C1122 scheme, normalized one-dimensional cost function $c_1(\kappa, \sigma)$ (long dashed blue lines), and normalized two-dimensional cost function $c_2(\kappa, \sigma)$ (dashed-dotted red lines). The corresponding non-filled and filled circles represent the 'optimal' working conditions respectively for the one and two dimensional cost function; the black dashed horizontal line corresponds to the stability limit σ_{max}.

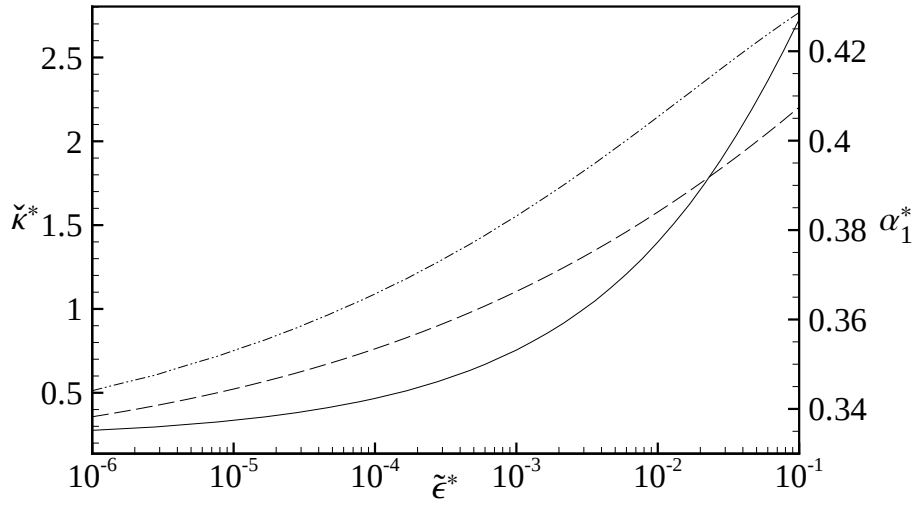

Figure 3.10: Optimal values of coefficients α_1 (solid line), non-optimal (dashed-line) and optimal (dash-dotted line) 'spatial resolving efficiency' $\check{\kappa}^*$ for the tridiagonal compact scheme $C1122$ of eq. (3.29).

Table 3.3: Spatial discretization coefficients of classical and optimized schemes.

scheme	$\alpha_1 \pm 10^{-6}$	$\check{\kappa}^*(\tilde{\epsilon})_{opt}$	$\check{\kappa}^*(\tilde{\epsilon})_{nonopt}$	$\overline{\kappa}_{max}$	$\overline{\kappa}_c(\epsilon)$ (Lele, 1992)	$e_1(\epsilon)$
$C1122$	0.33333			1.99	1.1043	0.3515
$C1122$epsm5	0.33750	0.7461	0.5223	2.01	1.1813	0.3760
$C1122$epsm4	0.34240	1.0901	0.7621	2.03	1.2878	0.4099
$C1122$epsm3	0.3532	1.5554	1.1042	2.08	1.5556	0.4952

resolving efficiency. Figure 3.11 compares the dispersive and dissipative properties of the $C1122$epsm5, $C12$epsm4, and $C12$epsm3 with the ones of $C1122$ scheme. Table 3.3 reports $\overline{\kappa}_{max}$ and $\overline{\kappa}_c$, which are respectively, the maximum value and the maximum resolvable scaled pseudo-wavenumber. The maximum resolvable wavenumber $\overline{\kappa}_c$ is calculated using the criterion of Lele (1992):

$$e_0(\kappa) \leq \epsilon, \tag{3.30}$$

$$e_1(\epsilon) = \overline{\kappa}_c/\pi, \tag{3.31}$$

where $e_1(\epsilon)$ is the resolving efficiency of the scheme, and the threshold has been set to $\epsilon = 10^{-3}$. Figure 3.11(a) and Tab. 3.3 show that the maximum value of $\overline{\kappa}(\kappa)/\pi$ does not vary sig-

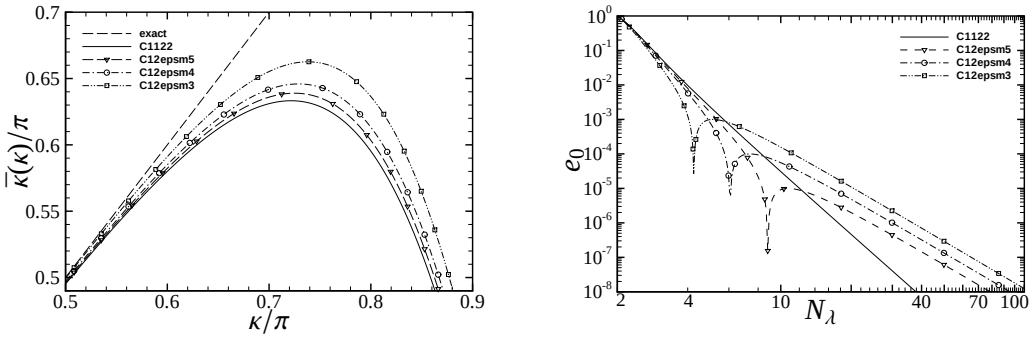

(a) (b)

Figure 3.11: Dispersive (a) and dissipative (b) errors for the $C1122$ and cost-optimized $C12\text{epsm}5$, $C12\text{epsm}4$, $C12\text{epsm}3$ schemes.

nificantly in the cost-optimized schemes, showing that the error-based spatial discretization does not give significant advantages in the dispersion properties. However, the dissipative error in Fig. 3.11(b) can be reduced by almost two orders of magnitude for selected wavenumbers. This provides an optimization methodology that is most applicable to linear wave propagation problems where the wave amplitude or the SPL are the critical parameters.

3.2.4 Prefactorization

To obtain the finite difference approximation $f_i^{'}$ from equation (3.24), a tridiagonal linear system of the form $Ax = b$ has to be solved. An alternative approach to the inversion of the A matrix has been proposed by Hixon (2000), consisting in a prefactorization that splits the derivative operator $f_i^{'}$ in a backward component $f_i'^B$ and a forward component $f_i'^F$, so that

$$f_i' = \frac{1}{2}\left(f_i'^F + f_i'^B\right). \tag{3.32}$$

This way, the inversion of the matrix is replaced by two independent matrix operations that involve bi-diagonal matrices, as follows

$$\alpha_F f_{i+1}'^F + \beta_F f_i'^F = \frac{1}{h}\left[b_F f_{i+1} + c_F f_i + d_F f_{i-1}\right] \tag{3.33}$$

$$\beta_B f_i'^B + \gamma_B f_{i-1}'^B = \frac{1}{h}\left[b_B f_{i+1} + c_B f_i + d_B f_{i-1}\right], \tag{3.34}$$

where the coefficients must be chosen such that when the two biased stencils are added, the original central compact scheme of eq. (3.24) is recovered. Hixon & Turkel (2000) reported that to obtain the C1122 scheme with sixth-order accuracy, that is $\alpha_1 = 1/3$ in eq. (3.25), the following relation among the coefficients hold:

$$\alpha_F = \gamma_B = \frac{1}{2} - \frac{1}{2\sqrt{5}}, \quad \beta_F = \beta_B = 1 - \alpha_F, \quad b_F = -d_B = 1 - \frac{1}{30\alpha_F}, \quad c_B = -c_F = 2b_F - 1, \quad b_B = -d_F = 1 - b_F. \tag{3.35}$$

This class of prefactored schemes has been optimized by Ashcroft & Zhang (2003) to enhance the wavenumber resolution characteristics, and recently by Rona *et al.* (2009) to minimize the computational cost for a given level of error.

To derive the cost-optimized prefactored compact schemes, the author follows from previous work of Hixon (2000) and Ashcroft & Zhang (2003). Compact schemes have the form of a MacCormack scheme. In a MacCormack scheme, the real (dispersive) components of the scaled pseudo-wavenumbers of the forward and backward stencils are equal and identical to the scaled pseudo-wavenumber of the original central scheme, whilst the imaginary (dissipative) components of the scaled pseudo-wavenumbers are equal and opposite. Let the original central scheme be in the form of eq. (3.24), and multiply eq. (3.24) by the constant factor $\frac{1}{1+2\alpha}$ (as in eq. (A.81) of Appendix A.3). From eqs.(3.25) and (3.27), the modified wavenumber of the generic compact C1122 scheme is given by:

$$\bar{\kappa}(\kappa) = \frac{\frac{2(\alpha_1+2)}{3(1+2\alpha_1)}\sin(\kappa) + \frac{(4\alpha_1-1)}{6(1+2\alpha_1)}\sin(2\kappa)}{\frac{1}{(1+2\alpha_1)} + \frac{2\alpha_1}{(1+2\alpha_1)}\cos(\kappa)}. \tag{3.36}$$

The scaled pseudo-wavenumber of the generic forward and backward operators may be determined in a similar manner from eqs. (3.33) and (3.34), using the Fourier analysis. The real and imaginary components of the scaled pseudo-wavenumber for the generic forward stencil are, respectively, given by:

$$Re\left(\bar{\kappa}^F(\kappa)\right) = \frac{(b_F\beta_F - c_F\alpha_F - d_F\beta_F)\sin(\kappa) - d_F\alpha_F\sin(2\kappa)}{\alpha_F^2 + \beta_F^2 + 2\alpha_F\beta_F\cos(\kappa)} \tag{3.37a}$$

$$Im\left(\bar{\kappa}^F(\kappa)\right) = \frac{-(b_F\alpha_F + c_F\beta_F) - (b_F\beta_F + c_F\alpha_F + d_F\beta_F)\cos(\kappa) - d_F\alpha_F\cos(2\kappa)}{\alpha_F^2 + \beta_F^2 + 2\alpha_F\beta_F\cos(\kappa)}, \tag{3.37b}$$

and for the backward stencil:

$$Re\left(\bar{\kappa}^B(\kappa)\right) = \frac{(b_B\beta_B + c_B\gamma_B - d_B\beta_B)\sin(\kappa) + b_B\gamma_B\sin(2\kappa)}{\beta_B^2 + \gamma_B^2 + 2\gamma_B\beta_B\cos(\kappa)} \tag{3.38a}$$

$$Im\left(\bar{\kappa}^B(\kappa)\right) = \frac{-(c_B\beta_B + d_B\gamma_B) - (b_B\beta_B + c_B\gamma_B + d_B\beta_B)\cos(\kappa) - b_B\gamma_B\cos(2\kappa)}{\beta_B^2 + \gamma_B^2 + 2\gamma_B\beta_B\cos(\kappa)}. \tag{3.38b}$$

In equations (3.37) and (3.38), by imposing the following restrictions on the coefficients of the backward stencil, it is ensured that the imaginary components of forward and backward operators are equal and opposite, and that the real components of the forward and backward operators are equal:

$$\beta_B = \beta_F,\ \gamma_B = \alpha_F,\ b_B = -d_F,\ c_B = -c_F,\ d_B = -b_F. \tag{3.39}$$

To ensure that in the regions of zero gradient the derivatives vanish, the following additional relation is introduced

$$b_F + c_F + d_F = 0. \tag{3.40}$$

Finally, by matching the various terms of eq. (3.37a) with the corresponding ones of eq. (3.36), the following system of equations is obtained

$$\begin{cases} b_F\beta_F - c_F\alpha_F - d_F\beta_F = \dfrac{2(\alpha_1+2)}{3(1+2\alpha_1)} \\ -d_F\alpha_F = \dfrac{4\alpha_1 - 1}{6(1+2\alpha_1)} \\ \alpha_F^2 + \beta_F^2 = \dfrac{1}{(1+2\alpha_1)} \\ 2\alpha_F\beta_F = \dfrac{2\alpha_1}{(1+2\alpha_1)} \\ b_F + c_F + d_F = 0 \end{cases} \tag{3.41}$$

Due to the quadratic term in the third element of eq. (3.41), the system of equations has two solutions. The lower value solution for α_F, as shown in of Appendix A.3, is selected to minimize the ratio $\frac{\alpha_F}{\beta_F}$, so that the influence of errors at the boundaries on the interior scheme is minimized. The new prefactored optimized coefficients are given in Tab. 3.4 and reported in eq. (A.83) of Appendix A.3.

Figure 3.12 reports the dispersive characteristics of the prefactored classical $C1122$ and cost-optimized $C12\text{epsm}5$, $C12\text{epsm}4$, and $C12\text{epsm}3$ schemes. Figure 3.12(a) shows the real

Table 3.4: Prefactored spatial discretization coefficients of the classical and optimized schemes.

	$C1122$	$C12epsm5$	$C12epsm4$	$C12epsm3$
α_F	0.276393202250021	0.279757059259305	0.283735092978311	0.292621799121854
β_F	0.723606797749979	0.720242940740695	0.716264907021689	0.707378200878146
b_F	0.87939886704167	0.875512058643197	0.871137465089563	0.862185198591157
c_F	-0.758797734083341	-0.751024117286394	-0.742274930179126	-0.724370397182313
d_F	-0.12060113295833	-0.124487941356803	-0.128862534910437	-0.137814801408843

component of the prefactored forward stencil from eq. (3.37a), which is equal to the real component of the prefactored backward stencil from eq. (3.38a), and to the scaled pseudo-wavenumber of the original central compact scheme reported in Fig.3.11(a). The scaled pseudo-wavenumber for the prefactored cost-optimized $C1122$ schemes is consistently above that of the classical $C1122$ scheme for all three level of cost-optimization. Fig. 3.12(b) shows the imaginary component of the prefactored forward and backward stencils, respectively from eq.(3.37b) and (3.38b). An enlarged view of the imaginary component of the forward stencil is shown in Fig. 3.12(c) and the imaginary component of the backward stencil is shown in Fig. 3.12(d). These two components are equal in magnitude and opposite in sign. Averaging together the real part of the backward and forward components gives the pseudo-wavenumber of the centred $C1122$ scheme. Averaging the imaginary forward and backward components results in an imaginary pseudo-wavenumber contribution of zero.

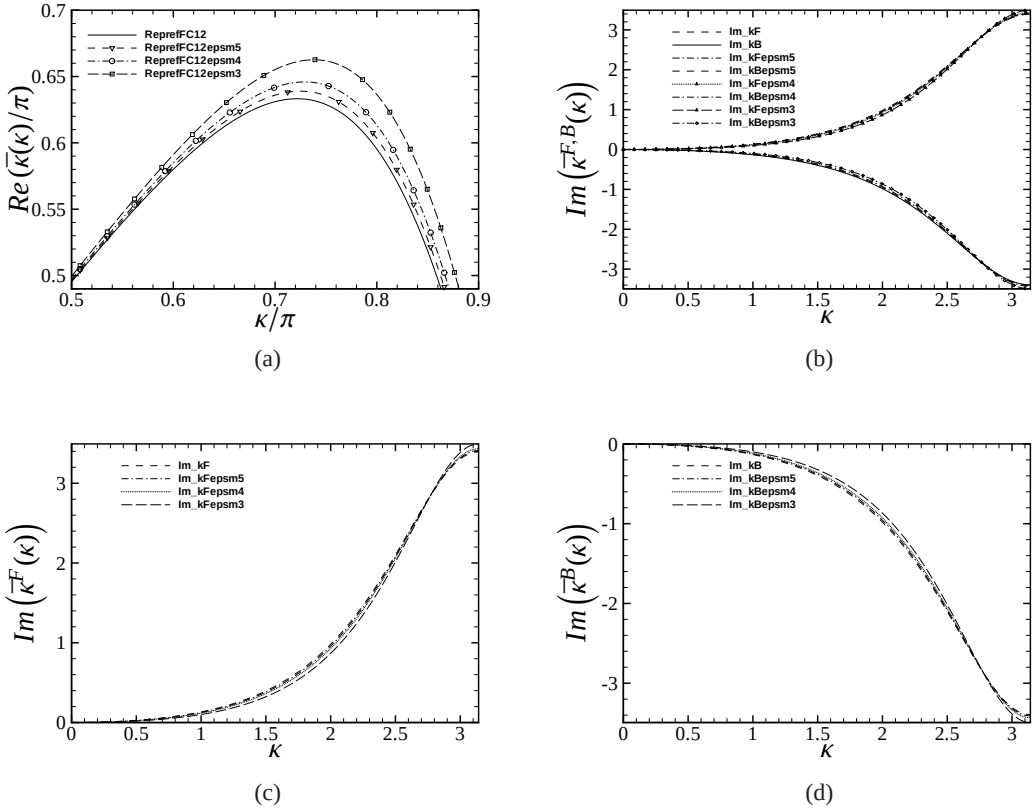

Figure 3.12: Dispersive characteristics of the prefactored classical $C1122$ and cost-optimized $C12\text{epsm}5$, $C12\text{epsm}4$, $C12\text{epsm}3$ schemes. (a) Real component of the prefactored forward stencil from eq. (3.37a). (b) Imaginary components of the prefactored forward and backward stencil, respectively from eq.(3.37b) and (3.38b). (c) Positive imaginary portion from (b). (d) Negative imaginary portion from (b).

3.3 Temporal Integration

The overall cost of the simulation is a function of the spatial discretization scheme, the number of spatial dimensions, and the time integration scheme as reported in Sec. 3.2.2. This section analyses the impact on the computational cost of using different time integration schemes for a two dimensional problem for various spatial discretization schemes. The analysis of Hu *et al.* (1996), Bogey & Bailly (2004), Berland *et al.* (2006), Bernardini & Pirozzoli (2009), and Ghillani (2012) points towards the RK3 and RK4 schemes as a good starting choice for the present work. This section identifies the appropriate number of RK steps and RK coefficients for a prescribed targeted level of error.

3.3.1 Effect of time integration

The effect of the time integration on the computational cost is considered for two-dimensional time-dependent simulations ($n_D = 2$), time-advanced by a third-stage third-order ($t = RK3$) and a fourth-stage fourth-order ($t = RK4$) RK time integration scheme in the manifold of eq. (3.28). The results of the analysis for $RK4$ has been shown in Figs. 3.7 and 3.8. Figures 3.13 and 3.15 report, respectively, the 'local' and the 'global' efficiency analysis for the same spatial discretization scheme as in Figs. 3.7 and 3.8, with a third-stage third-order ($t = RK3$).
Figures 3.13(a) and 3.15(a) show the effect of changing the spatial discretization on the cost-error functions. As already reported by Pirozzoli (2007) and Hu *et al.* (1996), increasing the accuracy more than outweighs the increased computational cost, and all the spatial discretization schemes coupled with RK4 time integration are found to outperform the RK3 ones. This is confirmed in Figs. 3.13(b) and 3.15(b), which report a selection of spatial discretization schemes coupled with RK3 and RK4 time integration. Figure 3.13(b) shows the 'local' and Fig. 3.15(b) the 'global' error as a function of the computational cost for the different schemes. In Fig. 3.13(b) each blue line identifying a spatial discretization scheme coupled with $t = RK4$ is below the corresponding black line identifying the same spatial discretization scheme coupled with $t = RK3$. In Fig. 3.15(b) a similar trend is shown except for the 'global' optimal cost-error of the Lui&Lele scheme for a low level of computational cost, over the range $3 \leq \check{c}_2^* \leq 70$. Figure 3.14 shows the contours of the 'normalized' local error function $e(\kappa, \sigma)$ for the $C1122$ spatial discretization scheme coupled with the RK3 and RK4 time integration schemes for a two-dimensional problem. This figure confirms that RK4 has a better 'optimal' performance compared to the RK3 time integration scheme over the whole wavenumber range. For $\kappa < 0.8$,

in the region of the *well-resolved* wavenumber spectrum, the RK4 time integration gives an increment in the optimal Courant number between 100% and 400%, as shown by the blue circles being above the black circles. For $\sigma \rightarrow 0$, where the assumption of zero time integration is valid from eq. (2.57), the $t = RK3$ and $t = RK4$ contours overlap.
Figures 3.13(c), 3.15(c) and 3.13(d), 3.15(d) show the effect of changing the spatial discretization scheme on the 'optimal' reduced wavenumber and Courant number in a two dimensional CAA computation, that uses $t = RK3$. This figures display the same trends as Figs. 3.7(b), 3.8(b) and 3.7(c), 3.8(c) for $t = RK4$ as discussed in Sec. 3.2.2. The wiggles present on the right-hand side of Figs. 3.13(c) and 3.15(c) for $C2233$ scheme are due to the limitation in the $\kappa - \sigma$ space resolution of this analysis. An increased resolution in the $\kappa - \sigma$ plane is likely to reduce these discretization effects. The optimal 'local' and 'global' Courant number for the $C0011/RK3$ scheme in 2D reported in Figs. 3.13(d) and 3.15(d) is drawn by an horizontal line because the 'optimal' condition for the 'local' and 'global' $C0011/RK3$ in 2D are beyond the stability limit σ_{max} as shown by the black dash-dotted line in Figs. A.18(a) and A.18(b).

3.3.2 Baseline temporal solver

On the basis on the discussion reported at the end of the previous section, the four-stage, fourth-order ($t = RK4$) RK scheme has been adopted as baseline temporal solver. The stability footprints, the dissipation rate $|r|$ and the phase error δ from eqs. (2.31) and (2.33) for the classical RK3 and RK4 time integration schemes are reported in Fig. A.21 of Appendix A.6. These results, well-documented in the literature (Butcher, 1987; Hirsch, 2007), are used as benchmark for the cost-optimized temporal solver analysis of Sec. 3.3.3.
The maps corresponding to RK5 and RK6 are not reported, since these schemes are unconditionally unstable, as stated by Bernardini & Pirozzoli (2009).

3.3.3 Cost-optimized temporal solver

A numerical optimization procedure has been performed to determine the coefficients γ_m which maximize the temporal resolving efficiency $\check{z}^*(\tilde{\epsilon})$ for a given value of the normalized error $\tilde{\epsilon}$:

$$\check{z}^*_{opt}(\tilde{\epsilon}) = \max\{\check{z} : \check{e}_t(\check{z}, \gamma_m) \leq \tilde{\epsilon}\} \tag{3.42}$$

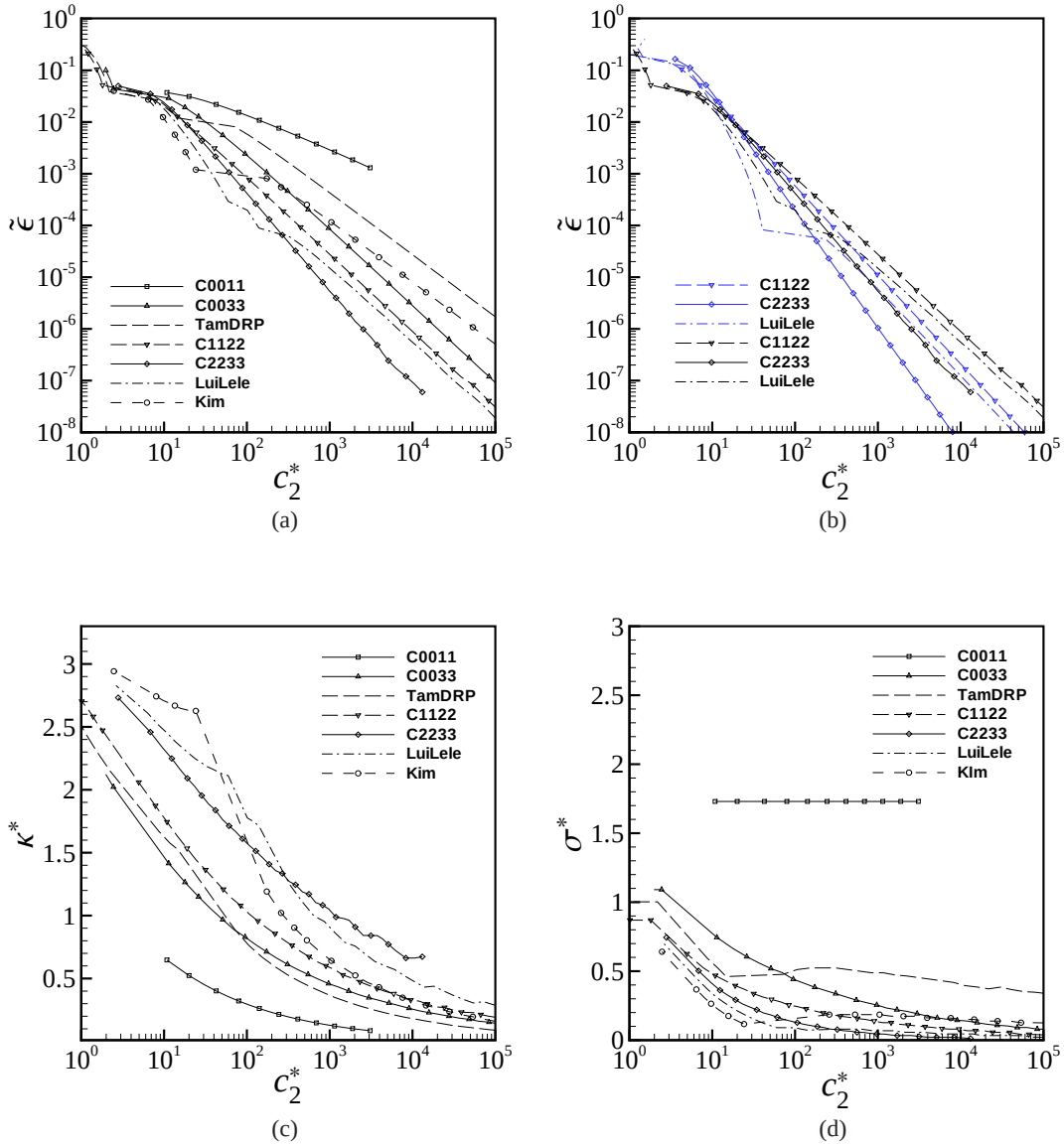

Figure 3.13: Optimal 'local' error (a, b), reduced wavenumber (c) and Courant number (d) as a function of cost for the centred spatial discretizations selected in Fig. 3.1 coupled with the RK3 time integration in two space dimensions. In subfigure (b), black and blue lines represent, respectively, spatial discretizations scheme coupled with RK3 and RK4.

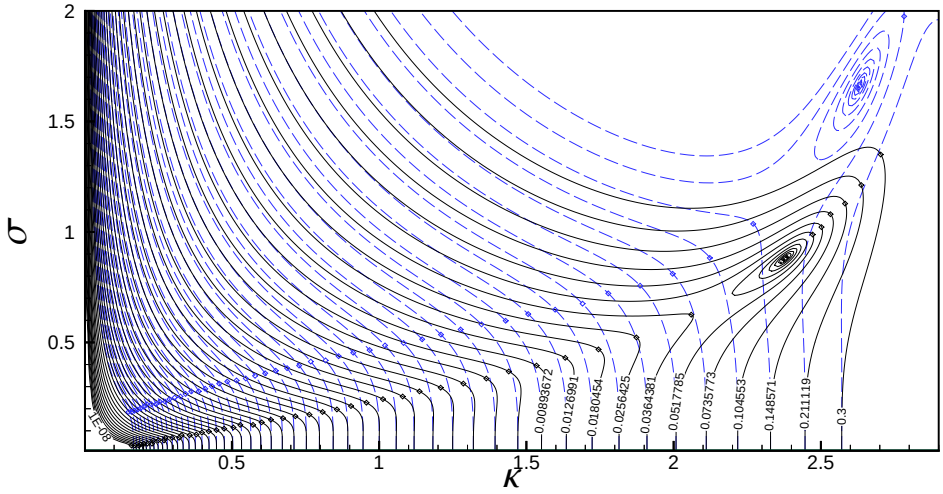

Figure 3.14: Contours of normalized 'local' error function $e(\kappa, \sigma)$ for C1122 scheme coupled with RK3 (black solid line) and RK4 (long dashed blue line) time integration scheme. Constant ratio $e(\kappa, \sigma)$ contour spacing of 0.7037 between 10^{-8} and 0.3. The corresponding symbols represent the 'optimal' working conditions for two dimensional cost function.

under the following stability constraint

$$\zeta \check{z}^*_{opt}(\tilde{\epsilon}) \leq z_s \tag{3.43}$$

where z_s is the stability limit defined in eq. (2.31). The factor ζ has been introduced to guarantee an extra stability margin beyond the range of well resolved angular frequencies z. The author has considered as representative example a four-stage, second-order RK scheme, i.e. set $\gamma_1 = 1$, $\gamma_2 = 1/2$, and left two free parameters γ_3, γ_4. A standard ordered search has been conducted in a sufficiently large neighbourhood of the baseline values $1/m!$ for γ_3 and γ_4, for different levels of target error $\tilde{\epsilon}$. For the selected second-order, four-stage *RK* time integration scheme, $\zeta = 1.1$ provides a good balance between performance and stability. The results of the analysis are plotted in Fig. 3.16 and reported in tabular form in Table 3.5, which lists the coefficients for the classical and optimized RK schemes and the corresponding performances. Figure 3.16 shows that the cost-optimized time integration schemes have smaller values of the coefficients γ_3 and γ_4 than the classical non-optimized RK scheme, for which $\gamma_3 = 1/3!$ and $\gamma_4 = 1/4!$, depicted with black arrows. The cost-optimized coefficients tend asymptotically to the value of the classical non-optimized schemes as the level of normalized error $\tilde{\epsilon}$ decreases. Using the cost-optimized coefficients increases the temporal resolving efficiency $\check{z}^*(\tilde{\epsilon})$ from

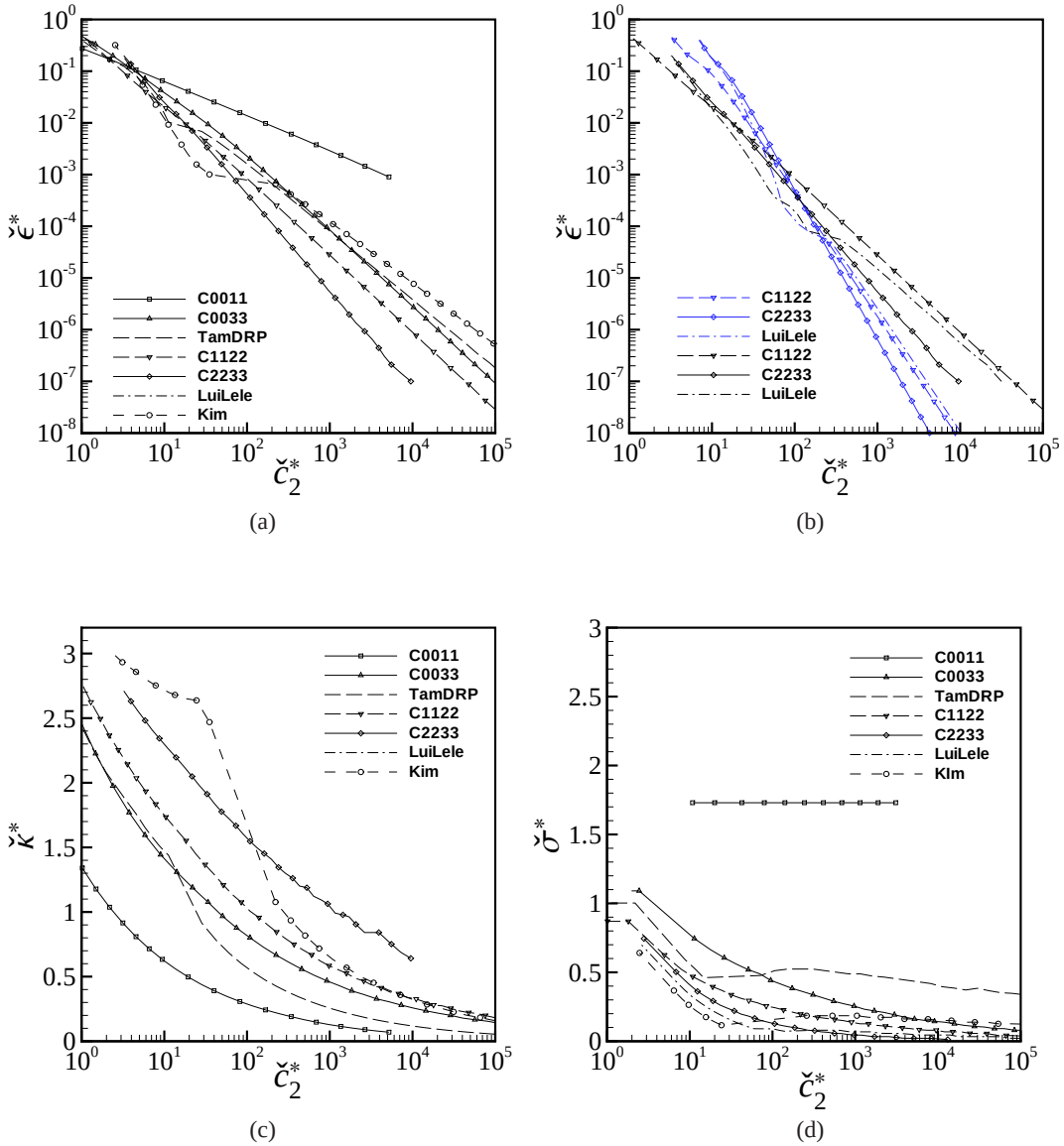

Figure 3.15: Optimal 'global' error (a), reduced wavenumber (b) and Courant number (c) as a function of cost for the centred spatial discretizations selected in Fig. 3.1 coupled with the RK3 time integration in two space dimensions. In subfigure (b), black and blue lines represent, respectively, spatial discretizations scheme coupled with RK3 and RK4.

13% up to 46% over the range $10^{-6} \leq \tilde{\epsilon} \leq 10^{-1}$, indicating a gain in temporal resolving efficiency from the cost-optimized temporal optimization.

Figure 3.17 indicates that the stability foot-prints of the cost-optimized schemes does not differ too much from the classical RK4 scheme, as the optimized schemes has a slightly larger footprint than the classical one. Figures 3.18 and 3.19 show the temporal dissipation and dispersion properties of the cost-optimized RK schemes compared with the classical RK scheme. The amplification rates $|r|$ and the differences in phase δ are plotted, respectively, in Fig. 3.18(a) and 3.18(b); the temporal dissipation E_d of eq. (2.34) and the phase error E_δ of eq. (2.35) are represented in logarithmic scale, respectively in Fig. 3.19(a) and 3.19(b) for the classical and optimized schemes. The cost-optimized algorithms are slightly less dissipative and less dispersive than the standard RK4 because their amplification rates $|r|$ are close to 1 and their differences in phase δ are close to 0 over the range of angular frequencies $0.5 \leq z \leq 1.78$, as highlighted in Fig. 3.19(a) and 3.19(b). The stability of the optimized algorithms, dictated by z_s and reported in Table 3.5, appears marginally lower than that of the classical RK4 algorithm. Figure 3.19(a) shows that the trend of the optimized schemes follows the trend of the classical one, whereas Fig. 3.19(b) indicates that the cost-optimized schemes has different local minima at specific values of angular frequencies z, instead of the classical RK4 scheme which has a single minimum at at $z = 1.87$.

Table 3.5 lists the accuracy limits for the dissipation z_d and the phase error z_δ using the criteria, respectively, $E_d \leq 10^{-3}$ and $E_\delta \leq 10^{-3}$, similarly to Berland *et al.* (2006). The cost-optimized schemes have a slightly higher value of z for which $E_d = 10^{-3}$ and $E_\delta = 10^{-3}$ than the classical RK4 scheme. This confirms that the cost-optimization gives a small advantage in terms of temporal dissipation and dispersion properties of the resulting schemes. A further comparison of the temporal cost-optimized schemes with the optimized RK schemes available in literature is given in Bernardini & Pirozzoli (2009).

Table 3.5: Runge-Kutta coefficients and performance for the classical and optimized time integration schemes; $\check{z}^*(\tilde{\epsilon})_{nonopt}$ is relative to the classical RK4 time integration scheme. For all schemes $\gamma_1 = 1$, $\gamma_2 = 1/2$.

scheme	γ_3^*	γ_4^*	z_s	$\check{z}^*(\tilde{\epsilon})_{opt}$	$\check{z}^*(\tilde{\epsilon})_{nonopt}$	$z_d : E_d = 10^{-3}$	$z_\delta : E_\delta = 10^{-3}$
$RK3$	$1/3!$		1.73				
$RK4$	$1/3!$	$1/4!$	2.83			0.7323	0.873
epsm5	0.166106296875	0.041111875	2.828	0.272	0.186	0.7414	0.911
epsm4	0.1652420703125	0.0402486328125	2.826	0.436	0.331	0.7476	0.973
epsm3	0.1636332734375	0.038639453125	2.819	0.709	0.589	0.7526	1.187

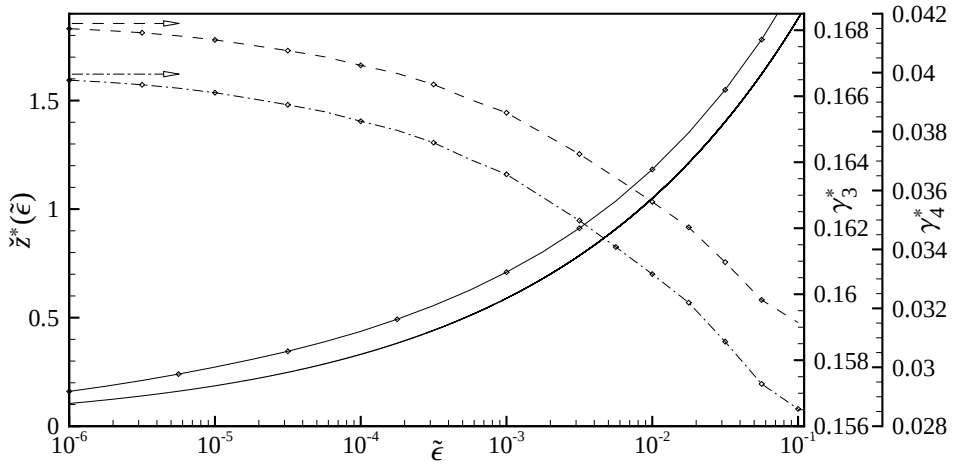

Figure 3.16: Optimal values of temporal resolving efficiencies $\check{z}^*(\tilde{\epsilon})$ (black solid line with diamond symbols), γ_3 (black dash-dotted line with diamond symbols) and γ_4 (black dashed lines with diamond symbols) for second order, four stage optimized RK time integration scheme. The black lines and arrows without symbols indicate the corresponding coefficients for the classical RK4 scheme.

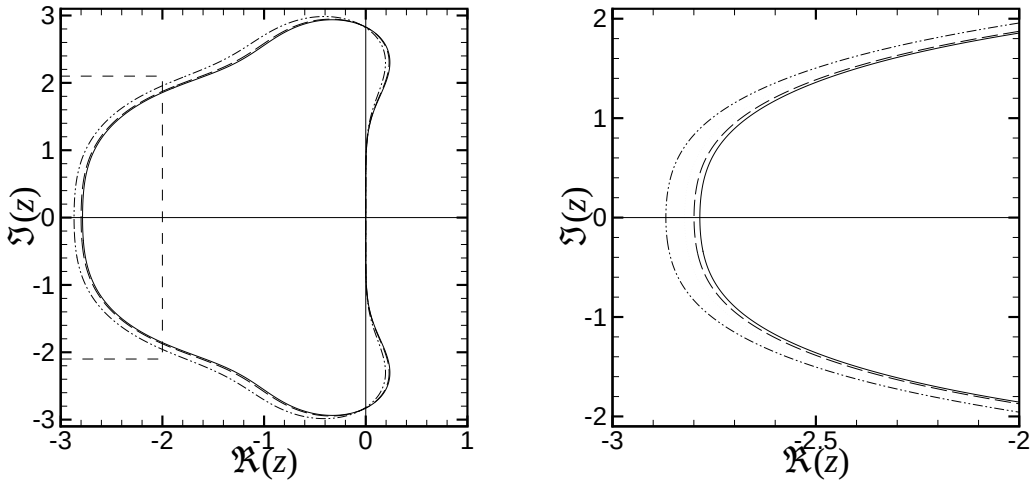

Figure 3.17: (a) Stability foot-prints for the classical (black solid line) and cost-optimized RK4 (epsm5 black long-dashed line, epsm4 black dotted line, epsm3 black dash-dotted line) time integration schemes. (b) Zoom of the rectangular area reported in (a).

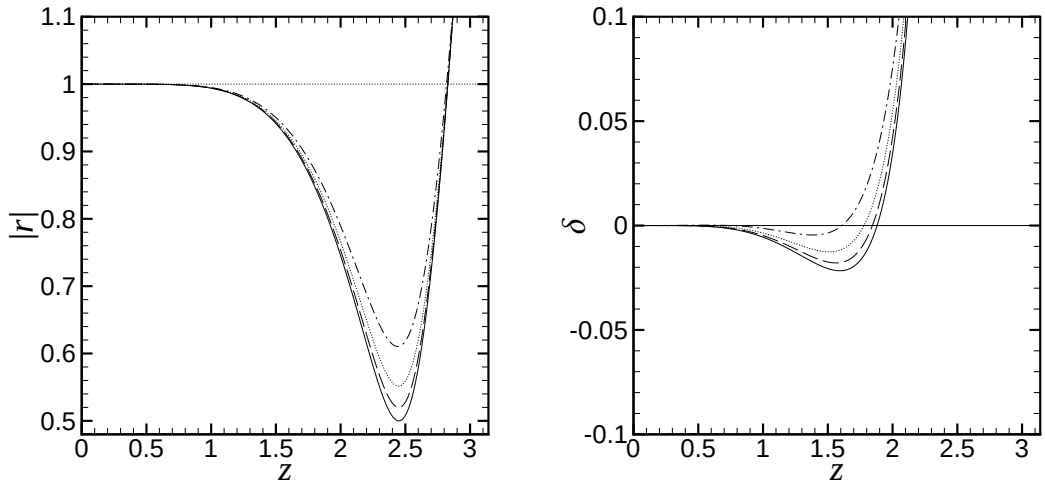

(a) (b)

Figure 3.18: (a) Amplification rate $|r|$ and (b) difference in phase δ for the classical and cost-optimized RK4 time integration schemes. Lines pattern as in Fig. 3.17.

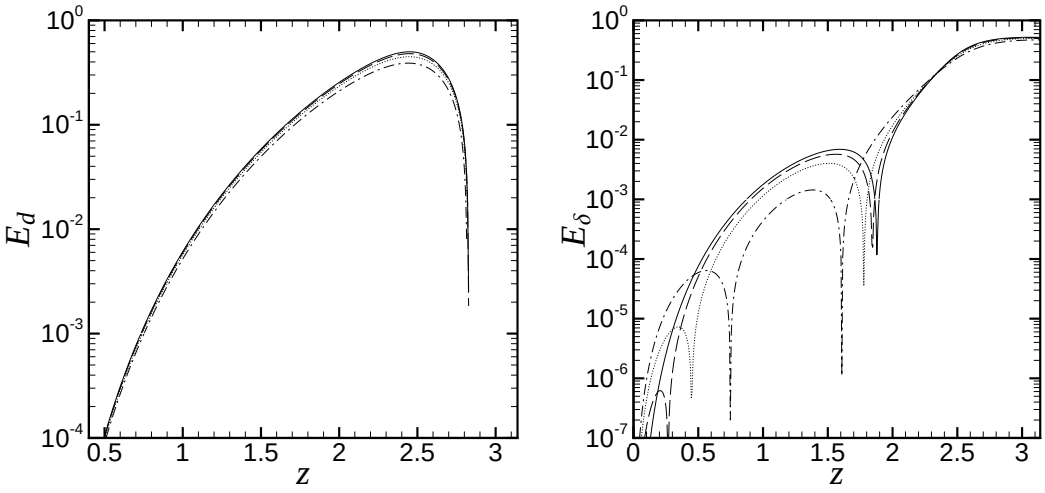

(a) (b)

Figure 3.19: (a) Temporal dissipation E_d and phase error E_δ in logarithmic scale for the classical and cost-optimized RK4 time integration schemes. Lines pattern as in Fig. 3.17.

3.4 Predicted performance of the cost-optimized schemes

To demonstrate the potential benefit of cost-optimization, finite-difference schemes that combine space and time cost-optimization for the same level of error have been developed. Figure 3.20(a) shows the contours of the normalized 'local' error function $e(\kappa, \sigma)$ for the cost-optimized epsm5 (solid line) and the corresponding non-optimized baseline solver $C1122/RK4$ (long dashed line). Figure 3.20(a) shows a spike-shaped iso-error contour labelled 10^{-5} in the region $0.6 \leq \kappa \leq 0.8$ for the optimized scheme. This spike changes the shape of the other iso-error contours (solid lines) with respect to the baseline solver (long dashed lines). Figure 3.20(b) reports a similar trend for the cost-optimized epsm3 scheme. The location of the spike on the $\kappa - \sigma$ plane shifts towards the right of the κ axis as the design target level of error increases. Figure 3.21(a) shows the contours for the normalized 'local' error function $e(\kappa, \sigma)$ of the cost-optimized epsm4 scheme by solid lines and of the baseline non-optimized $C1122/RK4$ scheme by long dashed lines. The corresponding optimal values of the wavenumber and Courant number pair $(\kappa^*(\tilde{\epsilon}), \sigma^*(\tilde{\epsilon}))$ are shown for the two-dimensional cost-function of eq. (2.67) for both schemes by symbols ($\bullet$, $\diamond$). Figure 3.21(a) clearly shows how the spike influences the $(\kappa^*(\tilde{\epsilon}), \sigma^*(\tilde{\epsilon}))$ pair for the epsm4 scheme near the design level of error $\tilde{\epsilon} = 10^{-4}$, in that the 'optimal' values $\kappa^*(\tilde{\epsilon})$ and $\sigma^*(\tilde{\epsilon})$ for the cost-optimized epsm4 scheme, in the $\kappa - \sigma$ plane, lie below the corresponding values for the baseline classical $C1122/RK4$ scheme. Figure 3.21(b) gives an enlarged view of the $\kappa - \sigma$ plane near the design level of error $\tilde{\epsilon} = 10^{-4}$ for the cost-optimized epsm4 scheme. Figure 3.22 reports the corresponding map for the epsm5 schemes, where a similar behaviour is observed near the design level of error $\tilde{\epsilon} = 10^{-5}$. The effect of the spike on $\kappa^*(\tilde{\epsilon})$ and $\sigma^*(\tilde{\epsilon})$ is to pull the $(\kappa^*(\tilde{\epsilon}), \sigma^*(\tilde{\epsilon}))$ pair towards the $\sigma = 0$ axis. This shows that the cost-optimized schemes can be run at lower Courant number for the same computational cost of the non-optimized scheme to resolve a target wavenumber κ.

The computational performance of the cost-optimized schemes is illustrated in Fig. 3.23 and summarized in Tab. 3.6. Figure 3.23(a) shows the effect of the scheme cost-optimization on the 'optimal' error versus cost curve. The cost-optimized schemes epsm$n$ (with $n = 3,4,5$), when working at their design level of error $\tilde{\epsilon} = 10^{-n}$, offer a substantial cost saving over the baseline $C1122/RK4$ scheme. For instance, the solid arrow in Figure 3.23(a) shows that the computational cost of running the baseline $C1122/RK4$ scheme to obtain an error $\tilde{\epsilon}$ of 10^{-4} is 2.8×10^2. The dotted line arrow shows that the computational cost of running the epsm4

scheme for the same level of error $\tilde{\epsilon} = 10^{-4}$ is 7.2×10^1. The distance between the two arrows on the abscissa indicates the computational gain of the epsm4 scheme with respect to the $C1122/RK4$ scheme. Figure 3.23(a) indicates an useful region of 'optimal' cost where the space and time cost-optimized schemes offer a computational cost saving over the non-optimized $C1122/RK4$ scheme. For instance, the epsm4 scheme outperforms the baseline scheme over the range $70 \leq c_2^* \leq 1300$. Similarly, the epsm5 scheme outperforms the baseline solver over the range $250 \leq c_2^* \leq 8000$. Figure 3.23(b) and 3.23(c) show the variation of 'optimal' reduced wavenumber κ^* and Courant number σ^* versus computational cost. These plots show where the cost-optimized schemes outperform the baseline schemes in terms of κ^* and σ^*. Consider, for instance, the epsm4 scheme working at its cost-optimal condition. The epsm4 scheme offers a computational saving over the baseline $C1122/RK4$ scheme when the available computational resources for a given monochromatic ('local') two-dimensional problem is $c_2^* \leq 1300$, in a wavenumber range of approximately $1.03 \leq \kappa^* \leq 1.07$, corresponding to an 'optimal' Courant number $\sigma^* \leq 0.4$. A plateau region in the case of epsm4 scheme occurs in the range $1.2 \times 10^2 \leq c_2^* \leq 1.1 \times 10^4$, corresponding to an error level of $5.5 \times 10^{-6} \leq \tilde{\epsilon} \leq 10^{-5}$, and a wavenumber region of $1.07 \leq \kappa^* \leq 0.27$. The error level range $5.5 \times 10^{-6} \leq \tilde{\epsilon} \leq 10^{-5}$ is below the design level of error $\tilde{\epsilon} = 10^{-4}$, for which $c_2^* = 72.78 \times 10^2$, $\kappa^* = 1.083$, and $\sigma^* = 0.389$, as indicated by the dotted arrows in Fig. 3.23. As a consequence, a given value of error level in this $\tilde{\epsilon}$ plateau corresponds to an 'optimal' computational cost c_2^* which varies by two decades. The presence of the plateau on the $\tilde{\epsilon}$ versus c_2^* curve from the cost-optimized schemes is the consequence of the spike which modifies the contours of the error function $e(\kappa, \sigma)$ and consequently, the 'optimal' working condition $(\kappa^*(\tilde{\epsilon}), \sigma^*(\tilde{\epsilon}))$, as highlighted in Fig. 3.21(b) for the epsm4 scheme. This $\tilde{\epsilon}$ plateau intercepts the $C1122/RK4$ line in Fig. 3.23(a) at a computational cost of $c_2^* \approx 1300$. The plateau to the right of the intercept is the region in which it is best not to use the optimized scheme epsm4. The suggestion is to use the cost-optimized schemes at their design level of error and not beyond the intercept with their classical counterpart scheme.

Table 3.6 reports the $2D$ percent cost reduction ΔC_2 of the cost-optimized schemes over the non-optimized $C1122/RK4$ scheme when working at their design level of error. A cost reduction of about 70% – 80% can be achieved in problems involving well-defined tonal spectra.

Figure 3.24 reports the iso-level of the normalized 'local' error function $e(\kappa, \sigma)$ for the cost-optimized epsm4 scheme (solid line) and of the two-dimensional cost function of eq. (2.67) (dash-dotted line). The two curves are tangent to one other at the (κ, σ) location shown by

Table 3.6: Performance of cost-optimized schemes for different target errors in two dimensional space.

scheme	$\tilde{\epsilon}$	c_2^*	$c^*_{2\,(C1122/RK4)}$	$\Delta C_2(\%)$
epsm5	10^{-5}	247.75	1052.87	76.47
epsm4	10^{-4}	72.78	276.837	73.70
epsm3	10^{-3}		73.166	

Table 3.7: Approximate optimal operating points of cost-optimized schemes for different target errors in two dimensional space.

scheme	$\tilde{\epsilon}$	$\sigma^*(\tilde{\epsilon})$	$z^*(\tilde{\epsilon})$	$\Delta z^*(\%)$	$\kappa^*(\tilde{\epsilon})$	$\Delta\kappa^*(\%)$
epsm5	10^{-5}	0.348	0.260 (0.272)	4.4	0.747 (0.7461)	0.12
epsm4	10^{-4}	0.389	0.421 (0.436)	3.44	1.083(1.0901)	0.65
epsm3	10^{-3}		(0.3532)			

a filled solid circle. This location represents the optimal operating point of the epsm4 at its design level of error.

The dashed line represents the locus of the (κ, σ) points for which the spatial differentiation error is $\tilde{\epsilon} = 10^{-4}$ as determined from eq. (2.57). The dotted line represents the locus of (κ, σ) points for which the temporal integration error is $\tilde{\epsilon} = 10^{-4}$ as determined from eq. (2.58). The intercept between these two lines is indicated by an open circle. This point represents an approximation to the solid circle. Specifically, the approximation is obtained by considering the spatial differentiation error separately from the temporal integration error as discussed respectively in Secs. 3.2.3 and 3.3.3. Figure 3.24 shows that the (κ, σ) operating condition that satisfies eqs. (2.57) and (2.58), reported by the open solid circle, is very close to the 'optimal' working condition of the filled solid circle. The distance between these two points is quantified in Table 3.7. Table 3.7 reports the approximate coordinates of the optimal operating points of the cost-optimized schemes for different target errors in two-dimensional space. The values in brackets in the columns $z^*(\tilde{\epsilon}) = \sigma^*(\tilde{\epsilon})\kappa^*(\tilde{\epsilon})$ and $\kappa^*(\tilde{\epsilon})$ are taken from Tabs. 3.3 and 3.5, for comparison purposes. These correspond to the coordinates of the open circle of Fig. 3.24. The $z^*(\tilde{\epsilon})$ and $\kappa^*(\tilde{\epsilon})$ in plain text in Tab. 3.7 correspond to the coordinates of the filled circle in Fig. 3.24. Δz^* is the absolute percent difference in $z^*(\tilde{\epsilon})$ between the z^* values reported in plain text and in brackets. Similarly, $\Delta\kappa^*$ is the absolute percent difference in κ^*. These percent differences are below 5%. Therefore, the values of optimal cost, reduced wavenumber and Courant number reported in Tabs. 3.3 and 3.5 by separately optimizing the space and time schemes agree well

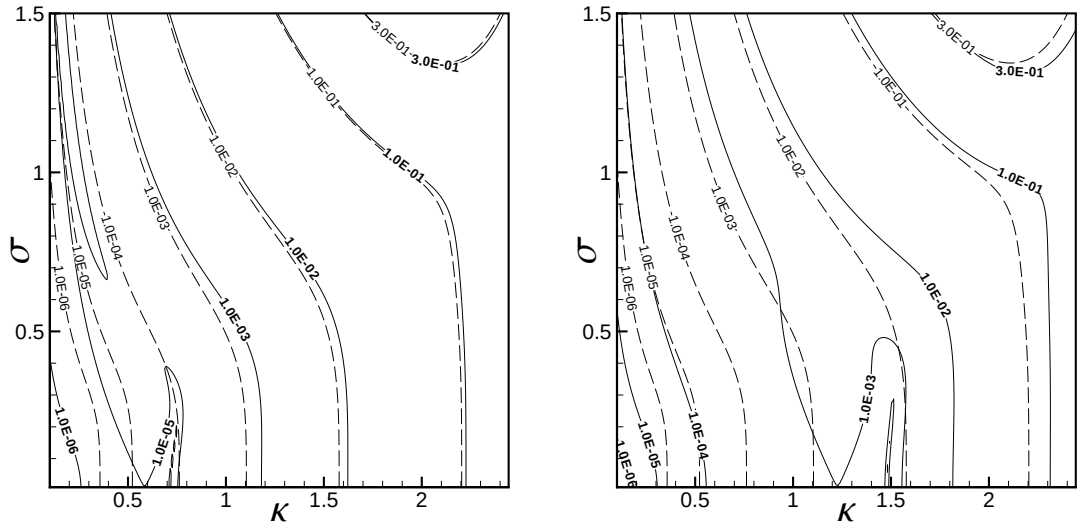

(a) (b)

Figure 3.20: Contours of normalized 'local' error function $e(\kappa, \sigma)$ for the cost-optimized schemes (solid black line) and the non-optimized baseline solver $C1122/RK4$ (long-dashed black line). (a) epsm5; (b) epsm3.

with the ones reported in Tab. 3.7, obtained by a combined cost minimization procedure for the cost-optimized scheme. This shows that, by optimizing separately the spatial and temporal components, a scheme is obtained, the performance of which is very close to the one obtained by a combined space and time optimization at the design level of error. This implies that the space and time optimized schemes can give a substantial saving in term of computational cost, of the order of 70% – 80% in a decade around their design error level, compared to the corresponding non-optimized $C1122/RK4$ benchmark. The cost-optimized schemes also decrease the optimal Courant number σ^* with respect to the baseline non-optimized scheme, as shown in Fig. 3.23(c). This makes the cost-optimized schemes very suitable for computational problems of narrow-band or tonal waves, such as cavity noise in aeroacoustics.

In conclusion, there is a computational advantage in prediction accuracy and computational cost by using cost-optimized schemes to model wave propagation problems at their design operational point $\left(\kappa^*(\tilde{\epsilon}), \sigma^*(\tilde{\epsilon}), c^*_{n_D}(\tilde{\epsilon})\right)$.

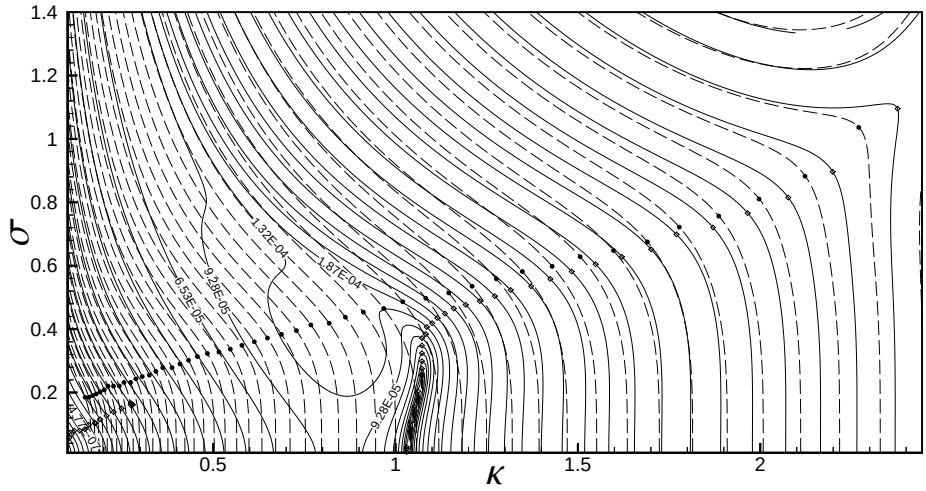

(a)

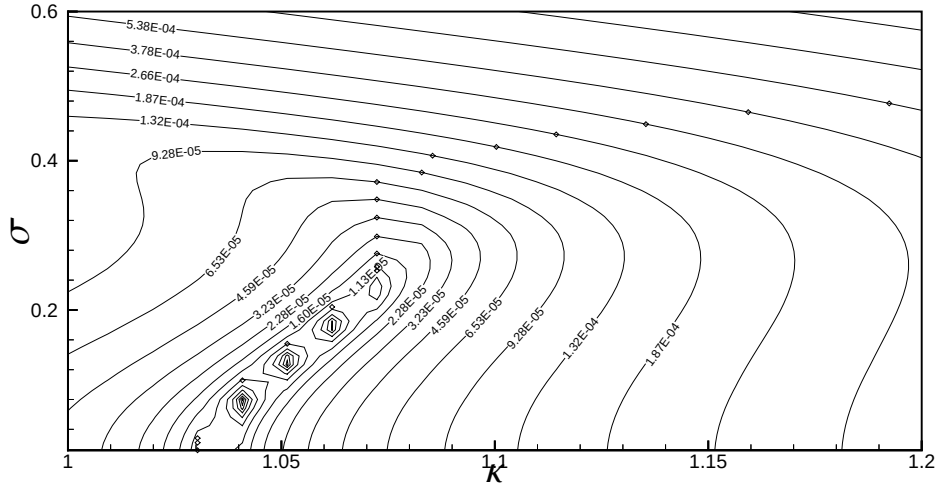

(b)

Figure 3.21: (a) Contours of normalized 'local' error function $e(\kappa, \sigma)$ for the cost-optimized epsm4 scheme (solid line) and for the corresponding non-optimal baseline $C1122/RK4$ scheme (long-dashed line). Constant ratio $e(\kappa, \sigma)$ contour spacing of 0.7037 between 10^{-8} and 0.3. The filled circles and the diamonds represent the corresponding 'optimal' working conditions of the respective schemes for the two dimensional cost function of eq. (2.67). (b) Enlarged view of the region near the design level of error $\tilde{\epsilon} = 10^{-4}$ for the cost-optimized epsm4 scheme.

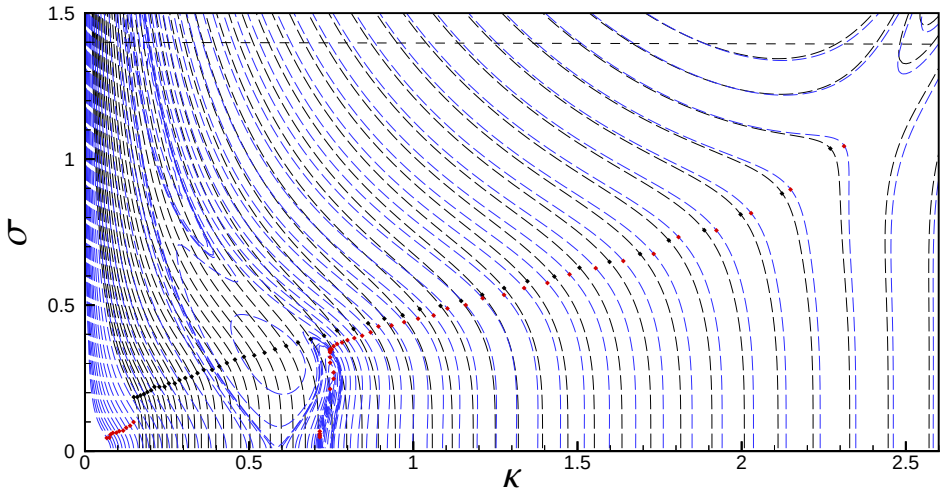

(a)

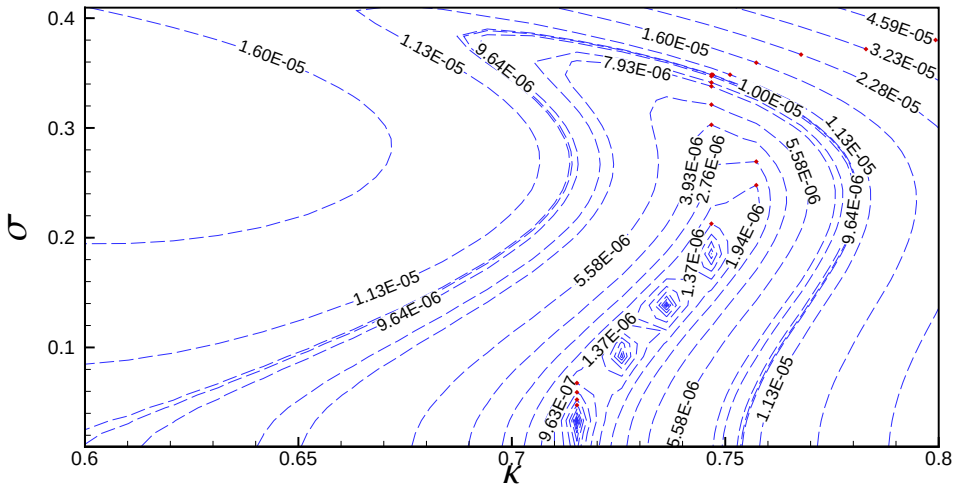

(b)

Figure 3.22: (a) Contours of normalized 'local' error function $e(\kappa, \sigma)$ for the cost-optimized epsm5 (long dashed blue line) and for the corresponding non-optimal baseline $C1122/RK4$ scheme (long dashed black line). The black and red diamonds represent the corresponding 'optimal' working conditions of the respective schemes for the two dimensional cost function of eq. (2.67). (b) Enlarged view of the region near the design level of error $\tilde{\epsilon} = 10^{-5}$ for the cost-optimized epsm5 scheme.

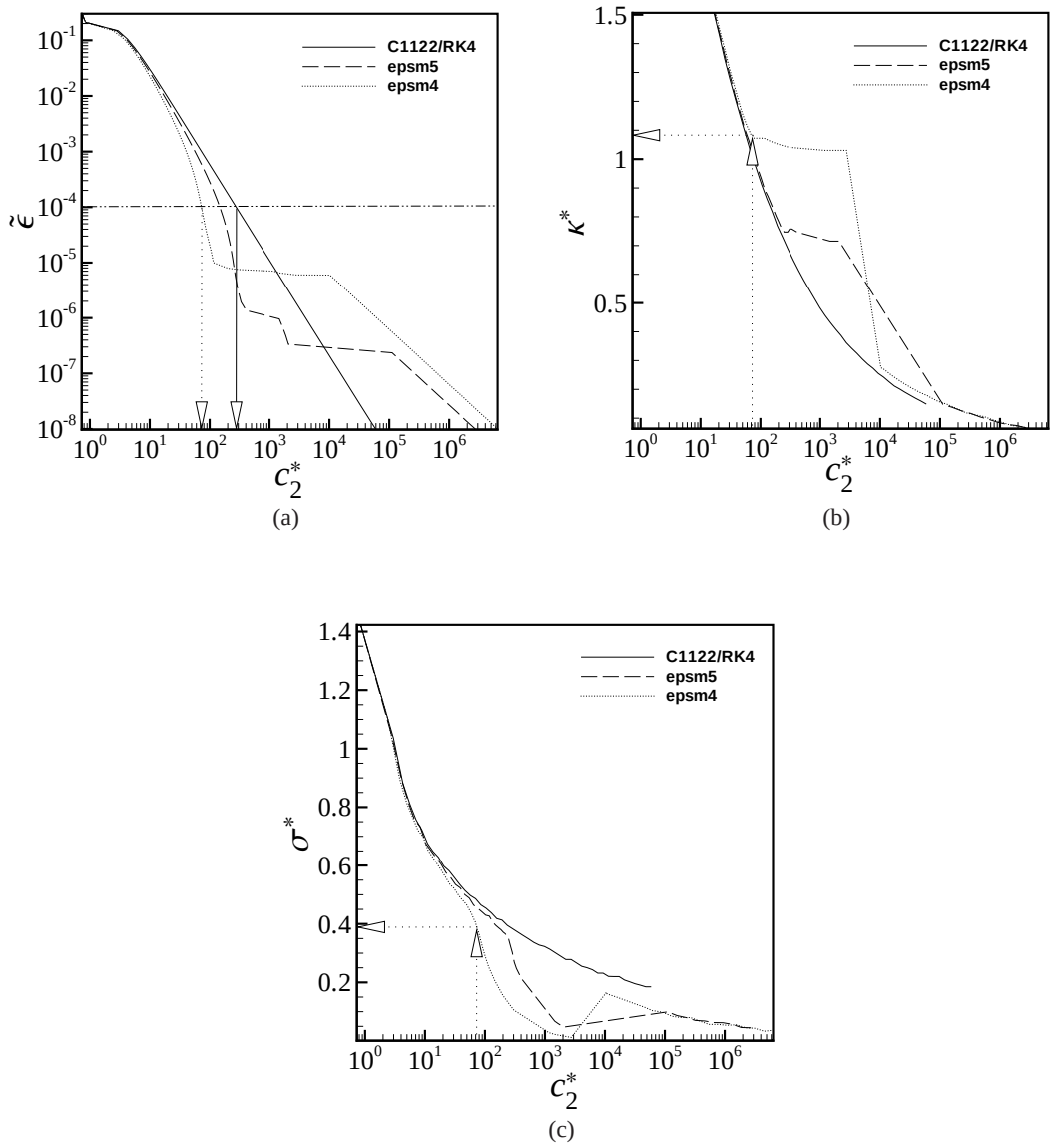

Figure 3.23: (a) Optimal 'local' error, (b) reduced wavenumber and (c) Courant number as a function of the two-dimensional cost for the baseline $C1122/RK4$ scheme and the cost-optimized epsm5, epsm4, epsm3 schemes. Line patterns as in Fig. 3.17.

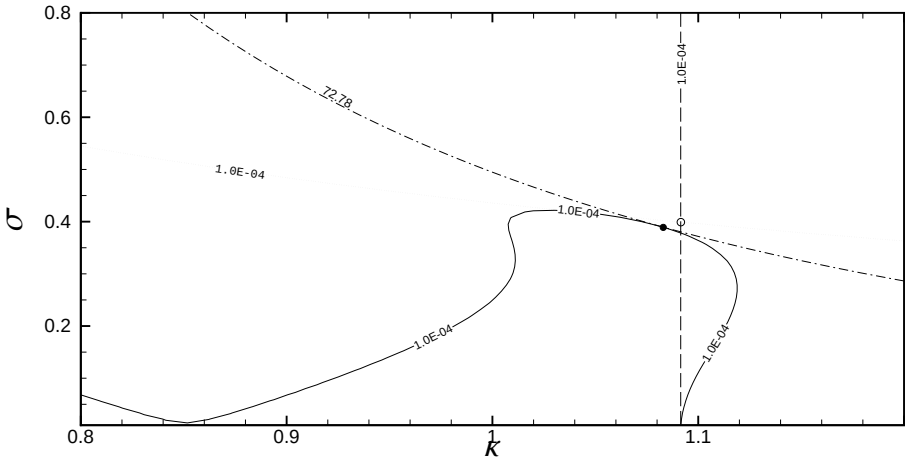

Figure 3.24: Iso-level of the normalized 'local' error function $e(\kappa, \sigma)$ for the cost-optimized epsm4 scheme (solid line) and of the cost function in two dimensional space (dash-dotted line). 'Optimal' (filled solid circle) and approximate working condition (open circle) at the design level of error $\tilde{\epsilon} = 10^{-4}$. The dashed and dotted lines represent, respectively, the approximations to the dash-dotted line given by eqs. (2.57) and (2.58).

3.5 Perimetrical scheme

3.5.1 Spatial Differentiation

In areas near the boundaries, the interior scheme cannot be applied because the stencil extends outside the computational domain, therefore a perimetrical scheme has to be used to close the discretized set of algebraic equations. This section starts by discussing the effect of the perimetrical scheme on the interior scheme. Then, two methods of treating near-boundary points are presented and compared against the boundary treatments of Hixon (2000) and Ashcroft & Zhang (2003). The first approach is to use a prefactored sixth-order explicit one-sided finite-difference scheme that uses a seven-point stencil, the second is to use a prefactored explicit central scheme with an 11-point stencil. Finally, the wave propagation characteristics of these boundary closures are examined.

Effect of perimetrical scheme on interior scheme

The boundary closure for a compact scheme has a much larger effect on the stability and accuracy of the scheme than the boundary closure for the equivalent explicit scheme (Carpenter *et al.*, 1993b, 1994; Hixon, 2000). The reason for this is that the error from the boundary stencil derivative can propagate many points into the computational domain. Following Hixon & Turkel (2000), a sixth-order scheme is used to study this boundary closure effect. Let ϵ_0 be a boundary error or perturbation at the beginning of the backward sweep:

$$\epsilon_0 = \left\{ f_0'^B \right\}_{\text{interior}} - \left\{ f_0'^B \right\}_{\text{boundary}}, \tag{3.44}$$

where the subscript ”interior” refers to the spatial derivative that the interior scheme would have obtained and the subscript ”boundary” refers to the derivative calculated by the boundary stencil. Substituting eq. (3.44) in eq. (3.34), as shown in Appendix A.7, the error in the computed derivative i grid points away from the boundary is:

$$\left\{ f_i'^B \right\}_{\text{interior}} = \left\{ f_i'^B \right\}_{\text{boundary}} + \left(-\frac{\alpha_F}{1-\alpha_F} \right)^i \epsilon_0, \tag{3.45}$$

or

$$\epsilon_i = \left(-\frac{\alpha_F}{1-\alpha_F} \right)^i \epsilon_0. \tag{3.46}$$

It is evident that the error propagates inwards from the boundary. For values of $\alpha_F < 0.3$ as stated in Table 3.4, the error ϵ_i decays exponentially with i. The error due to the boundary stencil used at the start of the forward or backward sweep has a much greater effect on the solution than the error of the boundary stencil used at the end of the sweep. Figure 3.25 illustrates the propagation of the boundary stencil error in the computational domain interior for the classical fourth-order $C1111$ and sixth-order $C1122$ compact schemes, and the cost-optimized $C11122epsm5$, $C11122epsm4$, $C11122epsm3$ compact schemes. The family of the $C1122$ schemes are more sensitive to the boundary stencil error than the $C1111$ scheme, due to their larger stencil. The cost-optimized schemes have a slightly lower performance compared to the baseline $C1122$ scheme in terms of reducing the boundary closure error with increasing distance from the boundary. The lower roll-off rate of the optimized schemes is due to the higher value of α_F compared to the baseline $C1122$ scheme, as reported in Table 3.4. These values are produced by the cost-optimization process of Sec. 3.2.3.

Equations (3.45) and (3.46) are valid for the fourth and sixth order compact schemes, but not for the eighth-order scheme. For such a scheme, a tridiagonal matrix is present on the L.H.S of eqs. (3.33) and (3.34) and, in this case, the stencil used at the start of the forward or backward sweep has a symmetric effect on the interior scheme, therefore the boundary error propagates hyperbolically in the computational domain interior.

Prefactored one-sided boundary stencil

To compute the state variables at the computational domain boundaries and wall points, explicit sixth-order one-sided derivative stencils are defined for the sixth-order compact scheme. To accomplish this, the Taylor series for the forward and backward interior derivatives was matched to the sixth order in Appendix A.8.2. The resulting boundary stencils for the backward sweep are:

$$f_1'^B = \frac{1}{h} \sum_{j=1}^{7} s_j f_j, \tag{3.47a}$$

$$f_N'^B = \frac{1}{h} \sum_{j=N-6}^{N} e_j f_j, \tag{3.47b}$$

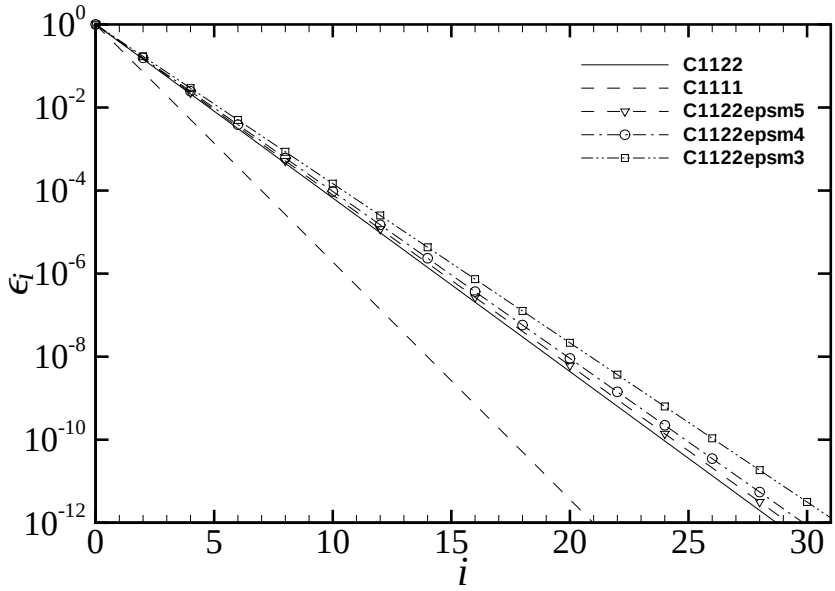

Figure 3.25: Boundary closure error propagation inside the computational domain.

and for the forward sweep:

$$f_1'^F = \frac{1}{h} \sum_{j=1}^{7} -e_{N+1-j} f_j, \tag{3.48a}$$

$$f_N'^F = \frac{1}{h} \sum_{j=N-6}^{N} -s_{N+1-j} f_j, \tag{3.48b}$$

where:

$$\begin{aligned}
s_1 &= -\frac{545 + 353\sqrt{5}}{150\left(1 + \sqrt{5}\right)} = -2.74887508613328 \\
s_2 &= \frac{1515 + 823\sqrt{5}}{150\left(1 + \sqrt{5}\right)} = 6.91226506738317 \\
s_3 &= -\frac{405 + 191\sqrt{5}}{30\left(1 + \sqrt{5}\right)} = -8.57098789320814 \\
s_4 &= \frac{35 + 16\sqrt{5}}{3\left(1 + \sqrt{5}\right)} = 7.29044096437489 \\
s_5 &= -\frac{95 + 43\sqrt{5}}{15\left(1 + \sqrt{5}\right)} = -3.93792558049996 \\
s_6 &= \frac{295 + 133\sqrt{5}}{150\left(1 + \sqrt{5}\right)} = 1.22040502059166 \\
s_7 &= -\frac{20 + 9\sqrt{5}}{75\left(1 + \sqrt{5}\right)} = -0.165322492508333,
\end{aligned} \tag{3.49}$$

and

$$\begin{aligned}
e_N &= \frac{95+191\sqrt{5}}{75\left(1+\sqrt{5}\right)} = 2.15112491386675 \\
e_{N-1} &= -\frac{285+977\sqrt{5}}{150\left(1+\sqrt{5}\right)} = -5.08773493261699 \\
e_{N-2} &= \frac{45+259\sqrt{5}}{30\left(1+\sqrt{5}\right)} = 6.42901210679221 \\
e_{N-3} &= -\frac{5+24\sqrt{5}}{3\left(1+\sqrt{5}\right)} = -6.04289236895886 \\
e_{N-4} &= \frac{35+139\sqrt{5}}{30\left(1+\sqrt{5}\right)} = 3.56207441950031 \\
e_{N-5} &= -\frac{65+227\sqrt{5}}{150\left(1+\sqrt{5}\right)} = -1.17959497940844 \\
e_{N-6} &= \frac{5+16\sqrt{5}}{75\left(1+\sqrt{5}\right)} = 0.168010840825015.
\end{aligned} \tag{3.50}$$

The rational form of the coefficients given in eqs. (3.49) and (3.50) enable the reader to compute s_j and e_j with an arbitrarily high precision, to match the computer hardware available.

Prefactored interior boundary stencils

In typical engineering CFD applications, computational boundaries exist where the flow state is known on both sides of the boundaries (periodic, symmetry, inter-block boundaries), so an appropriate spatial differencing scheme across these boundaries is required. An explicit central boundary stencil is used for this purpose. This stencil mimics the spectral characteristics of the prefactored compact interior scheme over the resolved range of wavenumbers. An 11-point explicit stencil is used that matches the Taylor series expansion of the interior stencil up to the eleventh order as shown in Appendix A.8.2, for shortness.

Figure 3.26 represents an interior boundary connection at $i = 1$ and $i = N$. The physical domain to the left of central point $i = N$ is connected to the physical domain to the right of the central point $i = 1$. The computational domain to the left is $i \leq N$, and to the right it is $i \geq 1$. The left and right domains share one overlap point $i = 1 \equiv N$. When the interior prefactored forward

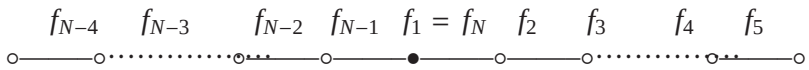

Figure 3.26: Sketch of the backward and forward sweeps at the interior boundary $i = 1 \equiv N$.

sweep of eq. (3.33) has reached the $i = N - 1$ point, it requires an estimate of the internal boundary derivative $f_N'^F = f_1'^F$. Similarly, when the prefactored interior backward sweep of eq. (3.34) has reached the $i = 2$ point, it requires an estimate of the internal boundary derivative $f_1'^B = f_N'^B$.

These interior boundary stencils are given by:

$$f_i'^F = \frac{1}{h} \sum_{j=-5}^{5} b_j f_{i+j}, \tag{3.51a}$$

$$f_i'^B = \frac{1}{h} \sum_{j=-5}^{5} -b_{-j} f_{i+j}, \tag{3.51b}$$

where

$$\begin{aligned}
b_{-5} &= -0.00048892760612052 \\
b_{-4} &= 0.00538269106033271 \\
b_{-3} &= -0.0264320102799523 \\
b_{-2} &= 0.0777993608366292 \\
b_{-1} &= -0.321981330625385 \\
b_0 &= -0.759829408040846 \\
b_1 &= 1.34468533604127 \\
b_2 &= -0.398391115353838 \\
b_3 &= 0.092615608767661 \\
b_4 &= -0.0144585787809353 \\
b_5 &= 0.00109837398118083.
\end{aligned} \tag{3.52}$$

These coefficients, given in double precision, are broadly similar to the ones for the 11-point boundary stencil given by Hixon (2000). The Hixon (2000) coefficients are given in single

precision and match the Taylor series expansion of the interior stencil up to the ninth order, with the last coefficient used to more closely match the spectral performance of the boundary stencil with that of the interior scheme. The coefficients of eq. (3.52) match the Taylor series expansion of the interior stencil up to the eleventh order. Therefore, the two sets of coefficients are numerically different from the third decimal digit.

Wave propagation characteristics of the boundary closures

By taking the Fourier transform of eq. (3.47a), the real $\mathfrak{R}\left(\widetilde{f_1'^B}\right)$ and imaginary $\mathfrak{I}\left(\widetilde{f_1'^B}\right)$ components of the prefactored backward one-sided boundary stencil on the first node $i = 1$ are obtained as:

$$\mathfrak{R}\left(\widetilde{f_1'^B}\right) = [s_2 \sin(\kappa) + s_3 \sin(2\kappa) + s_4 \sin(3\kappa) + s_5 \sin(4\kappa) + s_6 \sin(5\kappa) + s_7 \sin(6\kappa)]\,, \quad (3.53a)$$

$$\mathfrak{I}\left(\widetilde{f_1'^B}\right) = -[s_1 + s_2 \cos(\kappa) + s_3 \cos(2\kappa) + s_4 \cos(3\kappa) + s_5 \cos(4\kappa) + s_6 \cos(5\kappa) + s_7 \cos(6\kappa)]\,. \quad (3.53b)$$

Similarly, from eq. (3.48a), the real $\mathfrak{R}\left(\widetilde{f_1'^F}\right)$ and imaginary $\mathfrak{I}\left(\widetilde{f_1'^F}\right)$ components of the prefactored forward one-sided boundary stencil on the first node $i = 1$ are:

$$\mathfrak{R}\left(\widetilde{f_1'^F}\right) = -[e_{N-1} \sin(\kappa) + e_{N-2} \sin(2\kappa) + e_{N-3} \sin(3\kappa) + e_{N-4} \sin(4\kappa) + e_{N-5} \sin(5\kappa) + e_{N-6} \sin(6\kappa)]\,, \quad (3.54a)$$

$$\mathfrak{I}\left(\widetilde{f_1'^F}\right) = [e_N + e_{N-1} \cos(\kappa) + e_{N-2} \cos(2\kappa) + e_{N-3} \cos(3\kappa) + e_{N-4} \cos(4\kappa) + e_{N-5} \cos(5\kappa) + e_{N-6} \cos(6\kappa)]\,. \quad (3.54b)$$

Appendix A.8.3 reports the corresponding Fourier transform of the prefactored backward and forward one-sided boundary stencils at the last node $i = N$. These are related to eq. (3.53) and (3.54) by:

$$\mathfrak{R}\left(\widetilde{f_1'^B}\right) = \mathfrak{R}\left(\widetilde{f_N'^F}\right), \quad \mathfrak{I}\left(\widetilde{f_1'^B}\right) = -\mathfrak{I}\left(\widetilde{f_N'^F}\right). \quad (3.55)$$

Equation (3.55) is due to the permutation of the coefficients s_j between the two differential operators $f_1'^B$ of eq. (3.47a) and $f_N'^F$ of eq. (3.48b) that results in matched spectra in wavenumber space. Similarly, the real and imaginary Fourier components of the prefactored forward one-sided boundary stencil at $i = 1$ of eqs. (3.54a) and (3.54b) are related to the corresponding

backward one-sided boundary stencil components of eqs. (A.199) and (A.200) by:

$$\Re\left(\widetilde{f_1'^F}\right) = \Re\left(\widetilde{f_N'^B}\right), \quad \Im\left(\widetilde{f_1'^F}\right) = -\Im\left(\widetilde{f_N'^B}\right). \tag{3.56}$$

The above relations are given by the permutation of the coefficients e_j between the two differential operators $f_1'^F$ of eq. (3.48a) and $f_N'^B$ of eq. (3.47b).

Figure 3.27 shows the dispersive characteristics of the prefactored one-sided boundary stencils of eq. (3.47a) and eq. (3.48a) from Hixon (2000), compared against the interior $C1122$ sixth-order scheme of eq. (3.36) and the prefactored one-sided boundary formulations of Ashcroft & Zhang (2003). Figure 3.27(a) shows that the one-sided boundary stencils of eq. (3.47a) and eq. (3.48a), represented by the dashed lines, introduce a large dispersion error over the range $0.27 \leq \kappa/\pi \leq 1$. This error, which mainly affects the *poorly-resolved* waves, is due to biased nature of the forward/backward stencil. Figure 3.27(a) also shows, by the dashed-dotted lines, the dispersive characteristics of the $6/4$ one-sided boundary stencils of Ashcroft & Zhang (2003). These stencils introduce a lower dispersive error with respect to eqs. (3.47a) and (3.48a) and their dispersion characteristics are qualitatively more similar to the interior scheme. A common feature of the one-sided prefactored boundary stencils is the different spectral characteristics of their forward and backward components, as shown by the lines with and without symbols not overlapping one another in Fig. 3.27(a). This is unlike the spectral characteristics of the interior scheme, shown by the continuos line, that follows the MacCormack properties reported in eq. (3.39). Specifically, the derivation of the coefficients of eqs. (3.47a) and (3.48a) does not satisfy the relation $s_j = -e_{N+1-j}$ for $2 \leq j \leq 7$, because they have been constructed by matching the Taylor series expansion of the forward and backward prefactored operators up to sixth and third-order, respectively, by Hixon (2000) and Ashcroft & Zhang (2003). This process does not impose identical dispersive characteristics for the forward and backward components. Figure 3.27(b) is an enlarged view of Fig 3.27(a). It shows that the prefactored one-sided boundary stencils of eq. (3.47a) and eq. (3.48a) have a non-monotonic behaviour in the range $0.27 \leq \kappa/\pi \leq 0.5$, where they have a relative minimum. When propagating waves in this wavenumber range with the prefactored one-sided boundary stencils of eq. (3.48a), the numerical solution is affected by the introduction of spurious numerical waves that have to be removed. This non-monotonic behaviour is not present in the one-sided boundary stencils of Ashcroft & Zhang (2003). Figure 3.27(c) shows the dissipative characteristics of the prefactared one-sided boundary stencils for $i = 1$. The one-sided boundary stencils of

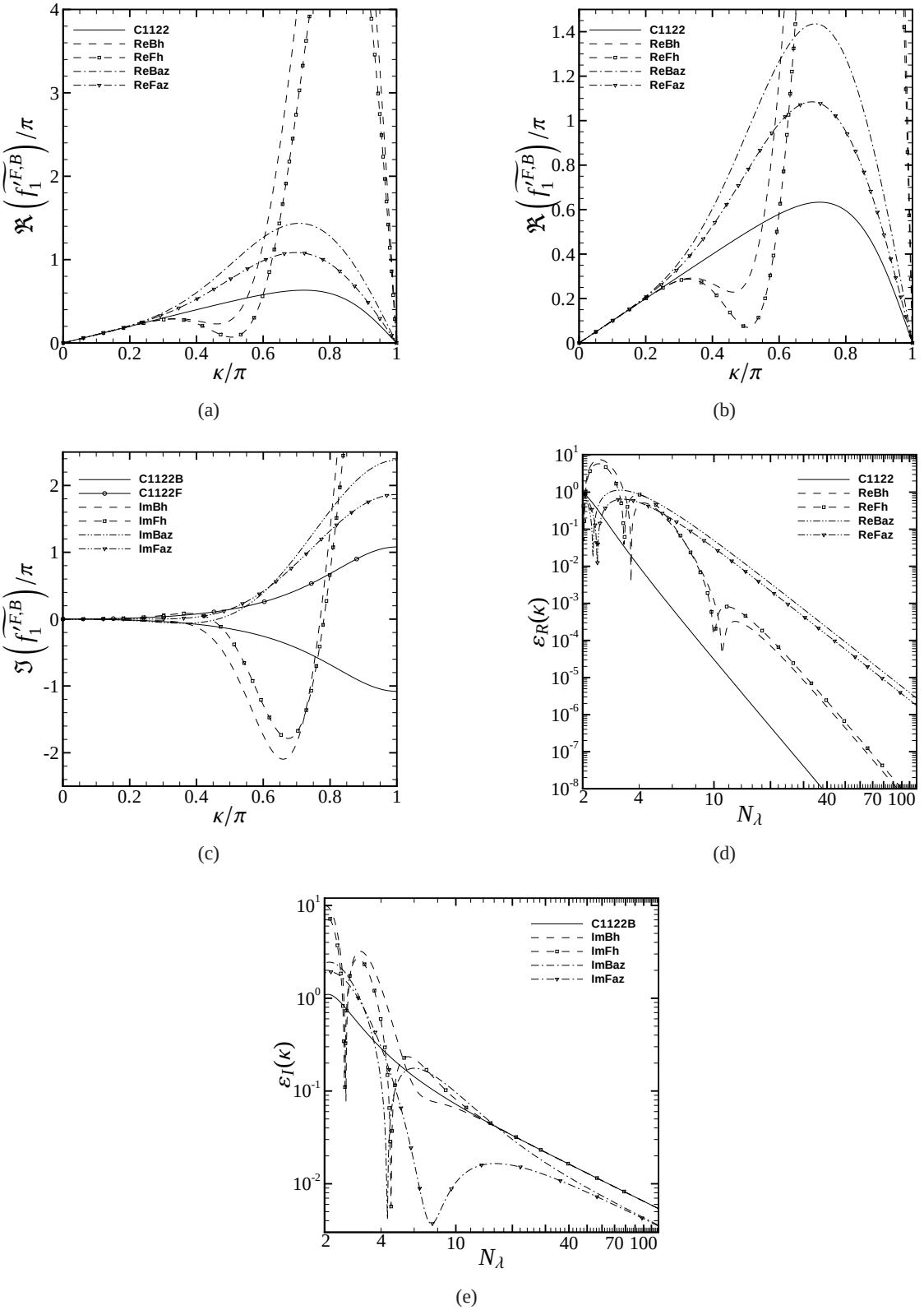

Figure 3.27: Dispersive characteristics of the prefactored one-sided boundary stencils for $i = 1$. (a,b) Real and (c) imaginary components of the Fourier transform. (d) Dispersive error from eq. (2.11). (e) Dissipative error from eq. (2.12).

eq. (3.47a) and eq. (3.48a) from Hixon (2000) introduce a large error in the range of the *poorly-resolved* waves, whereas the prefactored one-sided boundary stencils of Ashcroft & Zhang (2003) mimic the behaviour of the interior scheme and start to deviate from it in the range of the *poorly-resolved* waves. The dissipative characteristics of the prefactared one-sided boundary stencils for $i = N$ are equal and opposite to the dissipative characteristics of the prefactared one-sided boundary stencils for $i = 1$ of Fig. 3.27(c), as reported in eqs. (3.55) and (3.56). The net effect is that the dissipation resulting from the forward boundary stencil compensates the one generated by the backward boundary stencil.

Figure 3.27(d) reports the relative dispersive error from eq. (2.11) for the prefactored one-sided boundary stencils compared against the dispersive error of the interior sixth-order $C1122$ scheme. Figure 3.27(d) shows a difference in the error magnitude between the corresponding forward and backward components of the prefactored one-sided boundary stencils, due to their non-matched spectral characteristics. The prefactored one-sided boundary stencils have a greater relative error with respect to the interior scheme, except over the range $2 \leq N_\lambda \leq 3$, which represents *poorly-resolved* waves. The prefactored one-sided boundary stencils of Hixon (2000) have a lower dispersive error compared to the ones by Ashcroft & Zhang (2003), due to their higher order of accuracy. The prefactored one-sided boundary stencils of eq. (3.47a) and eq. (3.48a) present, as already reported by Hixon (2000), three troughs at different values of N_λ, two of which are in the region of *poorly-resolved* wavenumbers and the last one is in the *well-resolved* wavenumber range. At these troughs, the relative error is comparable to that of the interior scheme. A similar behaviour is shown by the relative error of the prefactored one-sided boundary stencils of Ashcroft & Zhang (2003), but with a single trough close to $N_\lambda = 2$. Figure 3.27(e) shows the dissipative error from eq. (2.12) for the prefactored one-sided boundary stencils compared against the corresponding error of the interior sixth-order $C1122$ scheme, in which the forward and backward stencils have the same error value, given by eq. (2.12). The relative error of the prefactored one-sided boundary stencils of eq. (3.47a) and eq. (3.48a) from Hixon (2000) shows two troughs over the *poorly-resolved* wavenumber range $2 \leq N_\lambda \leq 4.5$. The prefactored one-sided boundary stencils of Ashcroft & Zhang (2003) show two troughs at $N_\lambda = 4.3$ and $N_\lambda = 7.4$. At these troughs, the prefactored one-sided boundary stencils have individually a relative error lower than that of the interior scheme. For higher values of N_λ, that is for *well-resolved* waves, the prefactored one-sided boundary stencils follow the trend of the prefactored interior sixth-order $C1122$ scheme.

In conclusion, the effect of the real and imaginary errors are seen not so much on the waves that

propagate through the computation domain boundaries, as these are regions of one computational point thickness, but rather on the generation of reflections due to the boundary numerical impedance mis-match, which can be reduced by the application of Artificial Boundary Conditions of Sec. 3.6.2.

Kim (2007) derived a set of boundary closures, that maintain fourth-order accuracy by optimizing the boundary schemes in the spectral domain. These boundary closures achieve the best wavenumber resolution characteristics within a constraint for dispersion and dissipation errors appropriate for CAA.

Applying the Fourier transform to the eq. (3.51a), the real $\mathfrak{R}\left(\widetilde{f_i'^F}\right)$ and imaginary $\mathfrak{I}\left(\widetilde{f_i'^F}\right)$ components of the prefactored forward interior 11-point stencil on the i-th node are obtained as:

$$\mathfrak{R}\left(\widetilde{f_i'^F}\right) = [(-b_{-5}+b_5)\sin(5\kappa) + (-b_{-4}+b_4)\sin(4\kappa) + (-b_{-3}+b_3)\sin(3\kappa) + (-b_{-2}+b_2)\sin(2\kappa) + \\ + (-b_{-1}+b_1)\sin(\kappa)]\,, \tag{3.57a}$$

$$\mathfrak{I}\left(\widetilde{f_i'^F}\right) = -[(b_{-5}+b_5)\cos(5\kappa) + (b_{-4}+b_4)\cos(4\kappa) + (b_{-3}+b_3)\cos(3\kappa) + (b_{-2}+b_2)\cos(2\kappa) + \\ + (b_{-1}+b_1)\cos(\kappa) + b_0]\,. \tag{3.57b}$$

The real and imaginary Fourier components of the prefactored backward interior 11-points stencil for the i-th node of eq. (3.51b) are related to eqs. (3.57a) and (3.57b) by:

$$\mathfrak{R}\left(\widetilde{f_i'^B}\right) = \mathfrak{R}\left(\widetilde{f_i'^F}\right), \quad \mathfrak{I}\left(\widetilde{f_i'^B}\right) = -\mathfrak{I}\left(\widetilde{f_i'^F}\right), \tag{3.58}$$

due the permutation of the coefficients b_j between the two finite-difference approximations $f_i'^F$ of eq. (3.51a) and $f_i'^B$ of eq. (3.51b). Hence, the prefactored backward and forward interior 11-point stencils follow the same properties of the MacCormack schemes of eq. (3.39).

Figure 3.28 shows the dispersive characteristics of the forward prefactored interior 11-point stencil of eq. (3.51a) compared against the interior sixth-order $C1122$ scheme of eq. (3.36), the fourth-order three-point stencil prefactored compact scheme of Ashcroft & Zhang (2003), and the prefactored interior 11-point formulations of Hixon (2000) and of Ashcroft & Zhang (2003). The prefactored interior 11-point stencils of Ashcroft & Zhang (2003) match the Taylor series expansions of the forward and backward interior stencils to fourth-order accuracy and use the remaining free coefficients to more closely match the spectral characteristics of these sten-

cils with those of the interior scheme. Figure 3.28(a) shows the dispersive characteristics of the three interior schemes. The prefactored interior 11-point forward stencil of eq. (3.51a), shown by the (−−▽−−) line, has essentially the same dispersive properties of the Hixon (2000) scheme, shown by the dashed line (−−). Both schemes underestimate the scaled pseudo-wavenumber of the interior sixth-order $C1122$ scheme as shown by the maxima of the dashed lines being below the continuous line. This difference is marginally amplified by the cost-optimization process of Sec. 3.2.3, as shown by Fig. 3.11(a). The prefactored 11-point stencil of Ashcroft & Zhang (2003), shown by the (− · ·−) line, has a closer match to the exact analytical solution $\bar{\kappa}(\kappa) = \kappa$ compared to the prefactored 11-point stencil of eq. (3.51a) and of Hixon (2000), shown by the dashed lines.

Figure 3.28(b) shows the dissipative characteristics of the prefactored forward interior 11-point stencil schemes. The continuous lines represent the dissipative characteristics of the interior sixth-order $C1122$ compact scheme of eq. (3.36) and of the fourth-order three-point prefactored compact scheme of Ashcroft & Zhang (2003). The prefactored 11-point stencil of eq. (3.51a) has essentially the same dissipative properties of the prefactored 11-point stencil scheme of Hixon (2000), as shown by the dashed lines overlapping in Fig. 3.28(b), with both schemes following the continuous line of the interior $C1122$ scheme in the *well-resolved* wavenumber range $0 \leq \kappa/\pi \leq 0.55$. The prefactored interior 11-point stencil of Ashcroft & Zhang (2003), which is optimized to minimize the dissipation across the wavenumber range, is the closest to the abscissa of Fig. 3.28(b) among the three prefactored interior 11-point stencils.

Figure 3.28(c) reports the relative error from eq. (2.11) for the three prefactored interior 11-point stencil schemes. The continuous lines represent the dispersive error of the interior sixth-order $C1122$ compact scheme of eq. (3.36) and of the fourth-order three-point prefactored compact scheme of Ashcroft & Zhang (2003). The dispersive error of the prefactored interior 11-point stencil of Hixon (2000), shown by the (−−) line, follows that of the interior sixth-order $C1122$ compact scheme up to the error level 10^{-7}, where the dispersive error becomes constant due to the single precision of the coefficients in Hixon (2000). The prefactored interior 11-point stencil of Ashcroft & Zhang (2003), shown by the (− · ·−) line, has a trough at $N_\lambda = 4.3$, which is very close to the corresponding trough of the interior compact scheme of Ashcroft & Zhang (2003) denoted by (—□—). For $N_\lambda \geq 4.3$, the prefactored interior 11-point stencil of Ashcroft & Zhang (2003) follows the fourth-order dispersive error roll-off of its corresponding interior scheme. The dispersive error of the prefactored 11-point stencil of eq. (3.51a) follows the dispersive error of the prefactored interior 11-point stencil of Hixon

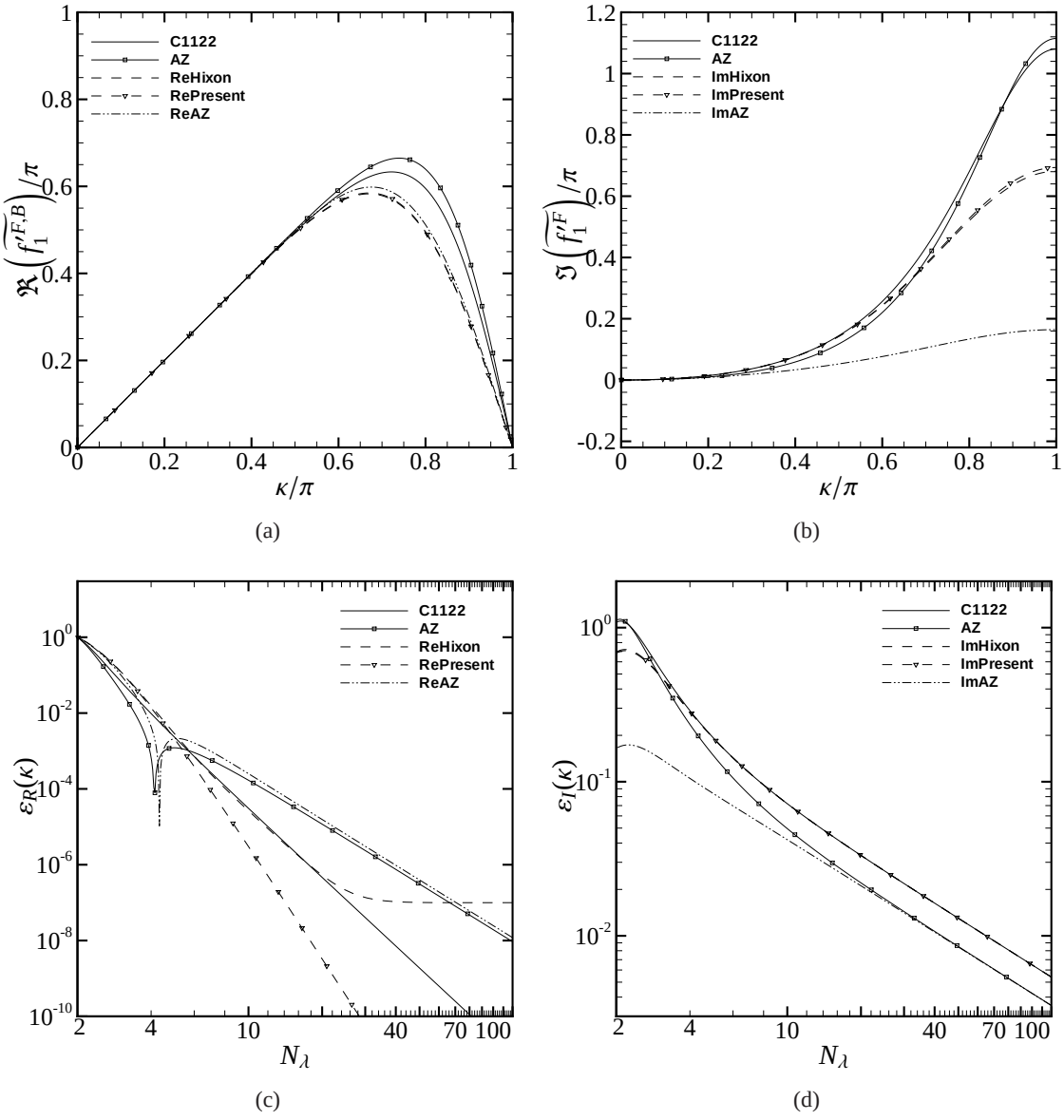

Figure 3.28: Dispersive characteristics of the forward prefactored interior 11-point stencils for *i*-th node. (a) Real and (b) imaginary components of the Fourier transform. (c) Dispersive error from eq. (2.11). (d) Dissipative error from eq. (2.12).

(2000) in the range of *poorly-resolved* wavenumbers up to $N_\lambda = 4$. For $N_\lambda > 4$, the scheme of eq. (3.51a) has the lowest dispersive error among the prefactored interior 11-point stencil schemes. This is due to the eleventh formal order of accuracy of eq. (3.51a), which is higher than the ninth and fourth-order closures used by Hixon (2000) and by Ashcroft & Zhang (2003). The optimization of the prefactored interior 11-point stencil followed by Hixon (2000) and Ashcroft & Zhang (2003) aims to match the dispersive error of the prefactored interior 11-point stencil with the corresponding interior scheme. The cost-optimization process of Sec. 3.2.3 modifies the dispersive error of the interior cost-optimized schemes, as shown in Fig. 3.11(b), with a single trough at different values of N_λ that are function of the epsm$n$ level of error (with $n = 3,4,5$). Therefore, it was elected to couple the cost-optimized scheme with a prefactored interior 11-point stencil scheme that has the lowest dispersive error for this stencil across the *well-resolved* wavenumber range.

Figure 3.28(d) shows the dissipative error from eq. (2.12) for the three prefactored interior 11-point stencil scheme, showed by the dashed and dashed-dotted lines. The continuous lines display the dissipative error of the interior sixth-order $C1122$ compact scheme of eq. (3.36) and of the fourth-order three-point prefactored compact scheme of Ashcroft & Zhang (2003). The dissipative error of the prefactored interior 11-point stencil of eq. (3.51a) is essentially the same as the one from the prefactored interior 11-point stencil of Hixon (2000), as shown by dashed lines overlapping in Fig. 3.28(d). Both schemes follow the dissipation error of the interior sixth-order $C1122$ scheme for $N_\lambda \geq 4$. The prefactored interior 11-point stencil scheme of Ashcroft & Zhang (2003) shows the lowest dissipative error across the whole wavenumber range. It follows the dissipation error of the corresponding interior scheme for *well-resolved* waves. Figures 3.28(c) and 3.28(d) show that the prefactored interior 11-point stencil of eq. (3.51a) has reduced the dispersive error in the *well-resolved* wavenumber range with respect to same stencil-size schemes in the literature, without introducing any appreciable additional dissipation.

Whereas the current formulation is satisfactory for the purpose of modelling the flow and noise in the test cases of Chapter 5, there is scope for further work to improve the spectral match between the interior implicit scheme of eq. (3.36) and the prefactored forward interior eleven-point stencil of eq. (3.57a) and (3.57b). The Fourier series of eq. (3.57a) and (3.57b) can be Padè transformed into rational functions, to match the rational function form of eq. (3.36).

Prior to the application to the test-cases of Chapter 5, the numerical stability of the cost-optimized schemes combined with the boundary closures is analysed in Sec 3.5.2.

3.5.2 Eigenvalue analysis

An eigenvalue analysis has been performed to verify under which conditions the prefactored cost-optimized schemes of Sec. 3.2.4 coupled with the boundary closures of Sec. 3.5.1 generate a numerically stable algorithm. This work follows the analysis by Lele (1992) as extended to prefactored schemes by Ashcroft & Zhang (2003). Firstly, the eigenvalue analysis is performed on the classical and the cost-optimized $C1122$ interior schemes of eq. (3.24), with the boundary closure of eq. (A.88). This analysis is reported in Appendix A.4. Then, the eigenvalue analysis is carried out on the prefactored counterpart schemes of eqs. (3.33) and (3.34) coupled with the boundary closure of eqs. (3.47) and (3.48). This stability analysis of the semi-discrete form of eq. (2.13) is based on the method of lines (Hirsch, 2007).

Consider the *LAE* of eq. (2.13) over the domain $0 \leq x \leq 1$ with a prescribed inflow boundary condition $u(0,t) = g(t)$. For the purpose of this stability analysis, $g(t)$ can be set to zero without loss of generality (Carpenter *et al.*, 1993a). The domain is discretised into N uniform intervals ($N+1$ nodes) of width $\Delta x = 1/N$. Imposing the boundary condition at the $i = 0$ node leads to N unknowns to be found ($i = 1, \cdots, N$). The spatial derivative $\dfrac{\partial u}{\partial x}$ of eq. (2.13) is evaluated by the prefactored finite difference approximation of eq. (3.32). This linear operator may be formally written in matrix form as

$$\mathbf{A}^F \, \mathbf{u'}^F = \frac{1}{h} \mathbf{B}^F \, \mathbf{u}, \tag{3.59a}$$

$$\mathbf{A}^B \, \mathbf{u'}^B = \frac{1}{h} \mathbf{B}^B \, \mathbf{u}, \tag{3.59b}$$

where $\mathbf{u}$, $\mathbf{u'^F}$ and $\mathbf{u'^B}$ are N-dimensional vectors representing, respectively, the values of the function and its prefactored finite difference approximation at the nodes $x_i = i/N$

$$\mathbf{u} = (u_1, u_2, \cdots, u_{N-1}, u_N)^T, \quad \mathbf{u'^F} = \left(u'^F_1, u'^F_2, \cdots, u'^F_{N-1}, u'^F_N\right)^T, \quad \mathbf{u'^B} = \left(u'^B_1, u'^B_2, \cdots, u'^B_{N-1}, u'^B_N\right)^T \tag{3.60}$$

and $\mathbf{A}^F$, $\mathbf{A}^B$, $\mathbf{B}^F$, $\mathbf{B}^B$ are $N \times N$ squared matrices. The system of equations (3.59) is applied at nodes $i = 1$ to N.

Substituting eq. (3.59a) and (3.59b) to eq. (2.13) yields to a system of *ODEs* which may be written as

$$\frac{d\mathbf{u}}{dt} = -\frac{c}{h} \mathbf{M} \, \mathbf{u}, \tag{3.61}$$

where $\mathbf{M}$ is an $N \times N$ matrix, which is determined from linear algebra.
Specifically, through the application of the boundary condition $g(t) = 0$, the forward matrices $\mathbf{A}^F$ and $\mathbf{B}^F$ are re-written as

$$\mathbf{A}^F = \begin{pmatrix} \beta_F & \alpha_F & 0 & \cdots & 0 & 0 \\ 0 & \beta_F & \alpha_F & 0 & \cdots & 0 \\ \vdots & \ddots & \ddots & \ddots & \vdots & \vdots \\ 0 & \cdots & 0 & \beta_F & \alpha_F & 0 \\ 0 & 0 & \cdots & 0 & \beta_F & \alpha_F \\ 0 & 0 & 0 & \cdots & 0 & 1 \end{pmatrix}, \quad \mathbf{B}^F = \begin{pmatrix} c_F & b_F & 0 & 0 & \cdots & \cdots & 0 \\ d_F & c_F & b_F & 0 & \cdots & \cdots & 0 \\ \vdots & \ddots & \ddots & \ddots & \ddots & \vdots & 0 \\ \vdots & \ddots & \ddots & \ddots & \ddots & \vdots & 0 \\ 0 & \cdots & 0 & d_F & c_F & b_F & 0 \\ 0 & 0 & \cdots & 0 & d_F & c_F & b_F \\ 0 & \cdots & -s_7 & \cdots & -s_3 & -s_2 & -s_1 \end{pmatrix}. \tag{3.62}$$

Similarly, the backward matrices $\mathbf{A}^B$ and $\mathbf{B}^B$ are

$$\mathbf{A}^B = \begin{pmatrix} \beta_B & 0 & 0 & \cdots & 0 & 0 \\ \gamma_B & \beta_B & 0 & 0 & \cdots & 0 \\ 0 & \ddots & \ddots & \ddots & \vdots & \vdots \\ 0 & 0 & \gamma_B & \beta_B & 0 & 0 \\ 0 & 0 & \cdots & \gamma_B & \beta_B & 0 \\ 0 & 0 & 0 & \cdots & 0 & 1 \end{pmatrix}, \quad \mathbf{B}^B = \begin{pmatrix} s_2^* & s_3^* & \cdots & s_7^* & \cdots & \cdots & 0 \\ d_B & c_B & b_B & 0 & \cdots & \cdots & 0 \\ 0 & \ddots & \ddots & \ddots & \ddots & \vdots & 0 \\ 0 & \ddots & \ddots & \ddots & \ddots & \vdots & 0 \\ 0 & 0 & 0 & d_B & c_B & b_B & 0 \\ 0 & \cdots & 0 & 0 & d_B & c_B & b_B \\ 0 & \cdots & e_{N-6} & \cdots & e_{N-2} & e_{N-1} & e_N \end{pmatrix} \tag{3.63}$$

where the coefficients s_i^* are

$$s_2^* = -\gamma_B (s_2 + c_B);\ s_3^* = -\gamma_B (s_3 + b_B);\ s_4^* = -\gamma_B s_4;\ s_5^* = -\gamma_B s_5;\ s_6^* = -\gamma_B s_6;\ s_7^* = -\gamma_B s_7. \tag{3.64}$$

The top row of the $\mathbf{B}^B$ matrix has been rearranged to eliminate $u_0'^B$, which is defined by the boundary condition on u_0, $g(t) = 0$ as detailed in Appendix A.4.
Using Eq. (3.32), $\mathbf{u}'$ may be expressed as:

$$\mathbf{u}' = \frac{1}{2}\left(\mathbf{u}'^F + \mathbf{u}'^B\right) = \frac{1}{2h}\left(\left(\mathbf{A}^F\right)^{-1}\mathbf{B}^F + \left(\mathbf{A}^B\right)^{-1}\mathbf{B}^B\right)\mathbf{u}, \tag{3.65}$$

from which

$$\mathbf{M} = \frac{1}{2}\left(\left(\mathbf{A}^F\right)^{-1}\mathbf{B}^F + \left(\mathbf{A}^B\right)^{-1}\mathbf{B}^B\right). \tag{3.66}$$

Since eq. (3.61) is a system of ODE's in time with constant coefficients, it admits as solution ortho-normal modes $\mathbf{u} = e^{st}\tilde{\mathbf{u}}$, with a constant s representing the rate of decay or amplification of the modes. Substituting $\mathbf{u} = e^{st}\tilde{\mathbf{u}}$ into eq. (3.61) leads to an eigenvalue problem

$$\tilde{\mathbf{u}} = -s^*\mathbf{M}\,\tilde{\mathbf{u}}, \tag{3.67}$$

where $s^* = \dfrac{c}{s\,h}$ is the dimensionless eigenvalue and $\tilde{\mathbf{u}}$ becomes the corresponding eigenvector. The eigenvalue s is in general complex and it depends on the size N of the matrix $\mathbf{M}$, the interior scheme, and the boundary closures. The matrix $\mathbf{M}$ is, in general, non-symmetric. To numerically determine its eigenvalues, a balancing procedure is firstly applied to reduce the norm of $\mathbf{M}$. Then, the matrix $\mathbf{M}$ is converted into its Hessenberg form, suitable for the *QR* transformation that gives the complex eigenvalues (Press & Firm, 1996).

The real parts of the eigenvalues are required to be equal or less than zero to guarantee the numerical stability of the interior scheme coupled with the boundary closure, i.e. $|e^{st}| \leq 1$.

Figure 3.29 plots the Laplace plane or eigenvalue spectrum s^*, which is the root-locus of the combined scheme. The effect of the boundary closures on the eigenvalue spectrum s^* for the classical Padè $C1111$ interior scheme, that is $\alpha_1 = 1/4$ in eq. (3.24), is reported. Figure 3.29 reproduces the results of Lele (1992).

Figure 3.30 presents the plot in the Laplace plane for $C1122$ classical sixth-order scheme and the cost-optimized $C1122$epsm5, $C1122$epsm4, $C1122$epsm3 schemes. They are coupled with a fourth-order non-centered compact $C4$ boundary closure at the $i = 1$ and $i = N$ mesh nodes, and a fifth-order non-centered compact $C5$ boundary scheme at the $i = 2$ and $i = N - 1$ mesh nodes, as detailed in eq. (A.88). The combined schemes are asymptotically stable (Carpenter *et al.*, 1993a), that is $\Re\,(s^*) \leq 0$ for all the value of N considered.

Figure 3.31 shows the eigenvalue spectrum s^* for the fourth-order prefactored compact $C1122$ scheme of Ashcroft & Zhang (2003) coupled with a three-point, fourth-order boundary stencil. Figure 3.31 shows that the combined is asymptotically stable. This plot matches the results of Ashcroft & Zhang (2003).

Figure 3.33(a) shows the eigenvalue spectrum s^* of the classical $C1122$ prefactored compact scheme of eqs. (3.33) and (3.34) coupled with the prefactored one-sided boundary stencils of eqs. (3.47) and (3.48). It is shown that the most of the eigenvalues are located in the left half

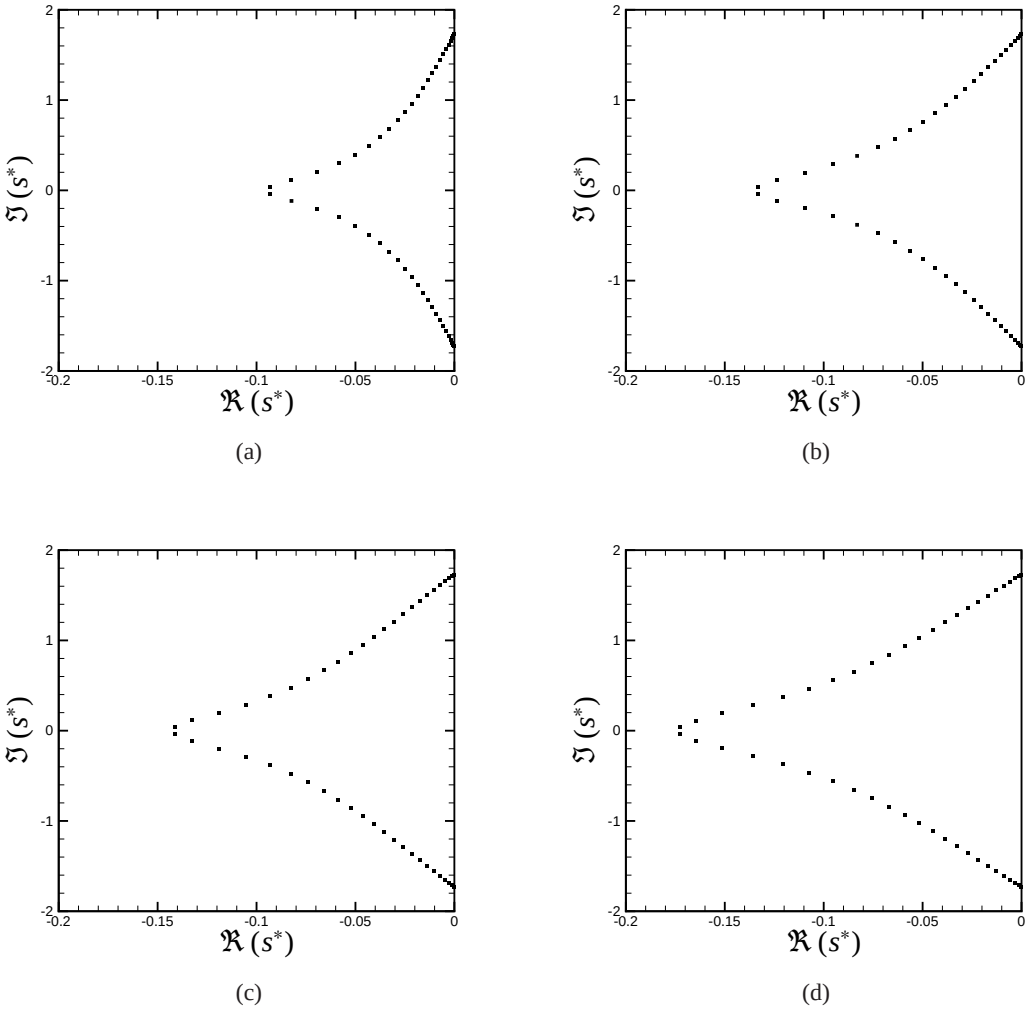

Figure 3.29: Effect of boundary closures of eq. (A.88) on the eigenvalue spectrum s^* for the classical Padè $C1111$ scheme ($\alpha_1 = 1/4$ in eq. (3.24)). $N = 49$. (a) First-order explicit scheme $E1$ at the boundaries. (b) Second-order explicit scheme $E2$ at the boundaries. (c) Second-order compact scheme $C2$ at the boundaries ($\alpha_{12} = 1$). (d) Third-order compact scheme $C3$ at the boundaries ($\alpha_{12} = 2$).

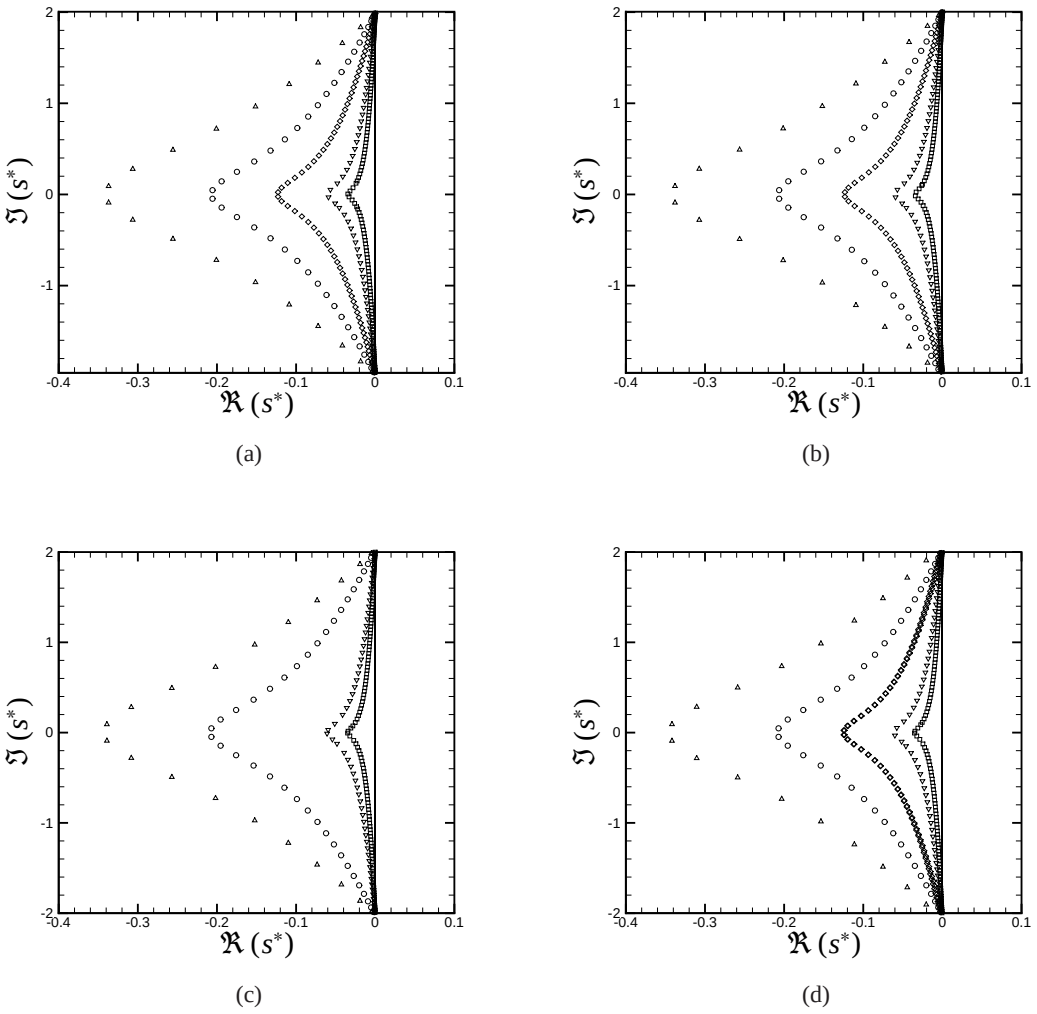

Figure 3.30: Eigenvalue spectrum for the classical $C1122$ scheme and the cost-optimized $C12\text{epsm}n$ schemes, with $n = 5, 4, 3$. ($\triangle$) $N = 21$, ($\circ$) $N = 41$, ($\diamond$) $N = 81$, ($\triangledown$) $N = 201$, ($\square$) $N = 401$ (a) $C1122$ (Carpenter *et al.*, 1993a). (b) $C1122\text{epsm}5$. (c) $C1122\text{epsm}4$. (d) $C1122\text{epsm}3$.

of the complex plane. However, some of them marginally cross the y-axis on the positive side. In particular, an eigenvalues pair acts as poles at the position $s^*_{1,2} \simeq (0.157, \pm 1.4)$. A similar behaviour is reported by Figs. 3.33(b), 3.33(c) and 3.33(d), which show the eigenvalue spectrum for the cost-optimized $C1122\mathsf{epsm}n$ (with $n = 5, 4, 3$) interior schemes, coupled with the same prefactored one-sided boundary stencils of eqs. (3.47) and (3.48). Table 3.8 reports the real parts of the first two pairs of positive eigenvalues $s^*_{1,2}$ and $s^*_{3,4}$ from eq. (3.67), obtained by varying the number of nodes N for the classical prefactored $C1122$ and the cost-optimized $C1122\mathsf{epsm}5$, $C1122\mathsf{epsm}4$ and $C1122\mathsf{epsm}3$ interior schemes. It is shown that the orders of magnitude of the real parts of the eigenvalue pair $s^*_{3,4}$ are relatively small and they tend to zero as the number of nodes N increases. As the number of nodes N becomes larger, the real parts of the eigenvalue pairs $s^*_{1,2}$ asymptotes to the constant value. It turns out that those components with real part are neutrally stable in practice and they do not cause any instabilities in the actual computations (Kim, 2007), as reported in Chapters 5. For reference, Fig. 3.32 shows the classical $C1122$ prefactored scheme coupled with the four points, third-order one-sided boundary stencils of Ashcroft & Zhang (2003). With such boundary stencils, the combined scheme results to be asymptotically stable.

This eigenvalue analysis has shown that the cost-optimized prefactored compact scheme coupled with the selected boundary closures are conditionally stable. These schemes, in coincidence with their application to the selected aeroacoustic problems, are reported in Chapters 5.

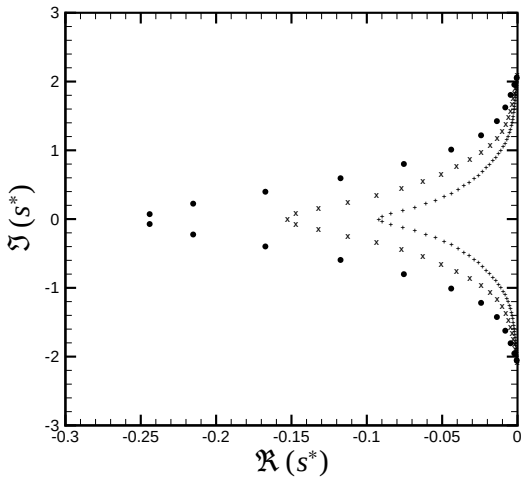

Figure 3.31: Eigenvalue spectrum for the fourth-order prefactored compact $C1122$ scheme of Ashcroft & Zhang (2003) coupled with third-order boundary closure: (•) $N = 26$; (X) $N = 51$; (+) $N = 101$.

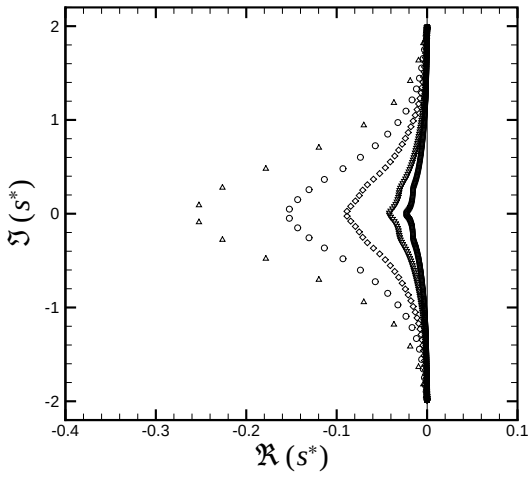

Figure 3.32: Eigenvalue spectrum for the prefactored classical $C1122$ scheme coupled with the four points, third-order one-sided boundary stencils of Ashcroft & Zhang (2003): (△) $N = 21$, (○) $N = 41$, (⋄) $N = 81$, (▽) $N = 201$, (□) $N = 401$.

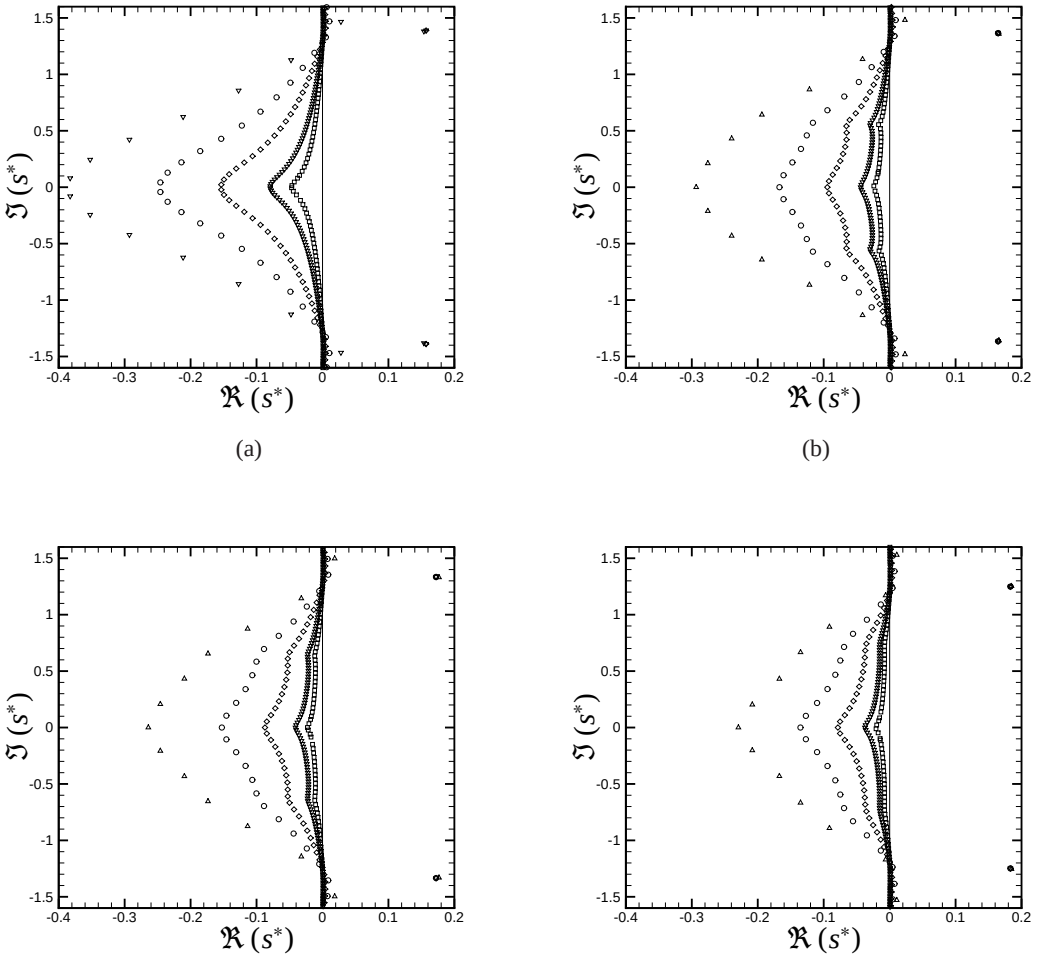

Figure 3.33: Eigenvalue spectrum for the prefactored classical $C1122$ scheme and the cost-optimized $C12\mathsf{epsm}n$ schemes with $n = 5, 4, 3$. ($\triangle$) $N = 21$, ($\circ$) $N = 41$, ($\diamond$) $N = 81$, ($\triangledown$) $N = 201$, ($\square$) $N = 401$. (a) $C1122$, (b) $C1122\mathsf{epsm}5$, (c) $C1122\mathsf{epsm}4$, (d) $C1122\mathsf{epsm}3$.

$C1122$ ($\alpha_1 = 1/3$)	N	$\Re\left(s^*_{1,2}\right)$	$\Re\left(s^*_{3,4}\right)$
	21	0.153812	0.0279661
	41	0.157185	0.0104212
	81	0.157096	0.00467175
	201	0.157096	0.00179513
	401	0.157096	0.000881983
$C1122$epsm5 ($\alpha_1 = 0.33750$)			
	21	0.165735	0.0232195
	41	0.16442	0.0091237
	81	0.164442	0.00452301
	201	0.164442	0.00168956
	401	0.164442	0.000831262
$C1122$epsm4 ($\alpha_1 = 0.34240$)			
	21	0.176703	0.00185276
	41	0.172182	0.00869214
	81	0.172233	0.00408224
	201	0.172233	0.0015743
	401	0.172233	0.000771996
$C1122$epsm3 ($\alpha_1 = 0.3532$)			
	21	0.184775	0.0010779
	41	0.183112	0.00732721
	81	0.183141	0.00347811
	201	0.183141	0.00131947
	401	0.183141	0.000648061

Table 3.8: Real part of the first two positive eigenvalue pairs $s^*_{1,2}$ and $s^*_{3,4}$ from eq. (3.67) for different number of nodes N. Classical prefactored $C1122$, cost-optimized $C1122$epsm5, $C1122$epsm4 and $C1122$epsm3 interior schemes.

3.6 Artificial Boundary Conditions

3.6.1 Characteristic based boundary conditions

The behaviour of a multi-dimensional prefactored compact finite difference method at the computational domain boundaries can be assessed in the context of the simpler problem of the one-dimensional advection dominated flow, in characteristic form. Recall the characteristic form of the governing LEE of eqs. (3.22) and (3.23) in Sec. 3.1.2.2. Under the one-dimensional x-direction flow approximation, at an orthonormal computational boundary $\frac{\partial \mathbf{U}^*}{\partial y^*} = 0$, the system of eqs. (3.23) simplifies into a set of Local One-Dimensional Inviscid (LODI) equations (Poinsot & Lele, 1992)

$$\frac{\partial \rho^*}{\partial t^*} + \left[L_2 + \frac{1}{2}(L_1 + L_4) \right] = 0 \tag{3.68a}$$

$$\frac{\partial u^*}{\partial t^*} + \left[\frac{1}{2}(L_4 - L_1) \right] = 0 \tag{3.68b}$$

$$\frac{\partial v^*}{\partial t^*} + L_3 = 0 \tag{3.68c}$$

$$\frac{\partial p^*}{\partial t^*} + \left[\frac{1}{2}(L_4 + L_1) \right] = 0. \tag{3.68d}$$

Equation (3.68) states the LODI system in the x-direction. Appendix A states the LODI system in the y-direction, where the term $B_0^* \frac{\partial \mathbf{U}^*}{\partial y^*}$ in the system of eq. (3.11) is replaced by the characteristic wave amplitude variations L_i estimated for the y-direction. Comparing the LEE of eq. (3.68) with the system of equations reported by Colonius (2004), the two set of equations coincide under the assumption that the characteristic wave L_2 is set to zero.

The treatment of corners in a two-dimensional domain requires an extension of the LODI procedure. Like any other formulation, the LODI approach for corners in a two-dimensional domain and edges in a three-dimensional domain requires some compatibility conditions to be satisfied at these locations. A general definition for all the possible combinations of boundary conditions at corners and edges is not available and appears to be even more difficult than the usual studies of well-posedness, as reported by Colonius (2004).

The LODI system of eqs. (3.68) is used to close the system of algebraic equations at the computational domain boundaries. At the computational domain boundaries, the LODI system of eqs. (3.68) is solved with the interior scheme of the system of eqs. (3.23) to predict the flow. The LODI relations of eqs. (3.17) are first used to estimate the wave amplitude variations L_i.

Then, the value of the flow state at the boundaries as well as at the computational domain interior is time-advanced by integrating the system of eqs. (3.22), starting from a known flow state at $t = 0$ (Thompson, 1987, 1990).

Most physical boundary conditions have a counterpart LODI relation. This is obtained by setting the amplitude of the characteristics waves L_i in the system of eqs. (3.22) according to the following condition. If the characteristic velocity λ_i points out the computational domain, the corresponding L_i is computed from the definition of eqs. (3.17), using one-sided derivative approximations of eqs. (3.47) and (3.48). Else, if λ_i points into the computational domain, L_i is specified from the boundary conditions.

The following Secs 3.6.1.1, 3.6.1.2, 3.6.1.3 report three examples of LODI implementation, respectively: subsonic inflow, subsonic outflow and inviscid wall. These boundary closures are used in the test-cases of Chapter 5. The LODI implementation for supersonic case is reported by Lele (1992).

3.6.1.1 Subsonic inflow

Figure 3.34 sketches a computational domain bounded by a and b, $a \leq x \leq b$, with a prescribed subsonic inflow boundary condition at the computational domain boundaries $x = a$ and $x = b$. This computational domain, having only inflow boundaries, is not intended to represent a physical flow but only to support the current description of the subsonic inflow boundary condition. In these domain, the corresponding directions of the characteristic velocities λ_i are shown in Fig. 3.34 and their values are

$$x = a \quad 0 < M_x < 1 \quad \lambda_1 = M_x - 1 < 0 \quad \lambda_2 = \lambda_3 = M_x > 0 \quad \lambda_4 = M_x + 1 > 0, \tag{3.69a}$$

$$x = b \quad -1 < M_x < 0 \quad \lambda_1 = M_x - 1 < 0 \quad \lambda_2 = \lambda_3 = M_x < 0 \quad \lambda_4 = M_x + 1 > 0. \tag{3.69b}$$

At the computational domain boundary $x = a$, the characteristic velocity λ_1 and the corresponding left going acoustic wave L_1 points out the computational domain. L_1 is an *outgoing wave* and it is computed by the one-sided derivative approximation of eqs. (3.47) and (3.48). The characteristic velocities λ_2, λ_3 and λ_4 are pointing into the computational domain and the corresponding $L_i's$ are *incoming waves*. Their amplitude is set to zero, that is $L_2 = L_3 = L_4 = 0$. At the computational domain boundary $x = b$, the characteristic velocities λ_1, λ_2, λ_3 and the corresponding characteristics waves $L_i's$ point into the computational domain. They are *incoming waves* and their amplitude is set to zero, $L_1 = L_2 = L_3 = 0$. The characteristic velocity

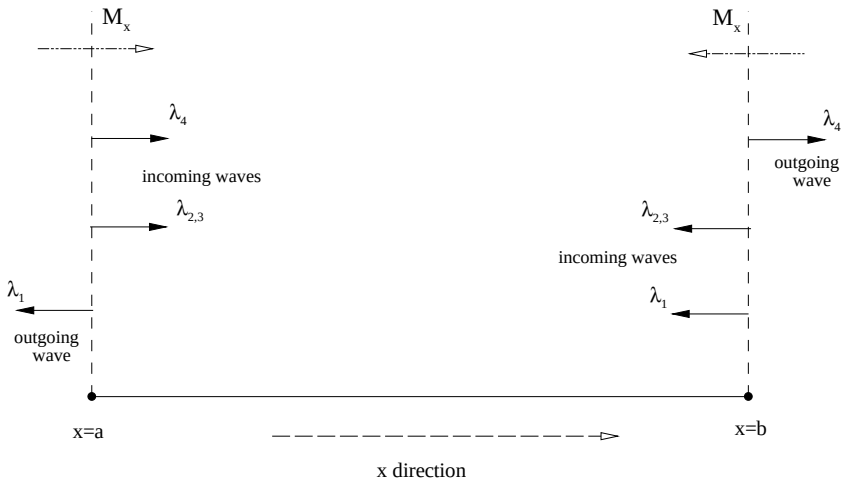

Figure 3.34: Characteristic velocities λ_i for subsonic inflow at $x = a$ and $x = b$.

λ_4 and the corresponding right going acoustic wave L_4 is pointing out the domain. L_4 is an *outgoing wave* and it is computed by the one-sided derivative approximation of eqs. (3.47) and (3.48).

3.6.1.2 Subsonic outflow

Figure 3.35 sketches a computational domain bounded by a and b, $a \leq x \leq b$, with a prescribed subsonic outflow boundary condition at the computational domain boundaries $x = a$ and $x = b$. This computational domain, having only outflow boundaries, is not intended to represent a physical flow but only to support the current description of the subsonic outflow boundary condition. In these domain, the corresponding directions of the characteristic velocities λ_i are shown in Fig. 3.35 and their values are

$$x = a \quad -1 < M_x < 0 \quad \lambda_1 = M_x - 1 < 0 \quad \lambda_2 = \lambda_3 = M_x < 0 \quad \lambda_4 = M_x + 1 > 0, \tag{3.70a}$$

$$x = b \quad 0 < M_x < 1 \quad \lambda_1 = M_x - 1 < 0 \quad \lambda_2 = \lambda_3 = M_x > 0 \quad \lambda_4 = M_x + 1 > 0. \tag{3.70b}$$

At the computational domain boundary $x = a$, the characteristic velocity λ_1, λ_2 and λ_3 and the corresponding characteristics waves $L_i's$ point out the computational domain. They are *outgoing waves* and they are computed by the one-sided derivative approximations of eqs. (3.47)

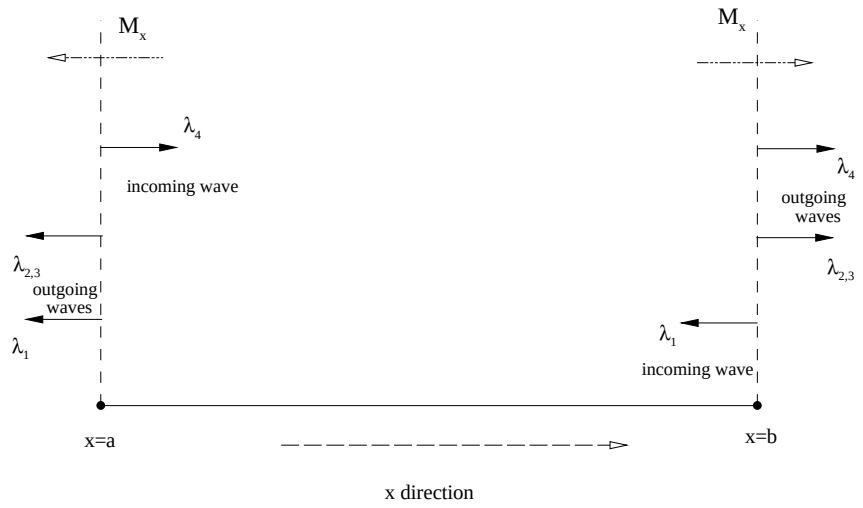

Figure 3.35: Characteristic velocities λ_i for subsonic outflow at $x = a$ and $x = b$.

and (3.48). The characteristic velocity λ_4 and the corresponding right going acoustic wave L_4 is pointing into the computational domain. L_4 is an *incoming wave* and its amplitude is set to zero, $L_4 = 0$.

At the computational domain boundary $x = b$, the characteristic velocity λ_1 and the corresponding left going acoustic wave L_1 point into the computational domain. L_1 is an *incoming wave* and its amplitude is set to zero, $L_1 = 0$. The characteristic velocities λ_2, λ_3 and λ_4 and the corresponding characteristic waves $L_i's$ point out the computational domain. They are *outgoing waves* and are computed by the one-sided derivative approximations of eqs. (3.47) and (3.48).

3.6.1.3 Inviscid wall

Figure 3.36 shows a computational domain bounded by a and b, $a \leq x \leq b$, with a subsonic inflow boundary condition at $x = a$ computational boundary, and an inviscid wall at $x = b$. Inside the domain the flow is quiescent. The values of the characteristics velocities λ_i at the computational boundary $x = b$ are

$$x = b \quad M_x = 0 \quad \lambda_1 = -1 < 0 \quad \lambda_2 = \lambda_3 = 0 \quad \lambda_4 = 1 > 0. \tag{3.71a}$$

Therefore, the characteristic velocities λ_2, λ_3 and the corresponding amplitude of the characteristic waves L_2 and L_3 are set to zero. The characteristic velocity λ_4 is equal to the non-

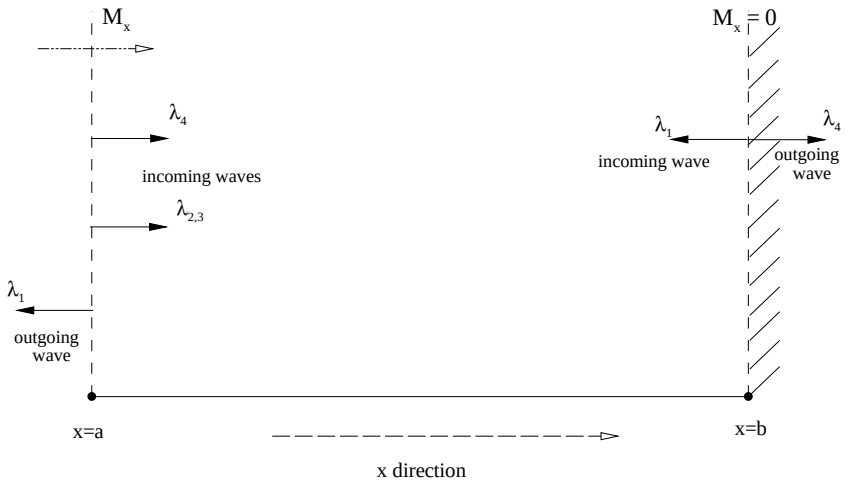

Figure 3.36: Characteristic velocities λ_i for a subsonic inflow at $x = a$ and an inviscid wall at $x = b$.

dimensional speed of sound and the corresponding right going acoustic wave L_4 points out the computational domain. L_4 is an *outgoing wave* and it is computed by the one-sided derivative approximation of eqs. (3.47) and (3.48). The characteristic velocity λ_1 is equal to the non-dimensional speed of sound too and it points into the computational domain. Its value is specified by the no-slip wall boundary condition, i.e. $u^* = v^* = 0$ and $\frac{\partial u^*}{\partial t^*} = 0$. By substituting these constraints in eq. (3.68b)

$$L_1 = L_4. \tag{3.72}$$

Equation (3.72) states that the amplitude of the left going acoustic *incoming wave* L_1 is set equal to the amplitude of the right going acoustic *outgoing wave* L_4. This means, physically, that the incoming wave is reflected back by the no-slip wall with the same amplitude.
Inviscid moving walls are useful boundary conditions in some computations. They are characterized by only one inviscid wall condition. In the case of non-zero wall normal velocity, the condition from eq. (3.68b) is

$$L_1 = L_4 + 2\frac{\partial u^*}{\partial t^*}. \tag{3.73}$$

Lodato *et al.* (2008) have extended the Navier-Stokes Characteristic Boundary Condition (NSCBC) to account for convection and pressure gradients in boundary planes, resulting in the 3D-NSCBC approach. This technique has shown significant reduction of flow distortion and

boundary reflection even when the configuration is characterized by high tridimensionality of the flow field, accompanied by obliquely propagating waves. This is the case of high-speed jet or shear flows, whereas the LODI relations make serious reflections without proper treatments or appropriate absorbing layers (Poinsot & Lele, 1992).

3.6.2 Absorbing layers

The present numerical scheme is designed to provide low dispersion and dissipation errors. Therefore, any inconsistency due to the numerical treatment at the computational boundaries will introduce errors or spurious wave reflections in the computation, which will eventually degrade the solution. To overcome this problem, an absorbing layer is introduced in the numerical model to enhance the efficacy of the Artificial Boundary Conditions. In this region, the governing equations are modified approaching the computational boundaries. These regions are referred in the literature as absorbing layers, fringe regions, or buffer zone. The absorbing layer concept was introduced by Israeli & Orszag (1981) in the context of modelling linear wave propagation problems. At that time, the technique they developed was motivated by difficulties in formulating a local non-reflecting boundary condition for the linearized wave propagation problem. Recent advancements of finite-thickness boundary treatments with non-reflecting properties are reported by Colonius (2004). Some of this development make use of absorbing layers for both linear and non-linear unsteady computations.

Absorbing layer treatments typically damp disturbances before the interact with an Artificial Boundary Condition. A simple way to do this is either by introducing artificial dissipation by upwinding (Lockard *et al.*, 1995; Zhuang & Chen, 1998), or by increasing the value of the fluid viscosity, or by adding an eddy viscosity (Tam *et al.*, 1993), or by adding a linear friction coefficient to the governing equations (Richards *et al.*, 2004).

The absorbing layer technique is relatively easy to implement in a computational scheme, but the inclusion of artificial damping within the absorbing layer means that the solution is locally non-physical. The absorbing layer is itself reflective and, without further modification, the only way to obtain a satisfactory result is to gradually increase the damping over a relatively long distance. This results in thick, computationally inefficient layers (Colonius, 2004). Alternative techniques to the absorbing layer are Asymptotic Expansion Method (Tam & Web, 1993) and Perfectly Matched Layer (Hu, 1996).

In the present work, two absorbing layer variants are analysed. The first one, referred as *Type* I

AL (Absorbing Layer), is a technique by Richards *et al.* (2004) that directly forces the solution to a target flow state within the absorbing layer. The second one, labelled as *Type* II *AL*, is a zonal characteristic based boundary condition proposed by Sandberg & Sandham (2006).

3.6.2.1 *Type* I Absorbing layer

In the *Type* I *AL*, the absorbing layer is a computational domain enclosing the physical domain in which damping is directly applied to the numerical solution vector **U** after each time step

$$\mathbf{U}^{n+1} = \overline{\mathbf{U}^{n+1}} - g(x)\left(\overline{\mathbf{U}^{n+1}} - \mathbf{U}_{target}\right), \tag{3.74}$$

where $\overline{\mathbf{U}^{n+1}}$ is the numerical solution vector after each time step and $\mathbf{U}_{target}$ is a given reference flow state. The damping coefficient $g(x)$ is defined as

$$g(x) = \alpha_2 \left|1 - \frac{w - x}{w}\right|^{\beta_1}, \tag{3.75}$$

where x is the distance from the inner boundary of the absorbing layer and w is the absorbing layer width, as sketched in Fig. 3.37. Parameters α_2 and β_1 are used to determine the shape of the damping coefficient $g(x)$. The damping coefficient $g(x)$ is set to zero at $x = 0$, which is the interface between the absorbing layer and the computational domain interior. Full damping is applied at $x = w$, at the outer edge of the buffer zone to damp the target solution. Within the absorbing layer, the damping coefficient $g(x)$ is varied smoothly to minimize possible reflections. In this way, the numerical solution vector $\mathbf{U}^{n+1}$ is gradually changed towards the set target value $\mathbf{U}_{target}$ at the outer edge of buffer zone, at $x = w$. At an outflow computational domain boundary $\mathbf{U}_{target}$ is set to the mean flow value.
Setting a target value for the numerical solution vector $\overline{\mathbf{U}^{n+1}}$ is the non-reflecting criterion upon which absorbing layer boundary conditions work. This type of absorbing layer approach generally involves coefficients that are flow-dependent and assume prior knowledge of the size of the flow structure to be damped.

3.6.2.2 *Type* II Absorbing layer

Sandberg & Sandham (2006) proposed to extend the LODI sytem of Sec. 3.1.2.2 from a boundary plane to a zone of finite thickness. The characteristic velocities λ_i and the corresponding

amplitudes of the characteristic waves $L_i's$ are computed within a specific absorbing layer. If L_i is an *outgoing wave*, its amplitude is computed by the one-sided derivative approximations of eqs. (3.47) and (3.48), and it is left unchanged within this region. Else, if L_i is an *incoming wave*, its amplitude is gradually ramped to zero at the outer edge of the buffer zone according to

$$\tilde{L}_i = s(x) \cdot L_i, \qquad s(x) = 0.5\left[1 + \cos\left(\frac{\pi\, x}{w}\right)\right]. \tag{3.76}$$

Figure 3.37 sketches an outflow absorbing layer at the computational domain boundary $x = b$. The characteristic velocities λ_i and the corresponding characteristic waves $L_i's$ are reported in eq. (3.70b). At the computational domain boundary $x = b$, the characteristic velocity λ_1 of the corresponding left going acoustic wave L_1 points into the computational domain. L_1 is an *incoming wave* and its amplitude is ramped to zero according to eq. (3.76) within the absorbing layer. The characteristic velocities λ_2, λ_3 and λ_4 of the corresponding characteristic waves L_1, L_2 and L_3 point out the computational domain. L_1, L_2 and L_3 are *outgoing waves* and are computed by the one-sided derivative approximations of eqs. (3.47) and (3.48) and they are left unchanged within this region. The technique is extended to the inflow boundary condition by multiplying the amplitudes $L_i's$ of the *incoming waves* by a ramping function within a zone, as described for L_1 in the case of an outflow boundary condition.

In contrast to most other zonal approaches, this method is free of coefficients that require calibration. The only parameter to be set is the width of the buffer zone w.

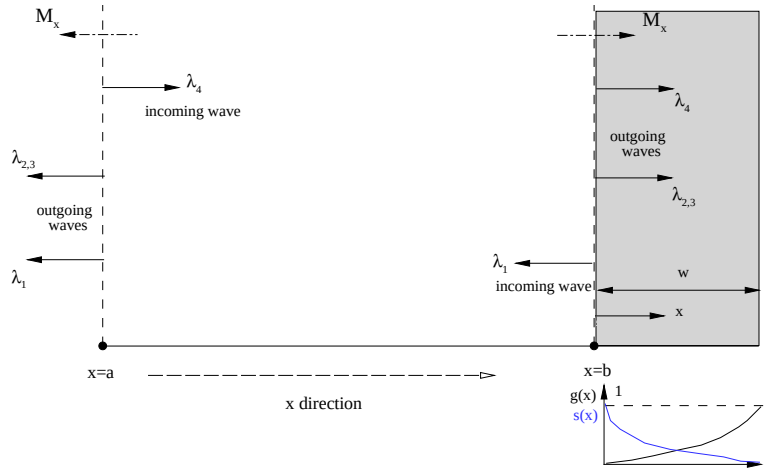

Figure 3.37: Sketch of the outflow absorbing layer at the computational domain boundary $x = b$.

3.7 Chapter summary and achievements

This chapter has presented the numerical method used in the present work.

Section 3.1 has reported the governing equations solved in the present study, that are the LAE and the LEE. The derivation of the LEE in non-dimensional and in characteristic form starting from the 2-D strong conservative form of the Euler equations has been reported.

Section 3.2 has introduced the spatial discretization method used. The most common finite-difference schemes used in CAA have been reviewed and compared in term of computational efficiency. The effect of the spatial discretization and the number of physical dimensions on the computational cost has been analysed. The spatial cost-optimization technique, based on the maximization of the spatial resolving efficiency $\check{\kappa}^*$ for a given value of normalized error $\tilde{\epsilon}$, has been presented. The cost-optimized schemes has been extended to the class of sixth-order prefactored compact schemes of Hixon (2000) and a new class of cost-optimized prefactored high-order compact scheme has been developed.

Section 3.3 has analysed the impact on the computational cost of using different time integration schemes for a two dimensional problem for various spatial discretization schemes. The temporal cost-optimization technique, based on the maximization of the temporal resolving efficiency $\check{z}^*$ for a given value of normalized error $\tilde{\epsilon}$, has been presented. A temporal stability and accuracy analysis has confirmed that the cost-optimization gives a small advantage in terms of temporal dissipation and dispersion properties of the resulting schemes.

Section 3.4 has shown the predicted performance of the combined space and time cost-optimization schemes for the same level of error. A computational advantage is predicted by using cost-optimized schemes to model wave propagation problems at their design operational point.

Section 3.5 has shown the effect of the perimetrical scheme on the interior scheme. Two methods of treating near-boundary points are presented and compared against the boundary treatments of Hixon (2000) and Ashcroft & Zhang (2003). The first approach is a prefactored sixth-order explicit one-sided finite-difference scheme that uses a seven-point stencil, the second is a prefactored explicit central scheme with an 11-point stencil. The wave propagation characteristics of these boundary closures have been examined. An new 11-point stencil with double precision accuracy has been derived, which has reduced the dispersive error in the *well-resolved* wavenumber range with respect to the same stencil-size schemes available in the literature, without introducing any appreciable additional dissipation.

An eigenvalue analysis has been performed and it has shown that the cost-optimized prefactored schemes coupled with the selected boundary closures are conditionally stable.
Section 3.6 details the artificial boundary conditions used in the present study. Three implementation of the LODI technique are shown: the subsonic inflow, the subsonic outflow and the inviscid wall. Two type of absorbing layer technique are discussed. The first one is the absorbing layer technique by Richards *et al.* (2004), that directly forces the solution to a target flow state within the absorbing layer. The second one is a zonal characteristic based boundary condition proposed by Sandberg & Sandham (2006).
The main achievements of this Chapter 3 are:

- The development of a new class of cost-optimized prefactored high-order compact schemes.
- The temporal stability and accuracy analysis has confirmed that the cost-optimization gives a small advantage in terms of temporal dissipation and dispersion properties of the resulting cost-optimized schemes.
- A computational advantage is predicted by using cost-optimized schemes to model wave propagation problems at their design operational point.
- The derivation of a prefactored interior 11-point stencil with double precision accuracy that has shown a better performance in spectral sense compared to the equivalent ones available in the literature.
- An eigenvalue analysis has been performed and it has shown that the cost-optimized prefactored schemes coupled with the selected boundary closures are conditionally stable.

Chapter 4

MPI single domain decomposition

4.1 Parallelization strategy

The compact finite-difference approximation of the spatial derivatives makes their parallelization challenging and non-trivial. The parallelization is achieved by domain decomposition, as shown in Fig. 4.1 for a two-dimensional Cartesian domain. The x an y axes are divided, respectively, in m and n segments, to obtain a total of $m \times n$ blocks. This multi-block parallel computation uses one processor per block and the method of communication between adjacent blocks is by finite-sized overlaps. At every time step, the solution is computed independently in each block with individual interior and boundary formulae as in single-block computations. The number of points in the interface overlap region is driven by the specific choice of the finite-difference approximation of the spatial derivative along the inter-block boundaries. This is estimated by the 11-point explicit prefactored interior boundary stencil of eq. (3.51), which gives a finite-sized overlap region of five points, as sketched in Fig. 4.1. The scheme has been tested to be stable and accurate on general curvilinear meshes and viscous flows (Ghillani, 2012).

The LEE in a two-dimensional Cartesian co-ordinate system of Sec. 3.1.2 are time-advanced using the explicit fourth-order RK time-marching schemes of Sec. 3.3. Datas are exchanged between adjacent blocks at the end of every RK stage. The structured mesh of the finite-sized overlap region gives an envelope of communication of constant size. This enables to use the MPI persistent calls, to speed up the communication (Message Passing Interface Forum, 2009).

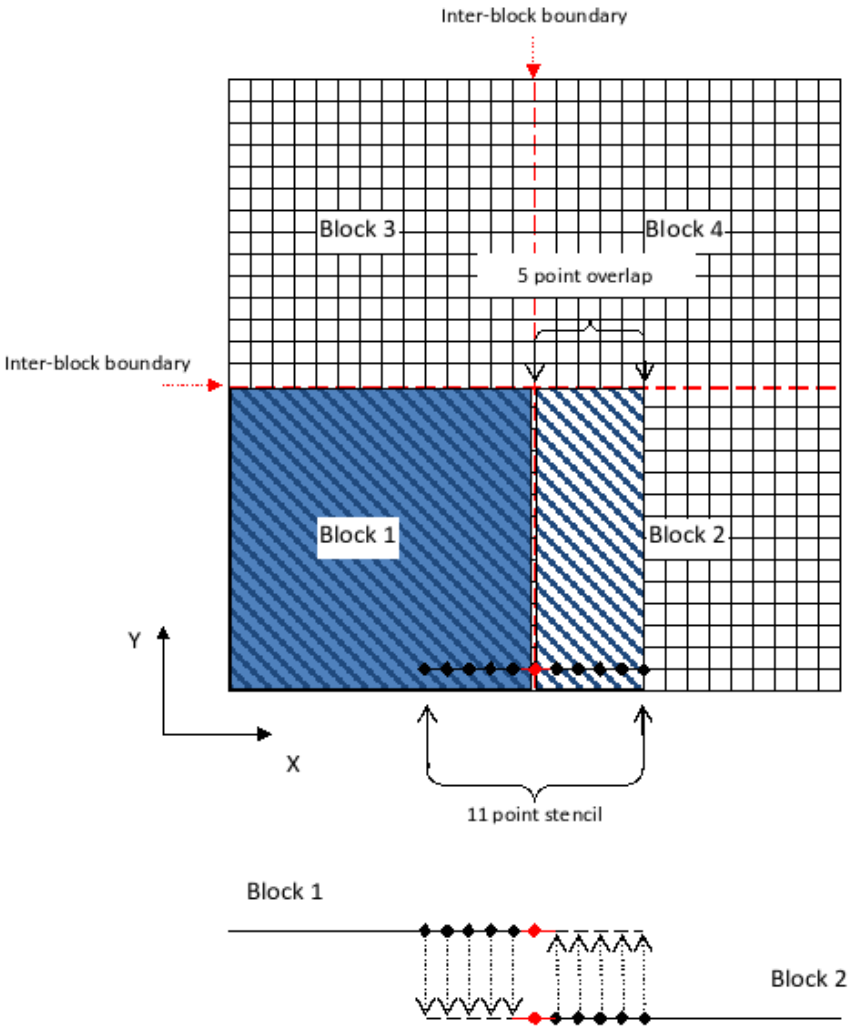

Figure 4.1: Domain decomposition and communication scheme with 4 blocks ($m = n = 2$).

4.2 Weak scalability tests

Weak scalability tests, that are the variation of the computational solution time with the number of processors p for a fixed problem size, have been carried out by using the propagation of an acoustic pulse in a two-dimensional unbounded domain of Sec. 5.2.1.

The classical $C1122$ scheme of eqs. (3.33) and (3.34) is used as interior prefactored scheme combined with the outflow LODI of Sec. 3.6.1 at the computational numerical boundaries. The classical $RK4$ scheme is used to time advance the numerical solution. Figure 4.2(a) shows the L_2 norm error of the non-dimensional density perturbation between the analytical and the numerical solutions of a two-dimensional acoustic pulse propagating in an unbounded do-

main (Hardin *et al.*, 1995), on progressively refined computational meshes (I. Spisso & Rona, 2009). The same results were obtained using the multi-block code with 4 and 16 blocks. The rate of the numerical error roll-off is parallel to the $-6\log(N)$ black dashed line, showing that the code preserves its design sixth-order accuracy with the inter-block boundaries.
The speed-up $= \frac{T_{ref}}{T_p}$, shown in Fig. 4.2(b), is defined as the ratio between T_{ref} the total time of execution (total wall clock time) using the minimum number of processors as reference ref, and T_p the time obtained using a greater number p of processors (or compute nodes). The speed-up varies among 0 and p. A value of p indicates an ideal value (linear scaling).
Figure 4.2(a) shows the computational speed-up versus the number of processors on the IBM $SP6$ cluster, with a number of processors as reference $ref = 4$, measured by instrumenting the code with system clock calls and SCALASCA (doc, Jülich SuperComputing Centre). The IBM SP6 cluster was in production in CINECA from September 2009 up to May 2012. The IBM SP6 cluster consisted of 168 Power6 575 compute nodes. Each node contained 32 cores with 128 GB of memory, with a peak performance of just over 100 Tflops (sp6, CINECA). The compiler used was the native `xlf` compiler of IBM with aggressive optimization using the following flags `FCFLAGS= -O3 -g -qarch=pwr6 -qtune=pwr6 -qmaxmem=-1 -qcache=auto -qhot=vector -qhot=simd -qenablevmx.`
The speed-up, shown in Fig. 4.2(a), indicates that the wall-clock time decreases almost linearly with the number of processors used, that is up to $p = 128$. This is possible because the MPI time per time step is a small fraction of the computational time and because the communication network of the SP6 used an Infiniband low latency high bandwidth network.

4.3 Further work

The MPI single domain decomposition described in the previous Sec. 4.1 has been implemented by finite-sized overlap. In the mesh point at the interface between two adjacent blocks, the approximation to the first derivative is evaluated with the 11-point explicit prefactored interior boundary stencil of eq. (3.51a) and (3.51b). In the interior points of the blocks, the compact prefactored classical $C1122$ and cost-optimized $C1122\mathsf{epsm}n$ schemes of eqs. (3.33) and (3.34) are used. By comparing the pseudo-wavenumber of the compact interior scheme of eq. (3.36) with the one of the 11-point explicit prefactored interior boundary stencil of eq. (3.57), a spectral mis-match is evident, due the approximation of a rational function in

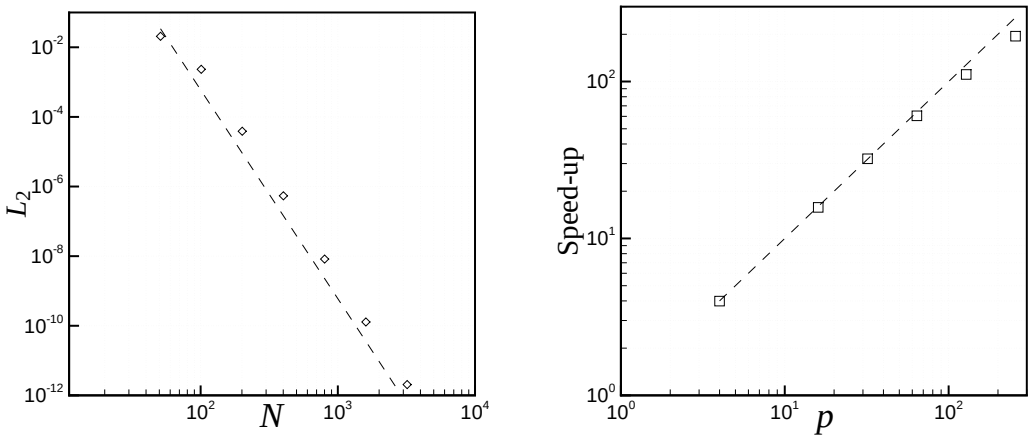

(a) Dashed line (−−) sixth-order logarithmic scale, black diamond (⋄) L_2 norm error from eq. (5.14).

(b) Speedup versus number of processors, computational domain with fixed total number of grid points (503×503).

Figure 4.2: Solution to test-case of Sec. 5.2.1 with the MPI domain decomposition.

eq. (3.36) with the Fourier series of eq. (3.57). The consequence of that mis-match is the introduction of an error on this parallelization strategy, which has not been revealed in the tests reported in Sec. 4.2.

An alternative approach to the use of the finite-sized overlap is the slab decomposition. Figure 4.3 shows that, with this parallelization strategy, the slice division is done for a given direction of parallelization. The solution is time-advanced in the single slices (or slabs) by using the boundary and interior formulation as in a serial job (Colonius, 2011). In this case, no error or approximation is introduced by the parallelization strategy. When the derivative in next direction has to be computed the data are transposed by using the the `MPI_AlltoAll` directives to transpose the data (Message Passing Interface Forum, 2009). For the extension to three dimensional space in HPC clusters, the parallel performance of the code can take advantage of the new 2D pencil domain decomposition already implemented in the 2DECOMP&FFT library, a software framework in Fortran to build large-scale parallel applications. It is designed for applications using three-dimensional structured mesh and spatially implicit numerical algorithms. This library is optimised for supercomputers and scales well to hundreds of thousands of cores (Guarrasi *et al.*, 2013; Li & Laizet, 2010).

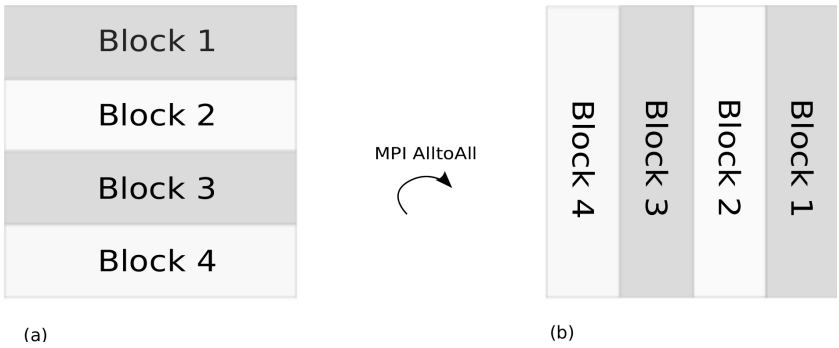

Figure 4.3: Domain decomposition and communication scheme with slab decomposition: (a) decomposition in Y direction; (b) decomposition in X direction.

4.4 Chapter summary and achievements

This chapter has presented the parellization strategy adopted for the serial code.

Section 4.1 has reported the parallelization strategy implemented in the actual code, based on MPI single domain decomposition and finite-sized overlap region.

Section 4.2 has shown the weak scalability tests on the state-of-art HPC cluster. Good scalability results are shown up to $p = 128$ number of processors.

Section 4.3 has described the further work on the parallelization strategy based on the slab decomposition.

The main achievements of this Chapter 4 are:

- A parallelization strategy based on MPI single domain decomposition and finite-sized overlap region has been implemented and tested on HPC cluster.
- The parallel version of the code has shown a good scalability, for execution on HPC clusters, up to 128 processors.

Chapter 5

Verification and Validation

5.1 One-Dimensional Test-Cases

5.1.1 Monochromatic sinusoidal wave

Description of the test case

To verify the order of accuracy of the method of Chapter 3 and demonstrate his stability characteristics, the classical $C1122$ and the cost-optimized $C1122\mathsf{epsm}n$ (with $n = 5, 4, 3$) interior prefactored compact schemes of eqs. (3.33) and (3.34) are coupled with the prefactored interior boundary stencils of eqs. (3.51a) and (3.51b). Consider the non-dimensional form of the LAE of eq. (2.13)

$$\frac{\partial u}{\partial t} + \frac{\partial u}{\partial x} = 0, \tag{5.1}$$

with the following initial condition

$$u(x, 0) = \sin(2\pi x), \tag{5.2}$$

where the superscript *, which represents the non-dimensional form, has been removed for shortness.

Computational Set-up

Equation (5.2) is solved numerically over the domain $0 \leq x \leq 1$, on a progressively refined uniform mesh. The interior prefactored scheme of eqs. (3.33) and (3.34) is combined with the prefactored interior boundary stencils of eqs. (3.51a) and (3.51b) at $x = 0$ and $x = 1$

Table 5.1: Stability and accuracy limits for the classical $C1122$ and the cost-optimized $C1122\mathsf{epsm}n$ (with $n = 5, 4, 3$) schemes. Standard $RK4$ is used for the time integration ($z_s = 2.83$, $z_d = 0.7323$).

scheme	σ_{max} from eq. (2.46)	σ_c from eq. (5.3)
$C1122/RK4$	1.422	0.6631
$C1122\mathsf{epsm}5/RK4$	1.407	0.6199
$C1122\mathsf{epsm}4/RK4$	1.394	0.5686
$C1122\mathsf{epsm}3/RK4$	1.360	0.4708

computational boundaries. The fourth-order, four-stage RK time integration scheme is used to time-march the semi-discrete *LAE* equation up to $t = 10$ (that is 10 periods), to check asymptotic stability. The Courant number is kept under the accuracy limit σ_c, which is calculated as

$$\sigma_c = \frac{z_d}{\overline{\kappa_c}(\kappa)}, \tag{5.3}$$

where the temporal dissipation accuracy limit z_d and the spatial accuracy limit $\overline{\kappa_c}$ are taken, respectively, from Tabs. 3.5 and 3.3. Table 5.1 summarizes the stability σ_{max} and accuracy σ_c limits for the classical $C1122$ and the cost-optimized $C1122\mathsf{epsm}n$ (with $n = 5, 4, 3$) schemes. The exact solution to the initial condition of eq. (5.2) is

$$u_{ex}(x, t) = \sin(2\pi(x - t)), \tag{5.4}$$

and the L_2 norm of the difference between the analytical and the numerical prediction is calculated as

$$L_2 = \sqrt{\frac{\sum_{i=1}^{N-1}(u_i - u_{ex})^2}{N - 1}} \tag{5.5}$$

where N is the number of grid points. The L_2 norm of eq. (5.5) has been calculated omitting the last node $i = N$ because, in the case of periodic boundary conditions, the last node $i = N$ is coincident with the first point $i = 1$.

Results and discussion

Figure 5.1(a) shows the comparison between the numerical prediction and the analytical solution of the *LAE* after one period ($t = 1$), using 51 uniformly spaced grid points. Figure 5.1(a) clearly shows that the numerical scheme is able to reproduce the advection of the passive scalar

u, within a tolerance that depends on the spatial mesh refinement and on integration time. Figure 5.1(b) shows the L_2 norm for the various levels of mesh refinement at the non-dimensional computational times $t = 0.1$, $t = 1$, and $t = 10$. The Courant number has been set at a very low level of $\sigma = 0.01$, to explore the error due to the spatial discretization. The L_2 norm for the classical $C1122/RK4$ scheme decreases exponentially with a sixth power roll-off for all three non-dimensional computational times. The $C1122/RK4$ scheme maintains a sixth-order accuracy with the prefactored interior boundary stencils of eqs. (3.51a) and (3.51b) up to a value of $L_2 \approx 10^{-15}$, close to the machine error, for the non-dimensional time $t = 0.1$, as shown by the black diamonds ($\diamond$) in Fig. 5.1(b). The L_2 norm at the non-dimensional computational times $t = 1$ and $t = 10$, shown, respectively, by the triangle ($\triangle$) and the circle ($\circ$), indicates the same sixth-order roll-off error by displaying an higher cumulative error due to the temporal integration by the RK algorithm. The double precision accuracy of the scheme is reached thanks to the coefficients of the prefactored interior boundary stencils of eqs. (3.51a) and (3.51b) calculated in double precision (i.e. 15 digits). The $C1122/RK4$ scheme coupled with the 11-point boundary stencil of Hixon (2000), shown by the continuous line with squared symbols (—□—), maintains the sixth-order accuracy up to $L_2 \approx 10^{-9}$ due to the single precision of its coefficients (i.e. 8 digits). Table A.5 in Appendix A.9 reports the spatial resolution used for the numerical tests reported in Fig. 5.1(b).

Figure 5.2(a) represents the monochromatic sinusoidal wave of eq. (5.2) over the extended domain $-2 \leq x \leq 3$, discretized with 10 grid points per wavelengths, $N_\lambda = 10$, corresponding to 11 points per period, $N_p = 11$. The extended domain over five periods has been analysed to study how the boundary closure error affects the L_2 error norm. Figure 5.2(b) shows the L_2 error norm calculated over the overall domain, $-2 \leq x \leq 3$, using the classical $C1122$ and the cost-optimized $C1122\mathsf{epsm}n$ interior prefactored compact schemes coupled with the 11-point prefactored interior boundary stencil of eqs. (3.51a) and (3.51b). The numerical solution is time-marched up to the non-dimensional computational time $t = 0.1$, using the classical $RK4$ time integration scheme. The Courant number used is $\sigma = 0.1$. The classical $C1122$ scheme, shown by the black diamond ($\diamond$), has a straight sixth-order roll-off, up to $L_2 \approx 10^{-13}$, whereas the cost-optimized $C1122\mathsf{epsm}n$ schemes, with $n = 5, 4, 3$, have a roll-off lower than fourth-order. For a given number of grid points N, the classical $C1122$ scheme has an absolute level of error lower than the optimized schemes, due to its higher formal order of accuracy. The absolute level of error of the cost-optimized $C1122\mathsf{epsm}n$ schemes is decreasing when the level of optimization n increases. Figure 5.2(c) shows the L_2 error norm calculated over the central

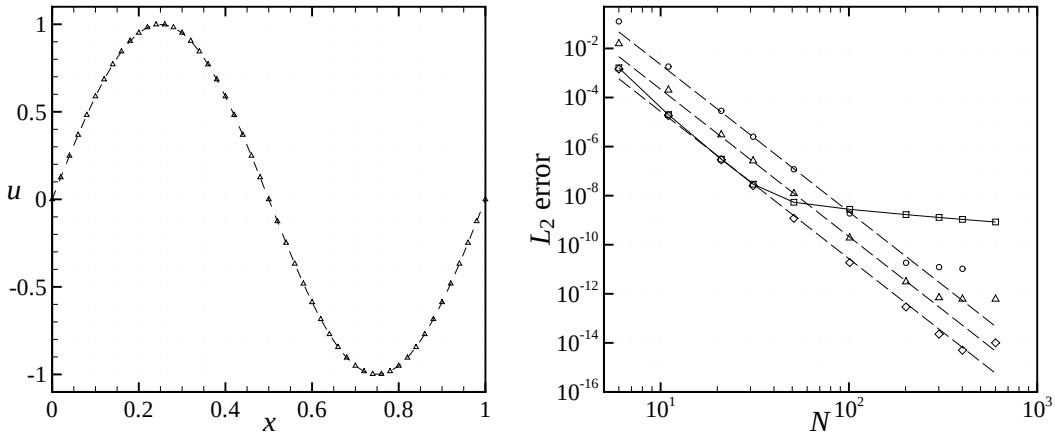

(a) Dashed line (−−) analytical solution, triangle (△) numerical prediction.

(b) Dashed line (−−), sixth-order logarithmic scale. Symbols, L_2 norm error from eq. (5.5): diamond (◇) $t = 0.1$, triangle (△) $t = 1$, circle (○) $t = 10$. Continuous lines with squared symbols (—□—), $t = 0.1$, interior scheme with boundary stencil of Hixon (2000).

Figure 5.1: Solution to *LAE* equation with monochromatic sinusoidal wave of eq. (5.2).

domain $0 \leq x \leq 1$. Again, the classical $C1122$ scheme has a sixth-order roll-off. Now, the cost-optimized $C1122$epsm$n$ schemes have a fourth-order straight line accuracy in the region of the well-resolved wavenumber spectrum ($N_p \geq 15$). The difference on the roll-off error of the cost-optimized schemes between Fig. 5.2(b) and Fig. 5.2(c) is due to the boundary error contribution, which in Fig. 5.2(c) is lower due to the boundaries being further away from the central domain. Figure 5.2(d) shows the L_2 norm error for the cost-optimized $C1122$epsm5 scheme, over the central domain $0 \leq x \leq 1$, at the non-dimensional computational times $t = 0.1$, $t = 1$, and $t = 10$ time marched with the classical $RK4$ scheme, at the same Courant number $\sigma = 0.1$. The L_2 norm error at the non-dimensional computational time $t = 0.1$, shown by the plain black triangle (▽), has a roll-off parallel to the fourth-order line in the region of the well-resolved wavenumber spectrum ($N_p \geq 15$). The L_2 norm at the non-dimensional computational times $t = 1$ and $t = 10$, shown respectively by the filled black (▼) and the filled blue (▼) triangles have a roll-off lower than fourth-order. This is due to the *RK* time integration scheme that propagates the boundary error into the computational domain. Figure A.22 in Appendix A.9.1 shows a similar trend for the cost-optimized $C1122$epsm4 and $C1122$epsm3 schemes. Table A.6 in Appendix A.9.1 reports the spatial resolution used for the numerical tests reported in Fig. 5.2.

Figures 5.2(c) and 5.2(d) display a cusp at number of points per period $N_p \leq 15$. This feature is discussed in the context of the following Fig. 5.3.

Figure 5.3 highlights Fig. 5.2(c) over the region $2 \leq N_\lambda \leq 80$. The computed L_2 norms in Fig. 5.2(c) has been normalized by the respective values of the L_2 norm at $N_\lambda = 2$, and plotted against the theoretical dispersive error e_0 of eq. (2.57). Figure 5.3 shows these comparison for the classical $C1122$ and the cost-optimized $C1122\mathsf{epsm}n$ schemes. e_0 is definition of the relative error in wavenumber space assuming zero time integration error. A low Courant number of $\sigma = 0.1$ is used to limit the contribution of the $RK4$ time integration scheme. Figure 5.3 shows that the normalized computed $\overline{L}_2$ norm error, computed for the discrete values of numbers of points per wavelength N_λ, follows the theoretical trend e_0 both for the classical and the cost-optimized schemes, matching the respecting sixth-order and fourth-order roll-off in the region of the well-resolved spectra ($N_\lambda \geq 15$). The optimized schemes also confirm the ability to resolve short wavenumbers waves around their error level of optimization with an error lower that the classical $C1122$, as discussed in the context of Fig. 3.11(b).

Figure 5.5 shows the comparison between the theoretical and the computed iso-contours of the normalized 'local' error function $e(\kappa, \sigma)$ for the monochromatic sinusoidal wave of eq. (5.2). The computed iso-contours of the normalized 'local' error function in Fig. 5.5(a) have been calculated using the baseline sixth-order $C1122$ scheme for the spatial discretization and the baseline $RK4$ scheme for time integration. The computed iso-contours of normalized 'local' error function shown in Figs. 5.5(b), 5.5(c) and 5.5(d) have been obtained using the cost-optimized $C1122\mathsf{epsm}n$ (with $n = 5, 4, 3$) interior prefactored compact schemes of Tab. 3.4 as the spatial discretization schemes, and the cost-optimized RK temporal solver $\mathsf{epsm}n$ (with $n = 5, 4, 3$) of Tab. 3.5 for the time integration. In all the cases, the spatial schemes are coupled with the 11-point prefactored interior boundary stencils of eqs. (3.51a) and (3.51b) as periodic boundary condition. The simulations have been computed over the extended domain $-2 \leq x \leq 3$ of Fig. 5.2(a). The simulations are advanced to a non-dimensional time $T = 1$. Table A.6 reports the spatial and temporal resolutions used for the numerical tests. Figure 5.4 in Appendix A.9.1 shows the numerical grid used to produce the iso-maps of Fig. 5.5, that is $[\sigma \times \kappa] = [55 \times 146]$. Table 5.2 shows the stability limits σ_{max} for the classical $C1122$ and the cost-optimized $C1122\mathsf{epsm}n$ schemes. The L_2 norm computed over the central domain $0 \leq x \leq 1$ has been normalized, according to eq. (2.42), by the initial amplitude of the sinu-

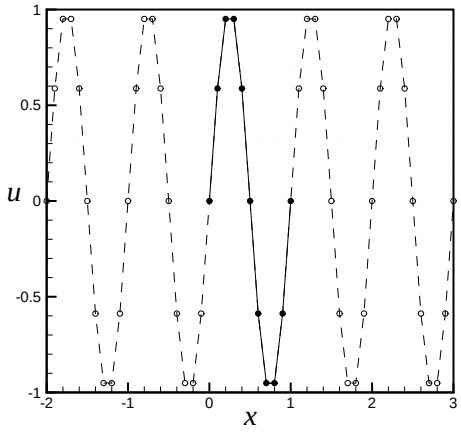

(a) Dashed line (−−) with plain circle, full domain over 5 periods. Continuous line with filled circle, central domain. Number of point per period $N_p = 11$.

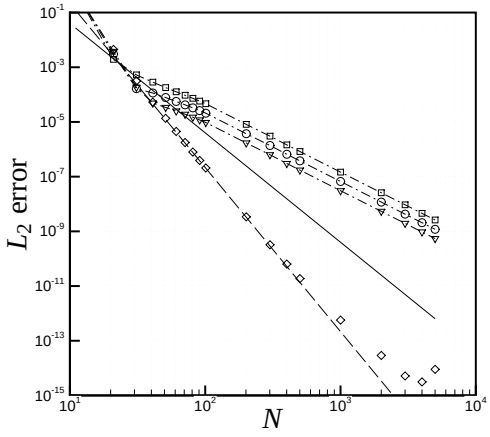

(b) L_2 norm error over the entire domain, $-2 \leq x \leq 3$.

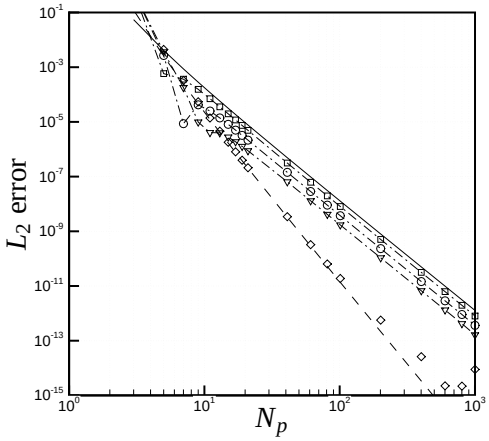

(c) L_2 norm error over the central domain, $0 \leq x \leq 1$.

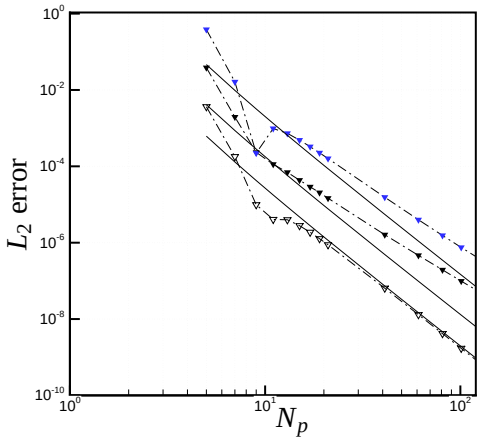

(d) L_2 norm error over the central domain, $0 \leq x \leq 1$; plain symbols $t = 0.1$, filled black symbols $t = 1$, filled blue symbols $t = 10$.

Figure 5.2: Solution to *LAE* equation with monochromatic sinusoidal wave of eq. (5.2), over the domain $-2 \leq x \leq 3$: (−−) sixth-order logarithmic scale, (−) fourth-order logatithmic scale, ($\diamond$) $C1122$, ($-\cdot-\triangledown-\cdot-$) $C1122$epsm5, ($-\cdot-\circ-\cdot-$) $C1122$epsm4, ($-\cdot-\square-\cdot-$) $C1122$epsm3.

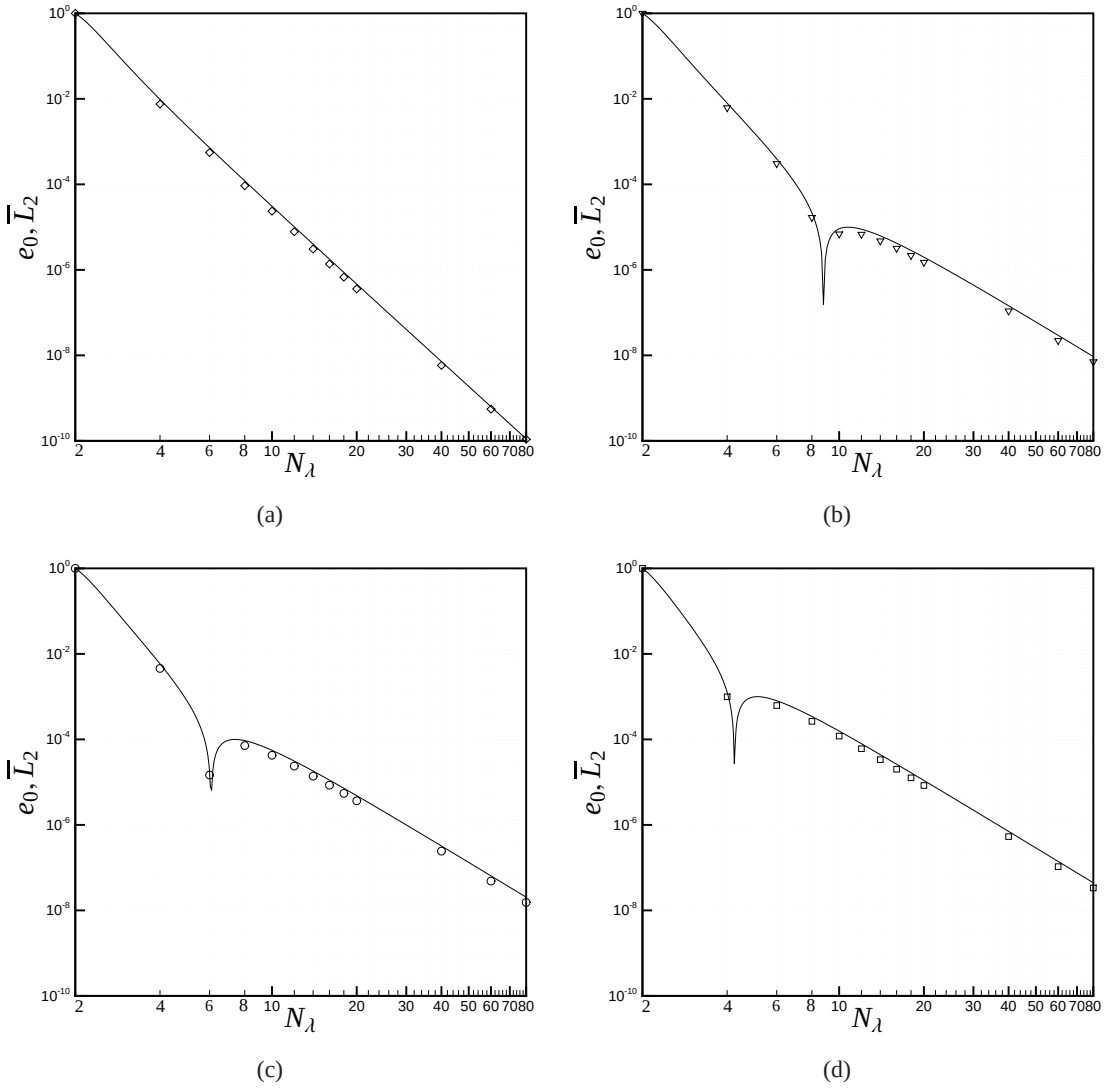

Figure 5.3: Comparison of the theoretical dissipative error e_0 from Fig. 3.11(b) with the computed normalized $\overline{L}_2$ norm error for the monochromatic sinusoidal wave; e_0 (−), $\overline{L}_2$ symbols as in Fig. 5.2: (a) $C1122/RK4$, (b) $C1122$epsm5, (c) $C1122$epsm4, (d) $C1122$epsm3.

Table 5.2: Stability limits for the classical $C1122$ and the cost-optimized epsm$n$ (with $n = 5, 4, 3$) schemes.

scheme	σ_{max} from eq. (2.46)
$C1122/RK4$	1.422
epsm5	1.407
epsm4	1.392
epsm3	1.355

soidal monochromatic wave of (5.2) as

$$E = \sqrt{\frac{\sum_{i=1}^{N-1}\left(u_i - u_i^{ex}\right)^2}{\sum_{i=1}^{N-1}\left(u_i^0\right)^2}}. \tag{5.6}$$

The computed iso-contours of the normalized 'local' error function reported in Figure 5.5 were calculated according to eq. (2.45), that is $e(\kappa,\sigma) = \dfrac{\epsilon}{ckT} \equiv \tilde{\epsilon}$, by taking into account, that for the present problem, the propagating speed of sound $c = 1$, the wavenumber $k = 2\pi$, and the final time $T = 1$.

For each iso-map, a total of $55 \times 146 = 8,030$ runs were computed. This parametric study was run using Dakota. This is an open-source multilevel parallel object-oriented framework for design optimization, parameter estimation, uncertainty quantification, and sensitivity analysis (Eldred *et al.*, 2013). The total wall-clock time to produce an iso-map is around 4 hours. The simulations have been performed in the DataPlex Cluster *PLX* cluster at CINECA. The *PLX* cluster consists of 274 IBM $X360M2$ 12-way compute nodes. Each node contains 2 Intel(®) Xeon(®) Westmere six-core $E5645$ processors, with a clock of 2.40GHz. The compute nodes have 48GB of memory (plx, CINECA). The simulations have been performed by reserving the full compute node. No interference with other running jobs were present during the runs in measuring the computational execution time of these simulations.

Figure 5.5(a) shows that the computed error maps for the baseline $C1122/RK4$ scheme are in good agreement with the theoretical ones in the well-resolved wavelength range $\kappa \leq 1.4$. The discrepancy between the error maps over the poorly resolved wavenumber range $\kappa > 1.4$ is a numerical artefact in the wavenumber range $1.4 \leq \kappa \leq \pi$, generated by having a coarsely spaced numerical grid over this wavenumber range, as shown by Fig. 5.4. This affects the placement of the contours of the computed errors in Fig. 5.5(a). Since an integer number of points per wavelength N_λ is required in these tests, this prevents the use of a refined computational mesh over this range.

Figures 5.5(b), 5.5(c) and 5.5(d) show that there is a good agreement between the iso-contours of the normalized 'local' error function $e(\kappa,\sigma)$ of the cost-optimized $C1122$epsm$n$ schemes and the corresponding theoretical estimates from Sec. 3 in the top left hand quadrant of each Figure ($\kappa \leq 1.4$, $\sigma \geq 0.8$). On the bottom left quadrant, over the range ($\kappa \leq 1.4$, $\sigma \leq 0.8$), the theoretical iso-error lines are able to capture the trend of computed cost-optimized schemes. Specifically, the iso-error lines are shown to the left with respect to the corresponding iso-error

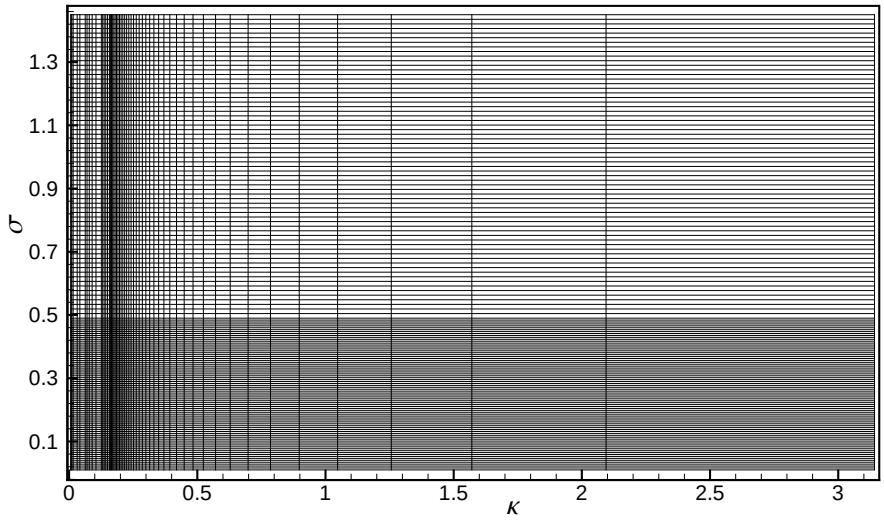

Figure 5.4: Numerical grid used for the computed iso-maps reported in Fig 5.5.

lines of Fig. 5.5(a), for all contour levels lower than the target level of error 10^{-n}. Conversely, the contour lines are shown to the right with respect to the corresponding iso-error lines of Fig. 5.5(a) for all contour levels greater than the target level of error 10^{-n}. At these very low Courant number $\sigma \rightarrow 0$, the iso-error lines of the cost-optimized schemes do not follow the straight vertical trend of the corresponding baseline iso-error lines of Fig. 5.5(a). At very low Courant number $\sigma \rightarrow 0$, the error is mainly a spatial type of error as reported in eq. (2.57). This gives a straight line as shown in Fig. 2.6(a) for the classical $C1122/RK4$ scheme. Conversely, the cost-optimized schemes show a non-straight line due to the presence of the spike in such a region.

The effect of the cost-optimization at the target level of error is better appreciated from Fig. A.23 in Appendix A.9.1 that shows an enlarged view of the computed contours of the normalized 'local' error function $e(\kappa, \sigma)$ in the region $0 \leq \kappa \leq 2$, with fifty constant logarithmically spaced iso-contour levels of errors between 10^{-8} and 10^{-1}. These figures highlight that the numerical epsm$n$ κ-σ iso-contours of the cost-optimized schemes are able to follow the trend of the corresponding theoretical ones with the exception of the spike region and the region immediately on its left-hand side. This region corresponds to the plateau in the optimal 'local' error versus cost analysis previously shown in Fig. 3.23, for a two-dimensional cost-analysis trade-off. Specifically, in the region on the left-hand side of the spike region, the computed iso-error lines, shown by the dashed $(--)$ lines, are shown to the left with respect to the corresponding

theoretical ones, shown by the continuous (−) line. The spike represents a locus of low error in the cost-optimization. This local reduction in the numerical implementation is not achieved as it is masked by the temporal integration error from the numerical implementation of the algorithm.

Figure 5.6 shows the theoretical and numerical contours of the 'local' error function $e(\kappa, \sigma)$, respectively with solid (−) and dashed (−−) lines, in conjunction with the one-dimensional normalized cost $c_1 = 1/(\sigma\kappa^2)$, represented by the continuous coloured lines, for the monochromatic sinusoidal wave test-case. The baseline $C1122/RK4$ scheme is shown in Fig. 5.6(a) and the cost-optimized epsm5 in Fig. 5.6(b). Figures A.24(a) and A.24(b) in Appendix A.9.1 show the corresponding iso-maps for the the cost-optimized epsm4 and epsm3 schemes. Figure 5.6 shows the tangency condition between the iso-contours of the normalized 'local' error function and the normalized one-dimensional cost function, and reports the optimal cost-error operational points $\left(\kappa^*(\tilde{\epsilon}), \sigma^*(\tilde{\epsilon}), c_1^*(\tilde{\epsilon})\right)$ with the corresponding coloured symbols. Figure 5.6(a) shows a good agreement between the theoretical and the numerical optimal cost-error operational points for the baseline $C1122/RK4$ scheme. The discrepancy increases where the level of error increases, due to the coarsely spaced numerical grid in Fig. 5.6(b) used to generate the $\kappa - \sigma$ iso-map over the poorly resolved wavenumber range. Figure 5.6(b) shows the comparison between the theoretical and the numerical optimal cost-error operational points for the cost-optimized epsm5 scheme. The theoretical and numerical optimal cost-error operational points are relatively further with respect to the path for the baseline $C1122/RK4$ scheme, and their proximity decreases with increasing κ, similarly to Fig. 5.6(a). It is interesting to notice that the Courant number associated to the cost-optimal computation at the design level of error $\tilde{\epsilon} = 10^{-5}$ is higher that other target levels of error. The theoretical and the numerical cost-optimal operational points at the design error level $\tilde{\epsilon} = 10^{-5}$ are located respectively at $(\kappa^*, \sigma^*) = (0.39, 0.67)$ and $(\kappa^*, \sigma^*) = (0.33, 0.82)$, as reported respectively by the red and blue diamond in Fig. 5.6(b). A spike in the optimization region, $[0.6 \leq \kappa \leq 0.8, \sigma \leq 0.45]$, is only present in the theoretical error forecast. This error minimum, together with its optimal cost-error operation point, is not achieved in the numerical implementation.

Table 5.3 reports the absolute percentage difference Δc_1^* between the theoretical and the numerical computational cost at the cost-optimal operational points for the eight levels of error $\tilde{\epsilon}$ shown in Figs. 5.6 and A.24 for the baseline $C1122/RK4$ and the cost-optimized epsm$n$ schemes. For the classical $C1122/RK4$ scheme, these percent differences are below 6% except for the error level $\tilde{\epsilon} = 10^{-1}$. A substantial percentage difference at $\tilde{\epsilon} \leq 10^{-7}$ is noticed for the

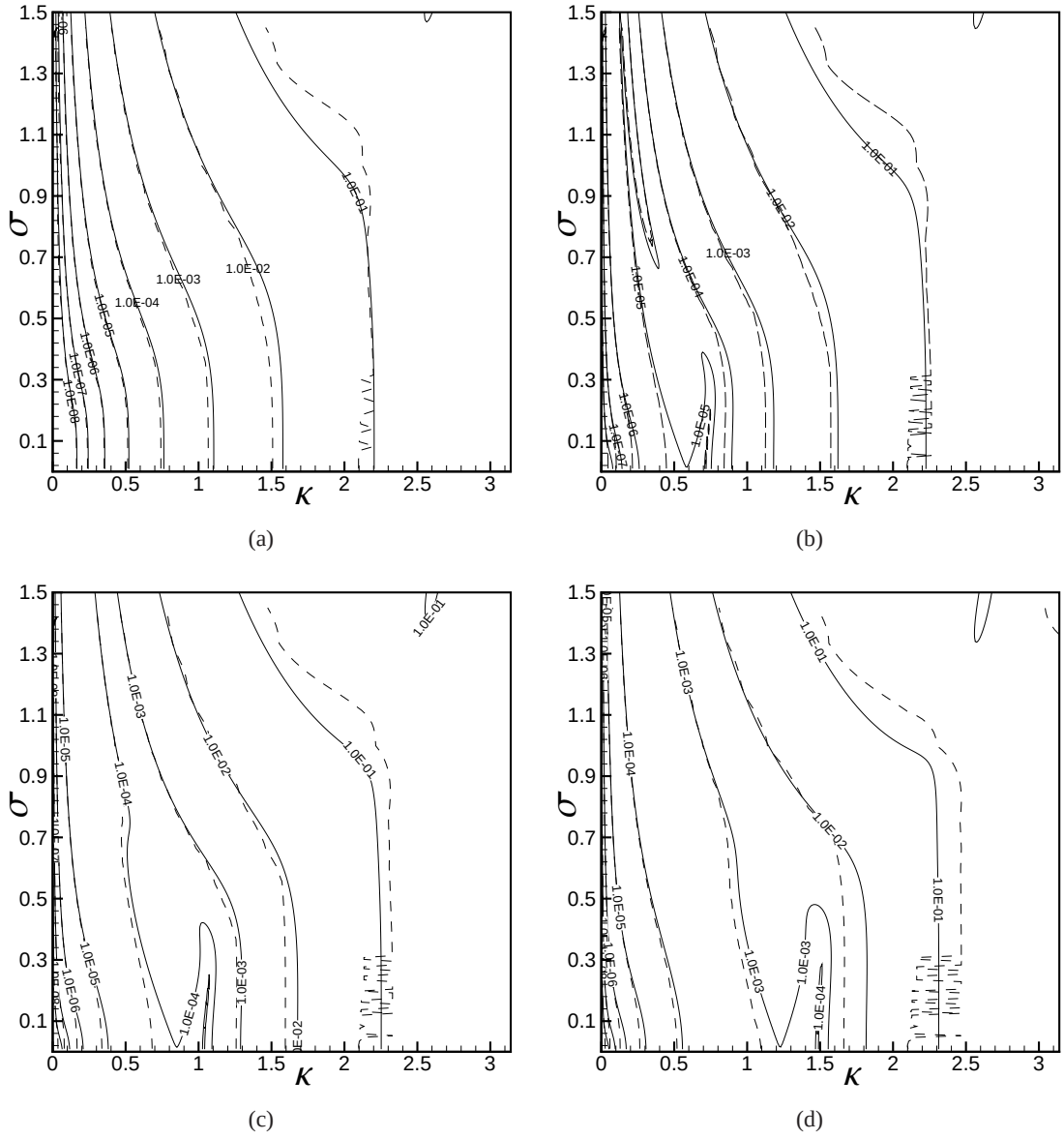

Figure 5.5: Comparison between the theoretical and the computed iso-contours of normalized 'local' error function $e(\kappa, \sigma)$ for the monochromatic sinusoidal wave. Continuous line $(-)$ theoretical, dashed line $(--)$ computed: (a) $C1122/RK4$; (b) epsm5, (c) epsm4, (d) epsm3.

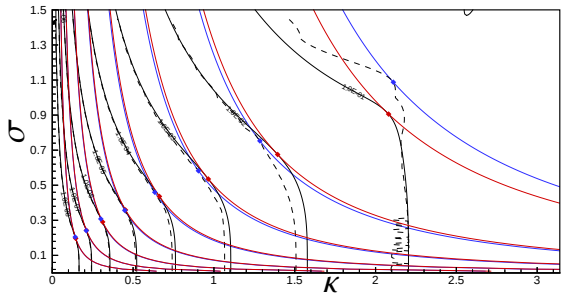

(a) $C1122/RK4$.

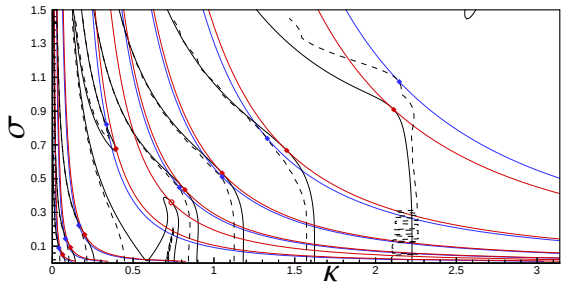

(b) epsm5.

Figure 5.6: Theoretical (black solid lines) and numerical (black dashed lines) contours of optimal 'local' error function $e(\kappa, \sigma)$ as a function of the one-dimensional cost $c_1 = 1/(\sigma\kappa^2)$ (continuous coloured lines) for the monochromatic sinusoidal wave. (a) $C1122/RK4$ (b) epsm5.

Table 5.3: Absolute percentage difference Δc_1^* between theoretical and numerical cost-optimal operating points as function of the one-dimensional cost for the monochromatic sinusoidal wave. The brackets report, respectively, theoretical and numerical cost-optimal values. The bold values are used in following Tab. 5.5.

$\tilde{\epsilon}$\scheme	$C1122/RK4$	epsm5	epsm4	epsm3
10^{-8}	0.4 (242.14, 243.15)	41.19 (4847.74, 6844.58)	47.47 (9480.87, 13982.07)	90.98 (16551.3825, 31611.26)
10^{-7}	1.2 (92.36, 93.52)	24.23 (848.37, 1053.96)	152.02 (848.37, 2138.07)	45.32 (2931.408, 4260.07)
10^{-6}	1.9 (35.40, 36.09)	12.53 (147.70, 166.22)	127.51 (147.70, 336.06)	19.31 (519.103, 619.37)
10^{-5}	2.6 (13.58, **13.94**)	13.8 (9.51, **10.83**)	473.44 (9.51, 54.57)	9.56 (91.632, 100.39)
10^{-4}	3.6 (5.21, **5.40**)	5.60 (3.41, 3.6)	45.67 (3.4165, **4.977**)	6.00 (15.73, 16.68)
10^{-3}	4.8 (2.00, **2.09**)	4.38 (1.69, 1.77)	14.74 (1.6985, 1.448)	6.54 (1.74, **1.855**)
10^{-2}	5.7 (0.76, 0.8)	7.43 (0.71, 0.76)	2.24 (0.7125, 0.6965)	2.12 (0.54, 0.5515)
10^{-1}	19.0 (0.25, 0.20)	18.05 (0.24, 0.20)	20.89 (0.2465, 0.195)	13.06 (0.21, 0.183)

cost-optimized epsm5 scheme. In such region, which is the bottom left quadrant of Fig. 5.6, the mismatch is due to the effect of the time integration at very low Courant numbers $\sigma \to 0$, which has been discussed in the context of Fig. 5.5(b). A similar trend is observed for the cost-optimized epsm4 scheme for $\tilde{\epsilon} \leq 10^{-5}$ and for the epsm3 scheme for $\tilde{\epsilon} \leq 10^{-7}$.

Figure 5.7 shows the computed optimal cost-error operational points compared against the theoretical ones, represented respectively by symbols and lines. The same algorithm used to calculate the theoretical cost-optimal operational point $\left(\kappa^*(\tilde{\epsilon}), \sigma^*(\tilde{\epsilon}), c^*_{n_D}(\tilde{\epsilon})\right)$ has been used to calculate the computed ones, to verify if the analytical findings of Sec. 3 are verified by this simple benchmark problem. Overall, there is satisfactory match between computed and theoretical cost-optimal points, as shown in Fig. 5.6 and in Tab. 5.3.

Figure 5.7(a) shows that at the design level of error $\tilde{\epsilon} = 10^{-n}$, the computational cost c_1^* for the cost-optimized schemes is lower than the corresponding computational cost c_1^* for the classical $C1122/RK4$ scheme. A cost-saving is therefore achieved in computations that allow an error within the range $10^{-5} \leq \tilde{\epsilon} \leq 10^{-2}$ for the cost-optimized epsm5 scheme, $10^{-4} \leq \tilde{\epsilon} \leq 10^{-2}$ for the epsm4 scheme, and $10^{-3} \leq \tilde{\epsilon} \leq 10^{-1}$ for the epsm3 scheme. Instead, for computations requiring an error level lower than the target level of error $\tilde{\epsilon} = 10^{-n}$, the computational cost of the cost-optimized epsm*n* scheme is higher than the baseline non-optimized scheme.

Figure 5.7(b) shows the optimal reduced wavenumber for the classical $C1122/RK4$ and the cost-optimized epsm*n* schemes. The cost-optimized epsm*n* schemes show a lower value of optimal wavenumber at their design level of error $\tilde{\epsilon} = 10^{-n}$ with respect to the baseline non-optimized $C1122/RK4$ scheme. This disagrees with the theoretical findings of Fig. 3.23(b), in which the optimal wavenumber at the design level of error for the cost-optimized scheme is

shown to be higher compared to the baseline non-optimized scheme. This is due to the numerical position of the cost-optimal operational points at the design level of error $\tilde{\epsilon} = 10^{-n}$, which is not located in the spike region, as discussed in the context of Fig. 5.6(b).

Figure 5.7(c) shows the optimal Courant number for the classical $C1122/RK4$ and the cost-optimized epsm$n$ schemes. The optimal operational point at the design level of error $\tilde{\epsilon} = 10^{-n}$ is higher with respect to the corresponding values for the baseline scheme. This, again, disagrees with the theoretical findings of Fig. 3.23(c), which predicts a lower value of Courant number at the design level of error $\tilde{\epsilon} = 10^{-n}$. This is a consequence, as in Fig. 3.23(b), of the actual numerical position of the cost-optimal operational points at the design level of error $\tilde{\epsilon} = 10^{-n}$, as seen in Fig. 5.6(b).

In order to verify the computational cost saving of the optimized schemes in the real computations, the code has been instrumented to measure the effective computed elapsed time during the numerical tests. This enables the comparison of the theoretical cost forecast $c_1 = 1/(\sigma\kappa^2)$ with the effective computed elapsed time recorded from the instrumented code. Moreover, it is possible to compare the percentage gain of the cost-optimized schemes with respect to the classical scheme in the case of the theoretical cost forecast $c_1 = 1/(\sigma\kappa^2)$ and the effective computed elapsed time. To obtain a precise measure of the elapsed computational time, the runs have been carried out with a full compute node allocated to the execution of the job, to avoid any interference with other running jobs. The elapsed computational time during the calculations has been determined using the intrinsic FORTRAN *system_call*, which measures the elapsed real time, and the intrinsic FORTRAN *cpu_time*, which measures the cpu-time. As the compute node was reserved, there is no appreciable difference between the measured elapsed real-time and the measured cpu-time. Different evaluations have been done for every operational point, taking an average of the significant values, not affected by the undesirable presence of the computational perturbations. The measured times take into account only the number crunching section of the code, excluding the part relative to the initialization, allocation of the variables, data writing and deallocation of the variables. The code has been preliminary profiled with *gprof*, to identify the most-called and time-consuming subroutines. The profiler indicates that the number crunching section takes around 85% of the total job execution time, for a typical run of $\tilde{\epsilon} = 10^{-5}$ with a number of time iterations of about a hundred.

Table 5.4 reports the measured computational elapsed *time* in seconds and the computed normalized $\overline{L}_2$ norm error for the classical $C1122$ and the cost-optimized epsm$n$ schemes at the computed optimal cost-error operational points at the final time $T = 1$ for the monochromatic

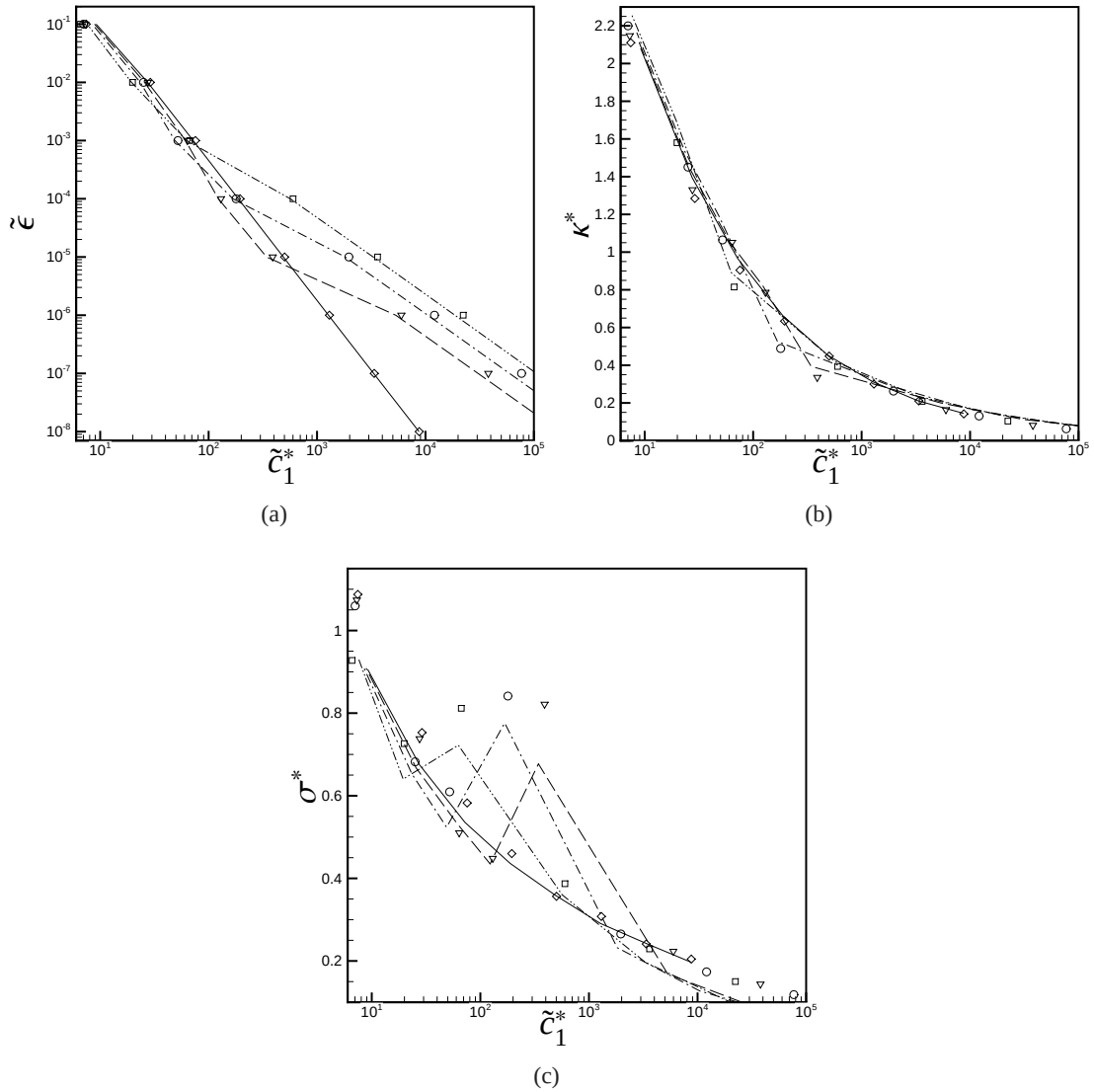

Figure 5.7: Comparison of the theoretical (lines) and numerical (symbols) optimal 'local' error versus cost (a), reduced wavenumber (b) and Courant number (c) as a function of the one-dimensional cost for the monochromatic sinusoidal wave. $(-, \diamond)$ $C1122$, $(--, \triangledown)$ $C1122$epsm5, $(- \cdot -, \circ)$ $C1122$epsm4, $(- \cdot\cdot -, \square)$ $C1122$epsm3.

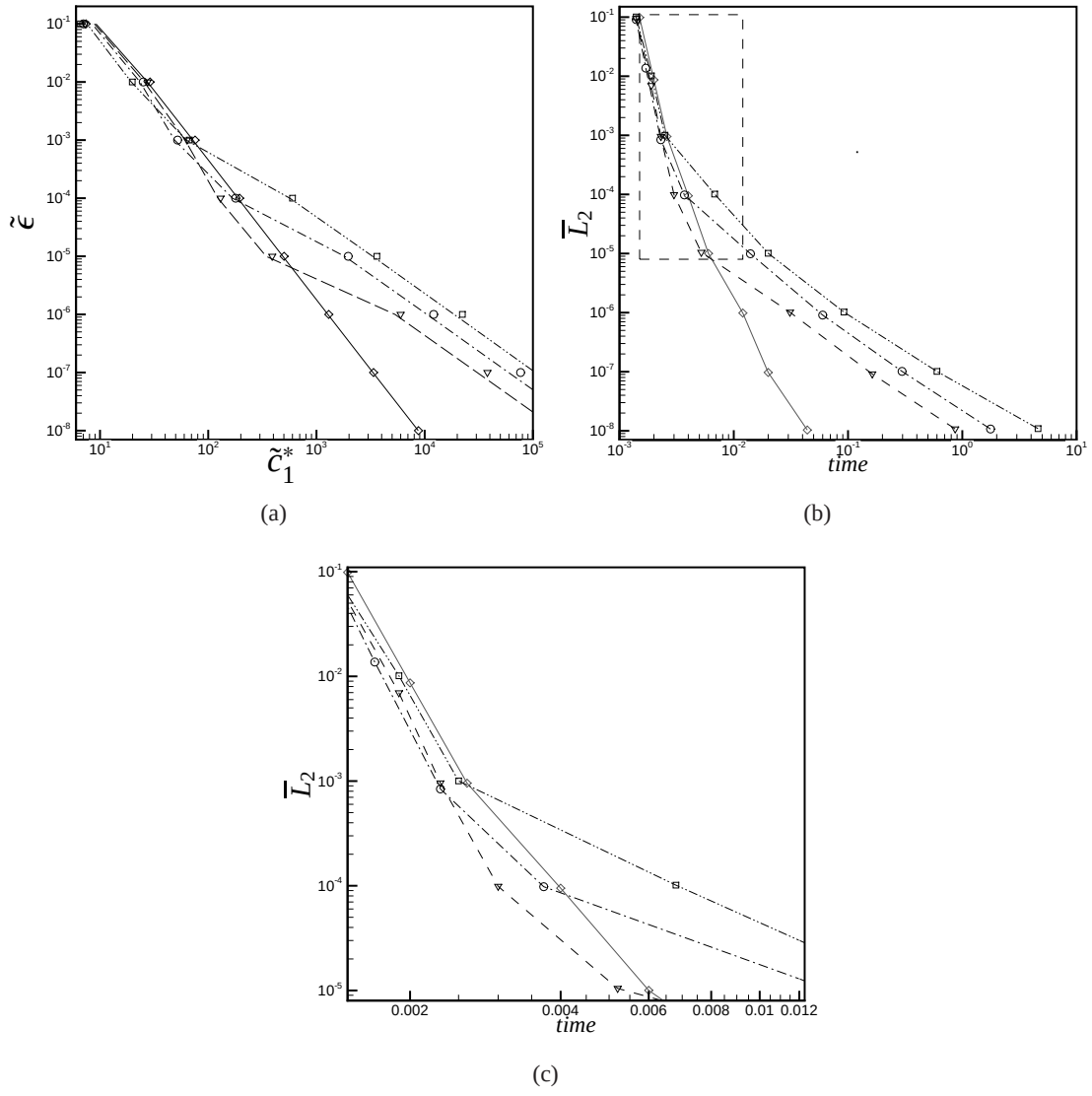

Figure 5.8: Theoretical (lines) and numerical (symbols) optimal 'local' error versus cost as a function of the one-dimensional cost function (a), and measured elapsed time versus the normalized computed $\overline{L}_2$ norm error (b) for the monochromatic sinusoidal wave. $(-, \diamond)$ $C1122$, $(--, \triangledown)$ $C1122$epsm5, $(- \cdot -, \circ)$ $C1122$epsm4, $(- \cdot \cdot -, \square)$ $C1122$epsm3. (c) Zoom of the rectangular area reported in (b).

Table 5.4: Measured computational elapsed *time* in secs. and computed normalized $\overline{L}_2$ norm error for the classical $C1122$ and the cost-optimized schemes epsm$n$ at the computed optimal cost-error operational points. Final non-dimensional time $T = 1$.

$\tilde{\epsilon}$	$C1122/RK4$		epsm5		epsm4		epsm3	
	time	$\overline{L}_2$	*time*	$\overline{L}_2$	*time*	$\overline{L}_2$	*time*	$\overline{L}_2$
10^{-8}	4.4E-02	1.0330E-08	0.866	1.0754E-08	1.765	1.0731E-08	4.6	1.0889E-08
10^{-7}	2.0E-02	9.7255E-08	0.163	9.1660E-08	0.297	1.0133E-07	0.6	1.0122E-07
10^{-6}	1.2E-02	9.8504E-07	3.1E-02	1.0158E-06	6.0E-02	9.0841E-07	9.2E-02	1.0214E-06
10^{-5}	6.0E-03	1.0024E-05	5.5E-03	1.0458E-05	1.4E-02	9.8967E-06	2.0E-02	1.0095E-05
10^{-4}	4.0E-03	1.0253E-04	3.0E-03	9.8729E-05	3.7E-03	1.0143E-04	6.8E-03	1.0132E-04
10^{-3}	2.6E-03	1.0019E-03	2.3E-03	9.5922E-04	2.3E-03	8.4095E-04	2.5E-03	1.0034E-03
10^{-2}	2.0E-03	8.6665E-03	1.9E-03	6.9636E-03	1.7E-03	1.3702E-02	1.9E-03	1.0122E-02
10^{-1}	1.5E-03	9.8487E-02	1.4E-03	9.5154E-02	1.4E-03	9.0776E-02	1.4E-03	1.0079E-01

sinusoidal wave.

Figure 5.8 compares the theoretical cost of the computation for a given target level of error $\tilde{\epsilon}$ with the measured cost, expressed in the form of measured elapsed time, at the corresponding numerical error. Figure 5.8(a) is a copy of Fig. 5.7(a). Figures 5.8(b) and 5.8(c) are the graphical representations of Table 5.4. There is a match between the trends reported in Fig. 5.8(a) and the corresponding ones of Fig. 5.8(b) both for the classical and the optimized schemes. Figure 5.8(a) shows a straight line representing the cost-optimal trend of the classical $C1122/RK4$ scheme, whereas a non-straight line is reported in Fig. 5.8(b) for the same scheme. This is partially due to the short computational final $T = 1$, which is slightly to affect the measurement of the computed elapsed time due to the presence of some jitter in the code execution time. Figure 5.8(c) shows an enlarged view of Fig. 5.8(b) in the cost-optimal region $1.5\times10^{-3} \leq time \leq 1.2\times10^{-2}$, $8\times10^{-6} \leq \overline{L}_2 \leq 1.1\times10^{-1}$, highlighted by the dashed rectangle in Fig. 5.8(b). This enlargement shows the effective computational cost saving in computations that allow an error within the range $10^{-5} \leq \overline{L}_2 \leq 10^{-2}$ for the cost-optimized epsm5 scheme, $10^{-4} \leq \overline{L}_2 \leq 10^{-2}$ for the epsm4 scheme, and $10^{-3} \leq \overline{L}_2 \leq 10^{-1}$ for the epsm3 scheme, compared to the computational cost of the classical baseline $C112/RK4$ scheme. This comparison is analogous to the cost-error function $c_1 = 1/(\sigma\kappa^2)$ shown in Fig. 5.8(a).

To have a better estimation of the computed elapsed time, the numerical tests for the classical and the optimized schemes have been registered up to the non-dimensional final times $T = 1, 10, 100$ and 500 at the nominal optimal design level of error $\tilde{\epsilon} = 10^{-n}$, with $n = 5, 4, 3$. Table 5.5 reports the aforementioned measured computational elapsed *time* in seconds and the corresponding $\overline{L}_2$ norm error for the classical $C1122$ and the cost-optimized epsm$n$ schemes.

Table 5.5: Measured computational elapsed *time* in secs. and computed normalized $\overline{L}_2$ norm error for the classical $C1122$ and the cost-optimized schemes epsm$n$ at the computed optimal cost-error operational points. Final non-dimensional time $T = 1, 10, 100, 500$.

T = 1	$C1122/RK4$		epsm5		epsm4		epsm3	
$\tilde{\epsilon}$	*time*	$\overline{L}_2$	*time*	$\overline{L}_2$	*time*	$\overline{L}_2$	*time*	$\overline{L}_2$
10^{-5}	6.2E-03	1.0024E-05	5.5E-03	1.0458E-05	-	-	-	
10^{-4}	4.0E-03	1.0254E-05	-	-	3.7E-03	1.0143E-04	-	
10^{-3}	2.6E-03	1.0019E-03	-	-	-	-	2.49E-03	1.0034E-03
T = 10	$C1122/RK4$		epsm5		epsm4		epsm3	
$\tilde{\epsilon}$	*time*	$\overline{L}_2$	*time*	$\overline{L}_2$	*time*	$\overline{L}_2$	*time*	$\overline{L}_2$
10^{-5}	2.8E-02	1.0110E-05	2.2E-02	1.0317E-05	-	-	-	-
10^{-4}	1.5E-02	1.0255E-04	-	-	1.37E-02	1.0783E-04	-	-
10^{-3}	7.6E-03	1.0089E-03	-	-	-	-	2.5E-03	1.043E-03
T = 100	$C1122/RK4$		epsm5		epsm4		epsm3	
$\tilde{\epsilon}$	*time*	$\overline{L}_2$	*time*	$\overline{L}_2$	*time*	$\overline{L}_2$	*time*	$\overline{L}_2$
10^{-5}	0.226	1.0013E-05	0.173	1.0306E-05	-	-	-	-
10^{-4}	9.3E-02	1.02047E-04	-	-	8.4E-02	1.0530E-04	-	-
10^{-3}	4.3E-02	9.0347E-04	-	-	-	-	3.75E-03	8.21E-04
T = 500	$C1122/RK4$		epsm5		epsm4		epsm3	
$\tilde{\epsilon}$	*time*	$\overline{L}_2$	*time*	$\overline{L}_2$	*time*	$\overline{L}_2$	*time*	$\overline{L}_2$
10^{-5}	1.09	1.0002E-05	0.832	1.0177E-05	-	-	-	-
10^{-4}	0.443	9.9264E-05	-	-	0.396	9.4586E-05	-	-
10^{-3}	0.195	4.4199E-04	-	-	-	-	0.163	3.28E-04

It is observed that the measured computational time for the cost-optimized epsm$n$ schemes at their design level of error $\tilde{\epsilon} = 10^{-n}$ is consistently lower than the measured computational time for the classical scheme. The value of the computed normalized $\overline{L}_2$ norm error is very close to the nominal design level of error $\tilde{\epsilon}$, except at the final times $T = 100$ and $T = 500$ for the epsm3 scheme, for which it is higher that the design level of error $\tilde{\epsilon}$ due to the propagation of the boundary error at these final times.

Finally, Table 5.6 reports the comparison of the percentage cost saving $\Delta\tilde{c}_1^*$ and the measured elapsed time saving $\Delta t\%$ of the cost optimized epsm$n$ schemes with respect to the classical baseline scheme, at the nominal optimal design levels of error $\tilde{\epsilon}$. The percentage cost-saving $\Delta\tilde{c}_1^*$ is taken from the numerical cost-optimal values as a function of the one-dimensional cost c_1 of Tab. 5.3 (in bold). The percentage difference in the measured computational times $\Delta t\%$ are recorded by the code running at the different non-dimensional final times as tabulated in Tab. 5.5. There is a good agreement between the theoretical percentage cost-saving $\Delta\tilde{c}_1^*$ with the measured percentage elapsed time saving $\Delta t\%$ at all the four final times reported. The discrepancy at the final time $T = 1$ is given by the jitter in the execution time of the same segment

Table 5.6: Comparison of the percentage cost-saving $\Delta\tilde{c}_1^*$ and measured elapsed time-saving $\Delta t\%$ of the cost optimized schemes with respect to the classical baseline scheme, at the nominal optimal design levels of error $\tilde{\epsilon}$. $\Delta\tilde{c}_1^*$ from Tab. 5.3, and $\Delta t\%$ from Tab. 5.5.

$\tilde{\epsilon}$	epsm5				
	$\Delta\tilde{c}_1^*\%$	$\Delta t\%_{T=1}$	$\Delta t\%_{T=10}$	$\Delta t\%_{T=100}$	$\Delta t\%_{T=500}$
10^{-5}	22.3	11.29	21.42	23.45	23.66
$\tilde{\epsilon}$	epsm4				
	$\Delta\tilde{c}_1^*\%$	$\Delta t\%_{T=1}$	$\Delta t\%_{T=10}$	$\Delta t\%_{T=100}$	$\Delta t\%_{T=500}$
10^{-4}	7.83	7.5	8.6	9.67	10.6
$\tilde{\epsilon}$	epsm3				
	$\Delta\tilde{c}_1^*\%$	$\Delta t\%_{T=1}$	$\Delta t\%_{T=10}$	$\Delta t\%_{T=100}$	$\Delta t\%_{T=500}$
10^{-3}	11.24	4.23	10.52	12.79	16.41

between successive runs. As far as the final time T increases, the match between $\Delta\tilde{c}_1^*$ and $\Delta t\%$ improves to within 5 percentage points.

According to Tab. 5.3 and Fig. 5.8(c), a bigger cost-saving is predicted when moving a decade below the design level of error $\tilde{\epsilon} = 10^{-n}$ for the cost-optimized epsm$n$ schemes. The above confirms that the theoretical cost-saving predicted in Sec. 3 are realizable from the numerical implementation of the cost-optimized algorithm applied to the advection of a monochromatic sinusoidal wave.

5.1.2 Gaussian pulse

Description of the test case

The initial condition for eq. (2.13) is given by the Gaussian profile:

$$u(x,0) = h \exp\left[-(\ln 2)\left(\frac{x}{b}\right)^2\right]. \tag{5.7}$$

Figure 5.10(a) shows the initial profile, with $h = 0.5$ and $b = 9$, discretized on a grid using $N = 101$ grid points, over the domain of non-dimensional length $D = 130$ with $-65 \leq x \leq 65$, using 15 points to resolve the half-width b of the Gaussian pulse (Poinsot & Lele, 1992). This initial Gaussian distribution specified here differs from the initial profile specified in the First Workshops on Benchmark problems for CAA (Hardin *et al.*, 1995). The distribution of eq. (5.7) presents a wider half-width b than the initial Gaussian profile of Hardin *et al.* (1995), whereas $b = 3$.

The exact solution to the initial condition of eq. (5.7) is:

$$u_{ex}(x,t) = h \exp\left[-(\ln 2)\left(\frac{x-t}{b}\right)^2\right]. \tag{5.8}$$

Modelling strategy

Some preliminary consideration on the discretized Gaussian pulse. The energy of eq. (5.7) may be expressed in Fourier space by the appropriate form of the Parseval's relation

$$E_\kappa = \int_0^\pi |(\hat{u}(\kappa))|^2 d\kappa, \tag{5.9}$$

where $\hat{u}(\kappa)$ is the discrete x-Fourier transform of the set u_j. The discrete energy, or square of the L_2 norm from eq. (5.5), calculated on the N number of points, can be equivalent expressed in the physical domain as

$$E_D = h \sum_j |(u_j)|^2. \tag{5.10}$$

The above relation is usually given for function defined on infinite interval $[-\infty, \infty]$, as reported by Vichnevetsky (1986).

Firstly, it has be checked that the discrete energy of eq. (5.10) which lies outside of the finite domain D is zero within the accuracy of the calculation, that is double precision accuracy (i.e.

15 digits). Secondly, the energy of the Fourier transform of the initial Gaussian

$$\tilde{u}(\kappa,0) = \left(\frac{\pi}{\ln 2}\right)^{1/2} hb \exp\left[-\frac{(\kappa b)^2}{4\ln 2}\right], \tag{5.11}$$

which lies outside the p band (see Sec. 3.2.1), has been verified to be less than 10^{-15} times the total energy

$$\int_{\alpha=p}^{\alpha=\pi} \tilde{u}(\alpha,0)\,d\alpha < 10^{-15} \int_{\alpha=0}^{\alpha=\pi} \tilde{u}(\alpha,0)\,d\alpha. \tag{5.12}$$

The classical $C1122$ scheme of eqs. (3.33) and (3.34) is used as interior prefactored scheme. The LODI inflow and outflow conditions of Sec. 3.6.1 are used at the computational domain boundaries. The advection of a passive scalar in eq. (2.13) is modelled by a flow which is inviscid and one-dimensional, therefore the LODI approximation in the case of the LAE of eq. (2.13) are exact conditions. The classical $RK4$ scheme is used to time advance the numerical solution, using different Courant numbers σ. The solution is time-advanced up to the non-dimensional final time $T = 100$, when the pulse has left the computational domain.

Numerical results and discussion

The sixth-order roll-off error is maintained when the number of grid point is increased, and similar results to Fig. 5.1(b) have been obtained.

The transmission of one-dimensional acoustic waves through a non-reflecting boundary is a well-known test to characterize the performance of the outlet boundary treatments for time-dependent flows.

The two types of waves, physical *"p"* and numerical *"q"* waves introduced in Sec. 3.2.1, are uncoupled in the interior but are usually coupled by the boundary conditions, when an inlet/outlet boundary closure is present. In fact, when *"q"* waves reach another boundary, for example an outlet boundary, they are reflected in the form of physical waves which are convected downstream again, as sketched in Fig. 5.9(a). As a result *"q"* waves create a feedback between inlet and outlet which is entirely numerical (Vichnevetsky & Bowles, 1982).

Although this result has been obtained for the *LAE* equation it can be extended to the acoustic theory (LEE equation). There is, however, an additional complexity for the Euler equations: acoustic waves can be reflected by boundaries into physical domains, as shown in Fig. 5.9(b). In a subsonic flow, an acoustic wave propagating at the speed $u+c$ and reaching a reflecting outlet boundary, will generate two reflected waves: the first will be a physical wave of type

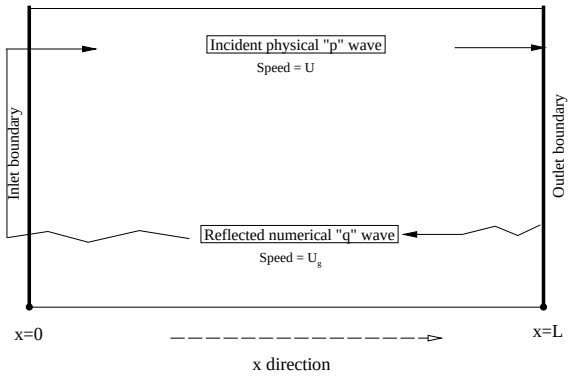

(a) LAE

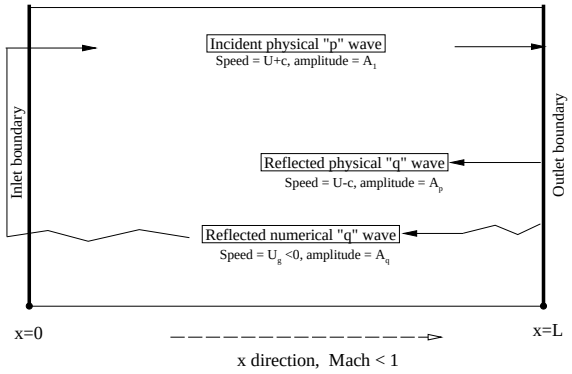

(b) LEE

Figure 5.9: Numerical and physical reflected waves at outlet boundary: Fig. 5.9(a) LAE; Fig. 5.9(b) LEE.

"p" propagating upstream at the speed *u-c*. This wave is the physically meaningful part of the reflected wave. A *"q"* wave will be also reflected and propagate upstream at the speed $u_g = k_g\,(u + c)$. In a supersonic flow, no reflected *"p"* wave will be created, but the *"q"* wave will still be generated. It will travel upstream at u_g, reach the inlet of the computational domain, and induce non-physical pertubations.

The strength of this numerical feedback is determined by the amplitude of the reflected numerical *"q"* wave. This amplitude is mainly fixed by the quality of the outflow boundary condition treatment. Poinsot & Lele (1992) suggested that, given the amplitude of the incident physical

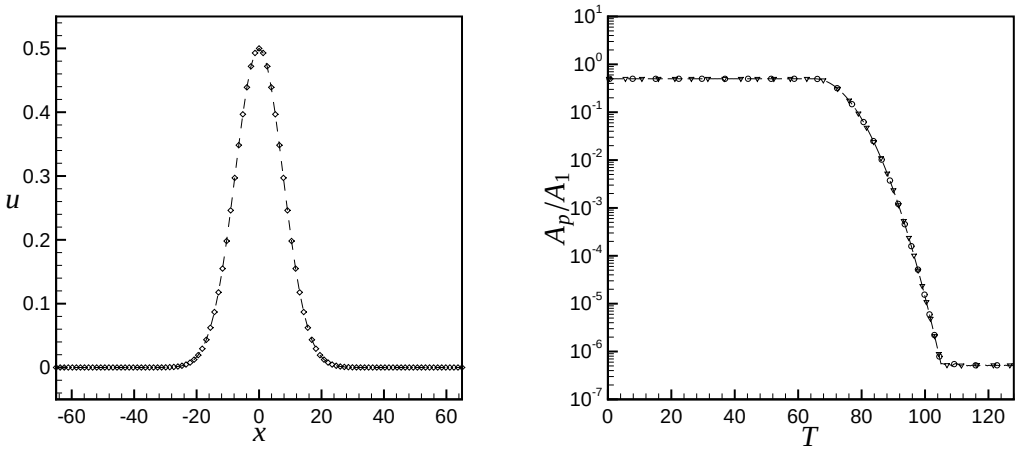

(a) Initial Gaussian profile of eq. (5.7) discretized with 101 mesh points.

(b) Dashed line (−−) $\sigma = 0.05$, triangle (∇) $\sigma = 0.25$, circle ($\circ$) $\sigma = 0.4$.

Figure 5.10: Solution to *LAE* equation with initial Gaussian profile.

wave A_1, two reflection coefficients must be used to characterize a given boundary condition treatment: the reflection coefficient of the physical waves A_p/A_1 and the reflection coefficient of the numerical waves A_q/A_1. In all cases, an adequate boundary condition treatment requires the amplitude of the numerical reflected waves to be small $A_q/A_1 \ll 1$. An adequate *non-reflecting* boundary condition treatment also requires small physical reflected waves ($A_p/A_1 \ll 1$).
The maximum value of the amplitude of the physical reflected waves A_p/A_1 for the given Gaussian pulse is reported in Fig. 5.10(b), and the level of error after the Gaussian pulse has left the domain is below 10^{-6} as reported by Poinsot & Lele (1992). Different tests have been done at three different Courant numbers $\sigma = 0.05$, 0.25 and 0.4, which have proved the invariance theorem of Vichnevetsky (1986) related to the reflection at the numerical boundaries. That is, the energy reflected at the boundaries is independent of the value of the time step, as shown in Fig. 5.10(b) for different values of σ below the stability limit $\sigma_{max} = 1.422$.

5.2 Two-Dimensional Test-Cases

5.2.1 Propagation of an acoustic wave in unbounded domain

Description of the test case

The linearized two-dimensional Euler equations on a uniform flow of eq. (3.11) are solved given an initial acoustic wave propagating in an unbounded domain

$$\begin{aligned} p &= \exp\left[-(\ln 2)\left(\frac{x^2+y^2}{9}\right)\right] \\ \rho &= \exp\left[-(\ln 2)\left(\frac{x^2+y^2}{9}\right)\right] \\ u &= v = 0. \end{aligned}$$

The computational domain extent is $-100 \leq x \leq 100$, $-100 \leq y \leq 100$. scheme.
The numerical predictions are compared against the non-dimensional analytical values given by Tam & Web (1993) and Hardin *et al.* (1995):

$$p = \rho = \frac{1}{2\alpha_1}\int_0^\infty e^{-\xi^2/4\alpha_1}\cos(\xi t)\, J_0(\xi\eta)\,\xi d\xi, \tag{5.13}$$

where $\alpha_1 = [(\ln 2)/9]$, $\eta = \left[\left(x^2+y^2\right)\right]^{1/2}$ and $J_0()$ is the zeroth-order Bessel function of the first kind.

Modelling strategy

The evaluation of the integral in eq. (5.13) has been done numerically by using the The Fortran interface to the GNU Scientific Library (FGSL), using the QAGI adaptive integration on semi-infinite intervals with the 15-point Gauss-Kronrod. An absolute error of $0.2e-14$ has been reached (Bader, 2007).
Boundary conditions are the LODI outflow at top, bottom, left and right, and the classical sixth-order $C1122$ prefactored scheme with 4^{th} order RK time advancement is employed. The Courant number has been set to a low level of $\sigma = 0.05$, to explore the error due to the spatial discretization.
A two-dimensional version of the L_2 norm of eq. (5.5) is used to measure the numerical error,

Run	$N = N_x = N_y$	h	$N_x \times N_y$	n. of iter.	L_2 norm from eq. (5.14)
serial1	51	4	2,601	150	0.02065480432795613
serial2	101	2	10,201	300	0.002327223066439975
serial3	201	1	40,401	600	3.874124288267828e-05
serial4	401	0.5	160,801	1200	5.409684508640224e-07
serial5	801	0.25	641,601	2400	8.240016161063194e-09
serial6	1601	0.125	2,563,201	4800	1.285551852175826e-10
serial7	3201	0.0625	10,246,401	9600	2.04502766168723e-12

Table 5.7: Numerical set-up for Fig. 5.11(c) with aggressive optimization.

which is

$$L_2 = \sqrt{\frac{\sum_{i=1}^{N}\sum_{j=1}^{N}\left(u_{i,j} - u_{i,j}^{exact}\right)^2}{N^2}}. \tag{5.14}$$

Numerical results and discussion

Figures 5.11(a,b) show the comparison between the numerical and the analytical solution of the two-dimensional propagation of the acoustic pulse on the unbounded domain, at the non-dimensional computational time $t = 30$, using a uniform grid spacing both in the x- and y direction, equal to $h = 0.25$ in a quiescent flow, that is $M_x = M_y = 0$. There is no appreciable azimuthal distortion of the wave, showing that the numerical solution does not suffer from any appreciable degradation, and the isotropy of the numerical scheme is preserved in a two dimensional space. Figure 5.11(c) and Table 5.7 show the L_2 norm at various levels of mesh refinement at the same non-dimensional time. It is evident that sixth-order accuracy is maintained with a good approximation up to $L_2 \approx 1.0e-12$.

In order to test the ability of the non-reflecting boundary conditions to accurately predict the exit from the computational domain of the acoustically active flow, further work has to take into account a plug flow of $M_x = 0.5$ in the x-direction.

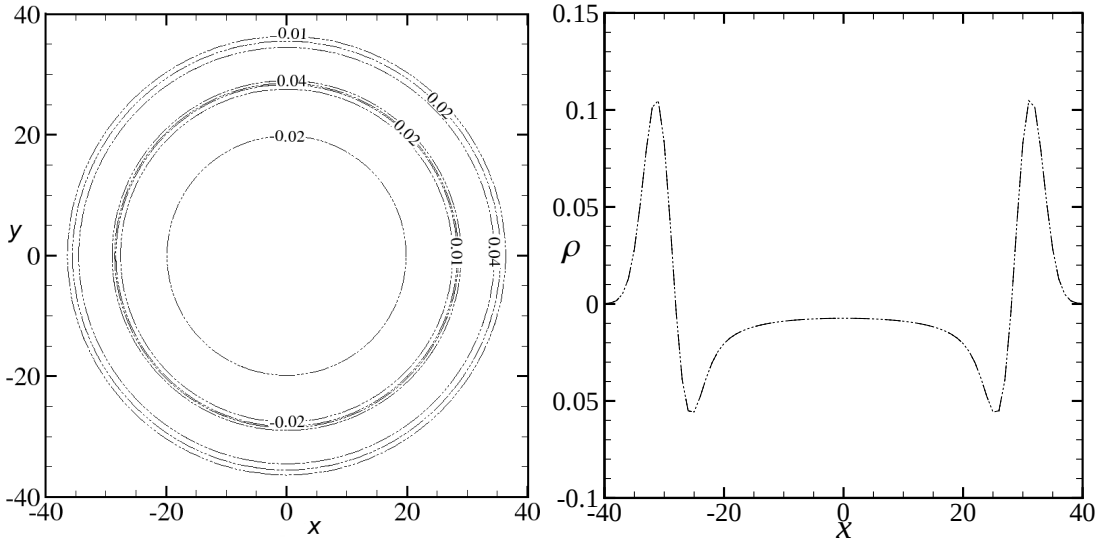

(a) Contours of non-dimensional density perturbation, contour levels: -0.02, 0.01, 0.02, 0.04.

(b) Non-dimensional density perturbation ρ along the y=0 line.

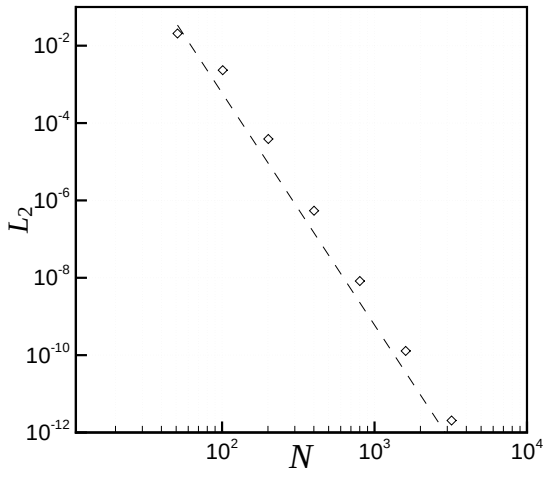

(c) Dashed line (−−) sixth-order logarithmic scale, black diamond (◇) L_2 norm error from eq. 5.14.

Figure 5.11: Propagation of a two-dimensional acoustic pulse on an unbounded domain at non-dimensional $t = 30$, fixed $\sigma = 0.05$; dotted line $(\cdots)$ numerical prediction, dashed line (−−) analytical solution.

5.3 Chapter summary and achievements

This chapter has presented the numerical tests used for the verification and validation of the numerical scheme.

Section 5.1 has presented the one-dimensional test-cases analysed. Section 5.1.1 has validated the numerical scheme against the monochromatic sinusoidal wave.

The classical $C1122/RK4$ scheme coupled with the 11-point boundary stencil of eqs. (3.51a) and (3.51b) has shown an L_2 norm error parallel to the sixth-order roll-off in double precision accuracy, whereas the classical $C1122/RK4$ scheme coupled with the 11-point boundary stencil of Hixon (2000) maintains the sixth-order roll-off in single precision.

The effect of the boundary closure on the L_2 norm error has been studied using the monochromatic sinusoidal wave over an extended domain, using the classical $RK4$ as time integration scheme. The classical C1122 scheme, coupled with the 11-point boundary stencil of eqs. (3.51a) and (3.51b), maintains a straight sixth-order roll-off in double precision accuracy both on the extended and central domain. The cost-optimized $C1122$epsm$n$ schemes present a roll-off lower than the formal fourth-order in the extended domain, whereas in the central domain they display a fourth-order straight line accuracy in double precision accuracy in the region of the well-resolved wavenumber spectrum. This difference in roll-off accuracy is given by the boundary error contribution.

The normalized computed $\overline{L}_2$ norm error, computed for the discrete values of numbers of points per wavelength N_λ, follows the theoretical trend e_0 both for the classical and the cost-optimized schemes, matching the respecting sixth- and fourth-order roll-off in the region of the well-resolved spectra.

A comparison between the theoretical and the computed iso-contours of the 'local' error function for the monochromatic sinusoidal wave have been shown using the classical $C1122/RK4$ scheme and the combined cost-optimized epsm$n$ ones. The computed error maps for the baseline $C1122/RK4$ scheme are shown in good agreement with the theoretical ones in the well-resolved wavenumber range. The computed error maps for the cost-optimized epsm$n$ schemes are in good agreement with the theoretical estimates on the top left hand quadrant of Figs 5.5. The discrepancy of the computed cost-optimized schemes with respect to the theoretical ones, shown on the bottom left quadrant of Figs 5.5, is given by the presence of the spike. The spike region and the region immediately on its left-hand side is not achieved in the numerical tests and it is masked by the temporal integration error from the numerical implementation of the

algorithm.

A good agreement between the theoretical and the numerical optimal cost-error operational points for the baseline $C1122/RK4$ and the cost-optimized epsm$n$ schemes has been achieved. A cost-saving is predicted for the cost-optimized epsm$n$ schemes, in computations running at the design level of error $\tilde{\epsilon} = 10^{-n}$ or a decade below.

In order to verify the computational theoretical cost saving of the optimized schemes in the real computations, the code has been instrumented to measure the effective computed elapsed time during the numerical tests. The measured elapsed time versus the normalized $\overline{L}_2$ norm error follows a similar trend to the theoretical cost-error relation. The measured computational time for the cost-optimized epsm$n$ schemes at their design level of error $\tilde{\epsilon} = 10^{-n}$ is consistently lower than the measured computational time for the classical scheme.

There is a good agreement between the theoretical percentage cost-saving $\Delta\tilde{c}_1^*$ with the measured percentage elapsed time saving $\Delta t\%$ for the simulations reported. Specifically, a measured percentage elapsed time saving up to a 22%, at the design level of error, has been recorded for the cost-optimized epsm5 scheme. This computational time saving is envisaged to be higher for a level of error one decade below the design level of error.

Section 5.1.2 has validated the baseline $C1122/RK4$ numerical scheme against the broadband Gaussian pulse. The ability to model broadband signal with sixth-order accuracy is confirmed by numerical tests. The maximum value of the amplitude of the physical reflected waves A_p/A_1 is satisfactory for an adequate non-reflecting outlet boundary condition. Different tests at different Courant numbers σ have proved the invariance theorem related to the reflection at the numerical boundaries.

Section 5.2 has presented the two-dimensional test-cases analysed. Section 5.2.1 has validated the baseline $C1122/RK4$ numerical scheme against the propagation of an acoustic wave in unbounded domain. The isotropy of the scheme is preserved in a two dimensional space. The L_2 norm roll-off error maintains the sixth-order accuracy up to $L_2 \approx 1.0e-12$.

The main achievements of this Chapter 5 are:

- The baseline scheme coupled with the new prefactored interior 11-point boundary stencil has shown an L_2 norm error parallel to the sixth-order roll-off in double precision accuracy, whereas the equivalent stencil available in literature Hixon (2000) maintains the sixth-order roll-off in single precision.

- The normalized computed $\overline{L}_2$ norm error, computed for the discrete values of numbers of points per wavelength N_λ, follows the theoretical trend e_0 both for the classical and the cost-optimized schemes.
- A good agreement between the theoretical and the numerical optimal cost-error operational points for the baseline and the cost-optimized schemes has been achieved.
- There is a good agreement between the theoretical percentage cost-saving $\Delta\tilde{c}_1^*$ with the measured percentage elapsed time saving $\Delta t\%$ for the simulations reported.
- A measured percentage elapsed time saving up to a 22%, at the design level of error, has been recorded for the cost-optimized epsm5 scheme. This computational time saving is envisaged to be higher for a level of error one decade below the design level of error.
- Sample applications to broad-band, that is the Gaussian pulse, and multi-dimensional space benchmark problems, that is the propagation of an acoustic wave in unbounded domain, have shown the low error-bounded and high-order accuracy characteristics of the baseline scheme.

Chapter 6

Conclusion

The major achievements that has been accomplished during this work are:

- A new class of prefactored cost-optimized schemes has been developed for low-speed error-bounded aeroacoustic applications. This work has extended Pirozzoli (2007)'s theory to the prefactored compact high-order scheme of Hixon (2000).
- Theoretical prediction for spatial and temporal error bounds were determined and compared against benchmark classical schemes. The performance of popular schemes for *CAA* applications and the cost-optimized schemes have been compared in terms of computational efficiency.
- High-order boundary closures, which are accurate and stable within a given Fourier space envelope, are coupled with the interior prefactored schemes. An eigenvalue analysis has verified the stability of the prefactored cost-optimized schemes coupled with these boundary closures.
- To aid parallelization, an appropriate interior boundary stencil was developed that was shown to be an improvement over the equivalent one of Hixon (2000) and Ashcroft & Zhang (2003).
- The scheme was shown to be scalable for execution on *HPC* clusters with a good scalability up to 128 processors.
- A monochromatic sinusoidal test-case verified the theoretical roll-off error against the computed $\overline{L}_2$ norm error, indicating that the cost-optimized schemes perform according to the design high-order accuracy characteristics for this class of problems.

- The design cost-optimization of the schemes was achieved, as verified by numerical experiments. A 22% computational cost-saving at the design level of error was recorded. The percentage cost-saving is envisaged to be higher for a level of error one decade below than the design level of error and even more in a multi-dimensional space.

- Sample applications to broad-band and multi-dimensional space benchmark problems (Hardin *et al.*, 1995) have shown the low error-bounded and high-order accuracy characteristics of the baseline scheme.

The ideal field of application of the newly developed schemes is in the Direct Noise Computation over large domains by solving the LEE, such in the case of low-speed aeroacoustic problems, or to predict the far-field sound radiation from a near-field solution over a closed boundary (Lighthill, 1978).

These newly developed cost-optimized schemes are not suitable for problems involving sharp changes of state variables. Such discontinuities are not modelled well by these high-order centred schemes, just like in Essentially Non-Oscillatory (ENO) schemes.

The main limitation of the cost-optimization analysis is that it does not strictly apply to problems where the selection of the grid spacing is dictated by physical constraints, such as in the computational set-up for boundary layers and in computational grids with severe stretching. The use of appropriate boundary closures that mimic the behaviour of the interior schemes in the spectral sense have to be addressed in further work.

Appendix A

Appendix

A.1 Derivation of the amplification factor for the time integration

This is the derivation of the amplification factor presented in sec. 2.2.

The temporal Fourier transform is obtained by replacing in (2.4) k with t, and κ with ω:

$$\tilde{f}(\omega) = \int_{0?}^{\infty} f(t)\, e^{-\mathrm{i}\,\omega\, t} dt, \tag{A.1}$$

Applying a temporal Fourier transform to eq. (2.24):

$$\tilde{\mathbf{U}}^{n+1} = \tilde{\mathbf{U}}^{n} + \sum_{j=1}^{p} \gamma_j\, \Delta t^j\, \frac{\partial^j \tilde{\mathbf{U}}^{n}}{\partial t^j} \qquad \text{using (2.18)} \tag{A.2a}$$

$$\tilde{\mathbf{U}}^{n+1} = \tilde{\mathbf{U}}^{n} \left\{ 1 + \sum_{j=1}^{p} \gamma_j \left(-\mathrm{i}\, c\, \bar{k}(k) \Delta t \right)^j \right\} \tag{A.2b}$$

$$r\,(\kappa, Co) = \frac{\tilde{\mathbf{U}}^{n+1}}{\tilde{\mathbf{U}}^{n}} = 1 + \sum_{j=1}^{p} \gamma_j \left(-\mathrm{i}\, \bar{\kappa}(\kappa)\, Co \right)^j = 1 + \sum_{j=1}^{p} \gamma_j \left(-\mathrm{i}\bar{z} \right)^j = |r^*\,(\omega \Delta t)|\, e^{i\omega^* \Delta t} \tag{A.2c}$$

A.2 LODI system along y axis

The following is a replication of section 3.1.2.2, where the boundaries are now located on the y axis.

Let consider the boundaries located at $y = 0$ and $y = L$. The governing equation (3.6) can be re-cast as:

$$\frac{\partial \mathbf{U}^*}{\partial t^*} + B_0 \frac{\partial \mathbf{U}^*}{\partial y^*} + C = 0 \quad C = A_0 \frac{\partial \mathbf{U}^*}{\partial x^*} \tag{A.3}$$

Where the C vector contains all remaining terms which do not involve elements of $\frac{\partial \mathbf{U}^*}{\partial y^*}$
Let's apply the characteristic decomposition to the B_0 matrix

$$det(B_0 - \lambda_i I) = 0 \tag{A.4}$$
$$\lambda_1 = M_y - 1, \qquad \lambda_2 = \lambda_3 = M_y, \qquad \lambda_4 = M_y + 1.$$

Eigenvalues λ_1 and λ_4 are the velocities of sound waves moving in the negative and positive y direction. λ_2 is the convection velocity (the speed at which entropy waves will travel), while λ_3 is the velocity at which the u-velocity is advected along the y-direction. Note that the characteristic velocities are constant because they derive from the linearized matrix (B_0 is a costant-element matrix).
The corresponding eigenvectors are given by:

$$\begin{aligned} l_1^T &= (0,\ 0,\ -1,\ 1) \quad \Longrightarrow l_1^T \cdot (A_0 - \lambda_1 I) = 0 \\ l_2^T &= (1,\ 0,\ 0,\ -1) \quad \Longrightarrow l_2^T \cdot (A_0 - \lambda_2 I) = 0 \\ l_3^T &= (0,\ 1,\ 0,\ 0) \quad \Longrightarrow l_3^T \cdot (A_0 - \lambda_3 I)^2 = 0 \\ l_4^T &= (0,\ 0,\ 1,\ 1) \quad \Longrightarrow l_4^T \cdot (A_0 - \lambda_4 I) = 0 \end{aligned} \tag{A.5}$$

The L_i's represent the amplitude of characteristic waves associated with each characteristic velocity λ_i

$$L_i = \lambda_i l_i^T \frac{\partial \mathbf{U}^*}{\partial x^*} \tag{A.6}$$

$$L_1 = \lambda_1 l_1^T \frac{\partial \mathbf{U}^*}{\partial y^*} = \lambda_1(0,\ 0,\ -1,\ 1)\frac{\partial}{\partial y^*}\begin{pmatrix} \rho^* \\ u^* \\ v^* \\ p^* \end{pmatrix} = \lambda_1\left(\frac{\partial p^*}{\partial y^*} - \frac{\partial v^*}{\partial y^*}\right) \tag{A.7}$$

$$L_2 = \lambda_2 l_2^T \frac{\partial \mathbf{U}^*}{\partial y} = \lambda_2(1,\ 0,\ 0,\ -1)\frac{\partial}{\partial y^*}\begin{pmatrix} \rho^* \\ u^* \\ v^* \\ p^* \end{pmatrix} = \lambda_2\left(\frac{\partial \rho^*}{\partial y^*} - \frac{\partial p^*}{\partial y^*}\right) \tag{A.8}$$

$$L_3 = \lambda_3 l_3^T \frac{\partial \mathbf{U}^*}{\partial y^*} = \lambda_3(0,\ 1,\ 0,\ 0)\frac{\partial}{\partial y^*}\begin{pmatrix} \rho^* \\ u^* \\ v^* \\ p^* \end{pmatrix} = \lambda_3\frac{\partial u^*}{\partial y^*} \tag{A.9}$$

$$L_4 = \lambda_4 l_4^T \frac{\partial \mathbf{U}^*}{\partial y^*} = \lambda_4(0,\ 0,\ 1,\ 1)\frac{\partial}{\partial y^*}\begin{pmatrix} \rho^* \\ u^* \\ v^* \\ p^* \end{pmatrix} = \lambda_4\left(\frac{\partial p^*}{\partial y^*} + \frac{\partial v^*}{\partial y^*}\right) \tag{A.10}$$

or

$$L = \begin{pmatrix} L_1 \\ L_2 \\ L_3 \\ L_4 \end{pmatrix} = \begin{bmatrix} \lambda_1\left(\frac{\partial p^*}{\partial y^*} - \frac{\partial v^*}{\partial y^*}\right) \\ \lambda_2\left(\frac{\partial \rho}{\partial y^*} - \frac{\partial p^*}{\partial y^*}\right) \\ \lambda_3\frac{\partial u^*}{\partial y^*} \\ \lambda_4\left(\frac{\partial p^*}{\partial y^*} + \frac{\partial v^*}{\partial y^*}\right) \end{bmatrix} \tag{A.11}$$

By using the prefactored scheme, for a given f fow state variable, we have that the OSD (One-Sided Difference Approximation) at the first and last node along the y-axis are given by:

$$\frac{\partial f_1}{\partial y} = \frac{1}{2}\left(\frac{\partial f_1^B}{\partial y} + \frac{\partial f_1^F}{\partial y}\right) \quad \frac{\partial f_1^B}{\partial y} = \frac{1}{\Delta y}\sum_{i=1}^{7} s_i f_i \quad \frac{\partial f_1^F}{\partial y} = \frac{1}{\Delta y}\sum_{i=1}^{7} -e_{N+1-i} f_i \tag{A.12}$$

$$\frac{\partial f_N}{\partial y} = \frac{1}{2}\left(\frac{\partial f_N^B}{\partial y} + \frac{\partial f_N^F}{\partial y}\right) \quad \frac{\partial f_N^B}{\partial y} = \frac{1}{\Delta y}\sum_{i=N-6}^{N} e_i f_i \quad \frac{\partial f_N^F}{\partial y} = \frac{1}{\Delta y}\sum_{i=N-6}^{N} -s_{N+1-i} f_i \tag{A.13}$$

The corresponding equation for the L_i's become

$$\begin{aligned}
L_1 &= \frac{1}{2}\left(L_1^B + L_1^F\right) \\
L_2 &= \frac{1}{2}\left(L_2^B + L_2^F\right) \\
L_3 &= \frac{1}{2}\left(L_3^B + L_3^F\right) \\
L_4 &= \frac{1}{2}\left(L_4^B + L_4^F\right) \\
L_1^B &= \lambda_1\left(\frac{\partial p^B}{\partial y} - \rho_0 c_0 \frac{\partial v^B}{\partial y}\right) \\
L_1^F &= \lambda_1\left(\frac{\partial p^F}{\partial y} - \rho_0 c_0 \frac{\partial v^F}{\partial y}\right) \\
L_2^B &= \lambda_2\left(c_0^2\frac{\partial \rho^B}{\partial y} - \frac{\partial p^B}{\partial y}\right) \\
L_2^F &= \lambda_2\left(c_0^2\frac{\partial \rho^F}{\partial y} - \frac{\partial p^F}{\partial y}\right) \\
L_3^B &= \lambda_3\frac{\partial u^B}{\partial y} \\
L_3^F &= \lambda_3\frac{\partial u^F}{\partial y} \\
L_4^B &= \lambda_4\left(\frac{\partial p^B}{\partial y} + \rho_0 c_0 \frac{\partial v^B}{\partial y}\right) \\
L_4^F &= \lambda_4\left(\frac{\partial p^F}{\partial y} + \rho_0 c_0 \frac{\partial v^F}{\partial y}\right)
\end{aligned} \tag{A.14}$$

Eq. A.11 can be inverted to give the *y*-derivatives of the primitives variables:

$$\frac{\partial \rho^*}{\partial y^*} = \frac{L_2}{\lambda_2} + \frac{1}{2}\left(\frac{L_4}{\lambda_4} + \frac{L_1}{\lambda_1}\right) \tag{A.15}$$

$$\frac{\partial u^*}{\partial y^*} = \frac{L_3}{\lambda_3} \tag{A.16}$$

$$\frac{\partial v^*}{\partial y^*} = \frac{1}{2}\left(\frac{L_4}{\lambda_4} - \frac{L_1}{\lambda_1}\right) \tag{A.17}$$

$$\frac{\partial p^*}{\partial y^*} = \frac{1}{2}\left(\frac{L_4}{\lambda_4} + \frac{L_1}{\lambda_1}\right) \tag{A.18}$$

$$\tag{A.19}$$

In the code, we need the prefactored OSD spatial derivatives, which can be obtained as:

$$\frac{\partial \rho^B}{\partial y} = \frac{1}{c_0^2}\left[\frac{L_2^B}{u_0} + \frac{1}{2}\left(\frac{L_4^B}{u_0 + c_0} + \frac{L_1^B}{u_0 - c_0}\right)\right] \tag{A.20}$$

$$\frac{\partial \rho^F}{\partial y} = \frac{1}{c_0^2}\left[\frac{L_2^F}{u_0} + \frac{1}{2}\left(\frac{L_4^F}{u_0 + c_0} + \frac{L_1^F}{u_0 - c_0}\right)\right] \tag{A.21}$$

$$\frac{\partial u^B}{\partial y} = \frac{L_3^B}{v_0} \tag{A.22}$$

$$\frac{\partial u^F}{\partial y} = \frac{L_3^F}{v_0} \tag{A.23}$$

$$\frac{\partial v^B}{\partial y} = \frac{1}{2\rho_0 c_0}\left[\frac{L_4^B}{v_0 + c_0} - \frac{L_1^B}{v_0 - c_0}\right] \tag{A.24}$$

$$\frac{\partial v^F}{\partial y} = \frac{1}{2\rho_0 c_0}\left[\frac{L_4^F}{v_0 + c_0} - \frac{L_1^F}{v_0 - c_0}\right] \tag{A.25}$$

$$\frac{\partial p^B}{\partial y} = \frac{1}{2}\left[\frac{L_4^B}{v_0 + c_0} + \frac{L_1^B}{v_0 - c_0}\right] \tag{A.26}$$

$$\frac{\partial p^F}{\partial y} = \frac{1}{2}\left[\frac{L_4^F}{v_0 + c_0} + \frac{L_1^F}{v_0 - c_0}\right] \tag{A.27}$$

$$\tag{A.28}$$

The S matrix and its inversion are given by:

$$S^{-1} = \begin{pmatrix} l_1^T \\ l_2^T \\ l_3^T \\ l_4^T \end{pmatrix} = \begin{bmatrix} 0 & 0 & -\rho_0 c_0 & 1 \\ c_0^2 & 0 & 0 & -1 \\ 0 & 1 & 0 & 0 \\ 0 & 0 & \rho_0 c_0 & 1 \end{bmatrix} \tag{A.29}$$

$$S = \begin{pmatrix} r_1 & r_2 & r_3 & r_4 \end{pmatrix} = \begin{bmatrix} \frac{1}{2c_0^2} & \frac{1}{c_0^2} & 0 & \frac{1}{2c_0^2} \\ 0 & 0 & 1 & 0 \\ \frac{-1}{2\rho_0 c_0} & 0 & 0 & \frac{1}{2\rho_0 c_0} \\ \frac{1}{2} & 0 & 0 & \frac{1}{2} \end{bmatrix} \tag{A.30}$$

Please note that $S^{-1}S = I$, and $l_i^T \cdot r_j = \delta_{ij}$, where δ_{ij} is the Kroneker's delta.

The **d** vector is given by:

$$\mathbf{d} = \begin{pmatrix} d_1 \\ d_2 \\ d_3 \\ d_4 \end{pmatrix} = S \cdot L = \begin{bmatrix} \frac{1}{2c_0^2} & \frac{1}{c_0^2} & 0 & \frac{1}{2c_0^2} \\ 0 & 0 & 1 & 0 \\ \frac{-1}{2\rho_0 c_0} & 0 & 0 & \frac{1}{2\rho_0 c_0} \\ \frac{1}{2} & 0 & 0 & \frac{1}{2} \end{bmatrix} \begin{pmatrix} L_1 \\ L_2 \\ L_3 \\ L_4 \end{pmatrix} = \begin{bmatrix} \frac{1}{c_0^2}\left(L_2 + \frac{1}{2}(L_1 + L_4)\right) \\ L_3 \\ \frac{1}{2\rho_0 c_0}(L_4 - L_1) \\ \frac{1}{2}(L_4 + L_1) \end{bmatrix} \tag{A.31}$$

The initial govering equation (3.6) can be now re-written in the desired form:

$$\frac{\partial \mathbf{U}^*}{\partial t^*} + \mathbf{d} + A_0 \frac{\partial \mathbf{U}}{\partial x} = 0 \tag{A.32}$$

or in extended form:

$$\begin{array}{lll}
\frac{\partial \rho}{\partial t} + \frac{1}{c_0^2}\left(L_2 + \frac{1}{2}(L_1 + L_4)\right) & +u_0\frac{\partial \rho}{\partial x} + \rho_0\frac{\partial u}{\partial x} & = 0 \\
\frac{\partial u}{\partial t} + \frac{1}{2\rho_0 c_0}(L_4 - L_1) & +u_0\frac{\partial u}{\partial x} & = 0 \\
\frac{\partial v}{\partial t} + L_3 & +u_0\frac{\partial v}{\partial x} & = 0 \\
\frac{\partial p}{\partial t} + \frac{1}{2}(L_4 + L_1) & +u_0\frac{\partial u}{\partial x} + \rho_0 c_0^2\frac{\partial u}{\partial x} & = 0
\end{array} \tag{A.33}$$

The LODI system in terms of primitive variables for the 2-D Linerized Euler equation along the *y* direction is formally identical to eq. (3.23); the only difference if given by the different equation for the $L_i's$ along the *x* and *y* direction, given, respectively, by eq. (3.17) and (A.11).

A.3 Coefficients for FD schemes

Classical centered explicit schemes

For the algebraic calculation of eq (2.1) and (2.9), recall the Taylor series expansion of the function $f_{i\pm\ell}(x)$, at the $(i \pm \ell)_{th}$ mesh point around the mesh point i:

$$f_{i+\ell} = f_i + \sum_{n=1}^{\infty} \frac{(\ell\, h)^n}{n!} \frac{\partial^n f_i}{\partial x^n} \tag{A.34}$$

$$f_{i-\ell} = f_i + \sum_{n=1}^{\infty} \left[\pm \frac{(\ell\, h)^n}{n!} \right] \frac{\partial^n f_i}{\partial x^n} (\text{ + for even } n, \text{ - for odd } n\ ) \tag{A.35}$$

and the Euler relation:

$$e^{\pm \mathbf{i} \ell \kappa} = \cos(\ell\kappa) \pm \mathbf{i} \sin(\ell\kappa) \tag{A.36}$$

The first unmatched coefficient determines the formal truncation error of eq. (2.1),(Lele, 1992):

$$2 \sum_{\ell=1}^{q} \ell a_\ell = 1 \qquad \text{(second order)} \tag{A.37}$$

$$2 \sum_{\ell=1}^{q} \ell^3 a_\ell = 0 \qquad \text{(fourth order)} \tag{A.38}$$

$$2 \sum_{\ell=1}^{q} \ell^5 a_\ell = 0 \qquad \text{(sixth order)} \tag{A.39}$$

$$2 \sum_{\ell=1}^{q} \ell^7 a_\ell = 0 \qquad \text{(eighth order)} \tag{A.40}$$

$$2 \sum_{\ell=1}^{q} \ell^9 a_\ell = 0 \qquad \text{(tenth order)} \tag{A.41}$$

$$2 \sum_{\ell=1}^{q} \ell^{11} a_\ell = 0 \qquad \text{(twelfth order)} \tag{A.42}$$

So, it is possible to enumerate the following schemes, with the relatives coefficients given in Tab. A.1:

- $C0011$, $Q = P = 0$, $S = R = 1$. Classical explicit second order scheme, three point

stencil

$$f_i' \simeq a_1 \frac{(f_{i+1} - f_{i-1})}{h} \tag{A.43}$$

$$\overline{\kappa}(\kappa) = 2a_1 \sin(\kappa) \tag{A.44}$$

$$\frac{\partial \overline{\kappa}(\kappa)}{\partial \kappa} = 2a_1 \cos(\kappa) \tag{A.45}$$

- $C0022$, $Q = P = 0$, $S = R = 2$. Classical explicit fourth order scheme, five point stencil

$$f_i' \simeq a_2 \frac{(f_{i+2} - f_{i-2})}{h} + a_1 \frac{(f_{i+1} - f_{i-1})}{h} \tag{A.46}$$

$$\overline{\kappa}(\kappa) = 2\left[a_1 \sin(\kappa) + a_2 \sin(2\kappa)\right] \tag{A.47}$$

$$\frac{\partial \overline{\kappa}(\kappa)}{\partial \kappa} = 2\left[a_1 \cos(\kappa) + 2a_2 \cos(2\kappa)\right] \tag{A.48}$$

- $C0033$, $Q = P = 0$, $S = R = 3$. Classical explicit sixth order scheme, seven point stencil

$$f_i' \simeq a_3 \frac{(f_{i+3} - f_{i-3})}{h} + a_2 \frac{(f_{i+2} - f_{i-2})}{h} + a_1 \frac{(f_{i+1} - f_{i-1})}{h} \tag{A.49}$$

$$\overline{\kappa}(\kappa) = 2\left[a_1 \sin(\kappa) + a_2 \sin(2\kappa) + a_3 \sin(3\kappa)\right] \tag{A.50}$$

$$\frac{\partial \overline{\kappa}(\kappa)}{\partial \kappa} = 2\left[a_1 \cos(\kappa) + 2a_2 \cos(2\kappa) + 3a_3 \cos(3\kappa)\right] \tag{A.51}$$

- $C0044$, $Q = P = 0$, $S = R = 4$. Classical explicit eighth order scheme, nine point stencil

$$f_i' \simeq a_4 \frac{(f_{i+4} - f_{i-4})}{h} + a_3 \frac{(f_{i+3} - f_{i-3})}{h} + a_2 \frac{(f_{i+2} - f_{i-2})}{h} + a_1 \frac{(f_{i+1} - f_{i-1})}{h} \tag{A.52}$$

$$\overline{\kappa}(\kappa) = 2\left[a_1 \sin(\kappa) + a_2 \sin(2\kappa) + a_3 \sin(3\kappa) + a_4 \sin(4\kappa)\right] \tag{A.53}$$

$$\frac{\partial \overline{\kappa}(\kappa)}{\partial \kappa} = 2\left[a_1 \cos(\kappa) + 2a_2 \cos(2\kappa) + 3a_3 \cos(3\kappa) + 4a_4 \cos(4\kappa)\right] \tag{A.54}$$

- $C0055$, $Q = P = 0$, $S = R = 5$. Classical explicit tenth order scheme, eleven point stencil

$$f_i' \simeq a_5 \frac{(f_{i+5} - f_{i-5})}{h} + a_4 \frac{(f_{i+4} - f_{i-4})}{h} + a_3 \frac{(f_{i+3} - f_{i-3})}{h} + a_2 \frac{(f_{i+2} - f_{i-2})}{h} + a_1 \frac{(f_{i+1} - f_{i-1})}{h} \tag{A.55}$$

$$\overline{\kappa}(\kappa) = 2\left[a_1 \sin(\kappa) + a_2 \sin(2\kappa) + a_3 \sin(3\kappa) + a_4 \sin(4\kappa) + a_5 \sin(5\kappa)\right] \tag{A.56}$$

$$\frac{\partial \overline{\kappa}(\kappa)}{\partial \kappa} = 2\left[a_1 \cos(\kappa) + 2a_2 \cos(2\kappa) + 3a_3 \cos(3\kappa) + 4a_4 \cos(4\kappa) + 5a_5 \cos(5\kappa)\right] \tag{A.57}$$

Scheme	C0011	C0022	C0033	C0044	C0055	C0066
a_1	0.5	2/3	3/4	4/5	5/6	6/7
a_2		-1/12	-3/20	-1/5	-5/21	-15/56
a_3			1/60	4/105	5/84	5/63
a_4				-1/280	-5/504	-1/56
a_5					1/1260	3/1155
a_6						-1/5544
$\bar{\kappa}_{max}$	0.99	1.37	1.58	1.73	1.83	1.92
stencil size	3	5	7	9	11	13
Order (n)	2	4	6	8	10	12

Table A.1: Coefficients of the classical centred explicit $CPQRS$ schemes, $P = Q = 0$, $R = S$, $\alpha_0 = 1$, $a_0 = 0$, $a_{-j} = a_j$.

- $C0066$, $Q = P = 0$, $S = R = 6$. Classical explicit twelfth order scheme, thirteen point stencil

$$f'_i \cong a_6\frac{(f_{i+6} - f_{i-6})}{h} + a_5\frac{(f_{i+5} - f_{i-5})}{h} + a_4\frac{(f_{i+4} - f_{i-4})}{h} + a_3\frac{(f_{i+3} - f_{i-3})}{h} + a_2\frac{(f_{i+2} - f_{i-2})}{h} + a_1\frac{(f_{i+1} - f_{i-1})}{h} \tag{A.58}$$

$$\bar{\kappa}(\kappa) = 2\left[a_1\sin(\kappa) + a_2\sin(2\kappa) + a_3\sin(3\kappa) + a_4\sin(4\kappa) + a_5\sin(5\kappa) + a_6\sin(6\kappa)\right] \tag{A.59}$$

$$\frac{\partial\bar{\kappa}(\kappa)}{\partial\kappa} = 2\left[a_1\cos(\kappa) + 2a_2\cos(2\kappa) + 3a_3\cos(3\kappa) + 4a_4\cos(4\kappa) + 5a_5\cos(5\kappa) + 6a_6\cos(6\kappa)\right] \tag{A.60}$$

Optimized centered explicit schemes

Tam & Web (1993) constructed a 7-point, 4^{th} order central difference scheme based on a minimalisation of the dispersion error of eq. (2.11). They have chosen the coefficients a_2 and a_3 to obtain a 4th-order accurate scheme, so the first two constrains (A.37), (A.38) are imposed; to assure a minimal dispersion, the coefficient a_1 in eq. (A.49) have been chosen to minimize E:

$$\frac{\partial E}{\partial a_1} = 0, \tag{A.61}$$

where the integral error E is the squared difference between the scaled pseudo-wavenumber $\bar{\kappa}$ and the scaled wavenumber κ:

$$E = \int_0^{\pi/2} |\bar{\kappa}(\kappa) - \kappa|^2 d\kappa. \tag{A.62}$$

Scheme	TamDRP7p	BBo9p	BBo11p	BBo13p
a_1	0.799266426974156	0.841570125482	0.872756993962	0.907646591371
a_2	-0.189413141579325	-0.244678631765	-0.286511173973	-0.337048393268
a_3	0.0265199520614978	0.059463584768	0.090320001280	0.132442885327
a_4		-0.007650904064	-0.020779405824	-0.045246480208
a_5			0.002484594688	0.011169294114
a_6				-0.001456501759
$\bar{\kappa}_{max}$	1.72	1.87	1.98	2.13
stencil size	7	9	11	13
Order (n)	4	4	6	8

Table A.2: Coefficients of the optimized centered explicit schemes, $Q = R = 0$, $\alpha_0 = 1$, $q = r$, $a_0 = 0$, $a_{-j} = a_j$.

The different coefficients, for the optimized scheme, denoted thereafter as $TamDRP7p$ are given in Tab. A.2.

Rock *et al.* (2004), in their overview, have reported the following different coefficients for the $TamDRP7p$ scheme:

$$\begin{aligned} a1 &= 0.77088238051822552 \\ a2 &= 0.166705904414580469 \\ a3 &= 0.02084314277031176, \end{aligned} \tag{A.63}$$

where the integral error has been minimized in the range $[0, 1.1]$.

Bogey & Bailly (2004), using the same theory as Tam and Webb, do not minimize the absolute difference between $\bar{\kappa}$ and κ, but the relative difference, optimizing the classical explicit eight order scheme, 9-point stencil $C0044$ (see eq A.52), the tenth order scheme, 11-point stencil $C0055$ (see eq A.55), and the twelfth order scheme, 13-point stencil $C0066$ (see eq A.58). These optimized schemes will be denoted respectively as $BBo9p$, $BBo11p$ and $BBo13p$.

The integrated error E then becomes:

$$E = \int_{\kappa_l}^{\kappa_h} \frac{|\bar{\kappa}(\kappa) - \kappa|}{\kappa} d\kappa = \int_{\ln(\kappa_l)}^{\ln(\kappa_h)} |\bar{\kappa}(\kappa) - \kappa| d(\ln \kappa) \tag{A.64}$$

This schemes are developed so that the dispersion error is small for a large range of wavenumbers up to $\kappa = \pi/2$. Two coefficients are chosen with the Taylor Series truncation method to

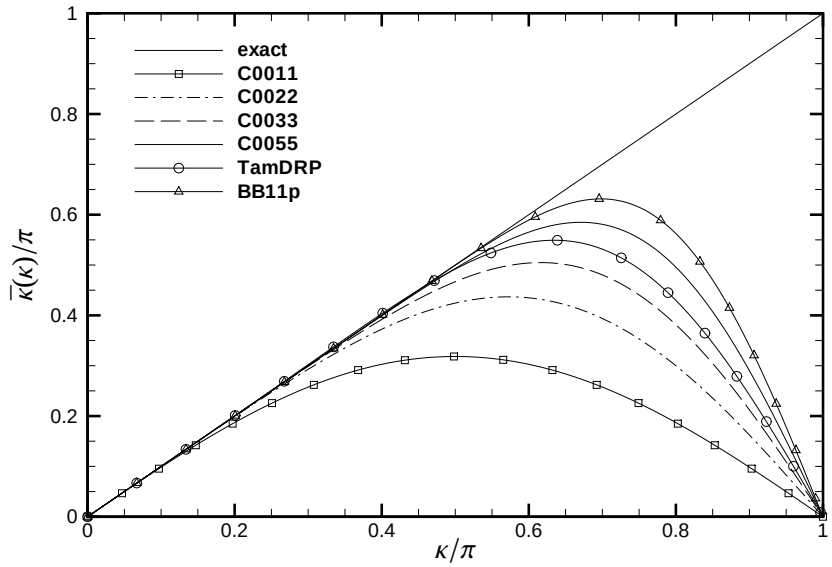

Figure A.1: Scaled pseudo-wavenumber diagram for a selection of explicit centered finite-difference schemes.

obtain a 4^{th} order accurate scheme, and the remaining coefficients a_j are defined to minimize the integral error E of eq. (A.64), where the wavenumbers limits are $\kappa_l = \pi/16$, and $\kappa_h = \pi/2$ for the $BBo9p$ and $BBo11p$, and $\kappa_l = \pi/16$, and $\kappa_h = 3\pi/5$ for the $BBop13$. The optimized coefficients are given in table A.2.

The relation between the scaled pseudo-wavenumber and the scaled wavenumber for the explicit classical and optimized schemes is shown in Fig. A.1. The DRP schemes are low dispersive as long as there is a good superposition with the line of exact differentiation. Increasing the number of points, from $N_\lambda = 3$ to 6, allows to decrease the dispersion error for short waves. It is adequate note that the grid-to-grid waves with $\kappa = \pi$ are never resolved.

The dispersive error is represented in logarithmic scales in Fig. A.2 for the standard and the optimized explicit schemes. The optimized schemes are clearly less dispersive than the standard equivalent stencil-size ones for short waves with $\kappa > \pi/4$, (i.e. $N_\lambda < 8$). The reduction of the error is particularly important for the wavenumbers near $\kappa \approx \pi/2$, (i.e. $N_\lambda \approx 4$) with at least one order of magnitude between the optimized and the standard schemes. The optimized schemes are also more dispersive for long waves, $N_\lambda > 8 - 10$ compared the their calssical counterpart, because of their lower formal order, but the dispersion error is then very small, about or less

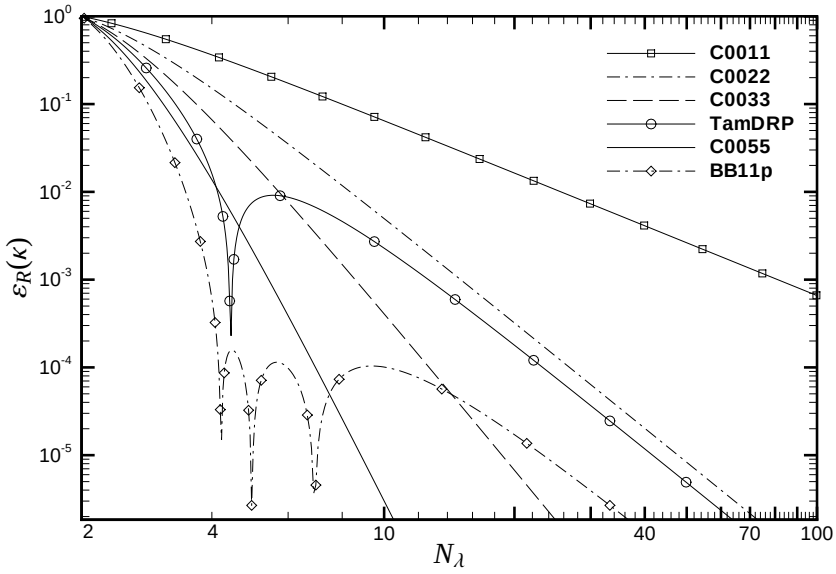

Figure A.2: Dispersive error for a selection of explicit centered finite-difference schemes.

than $10^{-4}/10^{-5}$.

Classical centred implicit schemes

The compact, (also implicit or Pade´), schemes are obtained when $P = Q \neq 0$ in eq (2.1), and a matrix has to be inverted to determine the unknown values of the approximation of the first derivatives, (L.H.S. of eq. 2.1). In the case of $Q = R = 1$ and $Q = R = 2$, a tridiagonal and a pentadiagonal system, respectively, has to be solved for every grid point. Equations (2.1) and (2.9) will be re-written as:

$$f'_i + \sum_{j=1}^{Q} \left[\alpha_j \left(f'_{i+j} + f'_{i-j}\right)\right] = \frac{1}{h} \sum_{j=1}^{S} \left[a_j \left(f_{i+j} - f_{i-j}\right)\right] + O(h^n), \tag{A.65}$$

$$\overline{\kappa}(\kappa) = \frac{\sum_{j=1}^{S} 2a_j \sin(j\kappa)}{1 + \sum_{j=1}^{Q} 2\alpha_j \cos(j\kappa)}, \tag{A.66}$$

The group velocity is:

$$\frac{c_g}{c} = \frac{\partial\bar{\kappa}(\kappa)}{\partial\kappa} = 2\frac{\left[\sum_{j=1}^{S} j a_j \cos(j\kappa)\right]\cdot\left[1+\sum_{j=1}^{Q} 2\alpha_j\cos(j\kappa)\right] + \left[\sum_{j=1}^{S} a_j \sin(j\kappa)\right]\cdot\left[\sum_{j=1}^{Q} 2j\alpha_j \sin(j\kappa)\right]}{\left[1+\sum_{j=1}^{Q} 2\alpha_j\cos(j\kappa)\right]^2}, \tag{A.67}$$

The relations of order become:

$$2\sum_{j=1}^{S} j a_j = 1 + 2\sum_{j=1}^{Q}\alpha_j \qquad \text{(second order)} \tag{A.68}$$

$$2\sum_{j=1}^{S} j^3 a_j = 2\frac{3!}{2!}\left(\alpha_1 + \sum_{j=2}^{Q} 2^j\alpha_j\right) \qquad \text{(fourth order)} \tag{A.69}$$

$$2\sum_{j=1}^{S} j^5 a_j = 2\frac{5!}{4!}\left(\alpha_1 + \sum_{j=2}^{Q} 2^{2j}\alpha_j\right) \qquad \text{(sixth order)} \tag{A.70}$$

$$2\sum_{j=1}^{S} j^7 a_j = 2\frac{7!}{6!}\left(\alpha_1 + \sum_{j=2}^{Q} 2^{3j}\alpha_j\right) \qquad \text{(eighth order)} \tag{A.71}$$

$$2\sum_{j=1}^{q} j^9 a_j = 2\frac{9!}{8!}\left(\alpha_1 + \sum_{j=2}^{Q} 2^{4j}\alpha_j\right) \qquad \text{(tenth order)} \tag{A.72}$$

$$2\sum_{j=1}^{q} j^{11} a_j = 2\frac{11!}{10!}\left(\alpha_1 + \sum_{j=2}^{Q} 2^{5j}\alpha_j\right) \qquad \text{(twelfth order)} \tag{A.73}$$

Tridiagonal classical and optimized schemes

Let's consider a family of tridiagonal schemes with five point stencil. This are generated in eq. (A.65) by setting $Q = 1$ and $S = 2$:

$$\alpha_1 f'_{i-1} + f'_i + \alpha_1 f'_{i+1} \cong a_2\frac{(f_{i+2} - f_{i-2})}{h} + a_1\frac{(f_{i+1} - f_{i-1})}{h} \tag{A.74}$$

$$\bar{\kappa}(\kappa) = \frac{2\left[a_1\sin(\kappa) + a_2\sin(2\kappa)\right]}{1 + 2\alpha_1\cos(\kappa)}, \tag{A.75}$$

$$\frac{\partial\bar{\kappa}(\kappa)}{\partial\kappa} = 2\frac{\left[a_1\cos(\kappa) + 2a_2\cos(2\kappa)\right]\left[1 + 2\alpha_1\cos(\kappa)\right] + \left[a_1\sin(\kappa) + a_2\sin(2\kappa)\right]\left[2\alpha_1\sin(\kappa)\right]}{\left[1 + 2\alpha_1\cos(\kappa)\right]^2} \tag{A.76}$$

By imposing fourth-order accuracy (using the eq. A.68 and A.69) the following relations are obtained:

$$\begin{cases} a_2 = -a_{-2} = \dfrac{1}{12}(4\alpha_1 - 1) \\ a_1 = -a_{-1} = \dfrac{1}{3}(\alpha_1 + 2) \end{cases} \tag{A.77}$$

where α is a free parameter:

- As $\alpha \to 0$, the classical explicit fourth order scheme $C0022$ of eq (A.46) is obtained.
- For $\alpha = 1/4$, the classical fourth-order Pade', 3 point stencil $C1111$ scheme is obtained.
- For $\alpha = 1/3$, the sixth order accurate, 5 point stencil $C1122$ scheme is obtained .

Hixon's notation and prefactorization

Hixon (2000) in his notation has re-written eq. (3.24) in the following form:

$$\gamma\left(f'_{i+2} + f'_{i-2}\right) + \beta\left(f'_{i+1} + f'_{i-1}\right) + (1 - \gamma - 2\beta)\, f'_i = \frac{1}{h}\left[\varphi\,(f_{i+2} - f_{i-2}) + \eta\,(f_{i+1} - f_{i-1})\right], \tag{A.78}$$

for sixth-order accuracy

$$\gamma = 0, \quad \beta = 1/5, \quad \varphi = 1/60, \quad \eta = 7/15. \tag{A.79}$$

By substituting the above in eq. (A.78):

$$\frac{1}{5}\left(f'_{i+1} + f'_{i-1}\right) + \frac{3}{5} f'_i = \frac{1}{h}\left[\frac{1}{60}\,(f_{i+2} - f_{i-2}) + \frac{7}{15}\,(f_{i+1} - f_{i-1})\right], \tag{A.80}$$

Pre-multiplying eq. (3.24) by the factor $\frac{1}{1+2\alpha}$, we get:

$$\frac{\alpha_1}{1+2\alpha_1} f'_{i-1} + \frac{1}{1+2\alpha_1} f'_i + \frac{\alpha_1}{1+2\alpha_1} f'_{i+1} = \frac{1}{h}\left(\frac{a_{-2}}{1+2\alpha_1} f_{i-2} + \frac{a_{-1}}{1+2\alpha_1} f_{i-1} + \frac{a_1}{1+2\alpha_1} f_{i+1} + \frac{a_2}{1+2\alpha_1} f_{i+2}\right) + O(h^4), \tag{A.81}$$

in the case of sixth-order accuracy, i.e. $\alpha_1 = 1/3$, eq. (A.81) is equivalent to eq. (A.80). In this case the relation for the scaled pseudo-wavenumber of eq.(3.27) becomes

$$\bar{\kappa}(\kappa) = \frac{\sum_{j=1}^{S} \frac{2a_j}{1+2\alpha_1} \sin(j\kappa)}{\frac{1}{1+2\alpha_1} + \sum_{j=1}^{Q} \frac{2\alpha_1}{1+2\alpha_1} \cos(j\kappa)}, \tag{A.82}$$

The solution to the system of equations (3.41) is:

$$\begin{cases} \alpha_F = \sqrt{\dfrac{1 \pm \sqrt{1-4\alpha_1^2}}{2(1+2\alpha_1)}} \\ \beta_F = \dfrac{\alpha_1}{\alpha_F(1+2\alpha_1)} \\ d_F = \dfrac{1-4\alpha_1}{6\alpha_F(1+2\alpha_1)} \\ b_F = \dfrac{\beta_F-\alpha_F}{\beta_F+\alpha_F} d_F + \dfrac{2\,(\alpha_1+2)}{3(\beta_F+\alpha_F)(1+2\alpha_1)} \\ c_F = -\,(d_F+b_F) \end{cases} \tag{A.83}$$

Pentadiagonal classical and optimized schemes

Now, let's focus on a family of pentadiagonal schemes with seven point stencil. This are generated in eq. (A.65) by setting $Q = 2$ and $S = 3$:

$$\alpha_2 f'_{i-2} + \alpha_1 f'_{i-1} + f'_i + \alpha_1 f'_{i+1} + \alpha_2 f'_{i+2} \cong a_3 \frac{(f_{i+3} - f_{i-3})}{h} + a_2 \frac{(f_{i+2} - f_{i-2})}{h} + a_1 \frac{(f_{i+1} - f_{i-1})}{h} \tag{A.84}$$

$$\bar{\kappa}(\kappa) = \frac{2\,[a_1 \sin(\kappa) + a_2 \sin(2\kappa) + a_3 \sin(3\kappa)]}{1 + 2\alpha_1 \cos(\kappa) + 2\alpha_2 \cos(2\kappa)}, \tag{A.85}$$

$$\begin{aligned} \frac{\partial \bar{\kappa}(\kappa)}{\partial \kappa} \;=\; 2 \Bigg\{ & \frac{[a_1 \cos(\kappa) + 2a_2 \cos(2\kappa) + 3a_3 \cos(3\kappa)]\,[1 + 2\alpha_1 \cos(\kappa) + 2\alpha_2 \cos(2\kappa)] +}{[1 + 2\alpha_1 \cos(\kappa) + 2\alpha_2 \cos(2\kappa)]^2} \\ & \frac{+\,[a_1 \sin(\kappa) + a_2 \sin(2\kappa) + a_3 \sin(3\kappa)]\,[2\alpha_1 \sin(\kappa) + 4\alpha_2 \sin(2\kappa)]}{[1 + 2\alpha_1 \cos(\kappa) + 2\alpha_2 \cos(2\kappa)]^2} \Bigg\} \end{aligned} \tag{A.86}$$

By imposing sixth-order accuracy (using the eq. A.68, A.69, A.70) the following relations are obtained:

$$\begin{cases} a_3 = -a_{-3} = \dfrac{1}{60} + \dfrac{1}{5}\alpha_2 - \dfrac{1}{20}\alpha_1 \\ a_2 = -a_{-2} = -\dfrac{3}{20} + \dfrac{31}{30}\alpha_2 + \dfrac{8}{15}\alpha_1 \\ a_1 = -a_{-1} = \dfrac{3}{4} - \dfrac{5}{3}\alpha_2 + \dfrac{1}{12}\alpha_1 \end{cases} \tag{A.87}$$

where α_1 and α_2 are two free parameter.

The specific choice of $\alpha_1 = 1/2$ and $\alpha_2 = 1/20$ yields to the only tenth-order scheme $C2233$ in the family (see Tab 3.2).

Recently, Lui and Lele Lui & Lele (2001) employed the compact pentadiagonal scheme of

$E4$	α_{12}	α_{21}	α_{23}	b_{i1}	b_{i2}	b_{i3}	b_{i4}	b_{i5}
$i = 1$	0	0	0	-25/12	4	-3	4/3	-1/4
$i = 2$	0	0	0	-1/4	-5/6	3/2	-1/2	1/12
$C4$								
$i = 1$	3	0	0	-17/6	3/2	3/2	-1/6	0
$i = 2$	0	1/4	1/4	-3/4	0	3/4	0	0
$C3$ (Lele, 1992)								
$i = 1$	2	0	0	-7/6	2	1/2	0	0
$C5$ (Carpenter *et al.*, 1993a)								
$i = 2$		1/6	1/2	-5/9	-1/2	1	1/18	0

Table A.3: Coefficients for the boundary formulas at i-th point from eq. (A.88).

eq (A.84), imposing sixth order accuracy and interpolating exact differentiation at $\varphi_1 = 1.67$ and $\varphi_2 = 2.10$ (corresponding, respectively, to $N_{\lambda_1} = 3.76$ and $N_{\lambda_2} = 2.99$), for the computation of spatial developing compressible, turbulent mixing layers. The specific values of α_1 and α_2 for the optimized scheme, labeled *Lui&Lele* thereafter, are reported in Tab. 3.2. Insert specs. of Kim

Non-centered boundary closures

$$i = 1 \quad f'_1 + \alpha_{12} f'_2 \cong \frac{1}{h} \sum_{m=1}^{n} b_{1m} f_m, \tag{A.88a}$$

$$i = 2 \quad \alpha_{21} f'_1 + f'_2 + \alpha_{23} f'_3 \cong \frac{1}{h} \sum_{m=1}^{n} b_{2m} f_m, \tag{A.88b}$$

$$i = N - 1 \quad \alpha_{23} f'_{N-2} + f'_{N-1} + \alpha_{21} f'_N \cong \frac{1}{h} \sum_{m=1}^{n} -b_{2m} f_{N-m+1}, \tag{A.88c}$$

$$i = N \quad \alpha_{12} f'_{N-1} + f'_N \cong \frac{1}{h} \sum_{m=1}^{n} -b_{1m} f_{N-m+1} \tag{A.88d}$$

Table A.3 reports the coefficients for the boundary formulas at i-th point according to eqs. (A.88) for fourth-order explicit (E4) and compact (C4) non-centered boundary closures. These coefficients for varying orders of accuracy can be obtained through the Taylor series term-matching procedure.

A.4 Eigenvalue spectrum

Consider the class of tridiagonal compact schemes with five point stencils $C1122$ of eq. (3.24) coupled with a generic boundary closure reported in eq. (A.88) of Sec. A.3. The matrices **A** and **B** of eq. (A.93), for this combination of interior scheme and boundary closures, are

$$\mathbf{A} = \begin{pmatrix} 1 & \alpha_{12} & 0 & \cdots & 0 & 0 & 0 & 0 & 0 \\ \alpha_{21} & 1 & \alpha_{23} & 0 & \cdots & 0 & 0 & 0 & 0 \\ 0 & \alpha_1 & 1 & \alpha_1 & 0 & \cdots & 0 & 0 & 0 \\ 0 & 0 & \alpha_1 & 1 & \alpha_1 & 0 & \cdots & 0 & 0 \\ \vdots & \ddots & \ddots & \ddots & \ddots & \ddots & \ddots & \vdots & \vdots \\ 0 & 0 & \cdots & 0 & \alpha_1 & 1 & \alpha_1 & 0 & 0 \\ 0 & 0 & 0 & \cdots & 0 & \alpha_1 & 1 & \alpha_1 & 0 \\ 0 & 0 & 0 & 0 & \cdots & 0 & \alpha_{23} & 1 & \alpha_{21} \\ 0 & 0 & 0 & 0 & 0 & \cdots & 0 & \alpha_{12} & 1 \end{pmatrix} \tag{A.89}$$

$$\mathbf{B} = \begin{pmatrix} b_{11} & b_{12} & b_{13} & \cdots & b_{1n} & 0 & 0 & \cdots & 0 \\ b_{21} & b_{22} & b_{23} & \cdots & b_{2n} & 0 & 0 & \cdots & 0 \\ -a_2 & -a_1 & 0 & a_1 & a_2 & 0 & 0 & \cdots & 0 \\ 0 & -a_2 & -a_1 & 0 & a_1 & a_2 & 0 & \cdots & 0 \\ \vdots & & \ddots & \ddots & \ddots & \ddots & \ddots & \ddots & \vdots \\ 0 & \cdots & 0 & -a_2 & -a_1 & 0 & a_1 & a_2 & 0 \\ 0 & 0 & \cdots & 0 & -b_{2n} & \cdots & -b_{23} & -b_{22} & -b_{21} \\ 0 & 0 & 0 & \cdots & -b_{1n} & \cdots & -b_{13} & -b_{12} & -b_{11} \end{pmatrix} \tag{A.90}$$

Pre-multiplying by **A** the spatially discretized form of *LAE* of eq. (2.13) and substituting the non-prefactored version of eq. (3.59) yields

$$\mathbf{A}\frac{d\mathbf{u}}{dt} = -\frac{c}{h}\mathbf{B}\,\mathbf{u}, \tag{A.91}$$

where $\frac{d\mathbf{u}}{dt}$ is a N-dimensional vector of the time derivative of the nodal values

$$\frac{d\mathbf{u}}{dt} = \left(\frac{du_1}{dt}, \frac{du_2}{dt}, \cdots, \frac{du_{N-1}}{dt}, \frac{du_N}{dt}\right)^T . \tag{A.92}$$

By inverting the A matrix in eq. (A.91), the problem can be re-cast as

$$\frac{d\mathbf{u}}{dt} = -\frac{c}{h}\mathbf{A^{-1}B}\,\mathbf{u}, \tag{A.93}$$

since eq. (3.61) is a system of ODE's in time with constant coefficients, it admits as solution orthonormal modes $\mathbf{u} = e^{st}\tilde{\mathbf{u}}$, with a constant s representing the rate of decay or amplification of the modes. Substituting $\mathbf{u} = e^{st}\tilde{\mathbf{u}}$ into eq. (3.61) leads to an eigenvalue problem

$$\tilde{\mathbf{u}} = -s^*\mathbf{M}\,\tilde{\mathbf{u}}, \tag{A.94}$$

where $\mathbf{M} = \mathbf{A}^{-1}\mathbf{B}$ and $s^* = \frac{c}{s\,h}$ is the dimensionless eigenvalue and $\tilde{\mathbf{u}}$ becomes the corresponding eigenvector. The eigenvalue s is in general complex and it depends on the size N of the matrices A and B, the interior scheme and the boundary closures. The matrix M is, in general, non-symmetric. To numerically determine its eigenvalues, firstly a balancing procedure is applied to reduce the norm of M. After, the matrix M is converted into an Hessenberg form, suitable for the QR transformation that gives the complex eigenvalues (Press & Firm, 1996).
The real parts of the eigenvalues are required to be equal or less than zero to guarantee the numerical stability of the interior scheme coupled with the boundary closure, i.e. $|e^{st}| \leq 1$. Section 3.5.2 shows the plot of the eigenvalue spectrum of the classical $C1122$ sixth-order scheme and the cost-optimized $C1122$epsm5, $C1122$epsm4, $C1122$epsm3 schemes coupled with the non-centered boundary closures of eq. (A.88). Figure 3.29 reports the effect of the boundary closures on the eigenvalue spectrum s^* for the classical Padè $C1111$ interior scheme ($\alpha_1 = 1/4$ in eq. (3.24)). For reference Fig.10 of Lele (1992).

Figure 3.30 shows the eigenvalue spectrum s^* from eq.(3.67) for the classical $C1122$ and the cost-optimized $C12$epsm$n$ (with $n = 5, 4, 3$) interior scheme, coupled with a fourth-order compact $C4$ boundary scheme at $i = 1$ and $i = N$ mesh nodes, and a fifth-order compact $C5$ boundary scheme at $i = 2$ and $i = N - 1$ mesh nodes.
Table A.4 and Fig. A.3 show the corresponding maximum real part of the eigenvalues from eq.(3.67) varying the number of nodes N. The classical $C1122$ internal scheme and the cost-

$C1122$ ($\alpha_1 = 1/3$)	N	$\max(\Re(s^*))$
	21	-0.00452508
	41	-0.000538793
	81	-6.58263e-05
	201	-4.15745e-06
	401	-5.17428e-07
$C1122$epsm5 ($\alpha_1 = 0.33750$)		
	21	-0.00464136
	41	-0.000553133
	81	-6.75728e-05
	201	-4.26683e-06
	401	-5.30988e-07
$C1122$epsm4 ($\alpha_1 = 0.34240$)		
	21	-0.00479122
	41	-0.000571708
	81	-6.98404e-05
	201	-4.40903e-06
	401	-5.48624e-07
$C1122$epsm3 ($\alpha_1 = 0.3532$)		
	21	-0.00517974
	41	-0.000620296
	81	-7.5794e-05
	201	-4.78311e-06
	401	-5.95049e-07

Table A.4: Maximum real parts of the eigenvalues from eq. (3.67) varying the number of nodes N for the classical $C1122$ and the cost-optimized $C12$epsm5, $C12$epsm4 and $C12$epsm3 interior schemes.

optimized $C1122$epsm5, $C1122$epsm4, $C1122$epsm3 schemes with such boundary closures are asymptotic stable (Carpenter *et al.*, 1993a), that is $\Re(s^*) \leq 0$ for the values of N reported. Figure A.3 shows the absolute maximum real part of the eigenvalues $|\max \Re(\omega^*)|$, varying the number of nodes N for the classical $C1122$ scheme. It follows the roll-off of the third-order logarithmic scale. A similar trend has been observed for the cost-optimized $C12$epsm$n$ schemes.

Determination of M for the prefactored schemes

Consider the class of prefactored scheme of eq. (3.33) and eq. (3.34) coupled with the prefactored one-sided boundary stencils of eq. (3.47) and eq. (3.48). The forward matrices $\mathbf{A}^F$ and

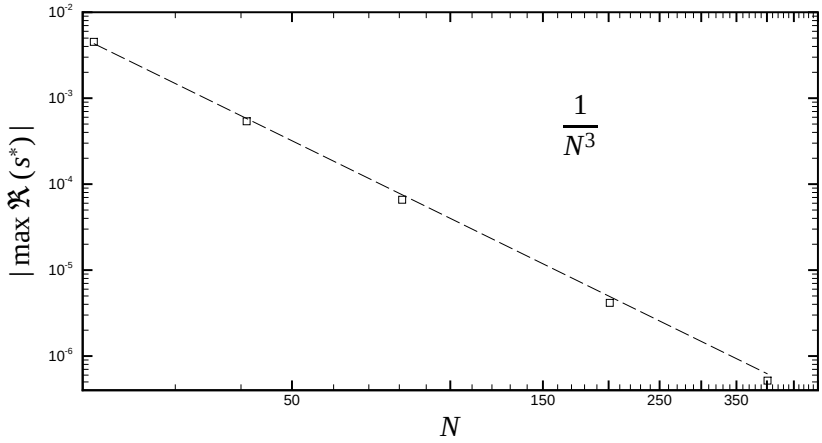

Figure A.3: Absolute maximum real parts of the eigenvalues of eq. (3.67) varying the number of nodes. (□) $C1122$, $(--)$ third-order logarithmic scale.

$\mathbf{B}^F$ are

$$\mathbf{A}^F = \begin{pmatrix} 1 & 0 & 0 & \cdots & 0 & 0 & 0 \\ 0 & \beta_F & \alpha_F & 0 & \cdots & 0 & 0 \\ 0 & 0 & \beta_F & \alpha_F & 0 & \cdots & 0 \\ \vdots & \ddots & \ddots & \ddots & \ddots & \vdots & \vdots \\ 0 & 0 & \cdots & 0 & \beta_F & \alpha_F & 0 \\ 0 & 0 & 0 & \cdots & 0 & \beta_F & \alpha_F \\ 0 & 0 & 0 & 0 & \cdots & 0 & 1 \end{pmatrix}, \mathbf{B}^F = \begin{pmatrix} -e_N & -e_{N-1} & -e_{N-2} & \cdots & -e_{N-6} & 0 & \cdots & 0 \\ d_F & c_F & b_F & 0 & 0 & \cdots & \cdots & 0 \\ 0 & d_F & c_F & b_F & 0 & \cdots & \cdots & 0 \\ \vdots & \ddots & \ddots & \ddots & \ddots & \ddots & \vdots & 0 \\ \vdots & \ddots & \ddots & \ddots & \ddots & \ddots & \vdots & 0 \\ 0 & \cdots & 0 & 0 & d_F & c_F & b_F & 0 \\ 0 & 0 & \cdots & 0 & 0 & d_F & c_F & b_F \\ 0 & \cdots & 0 & -s_7 & \cdots & -s_3 & -s_2 & -s_1 \end{pmatrix} \tag{A.95}$$

Similarly, the backward matrices $\mathbf{A}^B$ and $\mathbf{B}^B$ are

$$\mathbf{A}^B = \begin{pmatrix} 1 & 0 & 0 & \cdots & 0 & 0 & 0 \\ \gamma_B & \beta_B & 0 & 0 & \cdots & 0 & 0 \\ 0 & \gamma_B & \beta_B & 0 & 0 & \cdots & 0 \\ \vdots & \ddots & \ddots & \ddots & \ddots & \vdots & \vdots \\ 0 & \cdots & 0 & \gamma_B & \beta_B & 0 & 0 \\ 0 & 0 & 0 & \cdots & \gamma_B & \beta_B & 0 \\ 0 & 0 & 0 & 0 & \cdots & 0 & 1 \end{pmatrix}, \quad \mathbf{B}^B = \begin{pmatrix} s_1 & s_2 & s_3 & \cdots & s_7 & 0 & \cdots & 0 \\ d_B & c_B & b_B & 0 & 0 & \cdots & \cdots & 0 \\ 0 & d_B & c_B & b_B & 0 & \cdots & \cdots & 0 \\ \vdots & \ddots & \ddots & \ddots & \ddots & \ddots & \vdots & 0 \\ \vdots & \ddots & \ddots & \ddots & \ddots & \ddots & \vdots & 0 \\ 0 & \cdots & 0 & 0 & d_B & c_B & b_B & 0 \\ 0 & 0 & \cdots & 0 & 0 & d_B & c_B & b_B \\ 0 & \cdots & 0 & e_{N-6} & \cdots & e_{N-2} & e_{N-1} & e_N \end{pmatrix} \tag{A.96}$$

They are rearranged to eliminate the $f_0'^B$ and $f_0'^F$ from eq. (3.59). The finite difference approximations $f_0'^B$ and $f_0'^F$, according to eq. (3.47) and eq. (3.48), are re-written for the $i = 0$ nodes as

$$\begin{aligned} f_0'^B &= \frac{1}{h}\sum_{j=0}^{6} s_{j+1} f_j \\ f_0'^F &= \frac{1}{h}\sum_{j=0}^{6} -e_{N-j} f_j \end{aligned} \tag{A.97}$$

.For the backward loop, eq. (3.34) is rewritten for $i = 1$ node as

$$\beta_B f_1'^B + \gamma_B f_0'^B = \frac{1}{h}\left[b_B f_2 + c_B f_1 + d_B f_0\right], \tag{A.98}$$

By substituting the first of eq. (A.97) in the backward loop of eq. (A.98) and re-arranging ($f_0 = 0$ due to boundary condition)

$$\beta_B f_1'^B + \frac{\gamma_B}{h}\sum_{j=0}^{6} s_{j+1} f_j = \frac{1}{h}\left[b_B f_2 + c_B f_1\right] \tag{A.99}$$

$$\beta_B f_1'^B = -\frac{\gamma_B}{h}\sum_{j=0}^{6} s_{j+1} f_j + \frac{1}{h}\left[b_B f_2 + c_B f_1\right] \tag{A.100}$$

$$\beta_B f_1'^B = \frac{1}{h}\left[(-\gamma_B s_2 + c_B)\, f_1 + (-\gamma_B s_3 + b_B)\, f_2 - \gamma_B s_4 f_3 - \gamma_B s_5 f_4 - \gamma_B s_6 f_5 - \gamma_B s_7 f_6\right] \tag{A.101}$$

$$\beta_B f_1'^B = \frac{1}{h}\left[s_2^* f_1 + s_3^* f_2 + s_4^* f_3 + s_5^* f_4 + s_6^* f_5 + s_7^* f_6\right] \tag{A.102}$$

where the coefficients s_i^* are

$$s_2^* = (-\gamma_B s_2 + c_B);\ s_3^* = (-\gamma_B s_3 + b_B);\ s_4^* = -\gamma_B s_4;\ s_5^* = -\gamma_B s_5;\ s_6^* = -\gamma_B s_6;\ s_7^* = -\gamma_B s_7. \tag{A.103}$$

Matrices $\mathbf{A}^B$ and $\mathbf{B}^B$ are re-written as a $(N+1 \times N+1)$ matrix

$$\mathbf{A}^B = \begin{pmatrix} 1 & 0 & 0 & 0 & \cdots & 0 & 0 \\ \gamma_B & \beta_B & 0 & 0 & \cdots & 0 & 0 \\ 0 & \gamma_B & \beta_B & 0 & 0 & \cdots & 0 \\ \vdots & \ddots & \ddots & \ddots & \vdots & \vdots & \vdots \\ 0 & \cdots & 0 & \gamma_B & \beta_B & 0 & 0 \\ 0 & 0 & 0 & \cdots & \gamma_B & \beta_B & 0 \\ 0 & 0 & 0 & 0 & \cdots & 0 & 1 \end{pmatrix}, \quad \mathbf{B}^B = \begin{pmatrix} 0 & 0 & 0 & \cdots & 0 & \cdots & \cdots & 0 \\ s_1^* & s_2^* & s_3^* & \cdots & s_7^* & \cdots & \cdots & 0 \\ 0 & d_B & c_B & b_B & 0 & \cdots & \cdots & 0 \\ 0 & \ddots & \ddots & \ddots & \ddots & \ddots & \vdots & 0 \\ 0 & \ddots & \ddots & \ddots & \ddots & \ddots & \vdots & 0 \\ 0 & \cdots & 0 & 0 & d_B & c_B & b_B & 0 \\ 0 & 0 & \cdots & 0 & 0 & d_B & c_B & b_B \\ 0 & \cdots & 0 & e_{N-6} & \cdots & e_{N-2} & e_{N-1} & e_N \end{pmatrix} \tag{A.104}$$

where the first row of $\mathbf{B}^B$ has been set to zero due to the initial boundary condition. For the forward loop, eq. (3.33) at $i = 1$ node is

$$\alpha_F f_2'^F + \beta_F f_1'^F = \frac{1}{h}\left[b_F f_2 + c_F f_1 + d_F f_0\right], \tag{A.105}$$

which does not involve $f_0'^F$ ($f_0 = 0$). Matrices $\mathbf{A}^F$ and $\mathbf{B}^F$ are re-written as a $N+1 \times N+1$ matrix

$$\mathbf{A}^F = \begin{pmatrix} 1 & 0 & 0 & 0 & \cdots & 0 & 0 \\ 0 & \beta_F & \alpha_F & 0 & \cdots & 0 & 0 \\ 0 & 0 & \beta_F & \alpha_F & 0 & \cdots & 0 \\ \vdots & \ddots & \ddots & \ddots & \ddots & \vdots & \vdots \\ 0 & 0 & \cdots & 0 & \beta_F & \alpha_F & 0 \\ 0 & 0 & 0 & \cdots & 0 & \beta_F & \alpha_F \\ 0 & 0 & 0 & 0 & \cdots & 0 & 1 \end{pmatrix}, \quad \mathbf{B}^F = \begin{pmatrix} 0 & 0 & 0 & \cdots & 0 & \cdots & \cdots & 0 \\ d_F & c_F & b_F & 0 & 0 & \cdots & \cdots & 0 \\ 0 & d_F & c_F & b_F & 0 & \cdots & \cdots & 0 \\ \vdots & \ddots & \ddots & \ddots & \ddots & \ddots & \vdots & 0 \\ \vdots & \ddots & \ddots & \ddots & \ddots & \ddots & \vdots & 0 \\ 0 & \cdots & 0 & 0 & d_F & c_F & b_F & 0 \\ 0 & 0 & \cdots & 0 & 0 & d_F & c_F & b_F \\ 0 & \cdots & 0 & -s_7 & \cdots & -s_3 & -s_2 & -s_1 \end{pmatrix} \tag{A.106}$$

where the first row of $\mathbf{B}^F$ has been set to zero due to the initial boundary condition.
These matrices are used to construct the $\mathbf{M}$ of eq.(3.66). The eigenvalues are calculated by eliminating the first row and the first column, due to the initial boundary condition at the $i = 0$ node.

A.5 Efficiency comparison

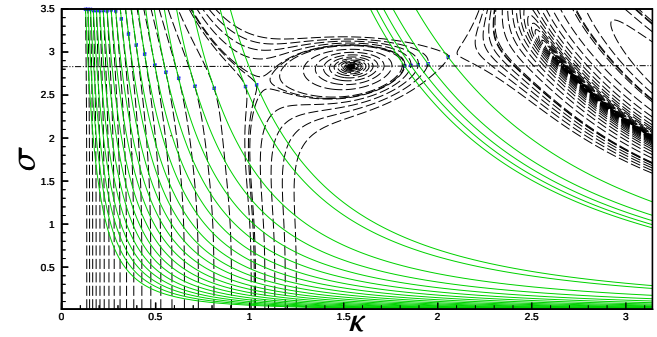

(a)

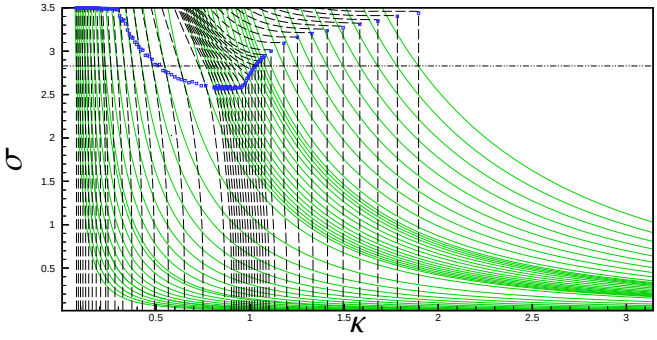

(b)

Figure A.4: Iso-contours of normalized 'local'(a) and 'global'(b) error function $e(\kappa, \sigma)$ (black dashed lines) $C0011/RK4$, and normalized one-dimensional cost function $c_1(\kappa, \sigma)$ (solid green line). The blue squared symbols represent the 'optimal' working condition, the black dash-dotted line (—· · —) corresponds to the stability limit σ_{max}.

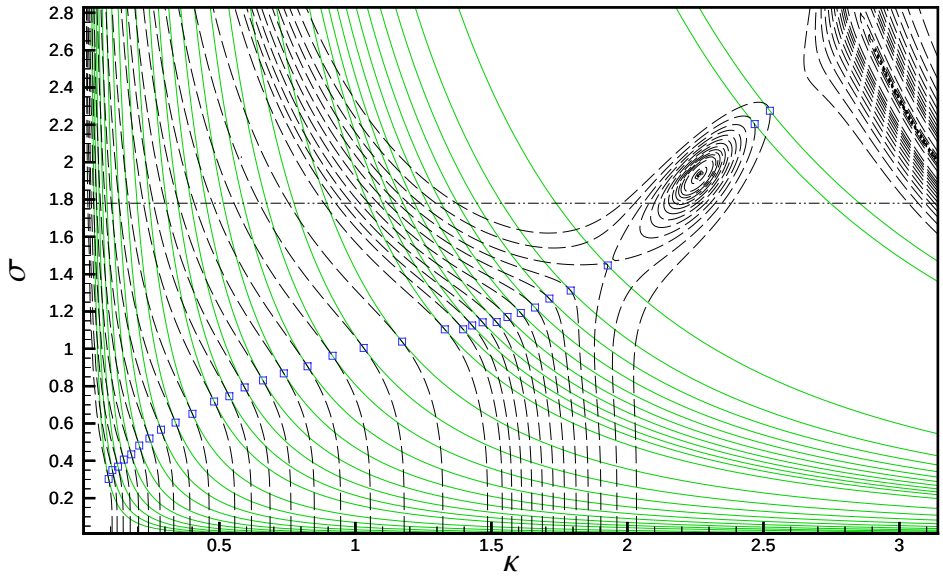

(a)

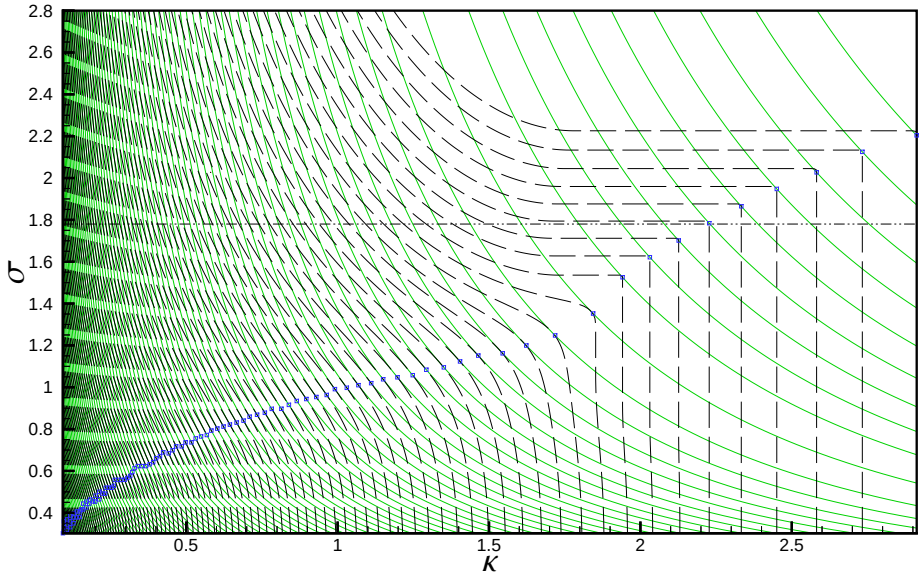

(b)

Figure A.5: Iso-contours of normalized 'local'(a) and 'global'(b) error function $e(\kappa,\sigma)$ (black dashed lines) $C0033/RK4$, and normalized one-dimensional cost function $c_1(\kappa,\sigma)$ (solid green line). The blue squared symbols represent the 'optimal' working condition; the black dash-dotted line (—· · —) corresponds to the stability limit σ_{max}.

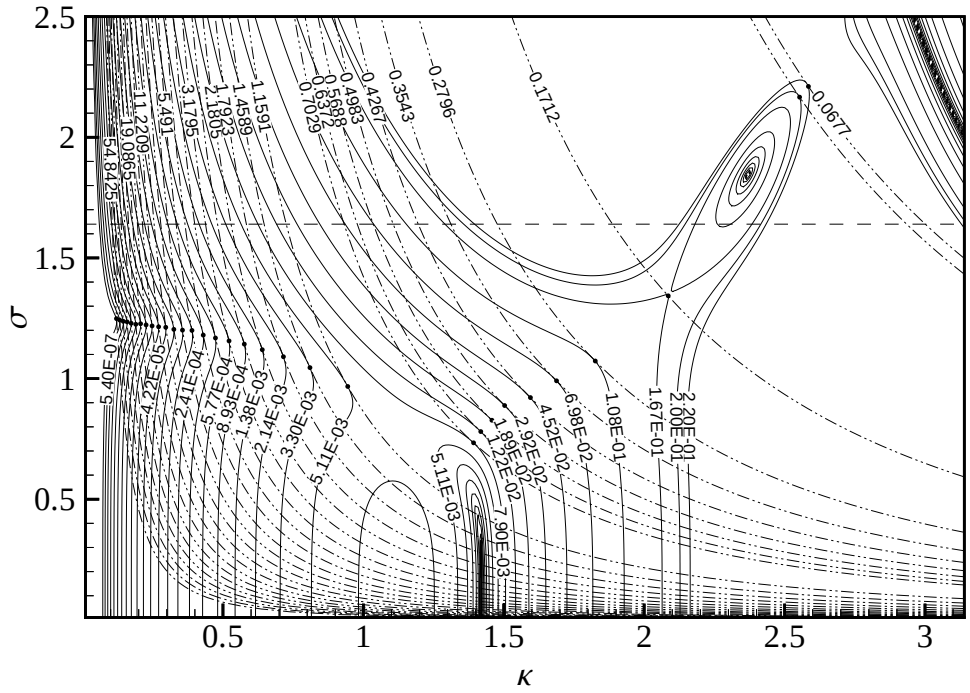

(a)

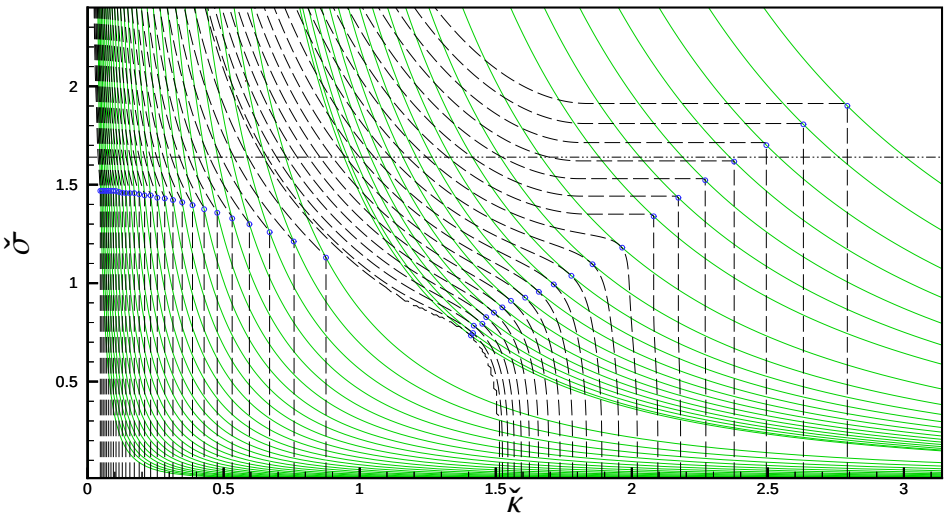

(b)

Figure A.6: Iso-contours of normalized 'local'(a) and 'global'(b) error function $e(\kappa, \sigma)$ (black dashed lines) $TamDRP/RK4$, and normalized one-dimensional cost function $c_1(\kappa, \sigma)$ (solid green line). The blue squared symbols represent the 'optimal' working condition; the black dash-dotted line (— · · —) corresponds to the stability limit σ_{max}.

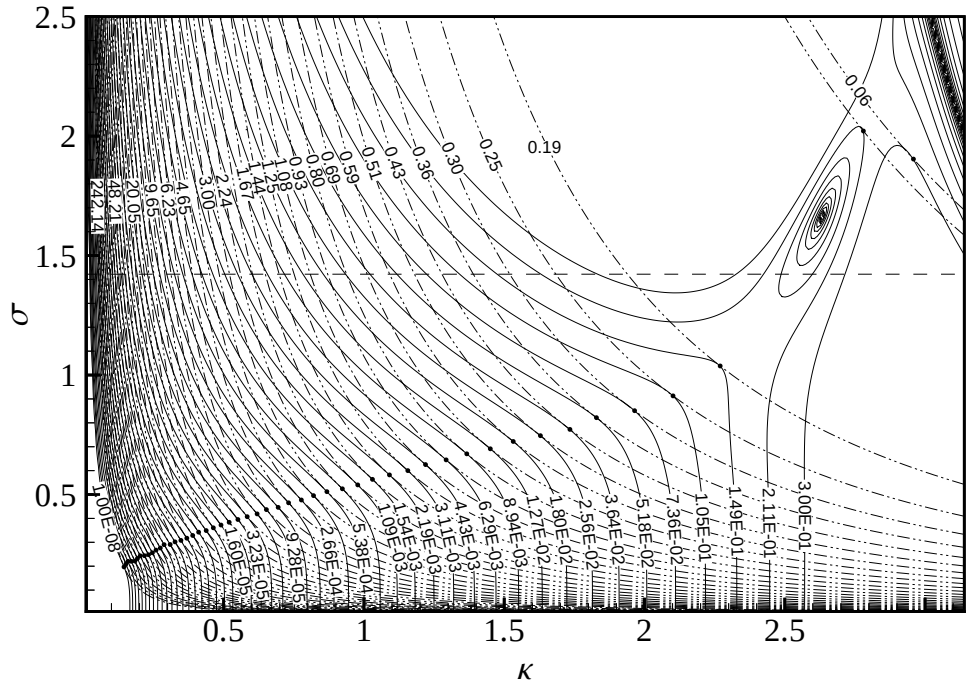

(a)

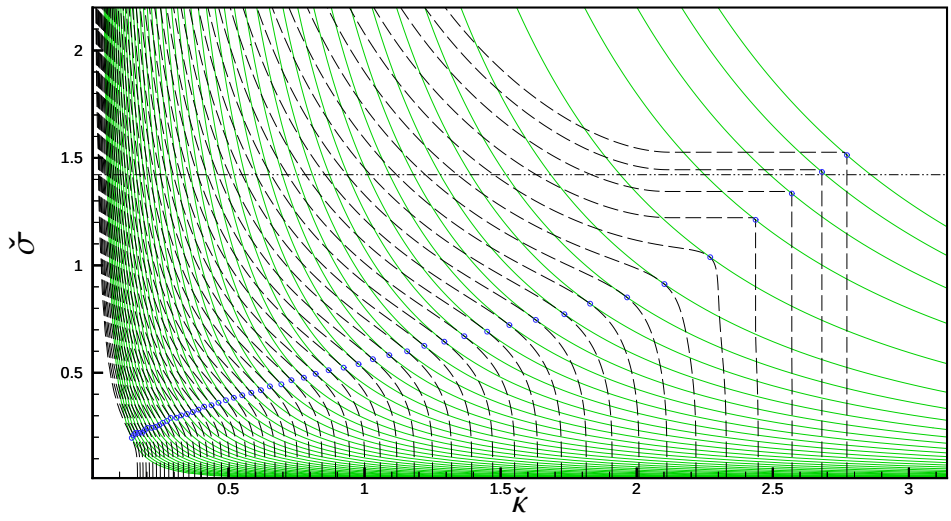

(b)

Figure A.7: Iso-contours of normalized 'local'(a) and 'global'(b) error function $e(\kappa,\sigma)$ (black dashed lines) $C1122/RK4$, and normalized one-dimensional cost function $c_1(\kappa,\sigma)$ (solid green line). The blue squared symbols represent the 'optimal' working condition; the black dash-dotted line (—· · —) corresponds to the stability limit σ_{max}.

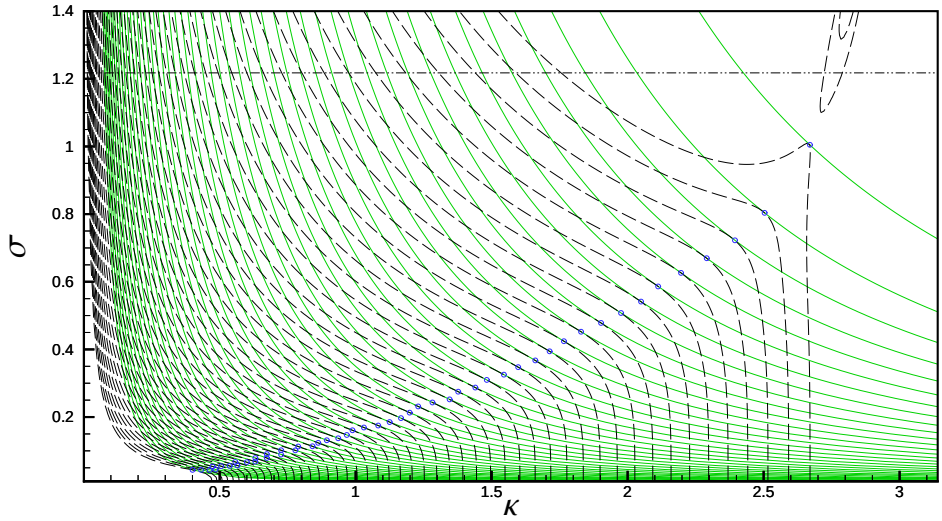

(a)

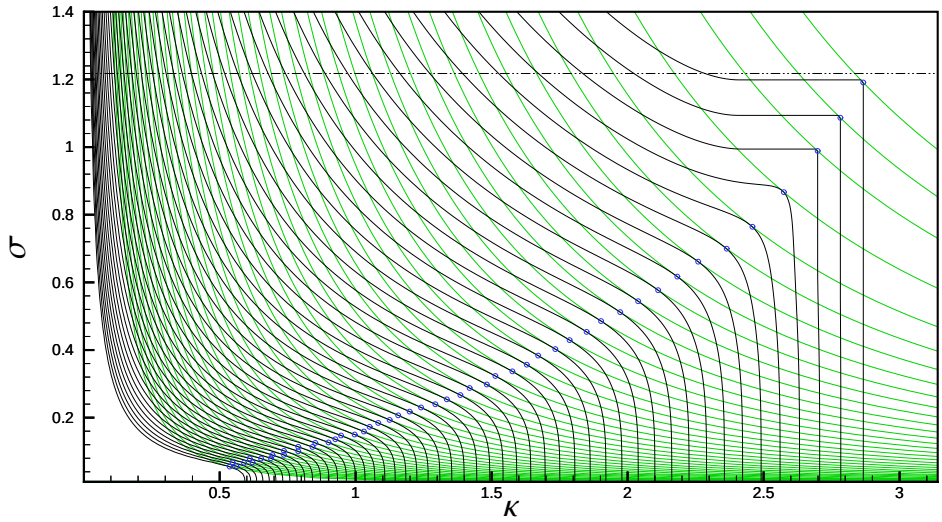

(b)

Figure A.8: Iso-contours of normalized 'local'(a) and 'global'(b) error function $e(\kappa, \sigma)$ (black dashed lines) $C2233/RK4$, and normalized one-dimensional cost function $c_1(\kappa, \sigma)$ (solid green line). The blue squared symbols represent the 'optimal' working condition; the black dash-dotted line (—· · —) corresponds to the stability limit σ_{max}.

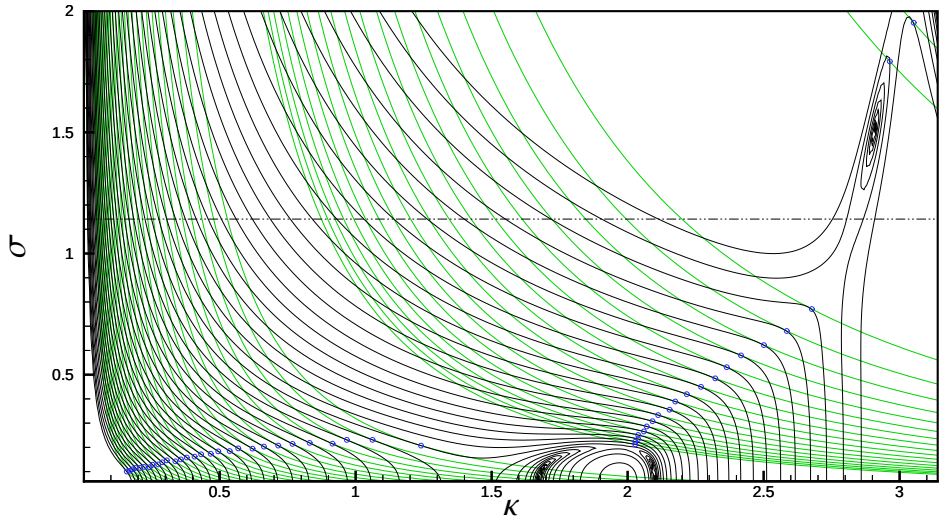

(a)

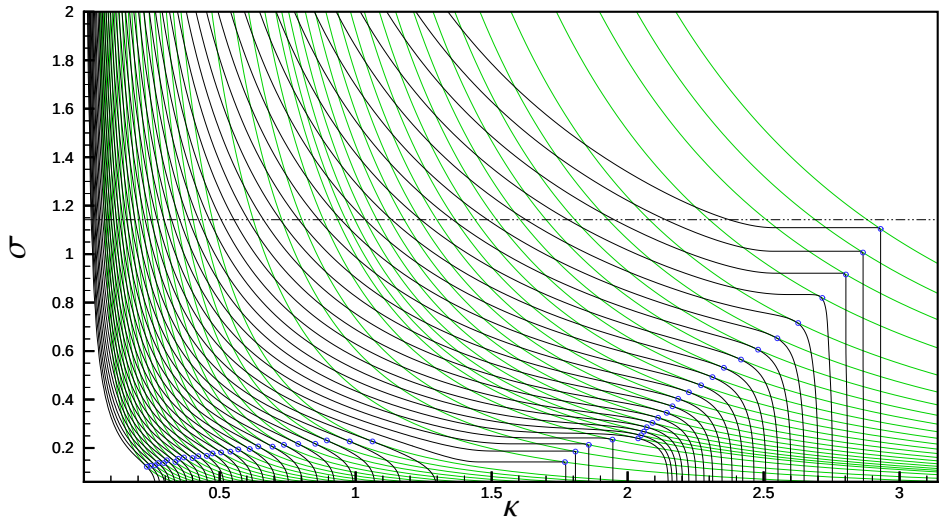

(b)

Figure A.9: Iso-contours of normalized 'local'(a) and 'global'(b) error function $e(\kappa, \sigma)$ (black dashed lines) *Lui*&*Lele*/*RK*4, and normalized one-dimensional cost function $c_1(\kappa, \sigma)$ (solid green line). The blue circles represent the 'optimal' working condition; the black dash-dotted line (—· · —) corresponds to the stability limit σ_{max}.

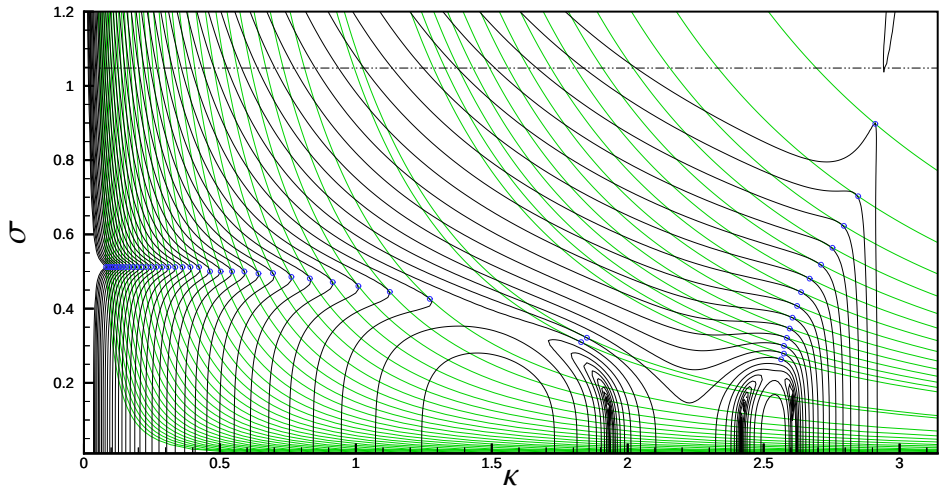

(a)

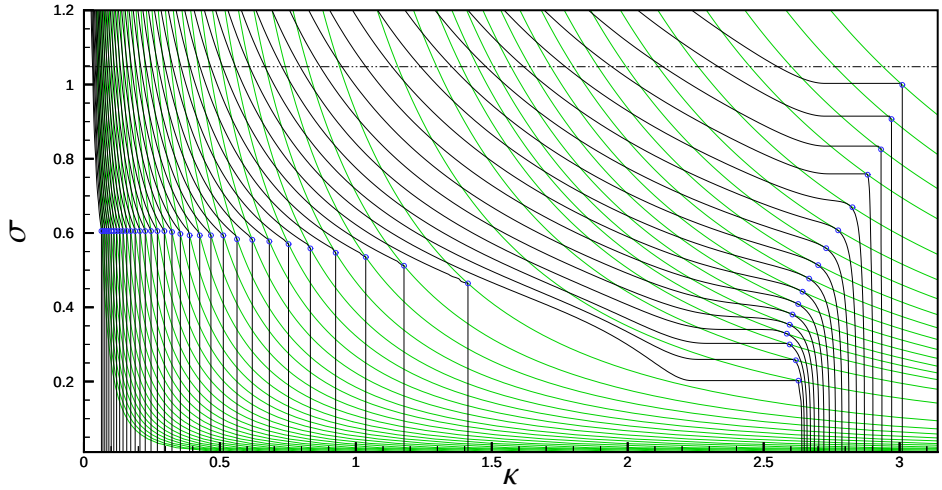

(b)

Figure A.10: Iso-contours of normalized 'local'(a) and 'global'(b) error function $e(\kappa, \sigma)$ (black dashed lines) $Kim/RK4$, and normalized one-dimensional cost function $c_1(\kappa, \sigma)$ (solid green line). The blue circles represent the 'optimal' working condition; the black dash-dotted line (—· · —) corresponds to the stability limit σ_{max}.

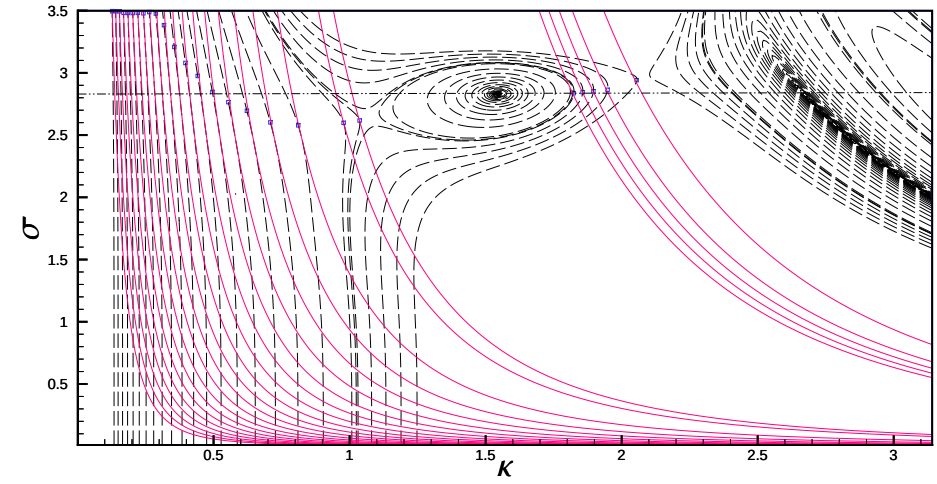

(a)

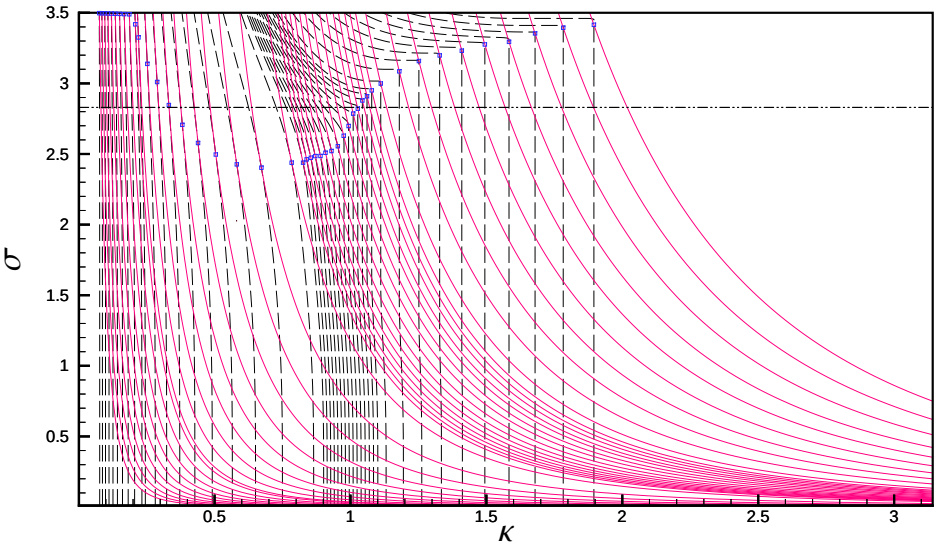

(b)

Figure A.11: Iso-contours of normalized 'local'(a) and 'global'(b) error function $e(\kappa, \sigma)$ (black dashed lines) $C0011/RK4$, and normalized two-dimensional cost function $c_2(\kappa, \sigma)$ (solid purple line). The blue squared symbols represent the 'optimal' working condition, the black dash-dotted line (—· · —) corresponds to the stability limit σ_{max}.

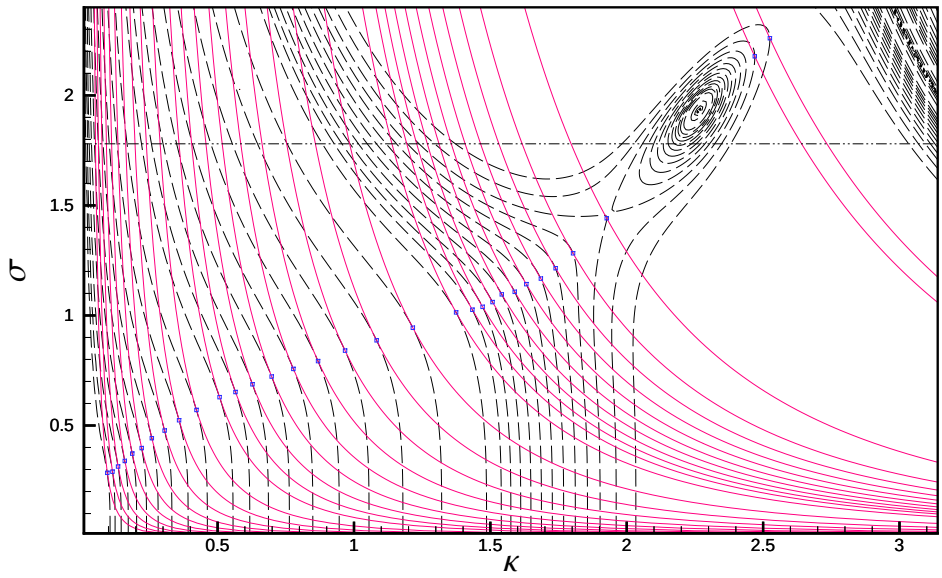

(a)

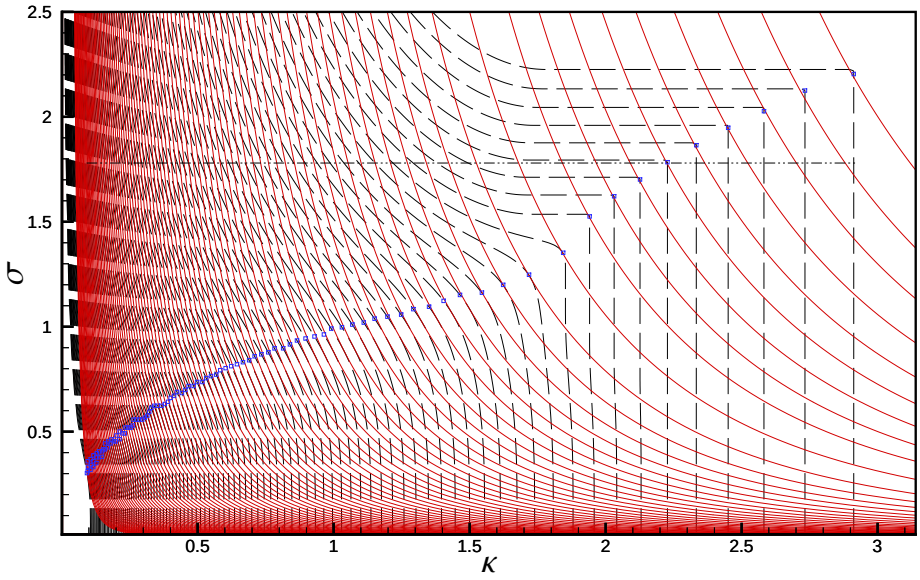

(b)

Figure A.12: Iso-contours of normalized 'local'(a) and 'global'(b) error function $e(\kappa, \sigma)$ (black dashed lines) $C0033/RK4$, and normalized two-dimensional cost function $c_2(\kappa, \sigma)$ (solid purple line). The blue squared symbols represent the 'optimal' working condition, the black dash-dotted line (—· · —) corresponds to the stability limit σ_{max}.

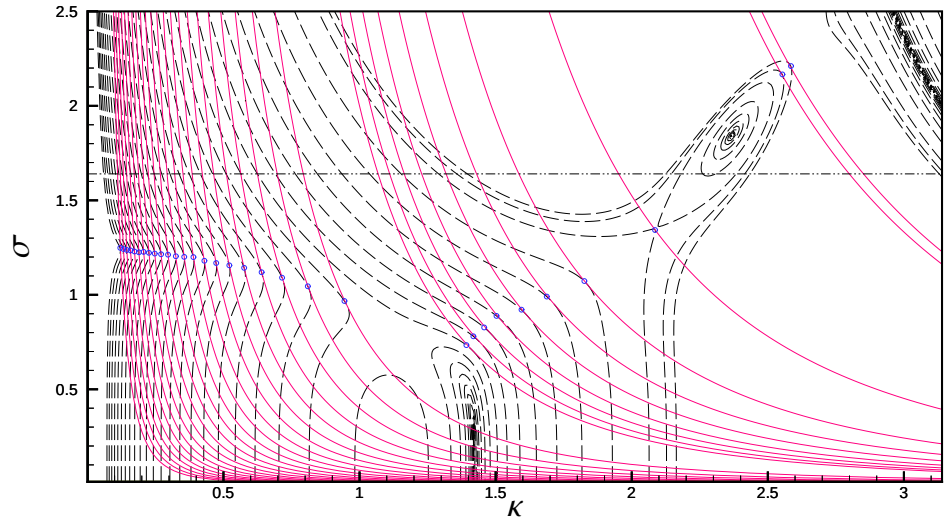

(a)

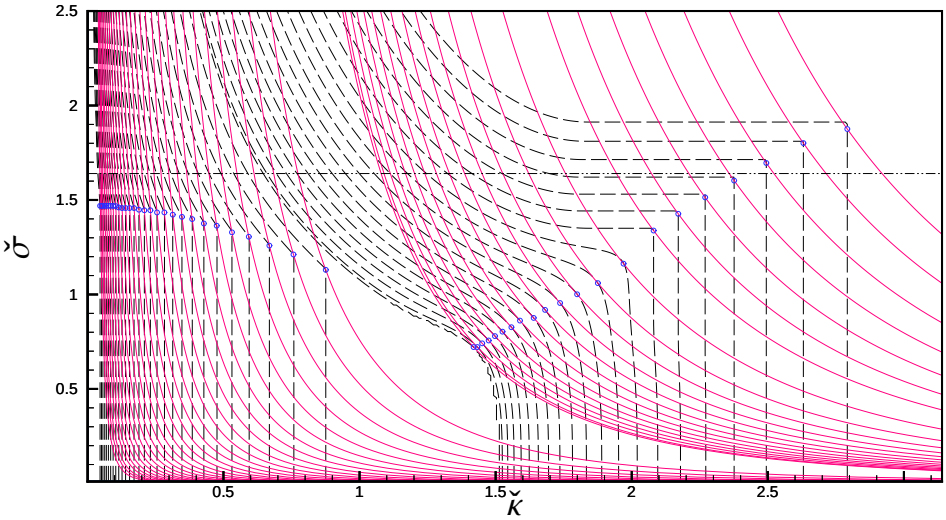

(b)

Figure A.13: Iso-contours of normalized 'local'(a) and 'global'(b) error function $e(\kappa,\sigma)$ (black dashed lines) $Tam/RK4$, and normalized two-dimensional cost function $c_2(\kappa,\sigma)$ (solid purple line). The blue squared symbols represent the 'optimal' working condition, the black dash-dotted line (—· · —) corresponds to the stability limit σ_{max}.

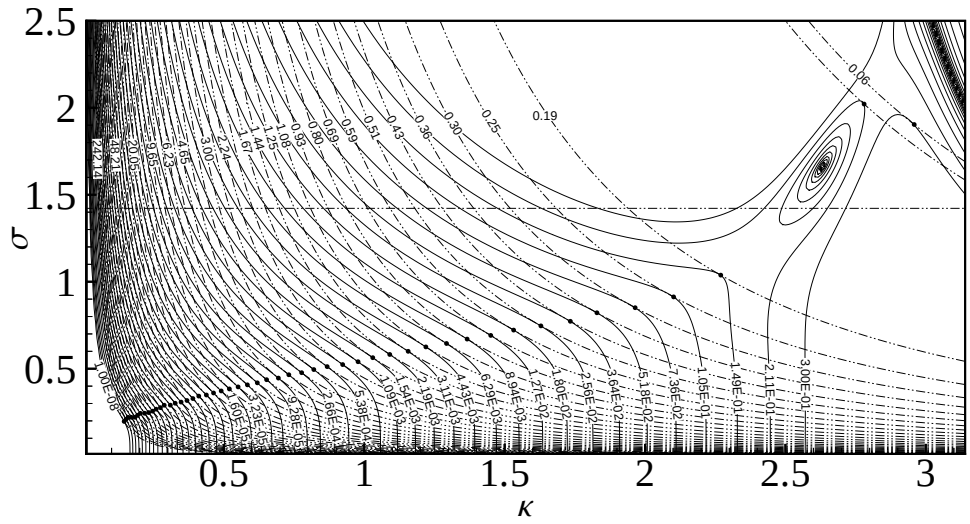

(a)

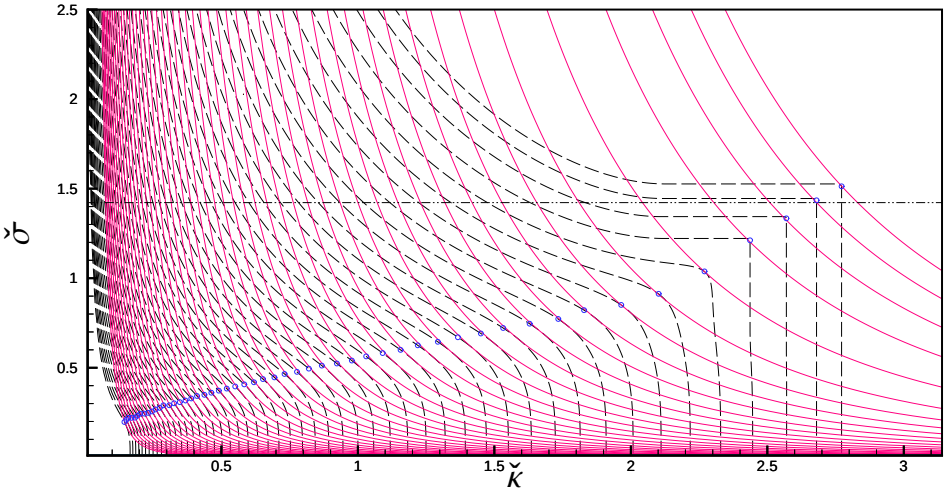

(b)

Figure A.14: Iso-contours of normalized 'local'(a) and 'global'(b) error function $e(\kappa, \sigma)$ (black dashed lines) $C12/RK4$, and normalized two-dimensional cost function $c_2(\kappa, \sigma)$ (solid purple line). The blue squared symbols represent the 'optimal' working condition, the black dash-dotted line (—· · —) corresponds to the stability limit σ_{max}.

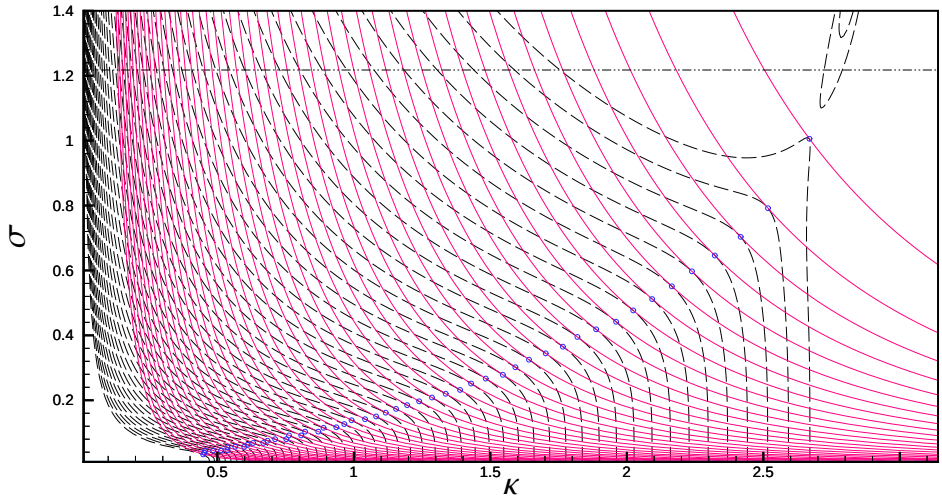

(a)

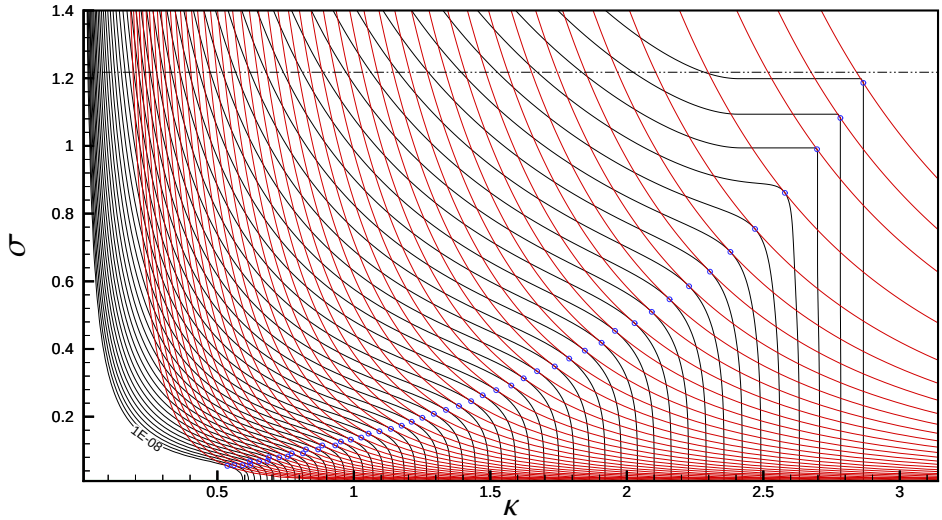

(b)

Figure A.15: Iso-contours of normalized 'local'(a) and 'global'(b) error function $e(\kappa,\sigma)$ (black dashed lines) $C2233/RK4$, and normalized two-dimensional cost function $c_2(\kappa,\sigma)$ (solid red line). The blue squared symbols represent the 'optimal' working condition; the black dash-dotted line (—· · —) corresponds to the stability limit σ_{max}.

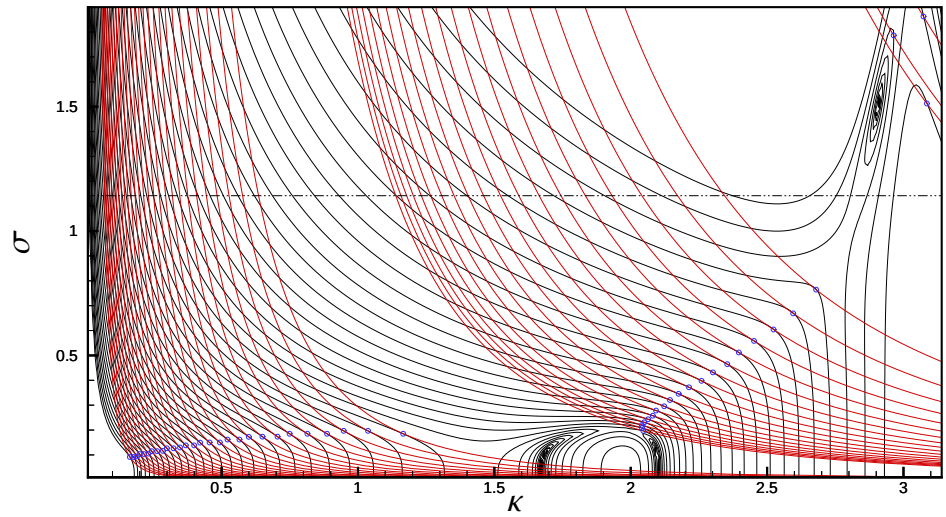

(a)

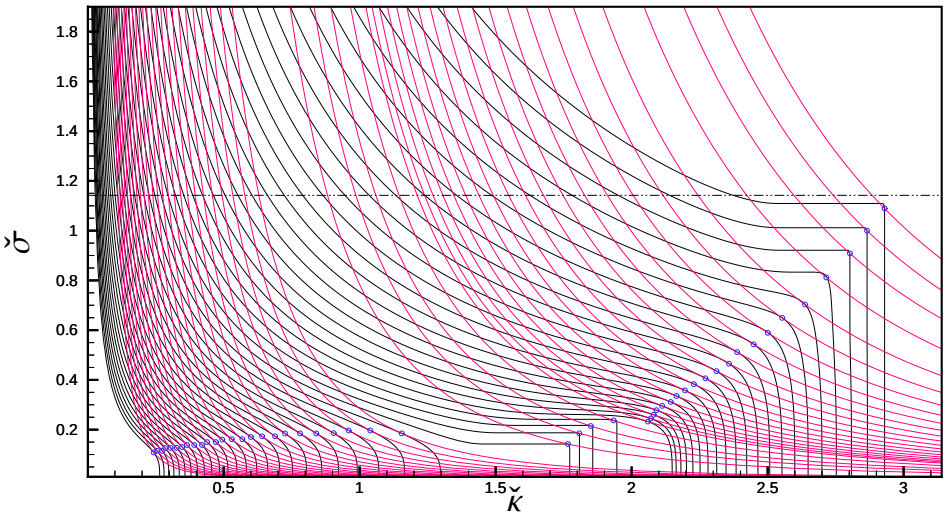

(b)

Figure A.16: Iso-contours of normalized 'local'(a) and 'global'(b) error function $e(\kappa, \sigma)$ (black dashed lines) *Lui&Lele*, and normalized two-dimensional cost function $c_2(\kappa, \sigma)$ (solid red line). The blue squared symbols represent the 'optimal' working condition; the black dash-dotted line (— · · —) corresponds to the stability limit σ_{max}.

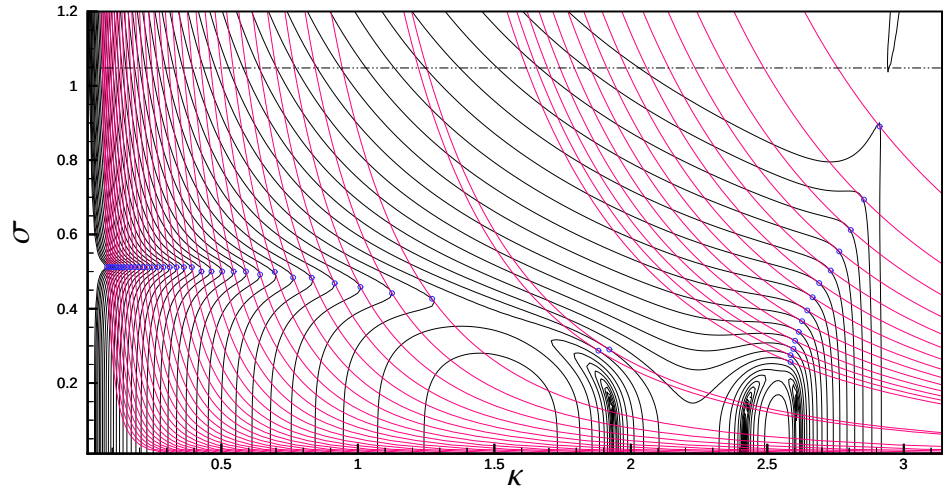

(a)

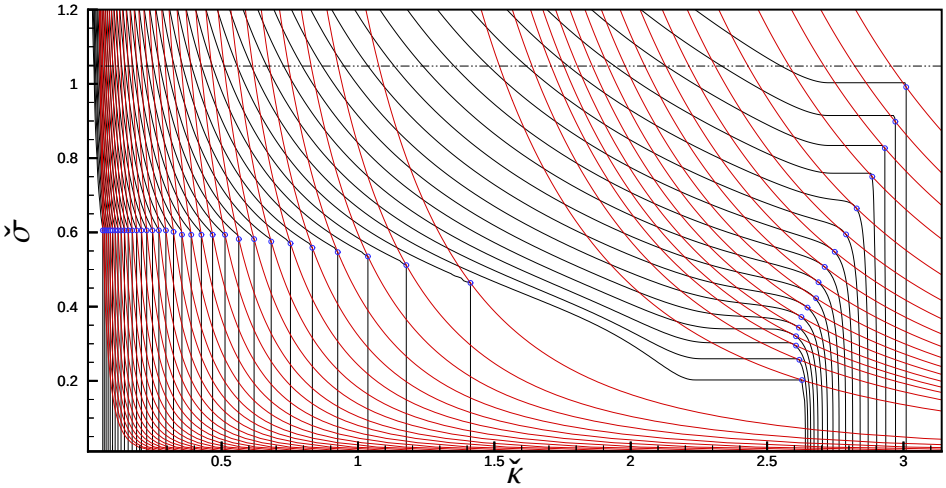

(b)

Figure A.17: Iso-contours of normalized 'local'(a) and 'global'(b) error function $e(\kappa,\sigma)$ (black dashed lines) $Kim/RK4$, and normalized one-dimensional cost function $c_1(\kappa,\sigma)$ (solid green line). The blue circles represent the 'optimal' working condition; the black dash-dotted line (—· · —) corresponds to the stability limit σ_{max}.

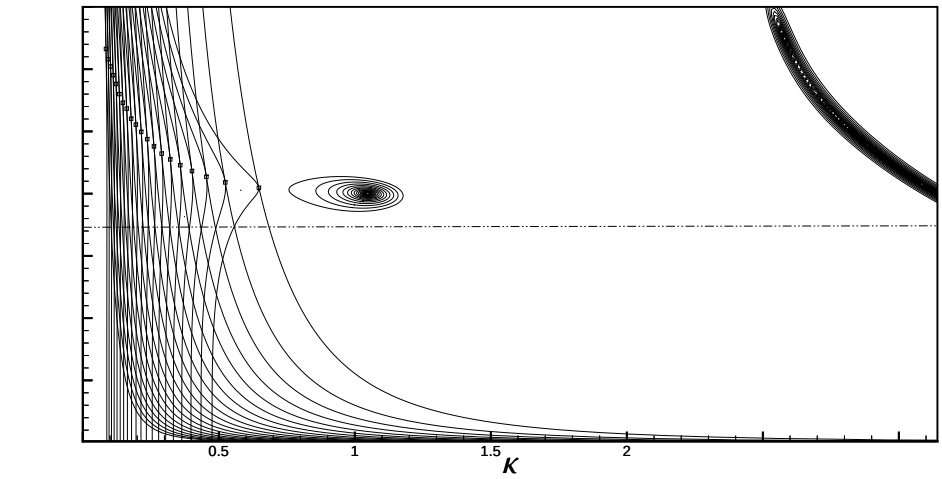

(a)

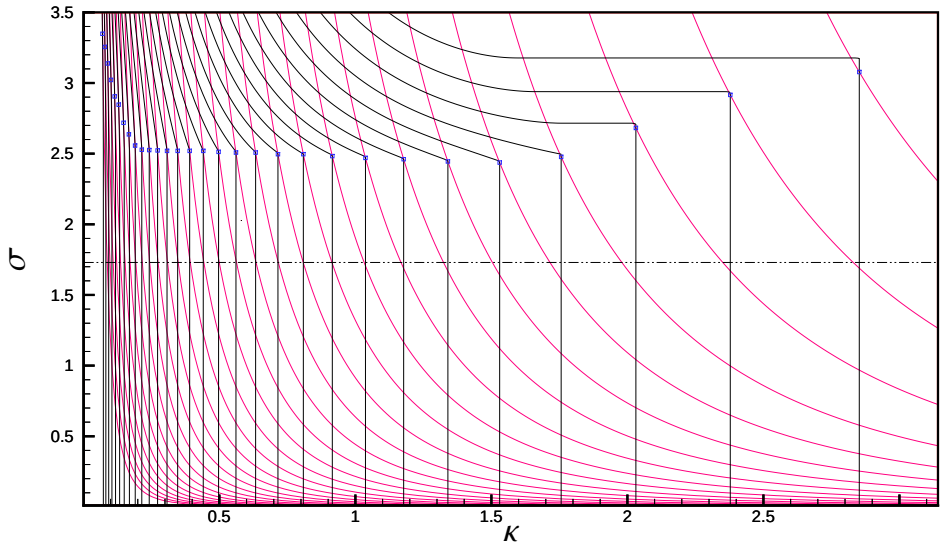

(b)

Figure A.18: Iso-contours of normalized 'local'(a) and 'global'(b) error function $e(\kappa, \sigma)$ (black dashed lines) $C0011/RK3$, and normalized two-dimensional cost function $c_2(\kappa, \sigma)$ (solid purple line). The blue squared symbols represent the 'optimal' working condition, the black dash-dotted line (—· · —) corresponds to the stability limit σ_{max}.

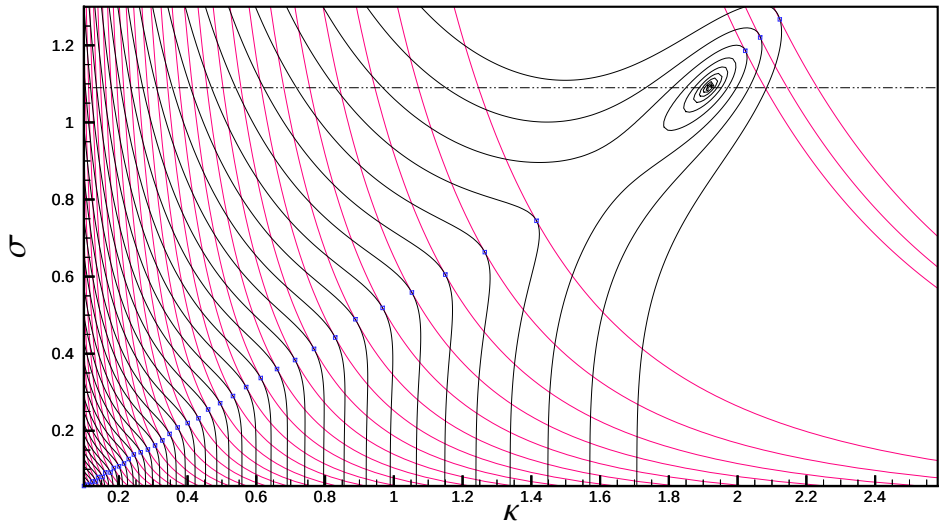

(a)

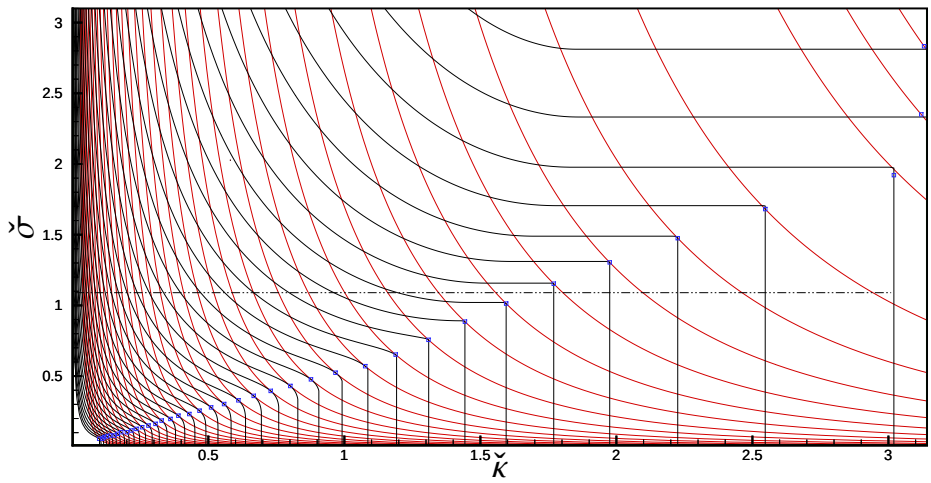

(b)

Figure A.19: Iso-contours of normalized 'local'(a) and 'global'(b) error function $e(\kappa, \sigma)$ (black dashed lines) $C0033/RK3$, and normalized two-dimensional cost function $c_2(\kappa, \sigma)$ (solid purple line). The blue squared symbols represent the 'optimal' working condition, the black dash-dotted line (—· · —) corresponds to the stability limit σ_{max}.

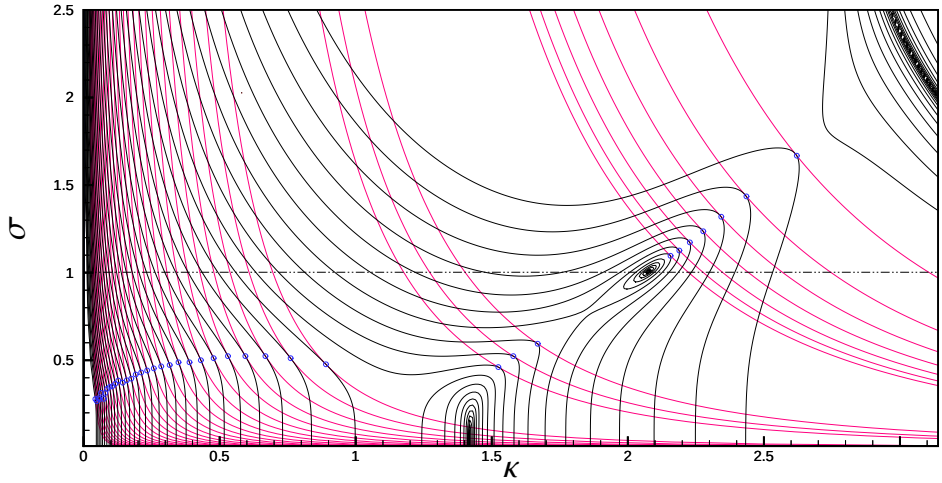

(a)

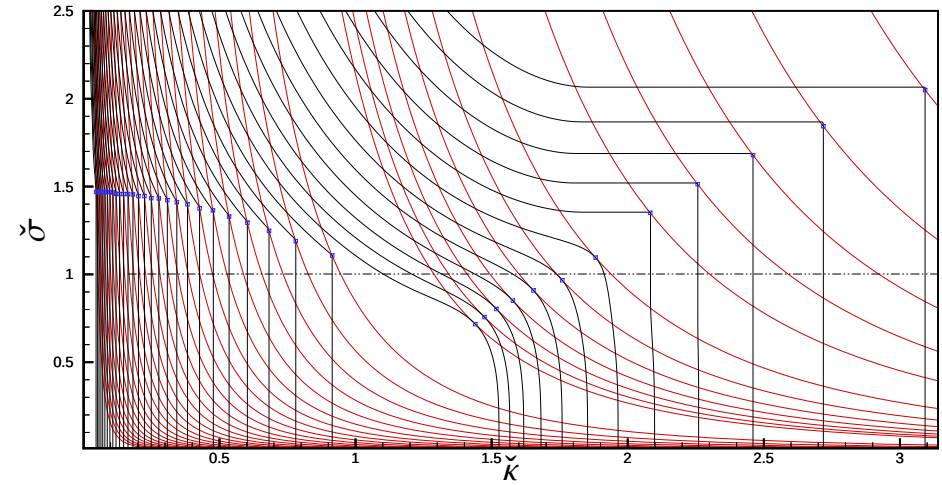

(b)

Figure A.20: Iso-contours of normalized 'local'(a) and 'global'(b) error function $e(\kappa, \sigma)$ (black dashed lines) $Tam/RK3$, and normalized two-dimensional cost function $c_2(\kappa, \sigma)$ (solid purple line). The blue squared symbols represent the 'optimal' working condition, the black dash-dotted line (—· · —) corresponds to the stability limit σ_{max}.

A.6 Time Integration

The following figures report the stability foot-prints, dissipation rate $|r|$ and phase error for the third-order RK3 (black dashed line) and fourth-order RK4 (black solid line) time integration schemes.

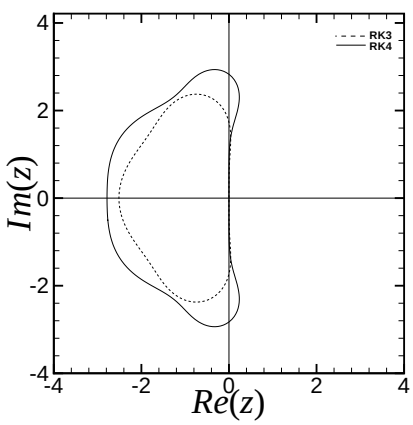

(a)

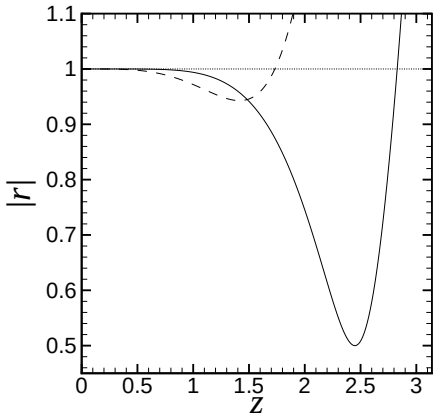

(b)

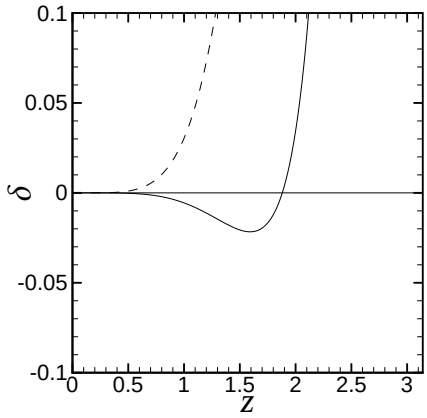

(c)

Figure A.21: (a) Stability foot-prints and (b) dissipation rate $|r|$ and (c) phase error δ for the third-order RK3 (black dashed line) and fourth-order RK4 (black solid line) time integration schemes.

A.7 Boundaries error

Eq. (3.34) can be rewritten, for $C1122$ scheme as:

$$(1-\alpha_F)\left\{f_i'^B\right\}+\alpha_F\left\{f_{i-1}'^B\right\}=\frac{1}{h}\left[b_B f_{i+1}+c_B f_i+d_B f_{i-1}\right]=q_{(i+1,i,i-1)} \tag{A.107}$$

This equation is valid for every point, included if $i-1$ is on the boundary. To calculate the value on the $i=1$ point

$$(1-\alpha_F)\left\{f_1'^B\right\}_{boundary}+\alpha_F\left\{f_0'^B\right\}_{boundary}=\frac{1}{h}\left[b_B f_2+c_B f_1+d_B f_0\right]=q_{(2,1,0)} \tag{A.108}$$

$$\left\{f_1'^B\right\}_{boundary}=\left(-\frac{\alpha_F}{1-\alpha_F}\right)\left\{f_0'^B\right\}_{boundary}+q_{(2,1,0)} \tag{A.109}$$

If the interior scheme should have been applied to obtain the spatial derivative at the boundary:

$$(1-\alpha_F)\left\{f_1'^B\right\}_{interior}+\alpha_F\left\{f_0'^B\right\}_{interior}=\frac{1}{h}\left[b_B f_2+c_B f_1+d_B f_0\right]=q_{(2,1,0)} \tag{A.110}$$

$$\left\{f_1'^B\right\}_{interior}=\left(-\frac{\alpha_F}{1-\alpha_F}\right)\left\{f_0'^B\right\}_{interior}+q_{(2,1,0)} \tag{A.111}$$

by using eq (3.44) applied to the $i=0$ node:

$$\left\{f_1'^B\right\}_{interior}=\left(-\frac{\alpha_F}{1-\alpha_F}\right)\left[\epsilon_0+\left\{f_0'^B\right\}_{boundary}\right]+q_{(2,1,0)}=\left(-\frac{\alpha_F}{1-\alpha_F}\right)\epsilon_0+\left(-\frac{\alpha_F}{1-\alpha_F}\right)\left\{f_0'^B\right\}_{boundary}+q_{(2,1,0)} \tag{A.112}$$

that is:

$$\left\{f_1'^B\right\}_{interior}=\left\{f_1'^B\right\}_{boundary}+\left(-\frac{\alpha_F}{1-\alpha_F}\right)\epsilon_0 \tag{A.113}$$

Similarly, for the point $i=2$:

$$\left\{f_2'^B\right\}_{boundary}=\left(-\frac{\alpha_F}{1-\alpha_F}\right)\left\{f_1'^B\right\}_{boundary}+q_{(3,2,1)}= \tag{A.114}$$

$$=\left(-\frac{\alpha_F}{1-\alpha_F}\right)\left[\left(-\frac{\alpha_F}{1-\alpha_F}\right)\left\{f_0'^B\right\}_{boundary}+q_{(2,1,0)}\right]+q_{(3,2,1)}=$$

$$=\left(-\frac{\alpha_F}{1-\alpha_F}\right)^2\left\{f_0'^B\right\}_{boundary}+\left(-\frac{\alpha_F}{1-\alpha_F}\right)q_{(2,1,0)}+q_{(3,2,1)}$$

$$\left\{f_2'^B\right\}_{interior} = \left(-\frac{\alpha_F}{1-\alpha_F}\right)\left\{f_1'^B\right\}_{interior} + q_{(3,2,1)} = \tag{A.115}$$

$$= \left(-\frac{\alpha_F}{1-\alpha_F}\right)\left[\left(-\frac{\alpha_F}{1-\alpha_F}\right)\epsilon_0 + \left(-\frac{\alpha_F}{1-\alpha_F}\right)\left\{f_0'^B\right\}_{boundary} + q_{(2,1,0)}\right] + q_{(3,2,1)} =$$

$$\left(-\frac{\alpha_F}{1-\alpha_F}\right)^2\epsilon_0 + \left(-\frac{\alpha_F}{1-\alpha_F}\right)^2\left\{f_0'^B\right\}_{boundary} + \left(-\frac{\alpha_F}{1-\alpha_F}\right)q_{(2,1,0)} + q_{(3,2,1)} =$$

$$= \left(-\frac{\alpha_F}{1-\alpha_F}\right)^2\epsilon_0 + \left\{f_2'^B\right\}_{boundary}$$

so:

$$\left\{f_2'^B\right\}_{interior} = \left(-\frac{\alpha_F}{1-\alpha_F}\right)^2\epsilon_0 + \left\{f_2'^B\right\}_{boundary} \tag{A.116}$$

and for a derivative i grid points away from the boundary

$$\left\{f_i'^B\right\}_{\text{interior}} = \left\{f_i'^B\right\}_{\text{boundary}} + \left(-\frac{\alpha_F}{1-\alpha_F}\right)^i\epsilon_0 \tag{A.117}$$

or

$$\epsilon_i = \left(-\frac{\alpha_F}{1-\alpha_F}\right)^i\epsilon_0, \tag{A.118}$$

.

A.8 Wavenumber performance of the FD schemes with closures

A.8.1 Derivation of the coefficients for the prefactored operators for higher-order accuracy

The prefactored forward and backward operators of eq.(3.32) in Section 3.2.4 has been derived up to sixth order accuracy. The Taylor series expansion up to the eleventh-order for the forward and backward operator can be written as (pg.526, Hixon (2000)), (Hixon & Turkel, 2000).

$$\frac{\partial f_i}{\partial x}^F = \frac{\partial f_i}{\partial x} + A\,h\frac{\partial^2 f_i}{\partial x^2} - B\,h^3\frac{\partial^4 f_i}{\partial x^4} + K\,h^5\frac{\partial^6 f_i}{\partial x^6} + D\,h^6\frac{\partial^7 f_i}{\partial x^7} + E\,h^7\frac{\partial^8 f_i}{\partial x^8} + F\,h^8\frac{\partial^9 f_i}{\partial x^9} + G\,h^9\frac{\partial^{10} f_i}{\partial x^{10}} + O(h^{11}) \tag{A.119}$$

$$\frac{\partial f_i}{\partial x}^B = \frac{\partial f_i}{\partial x} - A\,h\frac{\partial^2 f_i}{\partial x^2} + B\,h^3\frac{\partial^4 f_i}{\partial x^4} - K\,h^5\frac{\partial^6 f_i}{\partial x^6} + D\,h^6\frac{\partial^7 f_i}{\partial x^7} - E\,h^7\frac{\partial^8 f_i}{\partial x^8} + F\,h^8\frac{\partial^9 f_i}{\partial x^9} - G\,h^9\frac{\partial^{10} f_i}{\partial x^{10}} + O(h^{11}) \tag{A.120}$$

According to Hixon the even derivatives ($\frac{\partial^2 f_i}{\partial x^2}$, $\frac{\partial^4 f_i}{\partial x^4}$, $\frac{\partial^6 f_i}{\partial x^6}$ $\frac{\partial^8 f_i}{\partial x^8}$, $\frac{\partial^{10} f_i}{\partial x^{10}}$) are equal and opposite between the two operators, and cancel when the two operators are added. The odd derivatives ($\frac{\partial^7 f_i}{\partial x^7}$, $\frac{\partial^9 f_i}{\partial x^9}$) are equal and remain when the two operators are added.

By setting to zero the coefficients D and F, i.e. $D = F = 0$, the accuracy of the Taylor series expansion is extended up to the eleventh-order, that is:

$$\frac{\partial f_i}{\partial x}^F = \frac{\partial f_i}{\partial x} + A\,h\frac{\partial^2 f_i}{\partial x^2} - B\,h^3\frac{\partial^4 f_i}{\partial x^4} + K\,h^5\frac{\partial^6 f_i}{\partial x^6} + E\,h^7\frac{\partial^8 f_i}{\partial x^8} + G\,h^9\frac{\partial^{10} f_i}{\partial x^{10}} + O(h^{11}) \tag{A.121}$$

$$\frac{\partial f_i}{\partial x}^B = \frac{\partial f_i}{\partial x} - A\,h\frac{\partial^2 f_i}{\partial x^2} + B\,h^3\frac{\partial^4 f_i}{\partial x^4} - K\,h^5\frac{\partial^6 f_i}{\partial x^6} - E\,h^7\frac{\partial^8 f_i}{\partial x^8} - G\,h^9\frac{\partial^{10} f_i}{\partial x^{10}} + O(h^{11}) \tag{A.122}$$

By rewriting the prefactored algorithm for backward sweep: (Hixon, 2000; Rona & Spisso, 2007)

$$(1-a)\frac{\partial f_i}{\partial x}^B + a\frac{\partial f_{i-1}^B}{\partial x} = \frac{1}{h}\left[(1-b)f_{i+1} + (2b-1)f_i - b\,f_{i-1}\right] \tag{A.123}$$

Our aim is to substitute the eq. (A.120) in eq. (A.123) and by matching the coefficients find the values for A, B, K and D, E, F, G. Remembering that:

$$\frac{\partial f^B_{i-1}}{\partial x} = \frac{\partial f_{i-1}}{\partial x} - A\,h\frac{\partial^2 f_{i-1}}{\partial x^2} + B\,h^3\frac{\partial^4 f_{i-1}}{\partial x^4} - K\,h^5\frac{\partial^6 f_{i-1}}{\partial x^6} + D\,h^6\frac{\partial^7 f_{i-1}}{\partial x^7} - E\,h^7\frac{\partial^8 f_{i-1}}{\partial x^8} + F\,h^8\frac{\partial^9 f_{i-1}}{\partial x^9} - G\,h^9\frac{\partial^{10} f_{i-1}}{\partial x^{10}} + O(h^{11}) \tag{A.124}$$

$$f_{i+1} = f_i + (h)\frac{\partial f_i}{\partial x} + \frac{(h)^2}{2!}\frac{\partial^2 f_i}{\partial x^2} + \frac{(h)^3}{3!}\frac{\partial^3 f_i}{\partial x^3} + \frac{(h)^4}{4!}\frac{\partial^4 f_i}{\partial x^4} + \frac{(h)^5}{5!}\frac{\partial^5 f_i}{\partial x^5} + \frac{(h)^6}{6!}\frac{\partial^6 f_i}{\partial x^6} + \frac{(h)^7}{7!}\frac{\partial^7 f_i}{\partial x^7} + \frac{(h)^8}{8!}\frac{\partial^8 f_i}{\partial x^8} + \frac{(h)^9}{9!}\frac{\partial^9 f_i}{\partial x^9} + \frac{(h)^{10}}{10!}\frac{\partial^{10} f_i}{\partial x^{10}} + O(h^{11}) \tag{A.125}$$

$$f_{i-1} = f_i - (h)\frac{\partial f_i}{\partial x} + \frac{(h)^2}{2!}\frac{\partial^2 f_i}{\partial x^2} - \frac{(h)^3}{3!}\frac{\partial^3 f_i}{\partial x^3} + \frac{(h)^4}{4!}\frac{\partial^4 f_i}{\partial x^4} - \frac{(h)^5}{5!}\frac{\partial^5 f_i}{\partial x^5} + \frac{(h)^6}{6!}\frac{\partial^6 f_i}{\partial x^6} - \frac{(h)^7}{7!}\frac{\partial^7 f_i}{\partial x^7} + \frac{(h)^8}{8!}\frac{\partial^8 f_i}{\partial x^8} - \frac{(h)^9}{9!}\frac{\partial^9 f_i}{\partial x^9} + \frac{(h)^{10}}{10!}\frac{\partial^{10} f_i}{\partial x^{10}} + O(h^{11}) \tag{A.126}$$

$$\frac{\partial f_{i-1}}{\partial x} = \frac{\partial f_i}{\partial x} - (h)\frac{\partial^2 f_i}{\partial x^2} + \frac{(h)^2}{2!}\frac{\partial^3 f_i}{\partial x^3} - \frac{(h)^3}{3!}\frac{\partial^4 f_i}{\partial x^4} + \frac{(h)^4}{4!}\frac{\partial^5 f_i}{\partial x^5} - \frac{(h)^5}{5!}\frac{\partial^6 f_i}{\partial x^6} + \frac{(h)^6}{6!}\frac{\partial^7 f_i}{\partial x^7} - \frac{(h)^7}{7!}\frac{\partial^8 f_i}{\partial x^8} + \frac{(h)^8}{8!}\frac{\partial^9 f_i}{\partial x^9} - \frac{(h)^9}{9!}\frac{\partial^{10} f_i}{\partial x^{10}} + \frac{(h)^{10}}{10!}\frac{\partial^{11} f_i}{\partial x^{11}} + O(h^{11}) \tag{A.127}$$

$$\frac{\partial^2 f_{i-1}}{\partial x^2} = \frac{\partial^2 f_i}{\partial x^2} - (h)\frac{\partial^3 f_i}{\partial x^3} + \frac{(h)^2}{2!}\frac{\partial^4 f_i}{\partial x^4} - \frac{(h)^3}{3!}\frac{\partial^5 f_i}{\partial x^5} + \frac{(h)^4}{4!}\frac{\partial^6 f_i}{\partial x^6} - \frac{(h)^5}{5!}\frac{\partial^7 f_i}{\partial x^7} + \frac{(h)^6}{6!}\frac{\partial^8 f_i}{\partial x^8} - \frac{(h)^7}{7!}\frac{\partial^9 f_i}{\partial x^9} + \frac{(h)^8}{8!}\frac{\partial^{10} f_i}{\partial x^{10}} + -\frac{(h)^9}{9!}\frac{\partial^{11} f_i}{\partial x^{11}} + \frac{(h)^{10}}{10!}\frac{\partial^{12} f_i}{\partial x^{12}} + O(h^{11}) \tag{A.128}$$

$$\frac{\partial^3 f_{i-1}}{\partial x^3} = \frac{\partial^3 f_i}{\partial x^3} - (h)\frac{\partial^4 f_i}{\partial x^4} + \frac{(h)^2}{2!}\frac{\partial^5 f_i}{\partial x^5} - \frac{(h)^3}{3!}\frac{\partial^6 f_i}{\partial x^6} + \frac{(h)^4}{4!}\frac{\partial^7 f_i}{\partial x^7} - \frac{(h)^5}{5!}\frac{\partial^8 f_i}{\partial x^8} + \frac{(h)^6}{6!}\frac{\partial^9 f_i}{\partial x^9} - \frac{(h)^7}{7!}\frac{\partial^{10} f_i}{\partial x^{10}} + \frac{(h)^8}{8!}\frac{\partial^{11} f_i}{\partial x^{11}} + -\frac{(h)^9}{9!}\frac{\partial^{12} f_i}{\partial x^{12}} + \frac{(h)^{10}}{10!}\frac{\partial^{13} f_i}{\partial x^{13}} + O(h^{11}) \tag{A.129}$$

$$\frac{\partial^4 f_{i-1}}{\partial x^4} = \frac{\partial^4 f_i}{\partial x^4} - (h)\frac{\partial^5 f_i}{\partial x^5} + \frac{(h)^2}{2!}\frac{\partial^6 f_i}{\partial x^6} - \frac{(h)^3}{3!}\frac{\partial^7 f_i}{\partial x^7} + \frac{(h)^4}{4!}\frac{\partial^8 f_i}{\partial x^8} - \frac{(h)^5}{5!}\frac{\partial^9 f_i}{\partial x^9} + \frac{(h)^6}{6!}\frac{\partial^{10} f_i}{\partial x^{10}} - \frac{(h)^7}{7!}\frac{\partial^{11} f_i}{\partial x^{11}} + \frac{(h)^8}{8!}\frac{\partial^{12} f_i}{\partial x^{12}} + -\frac{(h)^9}{9!}\frac{\partial^{13} f_i}{\partial x^{13}} + \frac{(h)^{10}}{10!}\frac{\partial^{14} f_i}{\partial x^{14}} + O(h^{11}) \tag{A.130}$$

$$\frac{\partial^6 f_{i-1}}{\partial x^6} = \frac{\partial^6 f_i}{\partial x^6} - (h)\frac{\partial^7 f_i}{\partial x^7} + \frac{(h)^2}{2!}\frac{\partial^8 f_i}{\partial x^8} - \frac{(h)^3}{3!}\frac{\partial^9 f_i}{\partial x^9} + \frac{(h)^4}{4!}\frac{\partial^{10} f_i}{\partial x^{10}} - \frac{(h)^5}{5!}\frac{\partial^{11} f_i}{\partial x^{11}} + \frac{(h)^6}{6!}\frac{\partial^{12} f_i}{\partial x^{12}} - \frac{(h)^7}{7!}\frac{\partial^{13} f_i}{\partial x^{13}} + \frac{(h)^8}{8!}\frac{\partial^{14} f_i}{\partial x^{14}} + -\frac{(h)^9}{9!}\frac{\partial^{15} f_i}{\partial x^{15}} + \frac{(h)^{10}}{10!}\frac{\partial^{16} f_i}{\partial x^{16}} + O(h^{11}) \tag{A.131}$$

$$\frac{\partial^7 f_{i-1}}{\partial x^7} = \frac{\partial^7 f_i}{\partial x^7} - (h)\frac{\partial^8 f_i}{\partial x^8} + \frac{(h)^2}{2!}\frac{\partial^9 f_i}{\partial x^9} - \frac{(h)^3}{3!}\frac{\partial^{10} f_i}{\partial x^{10}} + \frac{(h)^4}{4!}\frac{\partial^{11} f_i}{\partial x^{11}} - \frac{(h)^5}{5!}\frac{\partial^{12} f_i}{\partial x^{12}} + \frac{(h)^6}{6!}\frac{\partial^{13} f_i}{\partial x^{13}} - \frac{(h)^7}{7!}\frac{\partial^{14} f_i}{\partial x^{14}} + \frac{(h)^8}{8!}\frac{\partial^{15} f_i}{\partial x^{15}} + -\frac{(h)^9}{9!}\frac{\partial^{16} f_i}{\partial x^{16}} + \frac{(h)^{10}}{10!}\frac{\partial^{17} f_i}{\partial x^{17}} + O(h^{11}) \tag{A.132}$$

$$\frac{\partial^8 f_{i-1}}{\partial x^8} = \frac{\partial^8 f_i}{\partial x^8} - (h)\frac{\partial^9 f_i}{\partial x^9} + \frac{(h)^2}{2!}\frac{\partial^{10} f_i}{\partial x^{10}} - \frac{(h)^3}{3!}\frac{\partial^{11} f_i}{\partial x^{11}} + \frac{(h)^4}{4!}\frac{\partial^{12} f_i}{\partial x^{12}} - \frac{(h)^5}{5!}\frac{\partial^{13} f_i}{\partial x^{13}} + \frac{(h)^6}{6!}\frac{\partial^{14} f_i}{\partial x^{14}} - \frac{(h)^7}{7!}\frac{\partial^{15} f_i}{\partial x^{15}} + \frac{(h)^8}{8!}\frac{\partial^{16} f_i}{\partial x^{16}} - \frac{(h)^9}{9!}\frac{\partial^{17} f_i}{\partial x^{17}} + \frac{(h)^{10}}{10!}\frac{\partial^{18} f_i}{\partial x^{18}} + O(h^{11}) \tag{A.133}$$

$$\frac{\partial^9 f_{i-1}}{\partial x^9} = \frac{\partial^9 f_i}{\partial x^9} - (h)\frac{\partial^{10} f_i}{\partial x^{10}} + \frac{(h)^2}{2!}\frac{\partial^{11} f_i}{\partial x^{11}} - \frac{(h)^3}{3!}\frac{\partial^{12} f_i}{\partial x^{12}} + \frac{(h)^4}{4!}\frac{\partial^{13} f_i}{\partial x^{13}} - \frac{(h)^5}{5!}\frac{\partial^{14} f_i}{\partial x^{14}} + \frac{(h)^6}{6!}\frac{\partial^{15} f_i}{\partial x^{15}} - \frac{(h)^7}{7!}\frac{\partial^{16} f_i}{\partial x^{16}} + \frac{(h)^8}{8!}\frac{\partial^{17} f_i}{\partial x^{17}} + -\frac{(h)^9}{9!}\frac{\partial^{18} f_i}{\partial x^{18}} + \frac{(h)^{10}}{10!}\frac{\partial^{19} f_i}{\partial x^{19}} + O(h^{11}) \tag{A.134}$$

$$\frac{\partial^{10} f_{i-1}}{\partial x^{10}} = \frac{\partial^{10} f_i}{\partial x^{10}} - (h)\frac{\partial^{11} f_i}{\partial x^{11}} + \frac{(h)^2}{2!}\frac{\partial^{12} f_i}{\partial x^{12}} - \frac{(h)^3}{3!}\frac{\partial^{13} f_i}{\partial x^{13}} + \frac{(h)^4}{4!}\frac{\partial^{14} f_i}{\partial x^{14}} - \frac{(h)^5}{5!}\frac{\partial^{15} f_i}{\partial x^{15}} + \frac{(h)^6}{6!}\frac{\partial^{16} f_i}{\partial x^{16}} - \frac{(h)^7}{7!}\frac{\partial^{17} f_i}{\partial x^{17}} + \frac{(h)^8}{8!}\frac{\partial^{18} f_i}{\partial x^{18}} + -\frac{(h)^9}{9!}\frac{\partial^{19} f_i}{\partial x^{19}} + \frac{(h)^{10}}{10!}\frac{\partial^{20} f_i}{\partial x^{20}} + O(h^{11}) \tag{A.135}$$

By Substituting in the $\frac{\partial f_{i-1}^B}{\partial x}$ the higher-order derivatives, and neglecting the term of $O(h^{11})$ and higher:

$$\frac{\partial f_{i-1}^B}{\partial x} = \frac{\partial f_{i-1}}{\partial x} - A\,h\frac{\partial^2 f_{i-1}}{\partial x^2} + B\,h^3\frac{\partial^4 f_{i-1}}{\partial x^4} - K\,h^5\frac{\partial^6 f_{i-1}}{\partial x^6} + D\,h^6\frac{\partial^7 f_{i-1}}{\partial x^7} - E\,h^7\frac{\partial^8 f_{i-1}}{\partial x^8} + F\,h^8\frac{\partial^9 f_{i-1}}{\partial x^9} - G\,h^9\frac{\partial^{10} f_{i-1}}{\partial x^{10}} + O(h^{11}) \tag{A.136}$$

$$\begin{aligned}
\frac{\partial f_{i-1}^B}{\partial x} = {} & \frac{\partial f_i}{\partial x} + \\
& -h\frac{\partial^2 f_i}{\partial x^2} + \frac{h^2}{2!}\frac{\partial^3 f_i}{\partial x^3} - \frac{h^3}{3!}\frac{\partial^4 f_i}{\partial x^4} + \frac{h^4}{4!}\frac{\partial^5 f_i}{\partial x^5} - \frac{h^5}{5!}\frac{\partial^6 f_i}{\partial x^6} + \frac{h^6}{6!}\frac{\partial^7 f_i}{\partial x^7} - \frac{h^7}{7!}\frac{\partial^8 f_i}{\partial x^8} + \frac{h^8}{8!}\frac{\partial^9 f_i}{\partial x^9} - \frac{h^9}{9!}\frac{\partial^{10} f_i}{\partial x^{10}} + \frac{h^{10}}{10!}\frac{\partial^{11} f_i}{\partial x^{11}} + \\
& -Ah\left[\frac{\partial^2 f_i}{\partial x^2} - h\frac{\partial^3 f_i}{\partial x^3} + \frac{h^2}{2!}\frac{\partial^4 f_i}{\partial x^4} - \frac{h^3}{3!}\frac{\partial^5 f_i}{\partial x^5} + \frac{h^4}{4!}\frac{\partial^6 f_i}{\partial x^6} - \frac{h^5}{5!}\frac{\partial^7 f_i}{\partial x^7} + \frac{h^6}{6!}\frac{\partial^8 f_i}{\partial x^8} - \frac{h^7}{7!}\frac{\partial^9 f_i}{\partial x^9} + \frac{h^8}{8!}\frac{\partial^{10} f_i}{\partial x^{10}} - \frac{h^9}{9!}\frac{\partial^{11} f_i}{\partial x^{11}} + ...\right] + \\
& +Bh^3\left[\frac{\partial^4 f_i}{\partial x^4} - h\frac{\partial^5 f_i}{\partial x^5} + \frac{h^2}{2!}\frac{\partial^6 f_i}{\partial x^6} - \frac{h^3}{3!}\frac{\partial^7 f_i}{\partial x^7} + \frac{h^4}{4!}\frac{\partial^8 f_i}{\partial x^8} - \frac{h^5}{5!}\frac{\partial^9 f_i}{\partial x^9} + \frac{h^6}{6!}\frac{\partial^{10} f_i}{\partial x^{10}} - \frac{h^7}{7!}\frac{\partial^{11} f_i}{\partial x^{11}} + ...\right] + \\
& -Kh^5\left[\frac{\partial^6 f_i}{\partial x^6} - h\frac{\partial^7 f_i}{\partial x^7} + \frac{h^2}{2!}\frac{\partial^8 f_i}{\partial x^8} - \frac{h^3}{3!}\frac{\partial^9 f_i}{\partial x^9} + \frac{h^4}{4!}\frac{\partial^{10} f_i}{\partial x^{10}} - \frac{h^5}{5!}\frac{\partial^{11} f_i}{\partial x^{11}} + ...\right] \\
& +Dh^6\left[\frac{\partial^7 f_i}{\partial x^7} - h\frac{\partial^8 f_i}{\partial x^8} + \frac{h^2}{2!}\frac{\partial^9 f_i}{\partial x^9} - \frac{h^3}{3!}\frac{\partial^{10} f_i}{\partial x^{10}} + \frac{h^4}{4!}\frac{\partial^{11} f_i}{\partial x^{11}} + ...\right] + \\
& -Eh^7\left[\frac{\partial^8 f_i}{\partial x^8} - h\frac{\partial^9 f_i}{\partial x^9} + \frac{h^2}{2!}\frac{\partial^{10} f_i}{\partial x^{10}} - \frac{h^3}{3!}\frac{\partial^{11} f_i}{\partial x^{11}} + ...\right] + \\
& +Fh^8\left[\frac{\partial^9 f_i}{\partial x^9} - h\frac{\partial^{10} f_i}{\partial x^{10}} + \frac{h^2}{2!}\frac{\partial^{11} f_i}{\partial x^{11}}...\right] + \\
& -Gh^9\left[\frac{\partial^{10} f_i}{\partial x^{10}} - h\frac{\partial^{11} f_i}{\partial x^{11}} + ...\right]
\end{aligned} \tag{A.137}$$

$$
\begin{aligned}
\frac{\partial f_{i-1}^{B}}{\partial x} = \frac{\partial f_i}{\partial x} + \\
&+\left[-h\frac{\partial^2 f_i}{\partial x^2} + \frac{h^2}{2!}\frac{\partial^3 f_i}{\partial x^3} - \frac{h^3}{3!}\frac{\partial^4 f_i}{\partial x^4} + \frac{h^4}{4!}\frac{\partial^5 f_i}{\partial x^5} - \frac{h^5}{5!}\frac{\partial^6 f_i}{\partial x^6} + \frac{h^6}{6!}\frac{\partial^7 f_i}{\partial x^7} - \frac{h^7}{7!}\frac{\partial^8 f_i}{\partial x^8} + \frac{h^8}{8!}\frac{\partial^9 f_i}{\partial x^9} - \frac{h^9}{9!}\frac{\partial^{10} f_i}{\partial x^{10}} + \frac{h^{10}}{10!}\frac{\partial^{11} f_i}{\partial x^{11}}\right] + \\
&-A\left[\ h\frac{\partial^2 f_i}{\partial x^2} - h^2\frac{\partial^3 f_i}{\partial x^3} + \frac{h^3}{2!}\frac{\partial^4 f_i}{\partial x^4} - \frac{h^4}{3!}\frac{\partial^5 f_i}{\partial x^5} + \frac{h^5}{4!}\frac{\partial^6 f_i}{\partial x^6} - \frac{h^6}{5!}\frac{\partial^7 f_i}{\partial x^7} + \frac{h^7}{6!}\frac{\partial^8 f_i}{\partial x^8} - \frac{h^8}{7!}\frac{\partial^9 f_i}{\partial x^9} + \frac{h^9}{8!}\frac{\partial^{10} f_i}{\partial x^{10}} - \frac{h^{10}}{9!}\frac{\partial^{11} f_i}{\partial x^{11}}\right] + \\
&+B\left[\ 0\frac{\partial^2 f_i}{\partial x^2} + 0\frac{\partial^3 f_i}{\partial x^3} + \ h^3\frac{\partial^4 f_i}{\partial x^4} - h^4\frac{\partial^5 f_i}{\partial x^5} + \frac{h^5}{2!}\frac{\partial^6 f_i}{\partial x^6} - \frac{h^6}{3!}\frac{\partial^7 f_i}{\partial x^7} + \frac{h^7}{4!}\frac{\partial^8 f_i}{\partial x^8} - \frac{h^8}{5!}\frac{\partial^9 f_i}{\partial x^9} + \frac{h^9}{6!}\frac{\partial^{10} f_i}{\partial x^{10}} - \frac{h^{10}}{7!}\frac{\partial^{11} f_i}{\partial x^{11}}\right] + \\
&-K\left[\ 0\frac{\partial^2 f_i}{\partial x^2} + 0\frac{\partial^3 f_i}{\partial x^3} + \ 0\frac{\partial^4 f_i}{\partial x^4} + \ 0\frac{\partial^5 f_i}{\partial x^5} + h^5\frac{\partial^6 f_i}{\partial x^6} - \ h^6\frac{\partial^7 f_i}{\partial x^7} + \frac{h^7}{2!}\frac{\partial^8 f_i}{\partial x^8} - \frac{h^8}{3!}\frac{\partial^9 f_i}{\partial x^9} + \frac{h^9}{4!}\frac{\partial^{10} f_i}{\partial x^{10}} - \frac{h^{10}}{5!}\frac{\partial^{11} f_i}{\partial x^{11}}\right] + \\
&+D\left[\ 0\frac{\partial^2 f_i}{\partial x^2} + 0\frac{\partial^3 f_i}{\partial x^3} + \ 0\frac{\partial^4 f_i}{\partial x^4} + \ 0\frac{\partial^5 f_i}{\partial x^5} + \ 0\frac{\partial^6 f_i}{\partial x^6} + \ h^6\frac{\partial^7 f_i}{\partial x^7} - h^7\frac{\partial^8 f_i}{\partial x^8} + \frac{h^8}{2!}\frac{\partial^9 f_i}{\partial x^9} - \frac{h^9}{3!}\frac{\partial^{10} f_i}{\partial x^{10}} + \frac{h^{10}}{4!}\frac{\partial^{11} f_i}{\partial x^{11}}\right] + \\
&-E\left[\ 0\frac{\partial^2 f_i}{\partial x^2} + 0\frac{\partial^3 f_i}{\partial x^3} + \ 0\frac{\partial^4 f_i}{\partial x^4} + \ 0\frac{\partial^5 f_i}{\partial x^5} + \ 0\frac{\partial^6 f_i}{\partial x^6} + 0\frac{\partial^7 f_i}{\partial x^7} + \ h^7\frac{\partial^8 f_i}{\partial x^8} - h^8\frac{\partial^9 f_i}{\partial x^9} + \frac{h^9}{2!}\frac{\partial^{10} f_i}{\partial x^{10}} - \frac{h^{10}}{3!}\frac{\partial^{11} f_i}{\partial x^{11}}\right] + \\
&+F\left[\ 0\frac{\partial^2 f_i}{\partial x^2} + 0\frac{\partial^3 f_i}{\partial x^3} + \ 0\frac{\partial^4 f_i}{\partial x^4} + \ 0\frac{\partial^5 f_i}{\partial x^5} + \ 0\frac{\partial^6 f_i}{\partial x^6} + 0\frac{\partial^7 f_i}{\partial x^7} + 0\frac{\partial^8 f_i}{\partial x^8} + \ h^8\frac{\partial^9 f_i}{\partial x^9} - h^9\frac{\partial^{10} f_i}{\partial x^{10}} + \frac{h^{10}}{2!}\frac{\partial^{11} f_i}{\partial x^{11}}\right] + \\
&-G\left[\ 0\frac{\partial^2 f_i}{\partial x^2} + 0\frac{\partial^3 f_i}{\partial x^3} + \ 0\frac{\partial^4 f_i}{\partial x^4} + \ 0\frac{\partial^5 f_i}{\partial x^5} + \ 0\frac{\partial^6 f_i}{\partial x^6} + 0\frac{\partial^7 f_i}{\partial x^7} + 0\frac{\partial^8 f_i}{\partial x^8} + \ 0\frac{\partial^9 f_i}{\partial x^9} + h^9\frac{\partial^{10} f_i}{\partial x^{10}} - \ h^{10}\frac{\partial^{11} f_i}{\partial x^{11}}\right]
\end{aligned}
\tag{A.138}
$$

$$
\begin{aligned}
\frac{\partial f_{i-1}^{B}}{\partial x} &= \frac{\partial f_i}{\partial x} - (1+A)h\frac{\partial^2 f_i}{\partial x^2} + \left(\frac{1}{2!}+A\right)h^2\frac{\partial^3 f_i}{\partial x^3} - \left(\frac{1}{3!}+\frac{A}{2!}-B\right)h^3\frac{\partial^4 f_i}{\partial x^4} + \\
&+ \left(\frac{1}{4!}+\frac{A}{3!}-B\right)h^4\frac{\partial^5 f_i}{\partial x^5} - \left(\frac{1}{5!}+\frac{A}{4!}-\frac{B}{2!}+K\right)h^5\frac{\partial^6 f_i}{\partial x^6} + \\
&+ \left(\frac{1}{6!}+\frac{A}{5!}-\frac{B}{3!}+K+D\right)h^6\frac{\partial^7 f_i}{\partial x^7} + \left(-\frac{1}{7!}-\frac{A}{6!}+\frac{B}{4!}-\frac{K}{2!}-D-E\right)h^7\frac{\partial^8 f_i}{\partial x^8} + \\
&+ \left(\frac{1}{8!}+\frac{A}{7!}-\frac{B}{5!}+\frac{K}{3!}+\frac{D}{2!}-E+F\right)h^8\frac{\partial^9 f_i}{\partial x^9} + \left(-\frac{1}{9!}-\frac{A}{8!}+\frac{B}{6!}-\frac{K}{4!}-\frac{D}{3!}+\frac{E}{2!}-F+G\right)h^9\frac{\partial^{10} f_i}{\partial x^{10}} \\
&+ \left(\frac{1}{10!}+\frac{A}{9!}-\frac{B}{7!}+\frac{K}{5!}+\frac{D}{4!}-\frac{E}{3!}+\frac{F}{2!}-G\right)h^{10}\frac{\partial^{11} f_i}{\partial x^{11}}
\end{aligned}
\tag{A.139}
$$

By substituting eq A.139 and A.120 in eq A.123

$$
\begin{aligned}
&(1-a)\frac{\partial f_i}{\partial x}^{B} + a\frac{\partial f_{i-1}^{B}}{\partial x} = \frac{1}{h}\left[(1-b)f_{i+1} + (2b-1)f_i - bf_{i-1}\right] \\
&(1-a)\left[\frac{\partial f_i}{\partial x} - Ah\frac{\partial^2 f_i}{\partial x^2} + Bh^3\frac{\partial^4 f_i}{\partial x^4} - Kh^5\frac{\partial^6 f_i}{\partial x^6} + Dh^6\frac{\partial^7 f_i}{\partial x^7} - Eh^7\frac{\partial^8 f_i}{\partial x^8} + Fh^8\frac{\partial^9 f_i}{\partial x^9} - Gh^9\frac{\partial^{10} f_i}{\partial x^{10}}\right] + \\
&a\left[\frac{\partial f_i}{\partial x} - (1+A)h\frac{\partial^2 f_i}{\partial x^2} + \left(\frac{1}{2!}+A\right)h^2\frac{\partial^3 f_i}{\partial x^3} - \left(\frac{1}{3!}+\frac{A}{2!}-B\right)h^3\frac{\partial^4 f_i}{\partial x^4} + \left(\frac{1}{4!}+\frac{A}{3!}-B\right)h^4\frac{\partial^5 f_i}{\partial x^5} + \right. \\
&\left. -\left(\frac{1}{5!}+\frac{A}{4!}-\frac{B}{2!}+K\right)h^5\frac{\partial^6 f_i}{\partial x^6} + \left(\frac{1}{6!}+\frac{A}{5!}-\frac{B}{3!}+K+D\right)h^6\frac{\partial^7 f_i}{\partial x^7} + \left(-\frac{1}{7!}-\frac{A}{6!}+\frac{B}{4!}-\frac{K}{2!}-D-E\right)h^7\frac{\partial^8 f_i}{\partial x^8} + \right. \\
+\quad &\left.\left(\frac{1}{8!}+\frac{A}{7!}-\frac{B}{5!}+\frac{K}{3!}+\frac{D}{2!}-E+F\right)h^8\frac{\partial^9 f_i}{\partial x^9} + \left(-\frac{1}{9!}-\frac{A}{8!}+\frac{B}{6!}-\frac{K}{4!}-\frac{D}{3!}+\frac{E}{2!}-F+G\right)h^9\frac{\partial^{10} f_i}{\partial x^{10}} + \right. \\
+\quad &\left.\left(\frac{1}{10!}+\frac{A}{9!}-\frac{B}{7!}+\frac{K}{5!}+\frac{D}{4!}-\frac{E}{3!}+\frac{F}{2!}-G\right)h^{10}\frac{\partial^{11} f_i}{\partial x^{11}}\right] \\
=\quad &\frac{1}{h}\left[(1-b)\left(f_i + (h)\frac{\partial f_i}{\partial x} + \frac{(h)^2}{2!}\frac{\partial^2 f_i}{\partial x^2} + \frac{(h)^3}{3!}\frac{\partial^3 f_i}{\partial x^3} + \frac{(h)^4}{4!}\frac{\partial^4 f_i}{\partial x^4} + \frac{(h)^5}{5!}\frac{\partial^5 f_i}{\partial x^5} + \frac{(h)^6}{6!}\frac{\partial^6 f_i}{\partial x^6} + \frac{(h)^7}{7!}\frac{\partial^7 f_i}{\partial x^7} + \frac{(h)^8}{8!}\frac{\partial^8 f_i}{\partial x^8} + \right.\right. \\
+\quad &\left.\left.\frac{(h)^9}{9!}\frac{\partial^9 f_i}{\partial x^9} + \frac{(h)^{10}}{10!}\frac{\partial^{10} f_i}{\partial x^{10}}\right) + \right. \\
+\quad &\left.(2b-1)\quad (f_i) + \right. \\
-\quad &\left. b\left(f_i - (h)\frac{\partial f_i}{\partial x} + \frac{(h)^2}{2!}\frac{\partial^2 f_i}{\partial x^2} - \frac{(h)^3}{3!}\frac{\partial^3 f_i}{\partial x^3} + \frac{(h)^4}{4!}\frac{\partial^4 f_i}{\partial x^4} - \frac{(h)^5}{5!}\frac{\partial^5 f_i}{\partial x^5} + \frac{(h)^6}{6!}\frac{\partial^6 f_i}{\partial x^6} - \frac{(h)^7}{7!}\frac{\partial^7 f_i}{\partial x^7} + \frac{(h)^8}{8!}\frac{\partial^8 f_i}{\partial x^8} + \right.\right. \\
-\quad &\left.\left.\frac{(h)^9}{9!}\frac{\partial^9 f_i}{\partial x^9} + \frac{(h)^{10}}{10!}\frac{\partial^{10} f_i}{\partial x^{10}}\right)\right] \\
&(1-a+a)\frac{\partial f_i}{\partial x} + \left[-(1-a)A - a(1+A)\right]h\frac{\partial^2 f_i}{\partial x^2} + \left(\frac{1}{2!}+A\right)ah^2\frac{\partial^3 f_i}{\partial x^3} + \left[(1-a)B - a\left(\frac{1}{3!}+\frac{A}{2!}-B\right)\right]h^3\frac{\partial^4 f_i}{\partial x^4} + \\
+\quad &a\left(\frac{1}{4!}+\frac{A}{3!}-B\right)h^4\frac{\partial^5 f_i}{\partial x^5} + \left[-(1-a)K - a\left(\frac{1}{5!}+\frac{A}{4!}-\frac{B}{2!}+K\right)\right]h^5\frac{\partial^6 f_i}{\partial x^6} + \\
+\quad &\left[(1-a)D + a\left(\frac{1}{6!}+\frac{A}{5!}-\frac{B}{3!}+K+D\right)\right]h^6\frac{\partial^7 f_i}{\partial x^7} + \left[-(1-a)E + a\left(-\frac{1}{7!}-\frac{A}{6!}+\frac{B}{4!}-\frac{K}{2!}-D-E\right)\right]h^7\frac{\partial^8 f_i}{\partial x^8} = \\
=\quad &\frac{1}{h}(1-b+2b-1-b)\,f_i + (1-b+b)\frac{\partial f_i}{\partial x} + \left(\frac{1}{2}(1-b)-\frac{b}{2}\right)h\frac{\partial^2 f_i}{\partial x^2} + \left(\frac{1}{3!}(1-b)+\frac{b}{3!}\right)h^2\frac{\partial^3 f_i}{\partial x^3} \\
+\quad &\left(\frac{1}{4!}(1-b)-\frac{b}{4!}\right)h^3\frac{\partial^4 f_i}{\partial x^4} + \left(\frac{1}{5!}(1-b)+\frac{b}{5!}\right)h^4\frac{\partial^5 f_i}{\partial x^5} + \left(\frac{1}{6!}(1-b)-\frac{b}{6!}\right)h^5\frac{\partial^6 f_i}{\partial x^6} + \left(\frac{1}{7!}(1-b)+\frac{b}{7!}\right)h^6\frac{\partial^7 f_i}{\partial x^7}
\end{aligned}
$$

At the end, we got:

$$
\begin{aligned}
&\frac{\partial f_i}{\partial x} + [-A-a]h\frac{\partial^2 f_i}{\partial x^2} + \left(\frac{1}{2}+A\right)ah^2\frac{\partial^3 f_i}{\partial x^3} + \left[B - \frac{a}{6} - \frac{aA}{2}\right]h^3\frac{\partial^4 f_i}{\partial x^4} + \left(\frac{a}{24}+\frac{aA}{6}-aB\right)h^4\frac{\partial^5 f_i}{\partial x^5} + \qquad \text{(A.140)} \\
+\quad &\left(-K - \frac{a}{120} - \frac{aA}{24} + \frac{aB}{2}\right)h^5\frac{\partial^6 f_i}{\partial x^6} + \left[\frac{a}{6!}+\frac{aA}{5!}-\frac{aB}{3!}+aK+D\right]h^6\frac{\partial^7 f_i}{\partial x^7} + \left(-\frac{1}{7!}-\frac{A}{6!}+\frac{B}{4!}-\frac{K}{2!}-D+E\right) = \\
=\quad &\frac{\partial f_i}{\partial x} + \left(\frac{1}{2}-b\right)h\frac{\partial^2 f_i}{\partial x^2} + \left(\frac{1}{6}\right)h^2\frac{\partial^3 f_i}{\partial x^3} + \left(\frac{1}{24}-\frac{b}{12}\right)h^3\frac{\partial^4 f_i}{\partial x^4} + \left(\frac{1}{120}\right)h^4\frac{\partial^5 f_i}{\partial x^5} + \left(\frac{1}{720}-\frac{b}{360}\right)h^5\frac{\partial^6 f_i}{\partial x^6} \\
+\quad &\left(\frac{1}{5040}\right)h^6\frac{\partial^7 f_i}{\partial x^7}
\end{aligned}
$$

By comparing member by member the last two equations:

$$h\frac{\partial^2 f_i}{\partial x^2} \quad \Rightarrow -A - a = \frac{1}{2} - b \quad A = -a + b - \frac{1}{2} \tag{A.141}$$

$$h^2\frac{\partial^3 f_i}{\partial x^3} \quad \Rightarrow \frac{1}{2}a + aA = \frac{1}{6} \qquad A = \frac{1}{6a} - \frac{1}{2} \tag{A.142}$$

$$h^3\frac{\partial^4 f_i}{\partial x^4} \quad \Rightarrow B - \frac{a}{6} - \frac{aA}{2} = \frac{1}{24} - \frac{b}{12} \quad B = \frac{aA}{2} + \frac{a}{6} + \frac{1-2b}{24} \tag{A.143}$$

$$h^4\frac{\partial^5 f_i}{\partial x^5} \quad \Rightarrow \frac{a}{24} + \frac{aA}{6} - aB = \frac{1}{120} \qquad B = \frac{A}{6} + \frac{1}{24} - \frac{1}{120a} \tag{A.144}$$

$$h^5\frac{\partial^6 f_i}{\partial x^6} \quad \Rightarrow \qquad K = -\frac{1}{720} + \frac{b}{360} - \frac{a}{120} - \frac{aA}{24} + \frac{aB}{2} \tag{A.145}$$

$$h^6\frac{\partial^7 f_i}{\partial x^7} \quad \Rightarrow \qquad D = \frac{1}{7!} - \frac{a}{6!} - \frac{aA}{5!} + \frac{aB}{3!} - aK \tag{A.146}$$

$$h^7\frac{\partial^8 f_i}{\partial x^8} \quad \Rightarrow -E - \frac{a}{7!} - \frac{Aa}{6!} + \frac{Ba}{4!} - \frac{Ka}{2!} - aD = \frac{1}{8!} - \frac{b}{4\times 7!}$$

$$E = -\frac{1}{8!} + \frac{b}{4\times 7!} - \frac{a}{7!} - \frac{Aa}{6!} + \frac{Ba}{4!} - \frac{Ka}{2!} - aD \tag{A.147}$$

$$h^8\frac{\partial^9 f_i}{\partial x^9} \quad \Rightarrow F + \frac{a}{8!} + \frac{aA}{7!} - \frac{aB}{5!} + \frac{aK}{3!} + \frac{aD}{2!} + aE = \frac{1}{9!}$$

$$F = \frac{1}{9!} - a\left(\frac{1}{8!} + \frac{A}{7!} - \frac{B}{5!} + \frac{K}{3!} + \frac{D}{2!} + E\right) \tag{A.148}$$

$$h^9\frac{\partial^{10} f_i}{\partial x^{10}} \quad \Rightarrow -G + a\left(-\frac{1}{9!} - \frac{A}{8!} + \frac{B}{6!} - \frac{K}{4!} - \frac{D}{3!} - \frac{E}{2!} - F\right) = \left(\frac{1}{10!} - \frac{b}{5\times 9!}\right)$$

$$G = -\frac{1}{10!} + \frac{b}{5\times 9!} + a\left(-\frac{1}{9!} - \frac{A}{8!} + \frac{B}{6!} - \frac{K}{4!} - \frac{D}{3!} - \frac{E}{2!} - F\right) \tag{A.149}$$

And so:

$$A = \frac{1}{3+3\sqrt{5}} = \frac{\sqrt{5}-1}{12} \qquad \text{from eq. (A.141) and (A.142)}$$

$$B = \frac{5+7\sqrt{5}}{720} \qquad \text{from eq. (A.143)and (A.144)}$$

$$K = \frac{-5+17\sqrt{5}}{21600} \qquad \text{from eq. (A.145)}$$

$$D = \frac{1}{2100} \qquad \text{from eq. (A.146)}$$

$$E = \frac{-25-227\sqrt{5}}{6048000} \qquad \text{from eq. (A.147)}$$

$$F = \frac{-277}{4536000} \qquad \text{from eq. (A.148)}$$

$$G = \frac{1475-839\sqrt{5}}{544320000} \qquad \text{from eq. (A.149)}$$

A.8.2 Boundary stencils

A.8.3 Prefactored one-sided boundary stencil

By rewriting the prefactored one-sided backward boundary stencil of eqs.(3.47):

$$\begin{aligned} \frac{\partial f_1^B}{\partial x} &= \frac{1}{h}\sum_{j=1}^{7} s_j f_j \\ \frac{\partial f_{jmax}^B}{\partial x} &= \frac{1}{h}\sum_{j=jmax-6}^{jmax} e_j f_j \end{aligned} \tag{A.150}$$

and for the forward sweep, the (3.48):

$$\begin{aligned} \frac{\partial f_1^F}{\partial x} &= \frac{1}{h}\sum_{j=1}^{7} -e_{jmax+1-j} f_j \\ \frac{\partial f_{jmax}^F}{\partial x} &= \frac{1}{h}\sum_{j=jmax-6}^{jmax} -s_{jmax+1-j} f_j \end{aligned} \tag{A.151}$$

A.8.3.1 Derivation of the coefficients

Prefactored one-sided boundary stencils

Calculate the coefficients on double precision for one-sided boundary stencil D_1^B. By rewriting it in extended form:

$$\frac{\partial f_1^B}{\partial x} = \frac{1}{h}\sum_{j=1}^{7} s_j f_j = \frac{1}{h}\left[s_1 f_1 + s_2 f_2 + s_3 f_3 + s_4 f_4 + s_5 f_5 + s_6 f_6 + s_7 f_7\right] \tag{A.152}$$

And for the last node $\frac{\partial f_{jmax}^B}{\partial x}$

$$\frac{\partial f^B_{jmax}}{\partial x} = \frac{1}{h}\sum_{j=jmax-6}^{jmax} e_j f_j = \frac{1}{h}\Big[e_{jmax-6} f_{jmax-6} + e_{jmax-5} f_{jmax-5} + e_{jmax-4} f_{jmax-4} + e_{jmax-3} f_{jmax-3} + + e_{jmax-2} f_{jmax-2} + e_{jmax-1} f_{jmax-1} + e_{jmax} f_{jmax}\Big] \quad \text{(A.153)}$$

Let us recall the Taylor series expansion of the function $f_{i+1}(x)$, at the mesh point $i+1$ around the mesh point i.

$$f_{i+1} = f_i + \sum_{n=1}^{\infty} \frac{(h)^n}{n!}\frac{\partial^n f}{\partial x^n} = f_i + (h)\frac{\partial f}{\partial x} + \frac{(h)^2}{2!}\frac{\partial^2 f}{\partial x^2} + \frac{(h)^3}{3!}\frac{\partial^3 f}{\partial x^3} + ... \quad \text{(A.154)}$$

And similarly for $f_{i-1}(x)$

$$f_{i-1} = f_i + \sum_{n=1}^{\infty}\left[\pm\frac{(h)^n}{n!}\right]\frac{\partial^n f}{\partial x^n} = f_i - h\frac{\partial f}{\partial x} + \frac{h^2}{2!}\frac{\partial^2 f}{\partial x^2} - \frac{h^3}{3!}\frac{\partial^3 f}{\partial x^3} + .. \text{(+ for even } n\text{, - for odd n)} \quad \text{(A.155)}$$

Consider the Taylor series expansion of the the function $f_2(x) = f_{1+1}(x)$, at the mesh point $i = 2$ around the mesh point $i = 1$ up to the sixth order, with an interval equal to h

$$f_2 = f_{1+1} \simeq f_1 + \sum_{n=1}^{6}\frac{(h)^n}{n!}\frac{\partial^n f_1}{\partial x^n} = f_1 + (h)\frac{\partial f_1}{\partial x} + \frac{(h)^2}{2!}\frac{\partial^2 f_1}{\partial x^2} + \frac{(h)^3}{3!}\frac{\partial^3 f_1}{\partial x^3} + \frac{(h)^4}{4!}\frac{\partial^4 f_1}{\partial x^4} + \frac{(h)^5}{5!}\frac{\partial^5 f_1}{\partial x^6} + \frac{(h)^6}{6!}\frac{\partial^6 f_1}{\partial x^6} + O(h)^7 \quad \text{(A.156)}$$

In a similar way consider the Taylor series expansion of the the function $f_3(x) = f_{1+2}(x)$, at the mesh point $i = 3$ around the mesh point $i = 1$ up to the sixth order, with an interval equal to $2h$ and so on up to $f_7 = f_{1+6}$

$$f_3 = f_{1+2} \simeq f_1 + \sum_{n=1}^{6}\frac{(2h)^n}{n!}\frac{\partial^n f}{\partial x^n} = f_1 + (2h)\frac{\partial f}{\partial x} + \frac{(2h)^2}{2!}\frac{\partial^2 f}{\partial x^2} + \frac{(2h)^3}{3!}\frac{\partial^3 f}{\partial x^3} + \frac{(2h)^4}{4!}\frac{\partial^4 f}{\partial x^4} + \frac{(2h)^5}{5!}\frac{\partial^5 f}{\partial x^6} + \frac{(2h)^6}{6!}\frac{\partial^6 f}{\partial x^6} + O(2h) \quad \text{(A.157)}$$

$$
\begin{aligned}
f_4 &= f_{1+3} \simeq f_1 + (3h)\frac{\partial f}{\partial x} + \frac{(3h)^2}{2!}\frac{\partial^2 f}{\partial x^2} + \frac{(3h)^3}{3!}\frac{\partial^3 f}{\partial x^3} + \frac{(3h)^4}{4!}\frac{\partial^4 f}{\partial x^4} + \frac{(3h)^5}{5!}\frac{\partial^5 f}{\partial x^6} + \frac{(3h)^6}{6!}\frac{\partial^6 f}{\partial x^6} + O(3h)^7 \\
f_5 &= f_{1+4} \simeq f_1 + (4h)\frac{\partial f}{\partial x} + \frac{(4h)^2}{2!}\frac{\partial^2 f}{\partial x^2} + \frac{(4h)^3}{3!}\frac{\partial^3 f}{\partial x^3} + \frac{(4h)^4}{4!}\frac{\partial^4 f}{\partial x^4} + \frac{(4h)^5}{5!}\frac{\partial^5 f}{\partial x^6} + \frac{(4h)^6}{6!}\frac{\partial^6 f}{\partial x^6} + O(4h)^7 \\
f_6 &= f_{1+5} \simeq f_1 + (5h)\frac{\partial f}{\partial x} + \frac{(5h)^2}{2!}\frac{\partial^2 f}{\partial x^2} + \frac{(5h)^3}{3!}\frac{\partial^3 f}{\partial x^3} + \frac{(5h)^4}{4!}\frac{\partial^4 f}{\partial x^4} + \frac{(5h)^5}{5!}\frac{\partial^5 f}{\partial x^6} + \frac{(5h)^6}{6!}\frac{\partial^6 f}{\partial x^6} + O(5h)^7 \\
f_7 &= f_{1+6} \simeq f_1 + (6h)\frac{\partial f}{\partial x} + \frac{(6h)^2}{2!}\frac{\partial^2 f}{\partial x^2} + \frac{(6h)^3}{3!}\frac{\partial^3 f}{\partial x^3} + \frac{(6h)^4}{4!}\frac{\partial^4 f}{\partial x^4} + \frac{(6h)^5}{5!}\frac{\partial^5 f}{\partial x^6} + \frac{(6h)^6}{6!}\frac{\partial^6 f}{\partial x^6} + O(6h)^7
\end{aligned}
\tag{A.158}
$$

And similarly for f_{jmax-1}, consider the Taylor series expansion of the the function $f_{jmax-1}(x)$, at the mesh point $j = jmax - 1$ around the mesh point $j = jmax$ up to the sixth order, with an interval equal to h

$$
\begin{aligned}
f_{jmax-1} &\simeq f_{jmax} + \sum_{n=1}^{6} \pm\frac{(h)^n}{n!}\frac{\partial^n f_{jmax}}{\partial x^n} = f_{jmax} - (h)\frac{\partial f_{jmax}}{\partial x} + \frac{(h)^2}{2!}\frac{\partial^2 f_{jmax}}{\partial x^2} - \frac{(h)^3}{3!}\frac{\partial^3 f_{jmax}}{\partial x^3} + \frac{(h)^4}{4!}\frac{\partial^4 f_{jmax}}{\partial x^4} + \\
&- \frac{(h)^5}{5!}\frac{\partial^5 f_{jmax}}{\partial x^6} + \frac{(h)^6}{6!}\frac{\partial^6 f_{jmax}}{\partial x^6} + O(h)^7
\end{aligned}
\tag{A.159}
$$

And so on up to f_{jmax-6}

$$
\begin{aligned}
f_{jmax-2} &= f_{jmax} - (2h)\frac{\partial f_{jmax}}{\partial x} + \frac{(2h)^2}{2!}\frac{\partial^2 f_{jmax}}{\partial x^2} - \frac{(2h)^3}{3!}\frac{\partial^3 f_{jmax}}{\partial x^3} + \frac{(2h)^4}{4!}\frac{\partial^4 f_{jmax}}{\partial x^4} - \frac{(2h)^5}{5!}\frac{\partial^5 f_{jmax}}{\partial x^6} + \\
&+ \frac{(2h)^6}{6!}\frac{\partial^6 f_{jmax}}{\partial x^6} + O(2h)^7 \\
f_{jmax-3} &= f_{jmax} - (3h)\frac{\partial f_{jmax}}{\partial x} + \frac{(3h)^2}{2!}\frac{\partial^2 f_{jmax}}{\partial x^2} - \frac{(3h)^3}{3!}\frac{\partial^3 f_{jmax}}{\partial x^3} + \frac{(3h)^4}{4!}\frac{\partial^4 f_{jmax}}{\partial x^4} - \frac{(3h)^5}{5!}\frac{\partial^5 f_{jmax}}{\partial x^6} \\
&+ \frac{(3h)^6}{6!}\frac{\partial^6 f_{jmax}}{\partial x^6} + O(3h)^7 \\
f_{jmax-4} &= f_{jmax} - (4h)\frac{\partial f_{jmax}}{\partial x} + \frac{(4h)^2}{2!}\frac{\partial^2 f_{jmax}}{\partial x^2} - \frac{(4h)^3}{3!}\frac{\partial^3 f_{jmax}}{\partial x^3} + \frac{(4h)^4}{4!}\frac{\partial^4 f_{jmax}}{\partial x^4} - \frac{(4h)^5}{5!}\frac{\partial^5 f_{jmax}}{\partial x^6} \\
&+ \frac{(4h)^6}{6!}\frac{\partial^6 f_{jmax}}{\partial x^6} + O(4h)^7 \\
f_{jmax-5} &= f_{jmax} - (5h)\frac{\partial f_{jmax}}{\partial x} + \frac{(5h)^2}{2!}\frac{\partial^2 f_{jmax}}{\partial x^2} - \frac{(5h)^3}{3!}\frac{\partial^3 f_{jmax}}{\partial x^3} + \frac{(5h)^4}{4!}\frac{\partial^4 f_{jmax}}{\partial x^4} - \frac{(5h)^5}{5!}\frac{\partial^5 f_{jmax}}{\partial x^6} \\
&+ \frac{(5h)^6}{6!}\frac{\partial^6 f_{jmax}}{\partial x^6} + O(5h)^7 \\
f_{jmax-6} &= f_{jmax} - (6h)\frac{\partial f_{jmax}}{\partial x} + \frac{(6h)^2}{2!}\frac{\partial^2 f_{jmax}}{\partial x^2} - \frac{(6h)^3}{3!}\frac{\partial^3 f_{jmax}}{\partial x^3} + \frac{(6h)^4}{4!}\frac{\partial^4 f_{jmax}}{\partial x^4} - \frac{(6h)^5}{5!}\frac{\partial^5 f_{jmax}}{\partial x^6} \\
&+ \frac{(6h)^6}{6!}\frac{\partial^6 f_{jmax}}{\partial x^6} + O(6h)^7
\end{aligned}
$$

By substituting the previous values in equation A.152 for the first node

$$
\begin{aligned}
\frac{\partial f_1^B}{\partial x} &= \frac{1}{h}\Bigg[s_1 f_1 + \\
&+ s_2\left(f_1 + (h)\frac{\partial f_1}{\partial x} + \frac{(h)^2}{2!}\frac{\partial^2 f_1}{\partial x^2} + \frac{(h)^3}{3!}\frac{\partial^3 f_1}{\partial x^3} + \frac{(h)^4}{4!}\frac{\partial^4 f_1}{\partial x^4} + \frac{(h)^5}{5!}\frac{\partial^5 f_1}{\partial x^6} + \frac{(h)^6}{6!}\frac{\partial^6 f_1}{\partial x^6}\right) \\
&+ s_3\left(f_1 + (2h)\frac{\partial f_1}{\partial x} + \frac{(2h)^2}{2!}\frac{\partial^2 f_1}{\partial x^2} + \frac{(2h)^3}{3!}\frac{\partial^3 f_1}{\partial x^3} + \frac{(2h)^4}{4!}\frac{\partial^4 f_1}{\partial x^4} + \frac{(2h)^5}{5!}\frac{\partial^5 f_1}{\partial x^6} + \frac{(2h)^6}{6!}\frac{\partial^6 f_1}{\partial x^6}\right) \\
&+ s_4\left(f_1 + (3h)\frac{\partial f_1}{\partial x} + \frac{(3h)^2}{2!}\frac{\partial^2 f_1}{\partial x^2} + \frac{(3h)^3}{3!}\frac{\partial^3 f_1}{\partial x^3} + \frac{(3h)^4}{4!}\frac{\partial^4 f_1}{\partial x^4} + \frac{(3h)^5}{5!}\frac{\partial^5 f_1}{\partial x^6} + \frac{(3h)^6}{6!}\frac{\partial^6 f_1}{\partial x^6}\right) \\
&+ s_5\left(f_1 + (4h)\frac{\partial f_1}{\partial x} + \frac{(4h)^2}{2!}\frac{\partial^2 f_1}{\partial x^2} + \frac{(4h)^3}{3!}\frac{\partial^3 f_1}{\partial x^3} + \frac{(4h)^4}{4!}\frac{\partial^4 f_1}{\partial x^4} + \frac{(4h)^5}{5!}\frac{\partial^5 f_1}{\partial x^6} + \frac{(4h)^6}{6!}\frac{\partial^6 f_1}{\partial x^6}\right) \\
&+ s_6\left(f_1 + (5h)\frac{\partial f_1}{\partial x} + \frac{(5h)^2}{2!}\frac{\partial^2 f_1}{\partial x^2} + \frac{(5h)^3}{3!}\frac{\partial^3 f_1}{\partial x^3} + \frac{(5h)^4}{4!}\frac{\partial^4 f_1}{\partial x^4} + \frac{(5h)^5}{5!}\frac{\partial^5 f_1}{\partial x^6} + \frac{(5h)^6}{6!}\frac{\partial^6 f_1}{\partial x^6}\right) \\
&+ s_7\left(f_1 + (6h)\frac{\partial f_1}{\partial x} + \frac{(6h)^2}{2!}\frac{\partial^2 f_1}{\partial x^2} + \frac{(6h)^3}{3!}\frac{\partial^3 f_1}{\partial x^3} + \frac{(6h)^4}{4!}\frac{\partial^4 f_1}{\partial x^4} + \frac{(6h)^5}{5!}\frac{\partial^5 f_1}{\partial x^6} + \frac{(6h)^6}{6!}\frac{\partial^6 f}{\partial x^6}\right)\Bigg]
\end{aligned}
$$

$$
\begin{aligned}
\frac{\partial f_1}{\partial x}^B &= \frac{1}{h}\Bigg[(s_1 + s_2 + s_3 + s_4 + s_5 + s_6 + s_7)\, f_1 + \\
&+ (s_2 + 2s_3 + 3s_4 + 4s_5 + 5s_6 + 6s_7)\, h\frac{\partial f_1}{\partial x} + \\
&+ \left(\frac{1^2}{2!}s_2 + \frac{2^2}{2!}s_3 + \frac{3^2}{2!}s_4 + \frac{4^2}{2!}s_5 + \frac{5^2}{2!}s_6 + \frac{6^2}{2!}s_7\right)h^2\frac{\partial^2 f_i}{\partial x^2} + \\
&+ \left(\frac{1^3}{3!}s_2 + \frac{2^3}{3!}s_3 + \frac{3^3}{3!}s_4 + \frac{4^3}{3!}s_5 + \frac{5^3}{3!}s_6 + \frac{6^3}{3!}s_7\right)h^3\frac{\partial^3 f_i}{\partial x^3} + \\
&+ \left(\frac{1^4}{4!}s_2 + \frac{2^4}{4!}s_3 + \frac{3^4}{4!}s_4 + \frac{4^4}{4!}s_5 + \frac{5^4}{4!}s_6 + \frac{6^4}{4!}s_7\right)h^4\frac{\partial^4 f_i}{\partial x^4} + \\
&+ \left(\frac{1^5}{5!}s_2 + \frac{2^5}{5!}s_3 + \frac{3^5}{5!}s_4 + \frac{4^5}{5!}s_5 + \frac{5^5}{5!}s_6 + \frac{6^5}{5!}s_7\right)h^5\frac{\partial^5 f_i}{\partial x^5} + \\
&+ \left(\frac{1^6}{6!}s_2 + \frac{2^6}{6!}s_3 + \frac{3^6}{6!}s_4 + \frac{4^6}{6!}s_5 + \frac{5^6}{6!}s_6 + \frac{6^6}{6!}s_7\right)h^6\frac{\partial^6 f_i}{\partial x^6} +
\end{aligned}
\tag{A.160}
$$

And similarly for the last node, substituting in eq A.191

$$
\begin{aligned}
\frac{\partial f^{B}_{jmax}}{\partial x} = \frac{1}{h}\Bigg[& \\
& e_{jmax-6}\left(f_{jmax} - (6h)\frac{\partial f_{jmax}}{\partial x} + \frac{(6h)^2}{2!}\frac{\partial^2 f_{jmax}}{\partial x^2} - \frac{(6h)^3}{3!}\frac{\partial^3 f_{jmax}}{\partial x^3} + \frac{(6h)^4}{4!}\frac{\partial^4 f_{jmax}}{\partial x^4} - \frac{(6h)^5}{5!}\frac{\partial^5 f_{jmax}}{\partial x^6} + \frac{(6h)^6}{6!}\frac{\partial^6 f_{jmax}}{\partial x^6}\right) + \\
& + e_{jmax-5}\left(f_{jmax} - (5h)\frac{\partial f_{jmax}}{\partial x} + \frac{(5h)^2}{2!}\frac{\partial^2 f_{jmax}}{\partial x^2} - \frac{(5h)^3}{3!}\frac{\partial^3 f_{jmax}}{\partial x^3} + \frac{(5h)^4}{4!}\frac{\partial^4 f_{jmax}}{\partial x^4} - \frac{(5h)^5}{5!}\frac{\partial^5 f_{jmax}}{\partial x^6} + \frac{(5h)^6}{6!}\frac{\partial^6 f_{jmax}}{\partial x^6}\right) + \\
& + e_{jmax-4}\left(f_{jmax} - (4h)\frac{\partial f_{jmax}}{\partial x} + \frac{(4h)^2}{2!}\frac{\partial^2 f_{jmax}}{\partial x^2} - \frac{(4h)^3}{3!}\frac{\partial^3 f_{jmax}}{\partial x^3} + \frac{(4h)^4}{4!}\frac{\partial^4 f_{jmax}}{\partial x^4} - \frac{(4h)^5}{5!}\frac{\partial^5 f_{jmax}}{\partial x^6} + \frac{(4h)^6}{6!}\frac{\partial^6 f_{jmax}}{\partial x^6}\right) + \\
& + e_{jmax-3}\left(f_{jmax} - (3h)\frac{\partial f_{jmax}}{\partial x} + \frac{(3h)^2}{2!}\frac{\partial^2 f_{jmax}}{\partial x^2} - \frac{(3h)^3}{3!}\frac{\partial^3 f_{jmax}}{\partial x^3} + \frac{(3h)^4}{4!}\frac{\partial^4 f_{jmax}}{\partial x^4} - \frac{(3h)^5}{5!}\frac{\partial^5 f_{jmax}}{\partial x^6} + \frac{(3h)^6}{6!}\frac{\partial^6 f_{jmax}}{\partial x^6}\right) + \\
& + e_{jmax-2}\left(f_{jmax} - (2h)\frac{\partial f_{jmax}}{\partial x} + \frac{(2h)^2}{2!}\frac{\partial^2 f_{jmax}}{\partial x^2} - \frac{(2h)^3}{3!}\frac{\partial^3 f_{jmax}}{\partial x^3} + \frac{(2h)^4}{4!}\frac{\partial^4 f_{jmax}}{\partial x^4} - \frac{(2h)^5}{5!}\frac{\partial^5 f_{jmax}}{\partial x^6} + \frac{(2h)^6}{6!}\frac{\partial^6 f_{jmax}}{\partial x^6}\right) + \\
& + e_{jmax-1}\left(f_{jmax} - (h)\frac{\partial f_{jmax}}{\partial x} + \frac{(h)^2}{2!}\frac{\partial^2 f_{jmax}}{\partial x^2} - \frac{(h)^3}{3!}\frac{\partial^3 f_{jmax}}{\partial x^3} + \frac{(h)^4}{4!}\frac{\partial^4 f_{jmax}}{\partial x^4} - \frac{(h)^5}{5!}\frac{\partial^5 f_{jmax}}{\partial x^6} + \frac{(h)^6}{6!}\frac{\partial^6 f_{jmax}}{\partial x^6}\right) + \\
& + e_{jmax}\ f_{jmax}\Bigg]
\end{aligned}
$$

$$
\begin{aligned}
\frac{\partial f^B_{jmax}}{\partial x} &= \frac{1}{h}\Bigg[\\
&\left(e_{jmax} + e_{jmax-1} + e_{jmax-2} + e_{jmax-3} + e_{jmax-4} + e_{jmax-5} + e_{jmax-6}\right) f_{jmax} + \\
&- \left(e_{jmax-1} + 2e_{jmax-2} + 3e_{jmax-3} + 4e_{jmax-4} + 5e_{jmax-5} + 6\, e_{jmax-6}\right) h\frac{\partial f_{jmax}}{\partial x} + \\
&+ \left(\frac{1^2}{2!}e_{jmax-1} + \frac{2^2}{2!}e_{jmax-2} + \frac{3^2}{2!}e_{jmax-3} + \frac{4^2}{2!}e_{jmax-4} + \frac{5^2}{2!}e_{jmax-5} + \frac{6^2}{2!}e_{jmax-6}\right) h^2\frac{\partial^2 f_i}{\partial x^2} + \\
&- \left(\frac{1^3}{3!}e_{jmax-1} + \frac{2^3}{3!}e_{jmax-2} + \frac{3^3}{3!}e_{jmax-3} + \frac{4^3}{3!}e_{jmax-4} + \frac{5^3}{3!}e_{jmax-5} + \frac{6^3}{3!}e_{jmax-6}\right) h^3\frac{\partial^3 f_i}{\partial x^3} + \\
&+ \left(\frac{1^4}{4!}e_{jmax-1} + \frac{2^4}{4!}e_{jmax-2} + \frac{3^4}{4!}e_{jmax-3} + \frac{4^4}{4!}e_{jmax-4} + \frac{5^4}{4!}e_{jmax-5} + \frac{6^4}{4!}e_{jmax-6}\right) h^4\frac{\partial^4 f_i}{\partial x^4} + \\
&- \left(\frac{1^5}{5!}e_{jmax-1} + \frac{2^5}{5!}e_{jmax-2} + \frac{3^5}{5!}e_{jmax-3} + \frac{4^5}{5!}e_{jmax-4} + \frac{5^5}{5!}e_{jmax-5} + \frac{6^5}{5!}e_{jmax6}\right) h^5\frac{\partial^5 f_i}{\partial x^5} + \\
&+ \left(\frac{1^6}{6!}e_{jmax-1} + \frac{2^6}{6!}e_{jmax-2} + \frac{3^6}{6!}e_{jmax-3} + \frac{4^6}{6!}e_{jmax-4} + \frac{5^6}{6!}e_{jmax-5} + \frac{6^6}{6!}e_{jmax-6}\right) h^6\frac{\partial^6 f_i}{\partial x^6}\Bigg]
\end{aligned}
\tag{A.161}
$$

Now, given the values of A B and K in eq A.150, by equating the second member of equation A.160 and A.120 up to sixth-order accuracy:

$$\begin{pmatrix} 1 & 1 & 1 & 1 & 1 & 1 & 1 \\ 0 & 1 & 2 & 3 & 4 & 5 & 6 \\ 0 & \frac{1}{2} & \frac{2^2}{2} & \frac{3^2}{2} & \frac{4^2}{2} & \frac{5^2}{2} & \frac{6^2}{2} \\ 0 & \frac{1}{6} & \frac{2^3}{6} & \frac{3^3}{6} & \frac{4^3}{6} & \frac{5^3}{6} & \frac{6^3}{6} \\ 0 & \frac{1}{24} & \frac{2^4}{24} & \frac{3^4}{24} & \frac{4^4}{24} & \frac{5^4}{24} & \frac{6^4}{24} \\ 0 & \frac{1}{120} & \frac{2^5}{120} & \frac{3^5}{120} & \frac{4^5}{120} & \frac{5^5}{120} & \frac{6^5}{120} \\ 0 & \frac{1}{720} & \frac{2^6}{720} & \frac{3^6}{720} & \frac{4^6}{720} & \frac{5^6}{720} & \frac{6^6}{720} \end{pmatrix} \begin{pmatrix} s_1 \\ s_2 \\ s_3 \\ s_4 \\ s_5 \\ s_6 \\ s_7 \end{pmatrix} = \begin{pmatrix} 0 & \Rightarrow f_i \ line \\ 1 & \Rightarrow \frac{\partial f_i}{\partial x} \ line \\ -A & \Rightarrow h\frac{\partial^2 f_i}{\partial x^2} \ line \\ 0 & \Rightarrow h^2\frac{\partial^3 f_i}{\partial x^3} \ line \\ B & \Rightarrow h^3\frac{\partial^4 f_i}{\partial x^4} \ line \\ 0 & \Rightarrow h^4\frac{\partial^5 f_i}{\partial x^5} \ line \\ -K & \Rightarrow h^5\frac{\partial^6 f_i}{\partial x^6} \ line \end{pmatrix} \tag{A.162}$$

By inverting the matrix and the L.H.S. and solving the system with matlab:

Ans so the coefficients are:

$$\begin{aligned} s_1 &= -\frac{545+353\sqrt{5}}{150\left(1+\sqrt{5}\right)} = -\frac{545+353\sqrt{5}}{150\left(1+\sqrt{5}\right)} = -2.74887508613328 \\ s_2 &= \frac{1515+823\sqrt{5}}{150\left(1+\sqrt{5}\right)} = \frac{1515+823\sqrt{5}}{150\left(1+\sqrt{5}\right)} = 6.91226506738317 \\ s_3 &= -\frac{405+191\sqrt{5}}{30\left(1+\sqrt{5}\right)} = -\frac{2025+955\sqrt{5}}{150\left(1+\sqrt{5}\right)} = -8.57098789320814 \\ s_4 &= \frac{35+16\sqrt{5}}{3\left(1+\sqrt{5}\right)} = \frac{1750+800\sqrt{5}}{150\left(1+\sqrt{5}\right)} = 7.29044096437489 \\ s_5 &= -\frac{95+43\sqrt{5}}{15\left(1+\sqrt{5}\right)} = -\frac{950+430\sqrt{5}}{150\left(1+\sqrt{5}\right)} = -3.93792558049996 \\ s_6 &= \frac{295+133\sqrt{5}}{150\left(1+\sqrt{5}\right)} = \frac{295+133\sqrt{5}}{150\left(1+\sqrt{5}\right)} = 1.22040502059166 \\ s_7 &= -\frac{20+9\sqrt{5}}{75\left(1+\sqrt{5}\right)} = -\frac{40+18\sqrt{5}}{150\left(1+\sqrt{5}\right)} = -0.165322492508333 \end{aligned} \tag{A.163}$$

For the e_j coefficients by equating the second member of A.161 and A.120

$$\begin{pmatrix} 1 & 1 & 1 & 1 & 1 & 1 & 1 \\ 0 & -1 & -2 & -3 & -4 & -5 & -6 \\ 0 & \frac{1}{2} & \frac{2^2}{2} & \frac{3^2}{2} & \frac{4^2}{2} & \frac{5^2}{2} & \frac{6^2}{2} \\ 0 & -\frac{1}{6} & -\frac{2^3}{6} & -\frac{3^3}{6} & -\frac{4^3}{6} & -\frac{5^3}{6} & -\frac{6^3}{6} \\ 0 & \frac{1}{24} & \frac{2^4}{24} & \frac{3^4}{24} & \frac{4^4}{24} & \frac{5^4}{24} & \frac{6^4}{24} \\ 0 & -\frac{1}{120} & -\frac{2^5}{120} & -\frac{3^5}{120} & -\frac{4^5}{120} & -\frac{5^5}{120} & -\frac{6^5}{120} \\ 0 & \frac{1}{720} & \frac{2^6}{720} & \frac{3^6}{720} & \frac{4^6}{720} & \frac{5^6}{720} & \frac{6^6}{720} \end{pmatrix} \begin{pmatrix} e_{jmax} \\ e_{jmax-1} \\ e_{jmax-2} \\ e_{jmax-3} \\ e_{jmax-4} \\ e_{jmax-5} \\ e_{jmax-6} \end{pmatrix} = \begin{pmatrix} 0 & \Rightarrow f_i \ line \\ 1 & \Rightarrow \frac{\partial f_i}{\partial x} \ line \\ -A & \Rightarrow h\frac{\partial^2 f_i}{\partial x^2} \ line \\ 0 & \Rightarrow h^2\frac{\partial^3 f_i}{\partial x^3} \ line \\ B & \Rightarrow h^3\frac{\partial^4 f_i}{\partial x^4} \ line \\ 0 & \Rightarrow h^4\frac{\partial^5 f_i}{\partial x^5} \ line \\ -K & \Rightarrow h^5\frac{\partial^6 f_i}{\partial x^6} \ line \end{pmatrix} \tag{A.164}$$

By inverting the matrix and the l.h.s and solving the system with matlab

Ans so the e_j coefficients are:

$$e_{jmax} = \frac{95 + 191\sqrt{5}}{75\left(1 + \sqrt{5}\right)} = \frac{190 + 382\sqrt{5}}{150\left(1 + \sqrt{5}\right)} = 2.15112491386675$$

$$e_{jmax-1} = -\frac{285 + 977\sqrt{5}}{150\left(1 + \sqrt{5}\right)} = -\frac{285 + 997\sqrt{5}}{150\left(1 + \sqrt{5}\right)} = -5.08773493261699$$

$$e_{jmax-2} = \frac{45 + 259\sqrt{5}}{30\left(1 + \sqrt{5}\right)} = \frac{225 + 1295\sqrt{5}}{150\left(1 + \sqrt{5}\right)} = 6.42901210679221$$

$$e_{jmax-3} = -\frac{5 + 24\sqrt{5}}{3\left(1 + \sqrt{5}\right)} = -\frac{250 + 1200\sqrt{5}}{150\left(1 + \sqrt{5}\right)} = -6.04289236895886$$

$$e_{jmax-4} = \frac{35 + 139\sqrt{5}}{30\left(1 + \sqrt{5}\right)} = \frac{175 + 695\sqrt{5}}{150\left(1 + \sqrt{5}\right)} = 3.56207441950031$$

$$e_{jmax-5} = -\frac{65 + 227\sqrt{5}}{150\left(1 + \sqrt{5}\right)} = -\frac{65 + 227\sqrt{5}}{150\left(1 + \sqrt{5}\right)} = -1.17959497940844$$

$$e_{jmax-6} = \frac{5 + 16\sqrt{5}}{75\left(1 + \sqrt{5}\right)} = \frac{10 + 32\sqrt{5}}{150\left(1 + \sqrt{5}\right)} = 0.168010840825015$$

Prefactored interior boundary stencil

The interior boundary stencils are given by eq. (3.51a) and (3.51b).
By rewriting the first of eq. (3.51a) in extended form:

$$\begin{aligned} f_i'^F &= \frac{1}{h}\Big[b_{-5}f_{j-5} + b_{-4}f_{j-4} + b_{-3}f_{j-3} + b_{-2}f_{j-2} + b_{-1}f_{j-1} + b_0 f_j + \\ &+ \quad b_1 f_{j+1} + b_2 f_{j+2} + b_3 f_{j+3} + b_4 f_{j+4} + b_5 f_{j+5}\Big] \end{aligned} \tag{A.165}$$

And expanding up to the 11th order the Taylor series expansions:

$$
\begin{aligned}
f_{i+1} &= f_i + \sum_{n=1}^{\infty} \frac{(h)^n}{n!} \frac{\partial^n f}{\partial x^n} = \\
&= f_i + (h)\frac{\partial f}{\partial x} + \frac{(h)^2}{2!}\frac{\partial^2 f}{\partial x^2} + \frac{(h)^3}{3!}\frac{\partial^3 f}{\partial x^3} + \frac{(h)^4}{4!}\frac{\partial^4 f}{\partial x^4} + \frac{(h)^5}{5!}\frac{\partial^5 f}{\partial x^5} + \frac{(h)^6}{6!}\frac{\partial^6 f}{\partial x^6} + \frac{(h)^7}{7!}\frac{\partial^7 f}{\partial x^7} + \\
&+ \frac{(h)^8}{8!}\frac{\partial^8 f}{\partial x^8} + \frac{(h)^9}{9!}\frac{\partial^9 f}{\partial x^9} + \frac{(h)^{10}}{10!}\frac{\partial^{10} f}{\partial x^{10}} + O(h^{11}) \\
f_{i-1} &= f_i - (h)\frac{\partial f}{\partial x} + \frac{(h)^2}{2!}\frac{\partial^2 f}{\partial x^2} - \frac{(h)^3}{3!}\frac{\partial^3 f}{\partial x^3} + \frac{(h)^4}{4!}\frac{\partial^4 f}{\partial x^4} - \frac{(h)^5}{5!}\frac{\partial^5 f}{\partial x^5} + \frac{(h)^6}{6!}\frac{\partial^6 f}{\partial x^6} - \frac{(h)^7}{7!}\frac{\partial^7 f}{\partial x^7} + \\
&+ \frac{(h)^8}{8!}\frac{\partial^8 f}{\partial x^8} - \frac{(2h)^9}{9!}\frac{\partial^9 f}{\partial x^9} + \frac{(h)^{10}}{10!}\frac{\partial^{10} f}{\partial x^{10}} + O(h^{11}) \\
f_{i+2} &= f_i + (2h)\frac{\partial f}{\partial x} + \frac{(2h)^2}{2!}\frac{\partial^2 f}{\partial x^2} + \frac{(2h)^3}{3!}\frac{\partial^3 f}{\partial x^3} + \frac{(2h)^4}{4!}\frac{\partial^4 f}{\partial x^4} + \frac{(2h)^5}{5!}\frac{\partial^5 f}{\partial x^5} + \frac{(2h)^6}{6!}\frac{\partial^6 f}{\partial x^6} + \frac{(2h)^7}{7!}\frac{\partial^7 f}{\partial x^7} + \\
&+ \frac{(2h)^8}{8!}\frac{\partial^8 f}{\partial x^8} + \frac{(2h)^9}{9!}\frac{\partial^9 f}{\partial x^9} + \frac{(2h)^{10}}{10!}\frac{\partial^{10} f}{\partial x^{10}} + O(2h^{11}) \\
f_{i-2} &= f_i - (2h)\frac{\partial f}{\partial x} + \frac{(2h)^2}{2!}\frac{\partial^2 f}{\partial x^2} - \frac{(2h)^3}{3!}\frac{\partial^3 f}{\partial x^3} + \frac{(2h)^4}{4!}\frac{\partial^4 f}{\partial x^4} - \frac{(2h)^5}{5!}\frac{\partial^5 f}{\partial x^5} + \frac{(2h)^6}{6!}\frac{\partial^6 f}{\partial x^6} - \frac{(2h)^7}{7!}\frac{\partial^7 f}{\partial x^7} + \\
&+ \frac{(2h)^8}{8!}\frac{\partial^8 f}{\partial x^8} - \frac{(2h)^9}{9!}\frac{\partial^9 f}{\partial x^9} + \frac{(2h)^{10}}{10!}\frac{\partial^{10} f}{\partial x^{10}} + O(2h^{11}) \\
f_{i+3} &= f_i + (3h)\frac{\partial f}{\partial x} + \frac{(3h)^2}{2!}\frac{\partial^2 f}{\partial x^2} + \frac{(3h)^3}{3!}\frac{\partial^3 f}{\partial x^3} + \frac{(3h)^4}{4!}\frac{\partial^4 f}{\partial x^4} + \frac{(3h)^5}{5!}\frac{\partial^5 f}{\partial x^5} + \frac{(3h)^6}{6!}\frac{\partial^6 f}{\partial x^6} + \frac{(3h)^7}{7!}\frac{\partial^7 f}{\partial x^7} + \\
&+ \frac{(3h)^8}{8!}\frac{\partial^8 f}{\partial x^8} + \frac{(3h)^9}{9!}\frac{\partial^9 f}{\partial x^9} + \frac{(3h)^{10}}{10!}\frac{\partial^{10} f}{\partial x^{10}} + O(3h^{11}) \\
f_{i-3} &= f_i - (3h)\frac{\partial f}{\partial x} + \frac{(3h)^2}{2!}\frac{\partial^2 f}{\partial x^2} - \frac{(3h)^3}{3!}\frac{\partial^3 f}{\partial x^3} + \frac{(3h)^4}{4!}\frac{\partial^4 f}{\partial x^4} - \frac{(3h)^5}{5!}\frac{\partial^5 f}{\partial x^5} + \frac{(3h)^6}{6!}\frac{\partial^6 f}{\partial x^6} - \frac{(3h)^7}{7!}\frac{\partial^7 f}{\partial x^7} + \\
&+ \frac{(3h)^8}{8!}\frac{\partial^8 f}{\partial x^8} - \frac{(3h)^9}{9!}\frac{\partial^9 f}{\partial x^9} + \frac{(3h)^{10}}{10!}\frac{\partial^{10} f}{\partial x^{10}} + O(3h^{11}) \\
f_{i+4} &= f_i + (4h)\frac{\partial f}{\partial x} + \frac{(4h)^2}{2!}\frac{\partial^2 f}{\partial x^2} + \frac{(4h)^3}{3!}\frac{\partial^3 f}{\partial x^3} + \frac{(4h)^4}{4!}\frac{\partial^4 f}{\partial x^4} + \frac{(4h)^5}{5!}\frac{\partial^5 f}{\partial x^5} + \frac{(4h)^6}{6!}\frac{\partial^6 f}{\partial x^6} + \frac{(4h)^7}{7!}\frac{\partial^7 f}{\partial x^7} + \\
&+ \frac{(4h)^8}{8!}\frac{\partial^8 f}{\partial x^8} + \frac{(4h)^9}{9!}\frac{\partial^9 f}{\partial x^9} + \frac{(4h)^{10}}{10!}\frac{\partial^{10} f}{\partial x^{10}} + O(4h^{11}) \\
f_{i-4} &= f_i - (4h)\frac{\partial f}{\partial x} + \frac{(4h)^2}{2!}\frac{\partial^2 f}{\partial x^2} - \frac{(4h)^3}{3!}\frac{\partial^3 f}{\partial x^3} + \frac{(4h)^4}{4!}\frac{\partial^4 f}{\partial x^4} - \frac{(4h)^5}{5!}\frac{\partial^5 f}{\partial x^5} + \frac{(4h)^6}{6!}\frac{\partial^6 f}{\partial x^6} - \frac{(4h)^7}{7!}\frac{\partial^7 f}{\partial x^7} + \\
&+ \frac{(4h)^8}{8!}\frac{\partial^8 f}{\partial x^8} - \frac{(4h)^9}{9!}\frac{\partial^9 f}{\partial x^9} + \frac{(4h)^{10}}{10!}\frac{\partial^{10} f}{\partial x^{10}} + O(4h^{11}) \\
f_{i+5} &= f_i + (5h)\frac{\partial f}{\partial x} + \frac{(5h)^2}{2!}\frac{\partial^2 f}{\partial x^2} + \frac{(5h)^3}{3!}\frac{\partial^3 f}{\partial x^3} + \frac{(5h)^4}{4!}\frac{\partial^4 f}{\partial x^4} + \frac{(5h)^5}{5!}\frac{\partial^5 f}{\partial x^5} + \frac{(5h)^6}{6!}\frac{\partial^6 f}{\partial x^6} + \frac{(5h)^7}{7!}\frac{\partial^7 f}{\partial x^7} + \\
&+ \frac{(5h)^8}{8!}\frac{\partial^8 f}{\partial x^8} + \frac{(5h)^9}{9!}\frac{\partial^9 f}{\partial x^9} + \frac{(5h)^{10}}{10!}\frac{\partial^{10} f}{\partial x^{10}} + O(5h^{11}) \\
f_{i-5} &= f_i - (5h)\frac{\partial f}{\partial x} + \frac{(5h)^2}{2!}\frac{\partial^2 f}{\partial x^2} - \frac{(5h)^3}{3!}\frac{\partial^3 f}{\partial x^3} + \frac{(5h)^4}{4!}\frac{\partial^4 f}{\partial x^4} - \frac{(5h)^5}{5!}\frac{\partial^5 f}{\partial x^5} + \frac{(5h)^6}{6!}\frac{\partial^6 f}{\partial x^6} - \frac{(5h)^7}{7!}\frac{\partial^7 f}{\partial x^7} + \\
&+ \frac{(5h)^8}{8!}\frac{\partial^8 f}{\partial x^8} - \frac{(5h)^9}{9!}\frac{\partial^9 f}{\partial x^9} + \frac{(5h)^{10}}{10!}\frac{\partial^{10} f}{\partial x^{10}} + O(5h^{11})
\end{aligned}
$$

By substituting in eq. (A.165):

$$
\begin{aligned}
&\frac{\partial f_i^F}{\partial x} = \frac{1}{h}\Bigg[\\
&b_{-5}\left(f_i - (5h)\frac{\partial f}{\partial x} + \frac{(5h)^2}{2!}\frac{\partial^2 f}{\partial x^2} - \frac{(5h)^3}{3!}\frac{\partial^3 f}{\partial x^3} + \frac{(5h)^4}{4!}\frac{\partial^4 f}{\partial x^4} - \frac{(5h)^5}{5!}\frac{\partial^5 f}{\partial x^5} + \frac{(5h)^6}{6!}\frac{\partial^6 f}{\partial x^6} - \frac{(5h)^7}{7!}\frac{\partial^7 f}{\partial x^7} + \right. \\
&\left. \frac{(5h)^8}{8!}\frac{\partial^8 f}{\partial x^8} - \frac{(5h)^9}{9!}\frac{\partial^9 f}{\partial x^9} + \frac{(5h)^{10}}{10!}\frac{\partial^{10} f}{\partial x^{10}} + O(5h^{11})\right) \\
&+ b_{-4}\left(f_i - (4h)\frac{\partial f}{\partial x} + \frac{(4h)^2}{2!}\frac{\partial^2 f}{\partial x^2} - \frac{(4h)^3}{3!}\frac{\partial^3 f}{\partial x^3} + \frac{(4h)^4}{4!}\frac{\partial^4 f}{\partial x^4} - \frac{(4h)^5}{5!}\frac{\partial^5 f}{\partial x^5} + \frac{(4h)^6}{6!}\frac{\partial^6 f}{\partial x^6} - \frac{(4h)^7}{7!}\frac{\partial^7 f}{\partial x^7} + \right. \\
&\left. \frac{(4h)^8}{8!}\frac{\partial^8 f}{\partial x^8} - \frac{(4h)^9}{9!}\frac{\partial^9 f}{\partial x^9} + \frac{(4h)^{10}}{10!}\frac{\partial^{10} f}{\partial x^{10}} + O(4h^{11})\right) \\
&+ b_{-3}\left(f_i - (3h)\frac{\partial f}{\partial x} + \frac{(3h)^2}{2!}\frac{\partial^2 f}{\partial x^2} - \frac{(3h)^3}{3!}\frac{\partial^3 f}{\partial x^3} + \frac{(3h)^4}{4!}\frac{\partial^4 f}{\partial x^4} - \frac{(3h)^5}{5!}\frac{\partial^5 f}{\partial x^5} + \frac{(3h)^6}{6!}\frac{\partial^6 f}{\partial x^6} - \frac{(3h)^7}{7!}\frac{\partial^7 f}{\partial x^7} + \right. \\
&\left. \frac{(3h)^8}{8!}\frac{\partial^8 f}{\partial x^8} - \frac{(3h)^9}{9!}\frac{\partial^9 f}{\partial x^9} + \frac{(3h)^{10}}{10!}\frac{\partial^{10} f}{\partial x^{10}} + O(3h^{11})\right) \\
&+ b_{-2}\left(f_i - (2h)\frac{\partial f}{\partial x} + \frac{(2h)^2}{2!}\frac{\partial^2 f}{\partial x^2} - \frac{(2h)^3}{3!}\frac{\partial^3 f}{\partial x^3} + \frac{(2h)^4}{4!}\frac{\partial^4 f}{\partial x^4} - \frac{(2h)^5}{5!}\frac{\partial^5 f}{\partial x^5} + \frac{(2h)^6}{6!}\frac{\partial^6 f}{\partial x^6} - \frac{(2h)^7}{7!}\frac{\partial^7 f}{\partial x^7} + \right. \\
&\left. \frac{(2h)^8}{8!}\frac{\partial^8 f}{\partial x^8} + \frac{(2h)^9}{9!}\frac{\partial^9 f}{\partial x^9} + \frac{(2h)^{10}}{10!}\frac{\partial^{10} f}{\partial x^{10}} + O(2h^{11})\right) \\
&+ b_{-1}\left(f_i - (h)\frac{\partial f}{\partial x} + \frac{(h)^2}{2!}\frac{\partial^2 f}{\partial x^2} - \frac{(h)^3}{3!}\frac{\partial^3 f}{\partial x^3} + \frac{(h)^4}{4!}\frac{\partial^4 f}{\partial x^4} - \frac{(h)^5}{5!}\frac{\partial^5 f}{\partial x^5} + \frac{(h)^6}{6!}\frac{\partial^6 f}{\partial x^6} - \frac{(h)^7}{7!}\frac{\partial^7 f}{\partial x^7} + \right. \\
&\left. \frac{(h)^8}{8!}\frac{\partial^8 f}{\partial x^8} - \frac{(h)^9}{9!}\frac{\partial^9 f}{\partial x^9} + \frac{(h)^{10}}{10!}\frac{\partial^{10} f}{\partial x^{10}} + O(h^{11})\right) + b_0\,(f_i) + \\
&+ b_1\left(f_i + (h)\frac{\partial f}{\partial x} + \frac{(h)^2}{2!}\frac{\partial^2 f}{\partial x^2} + \frac{(h)^3}{3!}\frac{\partial^3 f}{\partial x^3} + \frac{(h)^4}{4!}\frac{\partial^4 f}{\partial x^4} + \frac{(h)^5}{5!}\frac{\partial^5 f}{\partial x^5} + \frac{(h)^6}{6!}\frac{\partial^6 f}{\partial x^6} + \frac{(h)^7}{7!}\frac{\partial^7 f}{\partial x^7} + \frac{(h)^8}{8!}\frac{\partial^8 f}{\partial x^8} + \right. \\
&\left. \frac{(h)^9}{9!}\frac{\partial^9 f}{\partial x^9} + \frac{(h)^{10}}{10!}\frac{\partial^{10} f}{\partial x^{10}} + O(h^{11})\right) \\
&+ b_2\left(f_i + (2h)\frac{\partial f}{\partial x} + \frac{(2h)^2}{2!}\frac{\partial^2 f}{\partial x^2} + \frac{(2h)^3}{3!}\frac{\partial^3 f}{\partial x^3} + \frac{(2h)^4}{4!}\frac{\partial^4 f}{\partial x^4} + \frac{(2h)^5}{5!}\frac{\partial^5 f}{\partial x^5} + \frac{(2h)^6}{6!}\frac{\partial^6 f}{\partial x^6} + \frac{(2h)^7}{7!}\frac{\partial^7 f}{\partial x^7} + \right. \\
&\left. \frac{(2h)^8}{8!}\frac{\partial^8 f}{\partial x^8} + \frac{(2h)^9}{9!}\frac{\partial^9 f}{\partial x^9} + \frac{(2h)^{10}}{10!}\frac{\partial^{10} f}{\partial x^{10}} + O(2h^{11})\right) \\
&+ b_3\left(f_i + (3h)\frac{\partial f}{\partial x} + \frac{(3h)^2}{2!}\frac{\partial^2 f}{\partial x^2} + \frac{(3h)^3}{3!}\frac{\partial^3 f}{\partial x^3} + \frac{(3h)^4}{4!}\frac{\partial^4 f}{\partial x^4} + \frac{(3h)^5}{5!}\frac{\partial^5 f}{\partial x^5} + \frac{(3h)^6}{6!}\frac{\partial^6 f}{\partial x^6} + \frac{(3h)^7}{7!}\frac{\partial^7 f}{\partial x^7} + \right. \\
&\left. \frac{(3h)^8}{8!}\frac{\partial^8 f}{\partial x^8} + \frac{(3h)^9}{9!}\frac{\partial^9 f}{\partial x^9} + \frac{(3h)^{10}}{10!}\frac{\partial^{10} f}{\partial x^{10}} + O(3h^{11})\right) \\
&+ b_4\left(f_i + (4h)\frac{\partial f}{\partial x} + \frac{(4h)^2}{2!}\frac{\partial^2 f}{\partial x^2} + \frac{(4h)^3}{3!}\frac{\partial^3 f}{\partial x^3} + \frac{(4h)^4}{4!}\frac{\partial^4 f}{\partial x^4} + \frac{(4h)^5}{5!}\frac{\partial^5 f}{\partial x^5} + \frac{(4h)^6}{6!}\frac{\partial^6 f}{\partial x^6} + \frac{(4h)^7}{7!}\frac{\partial^7 f}{\partial x^7} + \right. \\
&\left. \frac{(4h)^8}{8!}\frac{\partial^8 f}{\partial x^8} + \frac{(4h)^9}{9!}\frac{\partial^9 f}{\partial x^9} + \frac{(4h)^{10}}{10!}\frac{\partial^{10} f}{\partial x^{10}} + O(4h^{11})\right) \\
&+ b_5\left(f_i + (5h)\frac{\partial f}{\partial x} + \frac{(5h)^2}{2!}\frac{\partial^2 f}{\partial x^2} + \frac{(5h)^3}{3!}\frac{\partial^3 f}{\partial x^3} + \frac{(5h)^4}{4!}\frac{\partial^4 f}{\partial x^4} + \frac{(5h)^5}{5!}\frac{\partial^5 f}{\partial x^5} + \frac{(5h)^6}{6!}\frac{\partial^6 f}{\partial x^6} + \frac{(5h)^7}{7!}\frac{\partial^7 f}{\partial x^7} + \right. \\
&\left. \frac{(5h)^8}{8!}\frac{\partial^8 f}{\partial x^8} + \frac{(5h)^9}{9!}\frac{\partial^9 f}{\partial x^9} + \frac{(5h)^{10}}{10!}\frac{\partial^{10} f}{\partial x^{10}} + O(5h^{11})\right)\Bigg]
\end{aligned}
$$

$$
\begin{aligned}
\frac{\partial f_1}{\partial x}^F &= \frac{1}{h}\Bigg[(b_{-5}+b_{-4}+b_{-3}+b_{-2}+b_{-1}+b_0+b_1+b_2+b_3+b_4+b_5)\, f_i + \\
&+ (-5b_{-5}-4b_{-4}-3b_{-3}-2b_{-2}-b_{-1}+b_1+2b_2+3b_3+4b_4+5b_5)\, h\frac{\partial f_i}{\partial x} + \\
&+ \left(\frac{5^2}{2!}b_{-5}+\frac{4^2}{2!}b_{-4}+\frac{3^2}{2!}b_{-3}+\frac{2^2}{2!}b_{-2}+\frac{1^2}{2!}b_{-1}+\frac{1^2}{2!}b_1+\frac{2^2}{2!}b_2+\frac{3^2}{2!}b_3+\frac{4^2}{2!}b_4+\frac{5^2}{2!}b_5\right) h^2\frac{\partial^2 f_i}{\partial x^2} + \\
&+ \left(-\frac{5^3}{3!}b_{-5}-\frac{4^3}{3!}b_{-4}-\frac{3^3}{3!}b_{-3}-\frac{2^3}{3!}b_{-2}-\frac{1^3}{3!}b_{-1}+\frac{1^3}{3!}b_1+\frac{2^3}{3!}b_2+\frac{3^3}{3!}b_3+\frac{4^3}{3!}b_4+\frac{5^3}{3!}b_5\right) h^3\frac{\partial^3 f_i}{\partial x^3} + \\
&+ \left(\frac{5^4}{4!}b_{-5}+\frac{4^4}{4!}b_{-4}+\frac{3^4}{4!}b_{-3}+\frac{2^4}{4!}b_{-2}+\frac{1^4}{4!}b_{-1}+\frac{1^4}{4!}b_1+\frac{2^4}{4!}b_2+\frac{3^4}{4!}b_3+\frac{4^4}{4!}b_4+\frac{5^4}{4!}b_5\right) h^4\frac{\partial^4 f_i}{\partial x^4} + \\
&+ \left(-\frac{5^5}{5!}b_{-5}-\frac{4^5}{5!}b_{-4}-\frac{3^5}{5!}b_{-3}-\frac{2^5}{5!}b_{-2}-\frac{1^5}{5!}b_{-1}+\frac{1^5}{5!}b_1+\frac{2^5}{5!}b_2+\frac{3^5}{5!}b_3+\frac{4^5}{5!}b_4+\frac{5^5}{5!}b_5\right) h^5\frac{\partial^5 f_i}{\partial x^5} + \\
&+ \left(\frac{5^6}{6!}b_{-5}+\frac{4^6}{6!}b_{-4}+\frac{3^6}{6!}b_{-3}+\frac{2^6}{6!}b_{-2}+\frac{1^6}{6!}b_{-1}+\frac{1^6}{6!}b_1+\frac{2^6}{6!}b_2+\frac{3^6}{6!}b_3+\frac{4^6}{6!}b_4+\frac{5^6}{6!}b_5\right) h^6\frac{\partial^6 f_i}{\partial x^6} + \\
&+ \left(-\frac{5^7}{7!}b_{-5}-\frac{4^7}{7!}b_{-4}-\frac{3^7}{7!}b_{-3}-\frac{2^7}{7!}b_{-2}-\frac{1^7}{7!}b_{-1}+\frac{1^7}{7!}b_1+\frac{2^7}{7!}b_2+\frac{3^7}{7!}b_3+\frac{4^7}{7!}b_4+\frac{5^7}{7!}b_5\right) h^7\frac{\partial^7 f_i}{\partial x^7} + \\
&+ \left(\frac{5^8}{8!}b_{-5}+\frac{4^8}{8!}b_{-4}+\frac{3^8}{8!}b_{-3}+\frac{2^8}{8!}b_{-2}+\frac{1^8}{8!}b_{-1}+\frac{1^8}{8!}b_1+\frac{2^8}{8!}b_2+\frac{3^8}{8!}b_3+\frac{4^8}{8!}b_4+\frac{5^8}{8!}b_5\right) h^8\frac{\partial^8 f_i}{\partial x^8} + \\
&+ \left(-\frac{5^9}{9!}b_{-5}-\frac{4^9}{9!}b_{-4}-\frac{3^9}{9!}b_{-3}-\frac{2^9}{9!}b_{-2}-\frac{1^9}{9!}b_{-1}+\frac{1^9}{9!}b_1+\frac{2^9}{9!}b_2+\frac{3^9}{9!}b_3+\frac{4^9}{9!}b_4+\frac{5^9}{9!}b_5\right) h^9\frac{\partial^9 f_i}{\partial x^9} + \\
&+ \left(\frac{5^{10}}{10!}b_{-5}+\frac{4^{10}}{10!}b_{-4}+\frac{3^{10}}{10!}b_{-3}+\frac{2^{10}}{10!}b_{-2}+\frac{1^{10}}{10!}b_{-1}+\frac{1^{10}}{10!}b_1+\frac{2^{10}}{10!}b_2+\frac{3^{10}}{10!}b_3+\frac{4^{10}}{10!}b_4+\frac{5^{10}}{10!}b_5\right) h^{10}\frac{\partial^{10} f_i}{\partial x^{10}}\Bigg]
\end{aligned}
\tag{A.166}
$$

By comparing eq. A.121 and eq A.166, finally we get:

$$
\begin{pmatrix}
1 & 1 & 1 & 1 & 1 & 1 & 1 & 1 & 1 & 1 & 1 \\
-5 & -4 & -3 & -2 & -1 & 0 & 1 & 2 & 3 & 4 & 5 \\
\frac{5^2}{2} & \frac{4^2}{2} & \frac{3^2}{2} & \frac{2^2}{2} & \frac{1^2}{2} & 0 & \frac{1^2}{2} & \frac{2^2}{2} & \frac{3^2}{2} & \frac{4^2}{2} & \frac{5^2}{2} \\
-\frac{5^3}{3!} & -\frac{4^3}{3!} & -\frac{3^3}{3!} & -\frac{2^3}{3!} & -\frac{1^3}{3!} & 0 & \frac{1^3}{3!} & \frac{2^3}{3!} & \frac{3^3}{3!} & \frac{4^3}{3!} & \frac{5^3}{3!} \\
\frac{5^4}{4!} & \frac{4^4}{4!} & \frac{3^4}{4!} & \frac{2^4}{4!} & \frac{1^4}{4!} & 0 & \frac{1^4}{4!} & \frac{2^4}{4!} & \frac{3^4}{4!} & \frac{4^4}{4!} & \frac{5^4}{4!} \\
-\frac{5^5}{5!} & -\frac{4^5}{5!} & -\frac{3^5}{5!} & -\frac{2^5}{5!} & -\frac{1^5}{5!} & 0 & \frac{1^5}{5!} & \frac{2^5}{5!} & \frac{3^5}{5!} & \frac{4^5}{5!} & \frac{5^5}{5!} \\
\frac{5^6}{6!} & \frac{4^6}{6!} & \frac{3^6}{6!} & \frac{2^6}{6!} & \frac{1^6}{6!} & 0 & \frac{1^6}{6!} & \frac{2^6}{6!} & \frac{3^6}{6!} & \frac{4^6}{6!} & \frac{5^6}{6!} \\
-\frac{5^7}{7!} & -\frac{4^7}{7!} & -\frac{3^7}{7!} & -\frac{2^7}{7!} & -\frac{1^7}{7!} & 0 & \frac{1^7}{7!} & \frac{2^7}{7!} & \frac{3^7}{7!} & \frac{4^7}{7!} & \frac{5^7}{7!} \\
\frac{5^8}{8!} & \frac{4^8}{8!} & \frac{3^8}{8!} & \frac{2^8}{8!} & \frac{1^8}{8!} & 0 & \frac{1^8}{8!} & \frac{2^8}{8!} & \frac{3^8}{8!} & \frac{4^8}{8!} & \frac{5^8}{8!} \\
-\frac{5^9}{9!} & -\frac{4^9}{9!} & -\frac{3^9}{9!} & -\frac{2^9}{9!} & -\frac{1^9}{9!} & 0 & \frac{1^9}{9!} & \frac{2^9}{9!} & \frac{3^9}{9!} & \frac{4^9}{9!} & \frac{5^9}{9!} \\
\frac{5^{10}}{10!} & \frac{4^{10}}{10!} & \frac{3^{10}}{10!} & \frac{2^{10}}{10!} & \frac{1^{10}}{10!} & 0 & \frac{1^{10}}{10!} & \frac{2^{10}}{10!} & \frac{3^{10}}{10!} & \frac{4^{10}}{10!} & \frac{5^{10}}{10!}
\end{pmatrix}
\begin{pmatrix} b_{-5} \\ b_{-4} \\ b_{-3} \\ b_{-2} \\ b_{-1} \\ b_0 \\ b_1 \\ b_2 \\ b_3 \\ b_4 \\ b_5 \end{pmatrix}
=
\begin{pmatrix}
0 & \Rightarrow f_i \ line \\
1 & \Rightarrow \frac{\partial f_i}{\partial x} \ line \\
A & \Rightarrow h\frac{\partial^2 f_i}{\partial x^2} \ line \\
0 & \Rightarrow h^2\frac{\partial^3 f_i}{\partial x^3} \ line \\
-B & \Rightarrow h^3\frac{\partial^4 f_i}{\partial x^4} \ line \\
0 & \Rightarrow h^4\frac{\partial^5 f_i}{\partial x^5} \ line \\
K & \Rightarrow h^5\frac{\partial^6 f_i}{\partial x^6} \ line \\
0 & \Rightarrow h^6\frac{\partial^7 f_i}{\partial x^7} \ line \\
E & \Rightarrow h^7\frac{\partial^8 f_i}{\partial x^8} \ line \\
0 & \Rightarrow h^8\frac{\partial^9 f_i}{\partial x^9} \ line \\
G & \Rightarrow h^9\frac{\partial^{10} f_i}{\partial x^{10}} \ line
\end{pmatrix}
$$

By inverting the matrix and the L.H.S. and solving the system with matlab file, the coefficients given in eq. (3.51a) and (3.51b) are obtained.

A.8.3.2 Wave propagation characteristics

Prefactored backward one-sided boundary stencil first node $i = 1$

Rewriting the backward prefactored derivative of eq. (3.47a) for $i = 1$ node:

$$f_1'^B = \frac{1}{h}\sum_{j=1}^{7} s_j f_j \tag{A.167}$$

or in extended form:

$$f_1'^B = \frac{1}{h}\left[s_1 f_1 + s_2 f_2 + s_3 f_3 + s_4 f_4 + s_5 f_5 + s_6 f_6 + s_7 f_7\right] \tag{A.168}$$

By taking the DFT of eq. A.168

$$i\,\bar{k}_j\,\hat{f}_j(\kappa) = \frac{1}{h}\left[s_1\,\hat{f}_j(\kappa) + s_2 e^{i\kappa}\,\hat{f}_j(\kappa) + s_3 e^{2i\kappa}\,\hat{f}_j(\kappa) + s_4 e^{3i\kappa}\,\hat{f}_j(\kappa) + s_5 e^{4i\kappa}\,\hat{f}_j(\kappa) + s_6 e^{5i\kappa}\,\hat{f}_j(\kappa) + s_7 e^{6i\kappa}\,\hat{f}_j(\kappa)\right] \tag{A.169}$$

or:

$$i\,\bar{\kappa}(\kappa)\,\hat{f}_j(\kappa) = \left[s_1\,\hat{f}_j(\kappa) + s_2 e^{i\kappa}\,\hat{f}_j(\kappa) + s_3 e^{2i\kappa}\,\hat{f}_j(\kappa) + s_4 e^{3i\kappa}\,\hat{f}_j(\kappa) + s_5 e^{4i\kappa}\,\hat{f}_j(\kappa) + s_6 e^{5i\kappa}\,\hat{f}_j(\kappa) + s_7 e^{6i\kappa}\,\hat{f}_j(\kappa)\right] \tag{A.170}$$

dividing by $\hat{f}_j(\kappa)$

$$i\,\bar{\kappa}(\kappa) = \left[s_1 + s_2 e^{i\kappa} + s_3 e^{2i\kappa} + s_4 e^{3i\kappa} + s_5 e^{4i\kappa} + s_6 e^{5i\kappa} + s_7 e^{6i\kappa}\right] \tag{A.171}$$

Applying the Euler relations:

$$\begin{aligned} i\,\bar{\kappa}(\kappa) &= s_1 + s_2\,(\cos(\kappa) + i\sin(\kappa)) + s_3\,(\cos(2\kappa) + i\sin(2\kappa)) + \\ &+ s_4\,(\cos(3\kappa) + i\sin(3\kappa)) + s_5\,(\cos(4\kappa) + i\sin(4\kappa)) + s_6\,(\cos(5\kappa) + i\sin(5\kappa)) + s_7\,(\cos(6\kappa) + i\sin(6\kappa)) \end{aligned} \tag{A.172}$$

By splitting Real and Im component on the R.H.S of previous equation:

$$\begin{aligned} i\,\bar{\kappa}(\kappa) &= [s_1 + s_2\cos(\kappa) + s_3\cos(2\kappa) + s_4\cos(3\kappa) + s_5\cos(4\kappa) + s_6\cos(5\kappa) + s_7\cos(6\kappa)] + \\ &+ i\ [s_2\sin(\kappa) + s_3\sin(2\kappa) + s_4\sin(3\kappa) + s_5\sin(4\kappa) + s_6\sin(5\kappa) + s_7\sin(6\kappa)] \end{aligned} \tag{A.173}$$

Dividing by i

$$\begin{aligned} \bar{\kappa}(\kappa) &= -i\ [s_1 + s_2\cos(\kappa) + s_3\cos(2\kappa) + s_4\cos(3\kappa) + s_5\cos(4\kappa) + s_6\cos(5\kappa) + s_7\cos(6\kappa)] + \\ &+ [s_2\sin(\kappa) + s_3\sin(2\kappa) + s_4\sin(3\kappa) + s_5\sin(4\kappa) + s_6\sin(5\kappa) + s_7\sin(6\kappa)] \end{aligned} \tag{A.174}$$

or:

$$\begin{aligned}\overline{\kappa}(\kappa) &= [s_2\sin(\kappa)+s_3\sin(2\kappa)+s_4\sin(3\kappa)+s_5\sin(4\kappa)+s_6\sin(5\kappa)+s_7\cos(6\kappa)]+ \\ &- i\,[s_1+s_2\cos(\kappa)+s_3\cos(2\kappa)+s_4\cos(3\kappa)+s_5\cos(4\kappa)+s_6\cos(5\kappa)+s_7\sin(6\kappa)]\end{aligned} \tag{A.175}$$

The real part of of the *modified wavenumber* $\Re\left(\widetilde{f_1^B}\right)$ is given by:

$$\Re\left(\widetilde{f_1^B}\right) = [s_2\sin(\kappa)+s_3\sin(2\kappa)+s_4\sin(3\kappa)+s_5\sin(4\kappa)+s_6\sin(5\kappa)+s_7\sin(6\kappa)] \tag{A.176}$$

The imaginary part of of the *modified wavenumber* $\Im\left(\widetilde{f_1^B}\right)$ is given by:

$$\Im\left(\widetilde{f_1^B}\right) = -[s_1+s_2\cos(\kappa)+s_3\cos(2\kappa)+s_4\cos(3\kappa)+s_5\cos(4\kappa)+s_6\cos(5\kappa)+s_7\cos(6\kappa)] \tag{A.177}$$

The group velocity is equal to:

$$\begin{aligned}\frac{c_g}{c} &= \frac{\partial\overline{\kappa}(\kappa)}{\partial\kappa} = \\ &= [s_2\cos(\kappa)+s_3\cos(2\kappa)+s_4\cos(3\kappa)+s_5\cos(4\kappa)+s_6\cos(5\kappa)+s_7\cos(6\kappa)]+ \\ &+ i\,[s_1+s_2\sin(\kappa)+s_3\sin(2\kappa)+s_4\sin(3\kappa)+s_5\sin(4\kappa)+s_6\sin(5\kappa)+s_7\sin(6\kappa)]\end{aligned} \tag{A.178}$$

Prefactored forward one-sided boundary stencil last node $i = N$

Rewriting the forward prefactored derivative of eq. (3.48b) for the $i = N$ mesh point:

$$\frac{\partial f^F_{jmax}}{\partial x} = \frac{1}{h}\sum_{j=jmax-6}^{jmax} -s_{jmax+1-j}\,f_j \tag{A.179}$$

or in extended form:

$$\begin{aligned}\frac{\partial f^F_{jmax}}{\partial x} &= \frac{1}{h}\sum_{j=jmax-6}^{jmax} s_{jmax+1-j}\,f_j = \frac{1}{h}\Big[-s_7 f_{jmax-6} - s_6 f_{jmax-5} - s_5 f_{jmax-4} - s_4 f_{jmax-3}+ \\ &-s_3 f_{jmax-2} - s_2 f_{jmax-1} + s_1 f_{jmax}\Big]\end{aligned} \tag{A.180}$$

By taking the DFT of eq. A.191

$$i\tilde{k}_j \hat{f}^F_{jmax}(\kappa) = \frac{1}{h}\left[-s_7 e^{-6i\kappa}\hat{f}_{jmax}(\kappa) - s_6 e^{-5i\kappa}\hat{f}_{jmax}(\kappa) - s_5 e^{-4i\kappa}\hat{f}_{jmax}(\kappa) - s_4 e^{-3i\kappa}\hat{f}_{jmax}(\kappa) - s_3 e^{-2i\kappa}\hat{f}_{jmax}(\kappa) + -s_2 e^{-i\kappa}\hat{f}_{jmax} - s_1\hat{f}_{jmax}\right] \quad (A.181)$$

or:

$$i\bar{\kappa}(\kappa)^F \hat{f}^F_{jmax}(\kappa) = \left[-s_7 e^{-6i\kappa}\hat{f}_{jmax}(\kappa) - s_6 e^{-5i\kappa}\hat{f}_{jmax}(\kappa) - s_5 e^{-4i\kappa}\hat{f}_{jmax}(\kappa) - s_4 e^{-3i\kappa}\hat{f}_{jmax}(\kappa) - s_3 e^{-2i\kappa}\hat{f}_{jmax}(\kappa) + -s_2 e^{-i\kappa}\hat{f}_{jmax} - s_1\hat{f}_{jmax}\right] \quad (A.182)$$

dividing by $\hat{f}_{jmax}(\kappa)$

$$i\bar{\kappa}^F(\kappa) = -\left[s_7 e^{-6i\kappa} + s_6 e^{-5i\kappa} + s_5 e^{-4i\kappa} + s_4 e^{-3i\kappa} + s_3 e^{-2i\kappa} + s_2 e^{-i\kappa} + s_1\right] \quad (A.183)$$

Applying the Euler relations:

$$i\bar{\kappa}(\kappa) = -s_7(\cos(6\kappa) - i\sin(6\kappa)) - s_6(\cos(5\kappa) - i\sin(5\kappa)) - s_5(\cos(4\kappa) - i\sin(4\kappa)) + -s_4(\cos(3\kappa) - i\sin(3\kappa)) - s_3(\cos(2\kappa) - i\sin(2\kappa)) - s_2(\cos(\kappa) - i\sin(\kappa)) - s_1 \quad (A.184)$$

By splitting Real and Im component on the R.H.S. of previous equation:

$$\begin{aligned} i\bar{\kappa}(\kappa) &= -[s_7\cos(6\kappa) + s_6\cos(5\kappa) + s_5\cos(4\kappa) + s_4\cos(3\kappa) + s_3\cos(2\kappa) + \\ &+ s_2\cos(\kappa) + s_1] + i[s_7\sin(6\kappa) + s_6\sin(5\kappa) + s_5\sin(4\kappa) + s_4\sin(3\kappa) + \\ &+ s_3\sin(2\kappa) + s_2\sin(\kappa)] \end{aligned} \quad (A.185)$$

Dividing by i:

$$\begin{aligned}\overline{\kappa}(\kappa) &= i\,[s_7\cos(6\kappa) + s_6\cos(5\kappa) + s_5\cos(4\kappa) + s_4\cos(3\kappa) + s_3\cos(2\kappa) + \\ &+ s_2\cos(\kappa) + s_1] + [s_7\sin(6\kappa) + s_6\sin(5\kappa) + s_5\sin(4\kappa) + s_4\sin(3\kappa) + \\ & s_3\sin(2\kappa) + s_2\sin(\kappa)]\end{aligned} \tag{A.186}$$

Or:

$$\begin{aligned}\overline{\kappa}(\kappa) &= [s_7\sin(6\kappa) + s_6\sin(5\kappa) + s_5\sin(4\kappa) + s_4\sin(3\kappa) + s_3\sin(2\kappa) + s_2\sin(\kappa)] \\ &+ i\,[s_7\cos(6\kappa) + s_6\cos(5\kappa) + s_5\cos(4\kappa) + s_4\cos(3\kappa) + s_3\cos(2\kappa) + s_2\cos(\kappa) + s_1]\end{aligned} \tag{A.187}$$

The real part of of the *modified wavenumber* $Re\left(\widetilde{\frac{\partial f^F_{jmax}}{\partial x}}\right)$ is given by:

$$Re\left(\widetilde{\frac{\partial f^F_{jmax}}{\partial x}}\right) = [s_7\sin(6\kappa) + s_6\sin(5\kappa) + s_5\sin(4\kappa) + s_4\sin(3\kappa) + s_3\sin(2\kappa) + s_2\sin(\kappa)] \tag{A.188}$$

The imaginary part of of the *modified wavenumber* $Im\left(\widetilde{\frac{\partial f^F_{jmax}}{\partial x}}\right)$ is given by:

$$Im\left(\widetilde{\frac{\partial f^F_{jmax}}{\partial x}}\right) = [s_7\cos(6\kappa) + s_6\cos(5\kappa) + s_5\cos(4\kappa) + s_4\cos(3\kappa) + s_3\cos(2\kappa) + s_2\cos(\kappa) + s_1] \tag{A.189}$$

Prefactored backward one-sided boundary stencil last node $i = N$

Rewriting the backward prefactored derivative of eq. (3.47b) for the $i = N$ mesh point:

$$\frac{\partial f^B_{jmax}}{\partial x} = \frac{1}{h}\sum_{j=jmax-6}^{jmax} e_j f_j \tag{A.190}$$

or in extended form:

$$\frac{\partial f^B_{jmax}}{\partial x} = \frac{1}{h}\sum_{j=jmax-6}^{jmax} e_j f_j = \frac{1}{h}\Big[e_{jmax-6} f_{jmax-6} + e_{jmax-5} f_{jmax-5} + e_{jmax-4} f_{jmax-4} + e_{jmax-3} f_{jmax-3} + \\ + e_{jmax-2} f_{jmax-2} + e_{jmax-1} f_{jmax-1} + e_{jmax} f_{jmax}\Big] \quad \text{(A.191)}$$

By taking the DFT of eq. A.191

$$i\tilde{k}_j \hat{f}^B_{jmax}(\kappa) = \frac{1}{h}\Big[e_{jmax-6} e^{-6i\kappa} \hat{f}_{jmax}(\kappa) + e_{jmax-5} e^{-5i\kappa} \hat{f}_{jmax}(\kappa) + e_{jmax-4} e^{-4i\kappa} \hat{f}_{jmax}(\kappa) + e_{jmax-3} e^{-3i\kappa} \hat{f}_{jmax}(\kappa) + \\ + e_{jmax-2} e^{-2i\kappa} \hat{f}_{jmax}(\kappa) + e_{jmax-1} e^{-i\kappa} \hat{f}_{jmax}(\kappa) + e_{jmax} \hat{f}_{jmax}(\kappa)\Big] \quad \text{(A.192)}$$

or:

$$i\bar{\kappa}(\kappa) \hat{f}^B_{jmax}(\kappa) = \Big[e_{jmax-6} e^{-6i\kappa} \hat{f}_{jmax}(\kappa) + e_{jmax-5} e^{-5i\kappa} \hat{f}_{jmax}(\kappa) + e_{jmax-4} e^{-4i\kappa} \hat{f}_{jmax}(\kappa) + e_{jmax-3} e^{-3i\kappa} \hat{f}_{jmax}(\kappa) + \\ + e_{jmax-2} e^{-2i\kappa} \hat{f}_{jmax}(\kappa) + e_{jmax-1} e^{-i\kappa} \hat{f}_{jmax}(\kappa) + e_{jmax} \hat{f}_{jmax}(\kappa)\Big] \quad \text{(A.193)}$$

dividing by $\hat{f}_{jmax}(\kappa)$

$$i\bar{\kappa}(\kappa) = \Big[e_{jmax-6} e^{-6i\kappa} + e_{jmax-5} e^{-5i\kappa} + e_{jmax-4} e^{-4i\kappa} + e_{jmax-3} e^{-3i\kappa} + e_{jmax-2} e^{-2i\kappa} + e_{jmax-1} e^{-i\kappa} + e_{jmax}\Big] \quad \text{(A.194)}$$

Applying the Euler relations:

$$i\bar{\kappa}(\kappa) = e_{jmax-6}\,(\cos(6\kappa) - i\sin(6\kappa)) + e_{jmax-5}\,(\cos(5\kappa) - i\sin(5\kappa)) + e_{jmax-4}\,(\cos(4\kappa) - i\sin(4\kappa)) + \\ + e_{jmax-3}\,(\cos(3\kappa) - i\sin(3\kappa)) + e_{jmax-2}\,(\cos(2\kappa) - i\sin(2\kappa)) + \\ + e_{jmax-1}\,(\cos(\kappa) - i\sin(\kappa)) + e_{jmax} \quad \text{(A.195)}$$

By splitting Real and Im component on the R.H.S. of previous equation:

$$
\begin{aligned}
i\,\overline{\kappa}(\kappa) &= \Big[e_{jmax-6}\cos(6\kappa) + e_{jmax-5}\cos(5\kappa) + e_{jmax-4}\cos(4\kappa) + e_{jmax-3}\cos(3\kappa) + e_{jmax-2}\cos(2\kappa) + \\
&+ e_{jmax-1}\cos(\kappa) + e_{jmax}\Big] - i\Big[e_{jmax-6}\sin(6\kappa) + e_{jmax-5}\sin(5\kappa) + e_{jmax-4}\sin(4\kappa) + e_{jmax-3}\sin(3\kappa) + \\
&+ e_{jmax-2}\sin(2\kappa) + e_{jmax-1}\sin(\kappa)\Big] \qquad \text{(A.196)}
\end{aligned}
$$

Dividing by i:

$$
\begin{aligned}
\overline{\kappa}(\kappa) &= -i\Big[e_{jmax-6}\cos(6\kappa) + e_{jmax-5}\cos(5\kappa) + e_{jmax-4}\cos(4\kappa) + e_{jmax-3}\cos(3\kappa) + e_{jmax-2}\cos(2\kappa) + \\
&+ e_{jmax-1}\cos(\kappa) + e_{jmax}\Big] - \Big[e_{jmax-6}\sin(6\kappa) + e_{jmax-5}\sin(5\kappa) + e_{jmax-4}\sin(4\kappa) + e_{jmax-3}\sin(3\kappa) + \\
&+ e_{jmax-2}\sin(2\kappa) + e_{jmax-1}\sin(\kappa)\Big] \qquad \text{(A.197)}
\end{aligned}
$$

or:

$$
\begin{aligned}
\overline{\kappa}(\kappa) &= -\Big[e_{jmax-6}\sin(6\kappa) + e_{jmax-5}\sin(5\kappa) + e_{jmax-4}\sin(4\kappa) + e_{jmax-3}\sin(3\kappa) + e_{jmax-2}\sin(2\kappa) \\
&+ e_{jmax-1}\sin(\kappa)\Big] - i\Big[e_{jmax-6}\cos(6\kappa) + e_{jmax-5}\cos(5\kappa) + e_{jmax-4}\cos(4\kappa) + e_{jmax-3}\cos(3\kappa) + \\
&+ +e_{jmax-2}\cos(2\kappa) + e_{jmax-1}\cos(\kappa) + e_{jmax}\Big] \qquad \text{(A.198)}
\end{aligned}
$$

The real part of of the *modified wavenumber* $Re\left(\widetilde{\frac{\partial f^B_{jmax}}{\partial x}}\right)$ is given by

$$
Re\left(\widetilde{\frac{\partial f^B_{jmax}}{\partial x}}\right) = -\Big[e_{jmax-6}\sin(6\kappa) + e_{jmax-5}\sin(5\kappa) + e_{jmax-4}\sin(4\kappa) + e_{jmax-3}\sin(3\kappa) + e_{jmax-2}\sin(2\kappa) + e_{jmax-1}\sin(\kappa)\Big] \qquad \text{(A.199)}
$$

The imaginary part of of the *modified wavenumber* $Im\left(\widetilde{\frac{\partial f^B_{jmax}}{\partial x}}\right)$ is given by:

$$
\begin{aligned}
Im\left(\widetilde{\frac{\partial f^B_{jmax}}{\partial x}}\right) &= -\Big[e_{jmax-6}\cos(6\kappa) + e_{jmax-5}\cos(5\kappa) + e_{jmax-4}\cos(4\kappa) + e_{jmax-3}\cos(3\kappa) + \\
&+ e_{jmax-2}\cos(2\kappa) + e_{jmax-1}\cos(\kappa) + e_{jmax}\Big] \qquad \text{(A.200)}
\end{aligned}
$$

Prefactored forward one-sided boundary stencil first node $i = 1$

Rewriting the forward prefactored derivative of eq. (3.48a) for the $i = 1$ node:

$$\frac{\partial f_1^F}{\partial x} = \frac{1}{h}\sum_{j=1}^{7} -e_{jmax+1-j} f_j \tag{A.201}$$

or in extended form:

$$\begin{aligned}\frac{\partial f_1^F}{\partial x} &= \frac{1}{h}\sum_{j=1}^{7} -e_{jmax+1-j} f_j = \frac{1}{h}\Big[-e_{jmax} f_1 - e_{jmax-1} f_2 - e_{jmax-2} f_3 - e_{jmax-3} f_4 + \\ &- e_{jmax-4} f_5 - e_{jmax-5} f_6 - e_{jmax-6} f_7\Big]\end{aligned} \tag{A.202}$$

By taking the DFT at $i = 1$ node of eq. A.191

$$\begin{aligned}i\tilde{k}_j \hat{f}_1^F(\kappa) &= \frac{1}{h}\Big[-e_{jmax}\hat{f}_1(\kappa) - e_{jmax-1}e^{i\kappa}\hat{f}_1(\kappa) - e_{jmax-2}e^{2i\kappa}\hat{f}_1(\kappa) - e_{jmax-3}e^{3i\kappa}\hat{f}_1(\kappa) + \\ &\quad -e_{jmax-4}e^{4i\kappa}\hat{f}_1(\kappa) - e_{jmax-5}e^{5i\kappa}\hat{f}_1(\kappa) - e_{jmax-6}e^{6i\kappa}\hat{f}_1(\kappa)\Big]\end{aligned} \tag{A.203}$$

or:

$$\begin{aligned}i\bar{\kappa}(\kappa)\hat{f}_1^F(\kappa) &= \Big[-e_{jmax}\hat{f}_1(\kappa) - e_{jmax-1}e^{i\kappa}\hat{f}_1(\kappa) - e_{jmax-2}e^{2i\kappa}\hat{f}_1(\kappa) - e_{jmax-3}e^{3i\kappa}\hat{f}_1(\kappa) + \\ &\quad -e_{jmax-4}e^{4i\kappa}\hat{f}_1(\kappa) - e_{jmax-5}e^{5i\kappa}\hat{f}_1(\kappa) - e_{jmax-6}e^{6i\kappa}\hat{f}_1(\kappa)\Big]\end{aligned} \tag{A.204}$$

dividing by $\hat{f}_1^F(\kappa)$

$$\begin{aligned}i\bar{\kappa}(\kappa) &= \Big[-e_{jmax} - e_{jmax-1}e^{i\kappa} - e_{jmax-2}e^{2i\kappa} - e_{jmax-3}e^{3i\kappa} + \\ &\quad -e_{jmax-4}e^{4i\kappa} - e_{jmax-5}e^{5i\kappa} - e_{jmax-6}e^{6i\kappa}\Big]\end{aligned} \tag{A.205}$$

Applying the Euler relations:

$$i\,\bar{\kappa}(\kappa) = -e_{jmax} - e_{jmax-1}\,(\cos(\kappa) + i\sin(\kappa)) - e_{jmax-2}\,(\cos(2\kappa) + i\sin(2\kappa)) - e_{jmax-3}\,(\cos(3\kappa) + i\sin(3\kappa)) + \\ -e_{jmax-4}\,(\cos(4\kappa) + i\sin(4\kappa)) - e_{jmax-5}\,(\cos(5\kappa) + i\sin(5\kappa)) - e_{jmax-6}\,(\cos(6\kappa) + i\sin(6\kappa)) \tag{A.206}$$

By splitting Real and Im component on the R.H.S. of previous equation:

$$i\,\bar{\kappa}(\kappa) = -\Big[e_{jmax} + e_{jmax-1}\cos(\kappa) + e_{jmax-2}\cos(2\kappa) + e_{jmax-3}\cos(3\kappa) + e_{jmax-4}\cos(4\kappa) + e_{jmax-5}\cos(5\kappa) + \\ +e_{jmax-6}\cos(6\kappa)\Big] - i\Big[e_{jmax-1}\sin(\kappa) + e_{jmax-2}\sin(2\kappa) + e_{jmax-3}\sin(3\kappa) + e_{jmax-4}\sin(4\kappa) + \\ + e_{jmax-5}\sin(5\kappa) + e_{jmax-6}\sin(6\kappa)\Big] \tag{A.207}$$

Dividing by i:

$$\bar{\kappa}(\kappa) = i\Big[e_{jmax} + e_{jmax-1}\cos(\kappa) + e_{jmax-2}\cos(2\kappa) + e_{jmax-3}\cos(3\kappa) + e_{jmax-4}\cos(4\kappa) + e_{jmax-5}\cos(5\kappa) + \\ +e_{jmax-6}\cos(6\kappa)\Big] - \Big[e_{jmax-1}\sin(\kappa) + e_{jmax-2}\sin(2\kappa) + e_{jmax-3}\sin(3\kappa) + e_{jmax-4}\sin(4\kappa) + \\ + e_{jmax-5}\sin(5\kappa) + e_{jmax-6}\sin(6\kappa)\Big] \tag{A.208}$$

Or:

$$\bar{\kappa}(\kappa) = -\Big[e_{jmax-1}\sin(\kappa) + e_{jmax-2}\sin(2\kappa) + e_{jmax-3}\sin(3\kappa) + e_{jmax-4}\sin(4\kappa) + e_{jmax-5}\sin(5\kappa) + e_{jmax-6}\sin(6\kappa)\Big] + \\ +i\Big[e_{jmax} + e_{jmax-1}\cos(\kappa) + e_{jmax-2}\cos(2\kappa) + e_{jmax-3}\cos(3\kappa) + e_{jmax-4}\cos(4\kappa) + e_{jmax-5}\cos(5\kappa) + \\ +e_{jmax-6}\cos(6\kappa)\Big] \tag{A.209}$$

The real part of the *modified wavenumber* $Re\left(\widetilde{\frac{\partial f_1^F}{\partial x}}\right)$ is given by:

$$Re\left(\widetilde{\frac{\partial f_1^F}{\partial x}}\right) = -\Big[e_{jmax-1}\sin(\kappa) + e_{jmax-2}\sin(2\kappa) + e_{jmax-3}\sin(3\kappa) + e_{jmax-4}\sin(4\kappa) + e_{jmax-5}\sin(5\kappa) + e_{jmax-6}\sin(6\kappa)\Big] \tag{A.210}$$

The imaginary part of the *modified wavenumber* $Im\left(\widetilde{\frac{\partial f_1^F}{\partial x}}\right)$ is given by:

$$Im\left(\widetilde{\frac{\partial f_1^F}{\partial x}}\right) = \Big[e_{jmax} + e_{jmax-1}\cos(\kappa) + e_{jmax-2}\cos(2\kappa) + e_{jmax-3}\cos(3\kappa) + e_{jmax-4}\cos(4\kappa) + e_{jmax-5}\cos(5\kappa) + e_{jmax-6}\cos(6\kappa)\Big] \tag{A.211}$$

Prefactored Forward interior boundaries stencil

Rewriting eq. (3.51a) for the generic *i-th* mesh point:

$$f_i'^F = \frac{1}{h}\sum_{j=-5}^{5} b_j f_{i+j}, \tag{A.212}$$

or in extended form:

$$\begin{aligned} f_i'^F &= \frac{1}{h}(b_{-5}f_{i-5} + b_{-4}f_{i-4} + b_{-3}f_{i-3} + b_{-2}f_{i-2} + b_{-1}f_{i-1} + \\ &+ b_0 f_i + b_1 f_{i+1} + b_2 f_{i+2} + b_3 f_{i+3} + b_4 f_{i+4} + b_5 f_{i+5}) \end{aligned} \tag{A.213}$$

By taking the DFT of eq. A.213:

$$\begin{aligned} i\bar{k}_j \hat{f}_j(\kappa) &= \frac{1}{h}[b_{-5}e^{-5i\kappa}\hat{f}_j(\kappa) + b_{-4}e^{-4i\kappa}\hat{f}_j(\kappa) + b_{-3}e^{-3i\kappa}\hat{f}_j(\kappa) + b_{-2}e^{-2i\kappa}\hat{f}_j(\kappa) + b_{-1}e^{-1i\kappa}\hat{f}_j(\kappa) + \\ &+ b_0\hat{f}_j(\kappa) + b_1 e^{i\kappa}\hat{f}_j(\kappa) + b_2 e^{2i\kappa}\hat{f}_j(\kappa) + b_3 e^{3i\kappa}\hat{f}_j(\kappa) + b_4 e^{4i\kappa}\hat{f}_j(\kappa) + b_5 e^{5i\kappa}\hat{f}_j(\kappa)] \end{aligned} \tag{A.214}$$

$$\begin{aligned} i\bar{\kappa}(\kappa) &= [b_{-5}e^{-5i\kappa} + b_{-4}e^{-4i\kappa} + b_{-3}e^{-3i\kappa} + b_{-2}e^{-2i\kappa} + b_{-1}e^{-1i\kappa} + \\ &+ b_0 + b_1 e^{i\kappa} + b_2 e^{2i\kappa} + b_3 e^{3i\kappa} + b_4 e^{4i\kappa} + b_5 e^{5i\kappa}] \end{aligned} \tag{A.215}$$

$$\begin{aligned} i\bar{\kappa}(\kappa) &= [b_{-5}(\cos(5\kappa) - i\sin(5\kappa)) + b_{-4}(\cos(4\kappa) - i\sin(4\kappa)) + b_{-3}(\cos(3\kappa) - i\sin(3\kappa)) + \\ &+ b_{-2}(\cos(2\kappa) - i\sin(2\kappa)) + b_{-1}(\cos(\kappa) - i\sin(\kappa)) + b_0 + b_1(\cos(\kappa) + i\sin(\kappa)) + \\ &+ b_2(\cos(2\kappa) + i\sin(2\kappa)) + b_3(\cos(3\kappa) + i\sin(3\kappa)) + b_4(\cos(4\kappa) + i\sin(4\kappa)) + b_5(\cos(5\kappa) + i\sin(5\kappa))] \end{aligned} \tag{A.216}$$

Table A.5: Spatial and temporal resolution for the numerical tests reported in Fig. 5.1(b).

test-cases	N	h	N_λ	κ	σ	n
N_1	6	0.2	5	$2\pi/5$	0.01	x
N_2	11	0.1	10	$\pi/5$	0.01	x
N_3	21	0.05	20	$\pi/10$	0.01	x
N_4	31	0.033	30	$\pi/15$	0.01	x
N_5	51	0.02	50	$\pi/25$	0.01	x
N_6	101	0.01	100	$\pi/50$	0.01	x
N_7	201	0.005	200	$\pi/100$	0.01	
N_8	401	0.0025	400	$\pi/200$	0.01	
N_9	601	0.0016	600	$\pi/400$	0.01	

$$
\begin{aligned}
i\,\overline{\kappa}(\kappa) &= [(b_{-5}+b_5)\cos(5\kappa)+(b_{-4}+b_4)\cos(4\kappa)+(b_{-3}+b_3)\cos(3\kappa)+ \\
&+ (b_{-2}+b_2)\cos(2\kappa)+(b_{-1}+b_1)\cos(\kappa)+b_0]+ \\
&+ i\,[(-b_{-5}+b_5)\sin(5\kappa)+(-b_{-4}+b_4)\sin(4\kappa)+(-b_{-3}+b_3)\sin(3\kappa)+ \\
&+ (-b_{-2}+b_2)\sin(2\kappa)+(-b_{-1}+b_1)\sin(\kappa)]
\end{aligned}
\tag{A.217}
$$

$$
\begin{aligned}
\overline{\kappa}(\kappa) &= -i\,[(b_{-5}+b_5)\cos(5\kappa)+(b_{-4}+b_4)\cos(4\kappa)+(b_{-3}+b_3)\cos(3\kappa)+(b_{-2}+b_2)\cos(2\kappa)+(b_{-1}+b_1)\cos(\kappa)+b_0] \\
&+ [(-b_{-5}+b_5)\sin(5\kappa)+(-b_{-4}+b_4)\sin(4\kappa)+(-b_{-3}+b_3)\sin(3\kappa)+(-b_{-2}+b_2)\sin(2\kappa)+(-b_{-1}+b_1)\sin(\kappa)]
\end{aligned}
$$

$$
Re(\overline{\kappa}(\kappa)) = [(-b_{-5}+b_5)\sin(5\kappa)+(-b_{-4}+b_4)\sin(4\kappa)+(-b_{-3}+b_3)\sin(3\kappa)+(-b_{-2}+b_2)\sin(2\kappa)+(-b_{-1}+b_1)\sin(\kappa)] \tag{A.218}
$$

$$
Im(\overline{\kappa}(\kappa)) = -[(b_{-5}+b_5)\cos(5\kappa)+(b_{-4}+b_4)\cos(4\kappa)+(b_{-3}+b_3)\cos(3\kappa)+(b_{-2}+b_2)\cos(2\kappa)+(b_{-1}+b_1)\cos(\kappa)+b_0] \tag{A.219}
$$

A.9 Validation results

A.9.1 Monochromatic sinusoidal wave

Table A.6: Spatial resolution for the numerical tests reported in iso-maps of Fig. 5.5, $k = 2\pi$. N_p is the number of point per period. Final time $t = 1$. $\sigma_{min} = 0.01$. $\sigma_{max} = 1.422$, see eq. (5.2).

test-cases	N	N_p	h	N_λ	κ	$\sigma_{min} \leq \sigma \leq \sigma_{max}$	n
N_1	11	3	1/2	10	$\pi \simeq 3.14 = \kappa_{max}$	0.1	2
N_2	16	4	1/3	25	$2\pi/3 \simeq 2.09$	0.1	4
N_3	21	5	1/4	20	$\pi/2 \simeq 1.57$	0.1	4
N_4	26	6	1/5	25	$2\pi/5 \simeq 1.25$	0.1	4
N_5	31	7	1/6	30	$\pi/3 \simeq 1.04$	0.1	6
N_6	36	8	1/7	35	$2\pi/7 \simeq 0.89$	0.1	6
N_7	41	9	1/8	40	$\pi/4 \simeq 0.78$	0.1	8
N_8	46	10	1/9	45	$2\pi/9 \simeq 0.69$	0.1	8
N_9	51	11	1/10	50	$\pi/5 \simeq 0.62$	0.1	10
N_{10}	56	12	1/11	55	$1\pi/11 \simeq 0.57$	0.1	10
N_{11}	61	13	1/12	60	$\pi/6 \simeq 0.52$	0.1	12
N_{12}	66	14	1/13	65	$2\pi/13 \simeq 0.48$	0.1	12
N_{13}	71	15	1/14	70	$\pi/7 \simeq 0.44$	0.1	15
N_{14}	76	16	1/15	75	$2\pi/15 \simeq 0.41$	0.1	15
N_{15}	81	17	1/16	80	$\pi/8 \simeq 0.39$	0.1	16
N_{16}	86	18	1/17	85	$2\pi/17 \simeq 0.36$	0.1	16
N_{17}	91	19	1/18	90	$\pi/9 \simeq 0.34$	0.1	18
N_{18}	96	20	1/19	95	$2\pi/19 \simeq 0.33$	0.1	18
N_{19}	101	21	1/20	100	$\pi/10 \simeq 0.31$	0.1	20
N_{20}	106	22	1/21	105	$2\pi/21 \simeq 0.29$	0.1	20
N_{21}	111	23	1/22	110	$\pi/11 \simeq 0.285$	0.1	20
N_{22}	116	24	1/23	115	$2\pi/23 \simeq 0.273$	0.1	20
N_{23}	121	25	1/24	120	$\pi/12 \simeq 0.261$	0.1	20
N_{24}	126	26	1/25	110	$2\pi/25 \simeq 0.251$	0.1	20
N_{25}	131	23	1/22	110	$\pi/11 \simeq 0.285$	0.1	20
N_{26}	136	28	1/27	135	$2\pi/27 \simeq 0.232$	0.1	20
N_{27}	141	29	1/28	140	$\pi/14 \simeq 0.224$	0.1	20
N_{28}	146	30	1/29	145	$2\pi/29 \simeq 0.216$	0.1	20
N_{29}	151	31	1/30	150	$\pi/15 \simeq 0.20$	0.1	20
N_{30}	156	32	1/31	155	$2\pi/31 \simeq 0.202$	0.1	20
N_{31}	161	33	1/32	160	$\pi/16 \simeq 0.196$	0.1	20
N_{32}	166	34	1/33	165	$2\pi/33 \simeq 0.19$	0.1	20
N_{33}	171	35	1/34	170	$\pi/17 \simeq 0.184$	0.1	20
N_{34}	176	36	1/35	175	$2\pi/35 \simeq 0.17$	0.1	20
N_{35}	181	37	1/36	180	$\pi/18 \simeq 0.174$	0.1	20
N_{36}	186	38	1/37	185	$2\pi/37 \simeq 0.169$	0.1	20
N_{37}	191	39	1/38	190	$\pi/19 \simeq 0.165$	0.1	20
N_{38}	196	40	1/39	195	$2\pi/39 \simeq 0.161$	0.1	20
N_{39}	201	41	1/40	200	$\pi/20 \simeq 0.15$	0.1	40
N_{40}	211	43	1/42	210	$\pi/21 \simeq 0.149$	0.1	40
N_{41}	221	45	1/44	220	$\pi/22 \simeq 0.142$	0.1	40
N_{42}	231	47	1/46	230	$\pi/23 \simeq 0.136$	0.1	40
N_{43}	241	49	1/48	240	$\pi/24 \simeq 0.130$	0.1	40
N_{44}	251	51	1/50	250	$\pi/25 \simeq 0.12$	0.1	60
N_{45}	301	61	1/60	300	$\pi/30 \simeq 0.10$	0.1	60
N_{46}	351	71	1/70	300	$\pi/35 \simeq 0.089$	0.1	60
N_{47}	401	81	1/80	400	$\pi/40 \simeq 0.07$	0.1	80
N_{48}	451	91	1/90	450	$\pi/45 \simeq 0.069$	0.1	80
N_{49}	501	101	1/100	500	$\pi/50 \simeq 0.06$	0.1	100
N_{50}	751	151	1/150	750	$\pi/75 \simeq 0.04$	0.1	100
N_{51}	1001	201	1/200	1000	$\pi/100 \simeq 0.03$	0.1	200
N_{52}	2001	401	1/400	2000	$\pi/200 \simeq 0.015$	0.1	400
N_{53}	3001	601	1/600	3000	$\pi/300 \simeq 0.010$	0.1	600
N_{54}	4001	801	1/800	4000	$\pi/400 \simeq 0.007$	0.1	800
N_{55}	5001	1001	1/1000	5000	$\pi/500 \simeq 0.006$	0.1	1000
N_{56}	10001	2001	1/2000	10000	$\pi/1000 \simeq 0.003 = \kappa_{min}$	0.1	1000

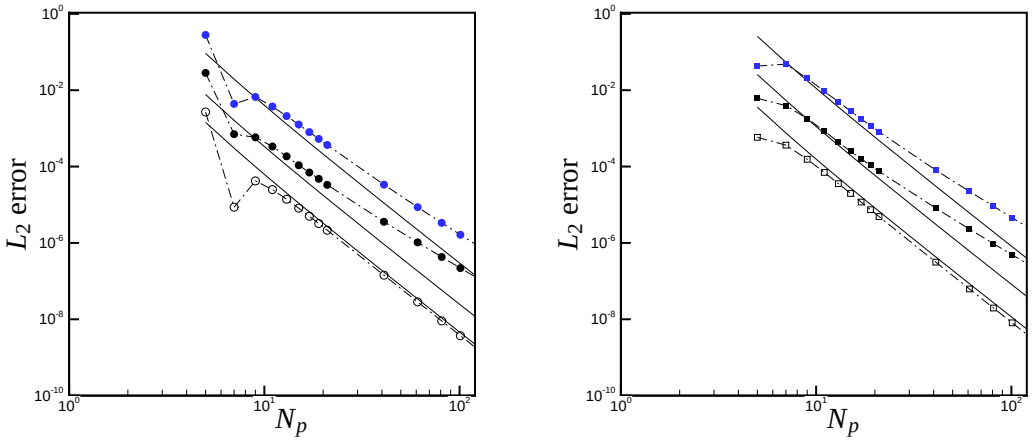

(a) $C1122$epsm4. (b) $C1122$epsm3.

Figure A.22: Solution to *LAE* equation with monochromatic sinusoidal wave of eq. (5.2), over the central domain $0 \leq x \leq 1$: (−) fourth-order logarithmic scale, (− · − ∘ − · −) $C1122$epsm4, (− · −□ − ·−) $C1122$epsm3; plain symbols $t = 0.1$, filled black symbols $t = 1$, filled blue symbols $t = 10$. Classical $RK4$ is used for time integration.

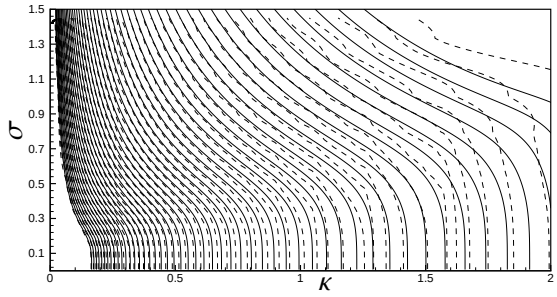

(a) $C1122$.

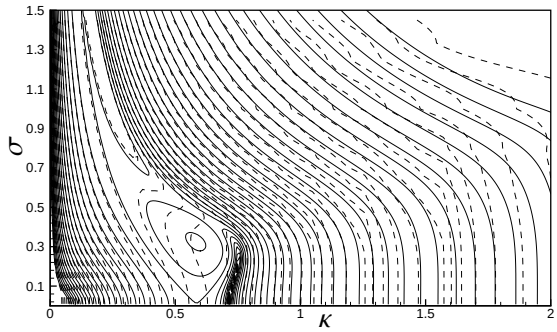

(b) epsm5.

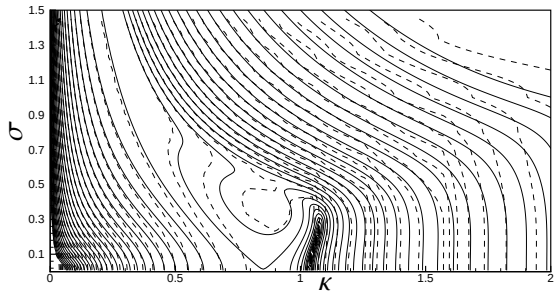

(c) epsm4.

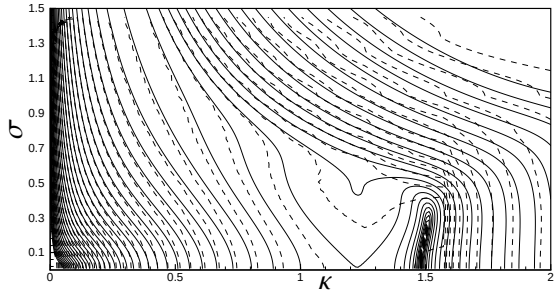

(d) epsm3.

Figure A.23: Enlarged view of the comparison between the theoretical and the computed 'local' error function $e(\kappa,\sigma)$ for the monochromatic sinusoidal wave. Fifty constant logarithmically spaced iso-contours errors between 10^{-8} and 10^{-1}. Continuous line $(-)$ theoretical, dashed line $(--)$ computed.

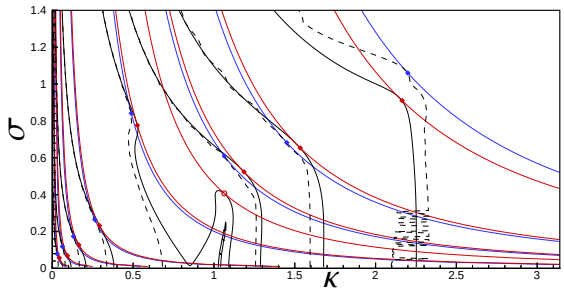

(a) epsm4.

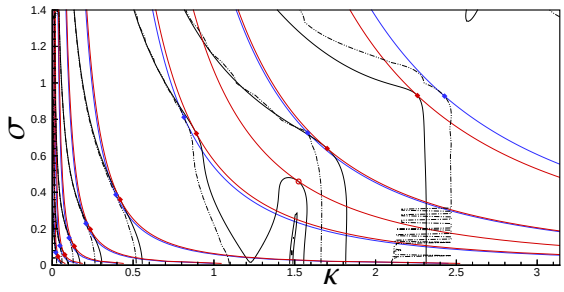

(b) epsm3.

Figure A.24: Theoretical (black solid lines) and numerical (black dashed lines) contours of optimal 'local' error error function $e(\kappa, \sigma)$ as a function of the one-dimensional cost $c_1 = 1/(\sigma\kappa^2)$ (continuous coloured lines) for the monochromatic sinusoidal wave. (a) epsm4 (b) epsm3.

References

(CINECA). *IBM PLX User Guide*. www.hpc.cineca.it/content/ibm-plx-gpu-user-guide-0 last access 19.09.2013.

(CINECA). *IBM SP6 User Guide*. http://hpc-dev.cineca.it/content/ibm-sp6-user-guide last access 20.09.2013.

(Jülich SuperComputing Centre). *Scalasca scalable parallel perfomance analysis toolset documentation*. http://www.scalasca.org/software/scalasca-2.x/documentation.html, last access 19.09.2013.

ACARE (2009). The Strategic Research Agenda SRA-1, SRA-2 and the 2008 Addendum to the Strategic Research Agenda. Tech. rep., http://www.acare4europe.org/.

Anderson, D., Tannehill, J. & Pletcher, R. (1984). *Computational Fluid Mechanics and Heat Transfer*. In Computational and Physical Processes in Mechanics and Thermal Sciences, 2nd edn.

Ashcroft, G. & Zhang, X. (2003). Optimized prefactored compact schemes. *Journal of Computational Physics*, **190**, 459–477.

Bader, R. (2007). FGSL: A GSL Fortran interface. Tech. Rep. Fortran Interface Manual, Edition 0.7 for GSL Version 1.8, Leibniz Computing Centre, available at http://www.lrz-muenchen.de/services/software/mathematik/gsl/fortran.

Berland, J., Bogey, C. & Bailly, C. (2006). Low-dissipation and low-dispersion fourth-order Runge–Kutta algorithm. *Computers &; Fluids*, **35**, 1459–1463.

Bernardini, M. & Pirozzoli, S. (2009). A general strategy for the optimization of Runge-Kutta schemes for wave propagation phenomena. *Journal of Computational Physics*, **228**, 4182–4199.

Bogey, C. & Bailly, C. (2004). A family of low dispersive and low dissipative explicit schemes for flow and noise computations. *Journal of Computational Physics*, **194**, 194–214.

Butcher, J.C. (1987). *The Numerical Analysis of Ordinary Differential Equations: Runge-Kutta and General Linear Methods*. John Wiley & Sons Inc.

Carpenter, M.H., Gottlieb, D. & Abarbanel, S. (1993a). The Stability of Numerical Boundary Treatments for Compact High-Order Finite-Difference Schemes. *Journal of Computational Physics*, **108**, 272–295.

Carpenter, M.H., Gottlieb, D. & Aberbanel, S. (1993b). Stable and accurate boundary treatments for compact, high-order finite-difference schemes. *Applied Numerical Mathematics*, **12**, 55–87.

Carpenter, M.H., Gottlieb, D. & Aberbanel, S. (1994). Time-stable boundary conditions for finite-difference schemes solving hyperbolic systems: methodology and application to high-order compact schemes. *Journal of Computational Physics*, **111**, 220–236.

Collis, S. & Colonius, T. (1997). A computational investigation of receptivity in high-speed flow near a swept leading edge. Techincal report TF-71, Department of Mechanical Engineering, Stanford University.

Colonius, T. (2004). Modeling artificial boundary conditions for compressible flow. *Annual Review of Fluid Mechanics*, **40**, 315–345.

Colonius, T. (2011). Computational aeroacoustics. In *Noise Sources in Turbulent Shear Flow*, International Centre for Mechanical Sciences (CISM) Course notes.

Colonius, T. & Lele, S. (2004). Computational aeroacoustics: progress on nonlinear problems of sound generation. *Progress in Aerospace Sciences*, **40**, 365–416.

Eldred, M.S., Brown, S.L., Adams, B.M., Dunlavy, D.M., Gay, D.M., Swiler, L.P., Giunta, A.A., Hart, W.E., Jean-PaulWatson, Eddy, J.P., Griffin, J.D., Hough, P.D., Kolda, T.G., Martinez-Canales, M.L. & J.Williams, P. (2013). DAKOTA, A Multilevel Parallel Object-Oriented Framework for Design Optimization, Parameter Estimation, Uncertainty Quantification, and Sensitivity Analysis: Version 5.0 Reference Manual. Tech. Rep. SAND2013-4055.

Ghillani, P. (2012). *Aeroacustic simulation of a linear cascade by a prefactored compact scheme*. Ph.D. thesis, University of Leicester, Leicester, UK.

Guarrasi, M., Frigio, S., Emerson, A. & Erbacci, G. (2013). Scalability Improvements for DFT Codes due to the Implementation of the 2D Domain Decomposition Algorithm. Tech. rep., PRACE White Paper available at `http://www.prace-ri.eu/IMG/pdf/wp85.pdf`.

Hardin, J. & Tam, C., eds. (1996). *Second Computational Aeroacoustics (CAA) Workshop on Benchmark Problems*, NASA Conference Publication, Hampton, Virginia, Langley Research Center.

Hardin, J., Ristorcelli, J.R. & Tam, C., eds. (1995). *ICASE/LaRC Workshop on Benchmark Problems in Computational Aeroacoustics (CAA)*, NASA Conference Publication 3300, Hampton, Virginia.

Hardin, J., Huff, D. & Tam, C., eds. (2000). *Third Computational Aeroacoustics (CAA) Workshop on Benchmark Problems*, NASA Conference Publication 2000-209790, Cleveland, Ohio, Langley Research Center.

Hirsch, C. (2007). *Numerical Computation of Internal and External flow*, vol. 1, Fundamental of Computational Fluid Dynamics. New York, 2nd edn.

Hixon, R. (1996). On Increasing the accuracy of MacCormack schemes for Aeroacoustic Applications. Nasa Contract Report 202311 ICOMP-96-11, NASA.

Hixon, R. (2000). Prefactored small-stencil compact schemes. *Journal of Computational Physics*, **165**, 522–41.

Hixon, R. & Turkel, E. (2000). Compact Implicit MacCormack-Type Schemes with High Accuracy. *Journal of Computational Physics*, **158**, 51–70.

Hu, F. (1996). On absorbing boundary conditions for linearized Euler equations by a perfectly matched layer. *Journal of Computational Physics*, **129**, 201–219.

Hu, F.Q., Hussaini, M.Y. & Manthey, J.L. (1996). Low-dissipation and low-dispersion Runge-Kutta schemes for computational acoustics. *Journal of Computational Physics*, **124**, 177–191.

I. Spisso, P.G. & Rona, A. (2009). Development of a multi-block interface for a high-order compact scheme applied to sound scattering problems in aeroacoustic: Part II. Tech. rep., Science and SuperComputing in Europe Report.

Israeli, M. & Orszag, S.A. (1981). Approximation of radiation boundary conditions. *Journal of Computational Physics*, **41**, 115–135.

Kim, J.W. (2007). Optimised boundary compact finite difference schemes for computational aeroacoustics. *Journal of Computational Physics*, **225**, 995–1019.

Kraft, D. & Motsinger, R. (1991). Design and Performance of Duct Acoustic Treatment. *Aeroacoustics of Flight Vehicles: Theory and Practice. NASA Reference Publication 1258, Vol. 2, WRDC TR 90-3052*, 165.

Kurbatskii, K.A. & Mankbadi, R.R. (2004). Review of computational aeroacoustics algorithms. *International Journal of Computational Fluid Dynamics*, **18**, 533–546.

Lele, S.K. (1992). Compact finite difference schemes with spectral-like resolution. *Journal of Computational Physics*, **103**, 16–42.

Li, N. & Laizet, S. (2010). 2DECOMP&FFT – A highly scalable 2D decomposition library and FFT interface. Tech. Rep. Cray User Group 2010 conference.

Lighthill, J. (1978). *Waves in Fluids*. Cambridge University Press.

Lockard, D.P., Brentner, K.S. & Atkins, H.L. (1995). High-accuracy algorithms for computational aeroacoustics. *AIAA Journal*, **33**, 246–251.

Lodato, G., Domingo, P. & Vervisch, L. (2008). Three-dimensional boundary conditions for direct and large-eddy simulation of compressible viscous flows. *Journal of Computational Physics*, **227**, 5105–5143.

Lui, C. & Lele, S.K. (2001). Direct Numerical Simulation of Spatially Developing, Compressible, Turbolent Mixing Layers. *AIAA paper*.

Message Passing Interface Forum (2009). MPI: A Message-Passing Interface Standard, Version 2.2. http://www.mpi-forum.org/docs/mpi-2.2/mpi22-report.pdf.

Pirozzoli, S. (2007). Performance analysis and optimazation of finite difference schemes for wave propagation problems. *Journal of Computational Physics*, **222**, 809–831.

Poinsot, T.J. & Lele, S.K. (1992). Boundary conditions for direct simulations of compressible viscous flows. *Journal of Computational Physics*, **101**, 104–129.

Press, W.H. & Firm, N.R.S. (1996). Numerical recipes in FORTRAN 77 and FORTRAN 90 the art of scientific and parallel computing.

Richards, S., Zhang, X., Chen, X. & Nelson, P. (2004). The evaluation of non-reflecting boundary conditions for duct acoustic computation. *Journal of Sound and Vibration*, **270**, 539–557.

Rock, W.D., Desmet, W., Baelmans, M. & Sas, P., eds. (2004). *An overview of high-order finite difference schemes for computational aeroacoustics*, Proceedings of the 2004 International Conference on Noise and Vibration Engineering, ISMA, Leuven, Belgium.

Rona, A. & Spisso, I. (2007). Implementation of a high-order finite difference scheme to model wave propagation. Conference paper 2007-3487, AIAA/CEAS Aeroacoustics Conference13^{th}, Rome.

Rona, A., Spisso, I., Bernardini, M. & Pirozzoli, S. (2009). Comparison of optimized high-order finite-difference compact scheme for computational aeroacoustics. Conference paper 2009-0498, Aerospace Sciences Meeting and Exhibit47^{th}, Orlando, Florida.

Sandberg, R.D. & Sandham, N.D. (2006). Non-reflecting Zonal Characteristic boundary condition for Direct Numerical Simulation of Aerodynamic Sound. Tech. Rep. Vol 44 No. 2, AIAA Journal.

Spisso, I. & Rona, A. (2007). A selective overview of high-order finite difference schemes for aeroacoustic applications. In *International Conference on Sound and Vibration*14^{th}, Cairns, Australia.

Tam, C. (2004). Computational Aeroacoustics: an Overview of Computational Challenges and Applications. *Int. J. Computational Fluid Dynamics*, **18**, 547–67.

Tam, C.K.W. (1995). Computational Aeroacoustics: Issues and Methods. *AIAA paper*, 95-0677.

TAM, C.K.W. & DONG, Z. (1993). Wall boundary conditions for high-order finite-difference schemes in computational aeroacoustics. *Theoretical and Computational Fluid Dynamics*, **6**, 303–322.

TAM, C.K.W. & WEB, J.C. (1993). Dispersion-Relation-Preserving finite difference schemes for Computational Acoustics. *Journal of Computational Physics*, **107**, 262–281.

TAM, C.K.W., WEB, J.C. & DONG, Z. (1993). A study of short wave components in computational acoustics. *J. Comput. Acoustics*, **1**, 1–30.

THOMPSON, K.W. (1987). Time dependent boundary conditions for hyperbolic systems. *Journal of Computational Physics*, **68**, 1–24.

THOMPSON, K.W. (1990). Time-dependent boundary conditions for hyperbolic systems, II. *Journal of Computational Physics*, **89**, 439–461.

UK, G. (2003). The Future of Air Transport, White Paper and the Civil Aviation Bill. Tech. rep., UK Department of Transport.

VICHNEVETSKY, R. (1986). Invariance theorems concerning reflection at numerical boundaries. *Journal of Computational Physics*, **63**, 268–282.

VICHNEVETSKY, R. (1987). Wave propagation analysis of difference schemes for hyperbolic equations. A review. *International Journal for Numerical Methods in Fluids*, **7**, 409–452.

VICHNEVETSKY, R. & BOWLES, J. (1982). *Fourier analysis of numerical approximations of hyperbolic equations*. SIAM, Philadelphia.

WALL, C., PIERCE, C.D. & MOIN, P. (2002). A Semi-implicit Method for Resolution of Acoustic Waves in Low Mach Number Flows. *Journal of Computational Physics*, **181**, 545–563.

WANG, M. & MOIN, P. (2000). Computation of Trailing-Edge Flow and Noise Using Large-Eddy Simulation. *AIAA Journal*, **38**, 2201–2209.

WHITHAM, G. (1974). *Linear and Nonlinear waves*. John Wiley Sons, New York.

ZHUANG, M. & CHEN, R. (1998). Optimized upwind dispersion-relation-preserving finite difference scheme for computational aeroacoustic. *AIAA Journal*, **36**, 2146–8.